RESOLUTION OF LATTICE DEFECTS IN METALS

BY POSITRON ANNIHILATION

A Thesis Submitted for the Degree of
Doctor of Philosophy by

MICHAEL JOHN MCGETRICK
B.Sc. (Hons) London

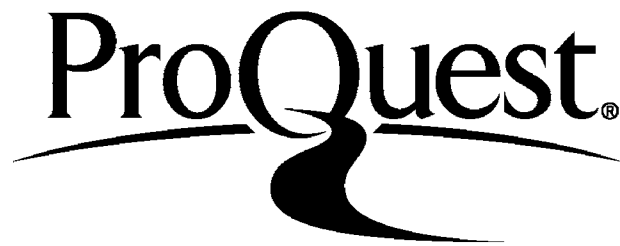· Physics Department
Bedford College
University of London

ProQuest Number: 10098414

All rights reserved

INFORMATION TO ALL USERS
The quality of this reproduction is dependent upon the quality of the copy submitted.

In the unlikely event that the author did not send a complete manuscript
and there are missing pages, these will be noted. Also, if material had to be removed,
a note will indicate the deletion.

ABSTRACT

Positron annihilation has now become a much-used technique for the study of defects in solids, particularly in metals and alloys. The work in this thesis describes measurements made on a Doppler-broadening spectroscopy system designed to study the annihilation radiation emerging from metal samples as a consequence of electron-positron interaction. Defects can be produced in metals by thermal, mechanical or irradiation treatments. For the metals Cu, Al, Ni, Fe and Ti, an assessment has been made of the nature and number of defect types encountered in the mechanically deformed state by analysis of the annihilation lineshapes. Defects in molybdenum produced by neutron-irradiation have also been studied. The defect environment is seen to be dependent on the irradiation temperature.

Running integrals of the difference between the annihilation lineshapes from defective and reference (annealed) samples have provided defect-specific parameters characterising the shape of the centre-of-mass momentum distributions resulting from annihilations at defect traps. In order to assess the defect species in the mechanically deformed state, these parameters have been used to monitor positron annihilation behaviour during isochronal annealing. Under favourable circumstances, individual defect-types have been characterised.

The nature of the electron environment and of the positron behaviour at a specific defect site has been assessed by fitting a model to the observed lineshapes to account for the electron and positron momentum distributions. Such analysis has yielded estimates of the positron zero-point energy and local Fermi electron energies associated with individual defect-types. In the case of copper and aluminium, the calculated zero-point energy of $\sim$ 6 eV associated with positron trapping at vacancies is found to be identical to that derived for dislocation trapping. It is concluded that positrons undergo point-like trapping at dislocations, either by trapping at jogs or at other irregularities along the dislocation line.

Trapping model fits to data from mechanically deformed samples reveal the nature of the stress-strain, work-hardening relationship associated with the mechanical deformation process.

<u>T A B L E   O F   C O N T E N T S</u>

CHAPTER 3: EXPERIMENTAL APPROACH

CHAPTER 4: LINESHAPE ANALYSIS

CHAPTER 5:   DEFECTS IN MECHANICALLY DEFORMED COPPER

CHAPTER 6:   DEFECTS IN MECHANICALLY DEFORMED ALUMINIUM

CHAPTER 1 : DEFECTS IN METALS

1.1 INTRODUCTION

All real solids possess defects. The existence of certain concentrations for certain types of defects in a solid state system is inevitable because nature has decreed that their presence is desirable. These are the defects necessary to achieve thermal equilibrium. At the same time there may be other defect types that nature has deemed undesirable because they prevent the state of thermal equilibrium from being achieved. These unnecessary defects are normally introduced to the system as a result of external influences. These influences may be due to plastic or elastic deformation, particle bombardment or even sudden changes in temperature. As real systems normally do not exist in isolation they are regularly subject to these external influences and so a finite probability exists that they contain undesirable defects.

Defects are likely to affect the properties of matter and so it is important to study them. It is unfortunate that certain kinds of defects (introduced by external influences) are likely to cause the failure of many materials. This is a problem inherent to the technological world where components, or parts of machinery, are continually subjected to stress and the consequences are sometimes disastrous. Recent air disasters, in which structural defects caused by fatigue have occurred, may be cited as evidence of this. Also, in the field of nuclear technology, defects produced in working parts of reactors by neutron bombardment have given cause for alarm. The Windscale incident of 1957 may be seen as evidence of this (Atomic Energy Office, 1957). On the other hand, the deliberate utilisation of defects can be of greater benefit to the technological world. For instance, the controlled addition of impurity defects into semiconductors has led us into the 'age of the microprocessor'. More recently research has been directed at utilising F centre defects in calcium fluoride to act as memory stores for possible future use in computer systems (R.C. Duncan, 1972). Defects can be a help rather than a hindrance!

It is the purpose of this thesis to shed light on the nature of defects by using the phenomenon of positron annihilation. The rest of this chapter is devoted to a discussion on defects, why they exist and how they may be produced, with special emphasis on the kinds of defect damage relevant to this study. This leads onto a discussion of defect detection and, finally, to discuss how positrons may be used for defect studies.

1.2 POINT DEFECTS

1.2.1 A Thermodynamical Approach

Point defects are generally considered to be those which have dimensions comparable with the size of an atom. Figure 1.2.1 illustrates a few of the more typical point defects encountered in metals. A vacancy is produced when an atom departs from its own equilibrium lattice position so leaving a vacancy. The dislodged atom may then go to the surface of the crystal or find some interstitial position and squeeze in there. If the dislodged atom goes to the surface then the vacancy is termed a Schottky defect. If, however, it squeezes in amongst other atoms in the lattice the vacancy-interstitial pair is termed a Frenkel defect. In figure 1.2.1 A and B represent a Frenkel pair. Impurities may also exist in the metallic lattice and are shown in figure 1.2.1 as C and D, where C is a substitutional impurity and D an interstitial impurity, and are so called for obvious reasons.

The concept of a naturally occurring imperfect lattice has been discussed in section 1.1. In fact, the whole lattice is in a constant state of disorder because of the effects of thermal vibrations. It is as a direct consequence of these vibrations, or phonons as they are called, that enough random energy can be deposited at any one atomic position at any particular time to allow a point defect to be generated. With the help of thermodynamics an attempt can be made to assess the amount of disorder, and to predict the concentration of point defects generated as a result of such thermal activity.

If the lattice is a thermodynamic system in equilibrium with its
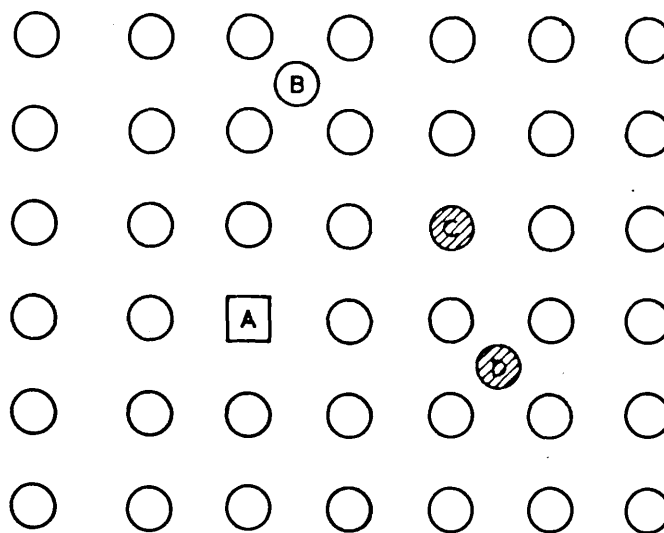
Figure 1.2.1   Simple point defects (Courtesy A E Hughes, 1975)

$$\frac{n}{N} = \exp\left(\frac{-1 \cdot 0\,eV}{kT}\right)$$
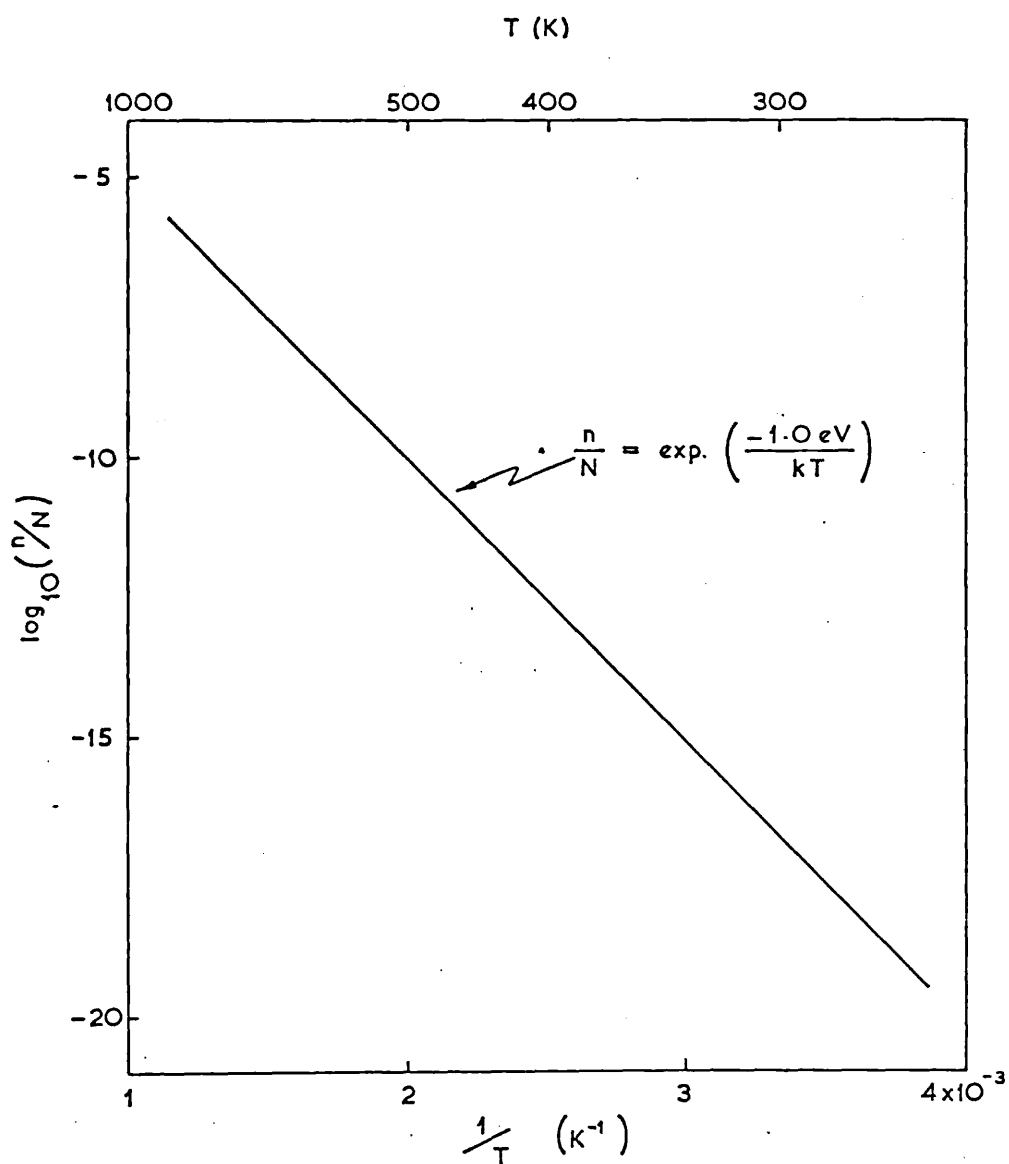
Figure 1.2.2   Variation of Schottky defect concentration with temperature (Courtesy A E Hughes, 1975)

surroundings, and both the volume and the temperature are constant, then the Helmholtz free energy, H, for the system may be described by

$$H = U - TS \qquad 1.2.1$$

where U is the internal energy, T the temperature and S the entropy of the system. The entropy is a quantity that expresses the disorder of the system. There are many more ways of disordering systems than ordering them, and nature reflects this phenomenon in the way it distributes its energy, thereby producing random distributions of point defects. The entropy due to the random distribution of point defects is given by the relation

$$S = k\log_e W \qquad 1.2.2$$

where W is the number of ways of arranging the defects in the lattice matrix and k Boltzmann's constant.

The presence of a defect will increase both the internal energy and entropy of the lattice. For thermal equilibrium to be achieved the resulting free energy will be kept to a minimum with respect to the defect concentration. Accordingly, it can be shown, using equations 1.2.1 and 1.2.2, that

$$C_r = \exp(\Delta S_{re}/k) \exp(-E_f^r/kT) \qquad 1.2.3$$

where C_r is the concentration of the rth type of defect, E_f^r the energy required to form the rth defect, and ΔS_{re} the change in phonon entropy per defect. It is apparent from equation 1.2.3 that for any T > 0 there exists a finite concentration of point defects in the crystal.

1.2.2 Vacancies and Interstitials

The energy required to produce a vacancy has been theoretically estimated to be about 1 eV. Experiment has also confirmed this

(e.g. Rice-Evans et al, 1976). If the presence of a vacancy has a small perturbing effect on the lattice vibrations then the entropy term in equation 1.2.3 will tend to unity. The concentration of vacancies may, therefore, be written as

$$C_V = \exp(- E_f^V/kT) \qquad\qquad 1.2.4$$

where E_f^V is the formation energy of a vacancy. Invoking equation 1.2.4 it is seen that the concentration of defects at room temperature will be approximately 10^{-18} - a vacancy for every 10^{18} atoms. However, if the temperature is raised to 1000°C a vacancy will occur for every 10,000 atoms. The effect of an increase in temperature has a dramatic effect on the equilibrium vacancy population. This temperature effect will, therefore, have implications for defect behaviour in components working at elevated temperatures (~ 200°C) where non-equilibrium defect populations have already been introduced by stress or fatigue. The variation of vacancy concentration with temperature is seen in figure 1.2.2 for the case of an energy formation of 1 eV.

Theoretical predictions estimate that the formation energy for the production of an interstitial is somewhat larger than for vacancies. This is to be expected because squeezing an atom into some interstitial position requires a lot of energy to re-arrange the surrounding lattice. Uusually an interstitial formation energy, E_f^i, is about twice that for vacancies (e.g. Meechan and Sosin, 1959). Equation 1.2.3 now predicts an interstitial concentration of 10^{-35} at room temperature for E = 2 eV. Clearly, the probability for the existence of an interstitial defect is several orders of magnitude lower than for vacancies. Thus, in thermal equilibrium nature favours the existence of Schottky rather than Frenkel defects.

1.3 EXTENDED DEFECTS

1.3.1 Line Defects

A line defect represents a defected region over many atomic

spacings. Dislocations are examples of line defects. Two special types of dislocations are illustrated in figure 1.3.1. An edge dislocation is usually produced as the result of atomic slip. The subsequent dislocation comes about due to the 'wedging in' of an extra plane on one half of the lattice. Figure 1.3.1a shows an edge dislocation and the region of the dislocation core A'B'C'D'. The line running through the crystal perpendicular to the plane A'B'C'D' is known as the dislocation line. It is apparent that the dislocation line represents a region of high stress and distortion. A special vector is normally used to represent the magnitude and direction of the distortion and is known as the Burger's vector $\underline{b}$. The Burger's vector is illustrated in figure 1.3.1a and represents the extra distance that must be travelled in order to complete a circuit such as ABCD. Clearly, the extra distance required in circuit A'B'C'D' is A'E' and is equal to the magnitude of $\underline{b}$. In the case of an edge dislocation it is seen that the direction of distortion is perpendicular to the dislocation line.

Figure 1.3.1b illustrates a screw dislocation. The dislocation results due to a shear distortion of $\underline{b}$ along the dislocation line. The effect around the dislocation core has been for successive atomic planes to be linked via a helical path.

Another type of line defect is known as the dislocation loop. Essentially, the dislocation core is now a circular line or loop rather than a straight line. These are normally produced as a result of the collapse of clusters of point defects. They will be discussed in more detail in section 1.5.2.1.

In reality combinations of the above dislocation types may exist making dislocation structure extremely complex. For instance dislocation dipoles may be created when two parallel dislocations of opposite sign are closely spaced together. Also, dislocation jogs may be formed when two dislocations meet and cut through each other. In such mechanisms a discontinuity, or jog, in the dislocation line is formed at the point of intersection.

Extra half-plane

Slip-plane
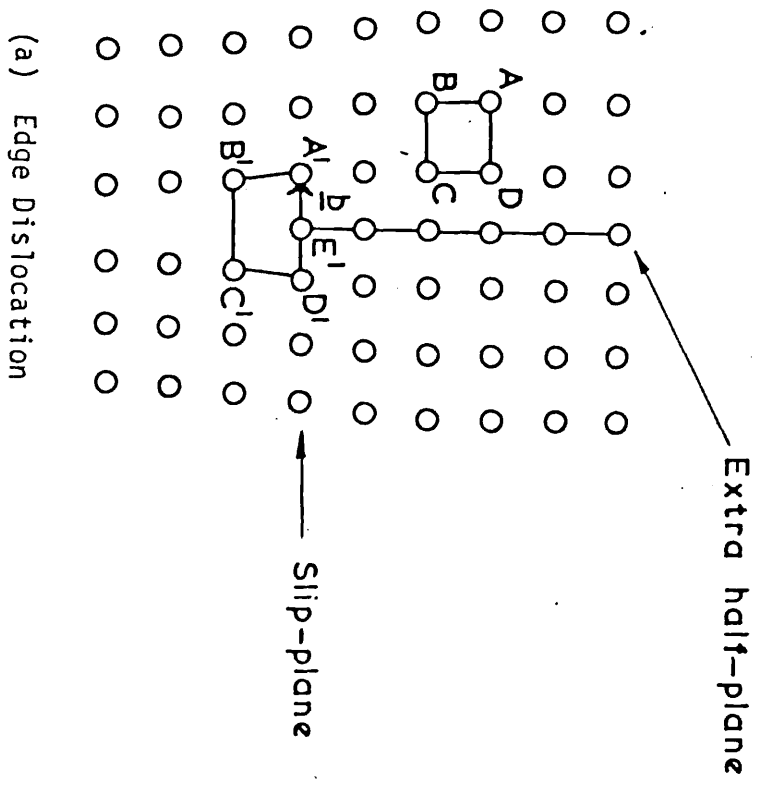
(a) Edge Dislocation

Figure 1.3.1 (Courtesy A E Hughes, 1975)
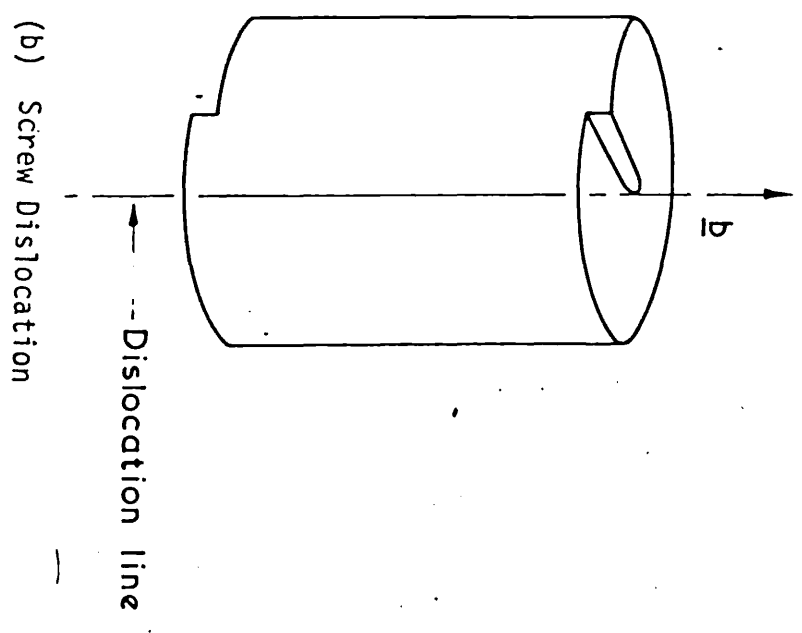
(b) Screw Dislocation

--Dislocation line

b

1.3.2 Grain Boundaries

A polycrystal is made up of many fine crystallites, or grains as they are called, and are randomly oriented. Consequently neighbouring grains never match up perfectly. The grain boundaries are areas of very complex defect structure. If the angle of mis-match is small the defects are predominantly arrays of line dislocations. However, as the angle of mis-match becomes greater the dislocation lengths become smaller eventually disappearing leaving an area of more complex atomic geometry.

1.3.3 Stacking Faults

Crystals stack their planes in certain regular arrangements. In hcp and fcc metals the planes are stacked hexagonally in order to minimise the unoccupied volume. The hcp structure is characterised by the familiar ABABAB .... notation whereas the fcc structure obeys the familiar ABCABC .... notation. Defects in the regular stacking may sometimes occur. For instance, the fcc structure may become ABABCA. Here, the third stacking arrangement has been lost.

1.3.4 Existence of Line Defects in Real Metals

1.3.4.1 A Thermodynamical Approach

Consider the existence of a dislocation in a metallic lattice. Both the internal energy and the entropy of the system will increase due to its presence. In order to predict how favourable it is for dislocations to exist in the lattice it is necessary to estimate the entropy and internal energy changes associated with it.

The formation energy of a screw dislocation can be calculated by considering the strain energy it has caused around it. The elastic stored energy per unit length E is given by

$$E = \frac{Gb^2}{4\pi} \log_e (R/r_c)$$ 1.3.1

where G is the shear modulus of elasticity, $\underline{b}$ the Burger's vector and r_c the radial distance from the core of the dislocation at which the stored energy becomes elastic. A similar expression can be obtained for edge dislocations. The radial distance R is effectively the length of the crystal. It has been shown (Cottrell, 1953) that the stored energy in the non-elastic core region is given approximately by $Gab^2/3$ where a is the atomic spacing. This region exists for $r_c \sim 10 \, \text{Å}$. If R is taken to be 1 cm, $G = 4 \times 10^{11}$ dynes/cm, $b \sim a$, then from equation 1.3.1 the elastic stored energy is found to be about 8 eV per atomic plane through which the dislocation passes. Using the expression for non-elastic energy, a value of about 1.3 eV is derived. Clearly, the elastic energy dominates the total stored energy.

A dislocation cannot be arranged in as many ways as point defects and hence its entropy will be low. In fact Cottrell (1953) has shown that the entropy due to the presence of a line dislocation is about 10^{-6} k. If a very flexible dislocation is postulated - that is one that can meander through nearest atomic planes - Cottrell estimated an entropy of about 2 k per atomic plane. Whatever the type of dislocation considered, its entropy is low compared to the elastic strain energy. Hence, to a good approximation using equation 1.2.1

$$\Delta H = E = U_f^d \qquad\qquad 1.3.2$$

where U_f^d is the energy of formation for one dislocation. Immediately equation 1.3.2 suggests that the presence of dislocations in thermal equilibrium is undesirable because there is no entropy term to help minimise the resulting free energy. Also, the Maxwell-Boltzmann probability of thermally generating 8 eV/ plane along a potential dislocation line at any particular oscillation, even for a temperature of 1000°C, is virtually non-existent. Even a 0.1 probability of generating just 8 eV at 1000°C would take 10^{12} years! It seems statistical thermodynamics does not predict the existence of dislocations in thermal equilibrium. However, dislocations do exist in crystals (section 1.3.4.2) and, as will be

discussed below, the weakness of metals can only be explained in terms of them.

1.3.4.2 Mechanical Properties and Evidence for Dislocations

The critical shear stress, or yield stress σ_c, is that which is required to achieve plastic deformation. A simple method for theoretically obtaining an estimate of this stress was initially proposed by Frenkel. Figure 1.3.2 shows two neighbouring atomic planes moving over each other. The argument assumes that the force required to achieve this is a periodic function of the lattice spacing a, and if x is the distance moved then the shear stress σ_s is given by

$$\sigma_s = \sigma_c \sin (2\pi x/ a) \qquad\qquad 1.3.3$$

If the stresses are small and the deformation elastic the shear strain $e = x/a = \sigma_s /G$ where G is the modulus of rigidity. Substituting in equation 1.3.3 and assuming sin x ⟶ x for small x one obtains

$$\sigma_c = G/2\pi \qquad\qquad 1.3.4$$

Equation 1.3.4 predicts the shear stress to be of the same order of magnitude as the rigidity modulus. However, experimental observation finds a discrepancy of about 10^4 between theoretical and measured stresses, the observed values being lower than the predicted ones. In other words, plastic deformation is much easier to achieve than the theory would indicate.

Peierls, Nabarro and Cottrell (Cottrell, 1953) have shown that if a dislocation exists in the lattice then the force required to move it is given by

$$\sigma = \frac{2G}{(1 - \nu)} \exp(- 2\pi a/b(1 - \nu)) \qquad\qquad 1.3.5$$

where ν is Poisson's ratio and the other symbols have their usual meanings. If equation 1.3.5 is evaluated for $\nu = 0.3$ and a = b, the shear stress turns out to be about 10^{-4} G. Rather convincingly, the factor 10^{-4} missing in equation 1.3.4 has now been accounted
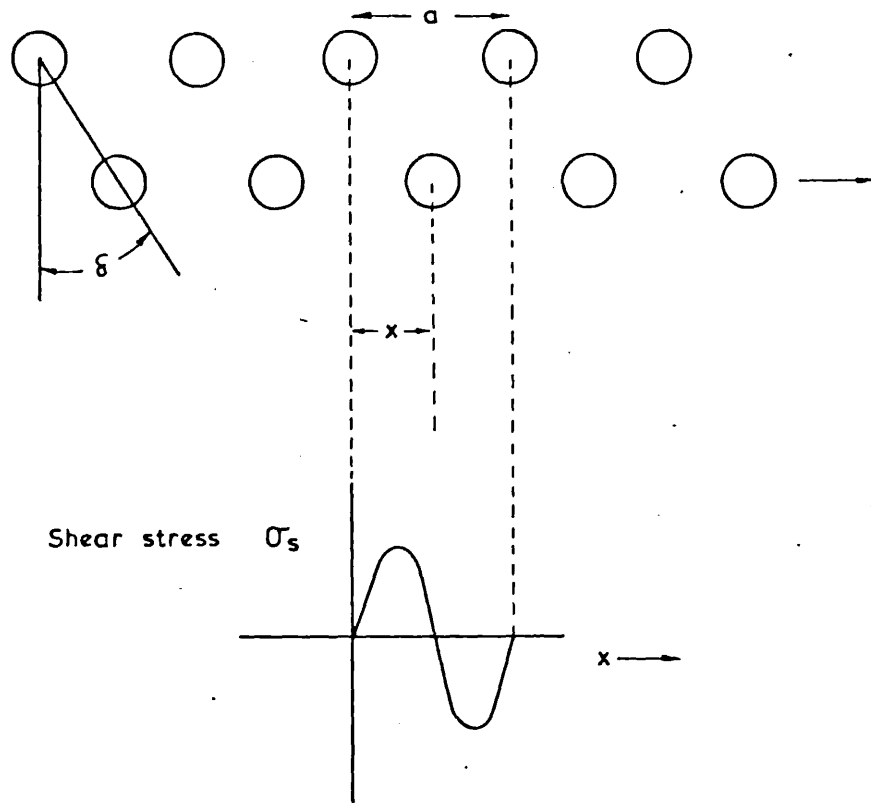
Figure 1.3.2   The shearing of ideal crystal planes (Courtesy
A E Hughes, 1975)
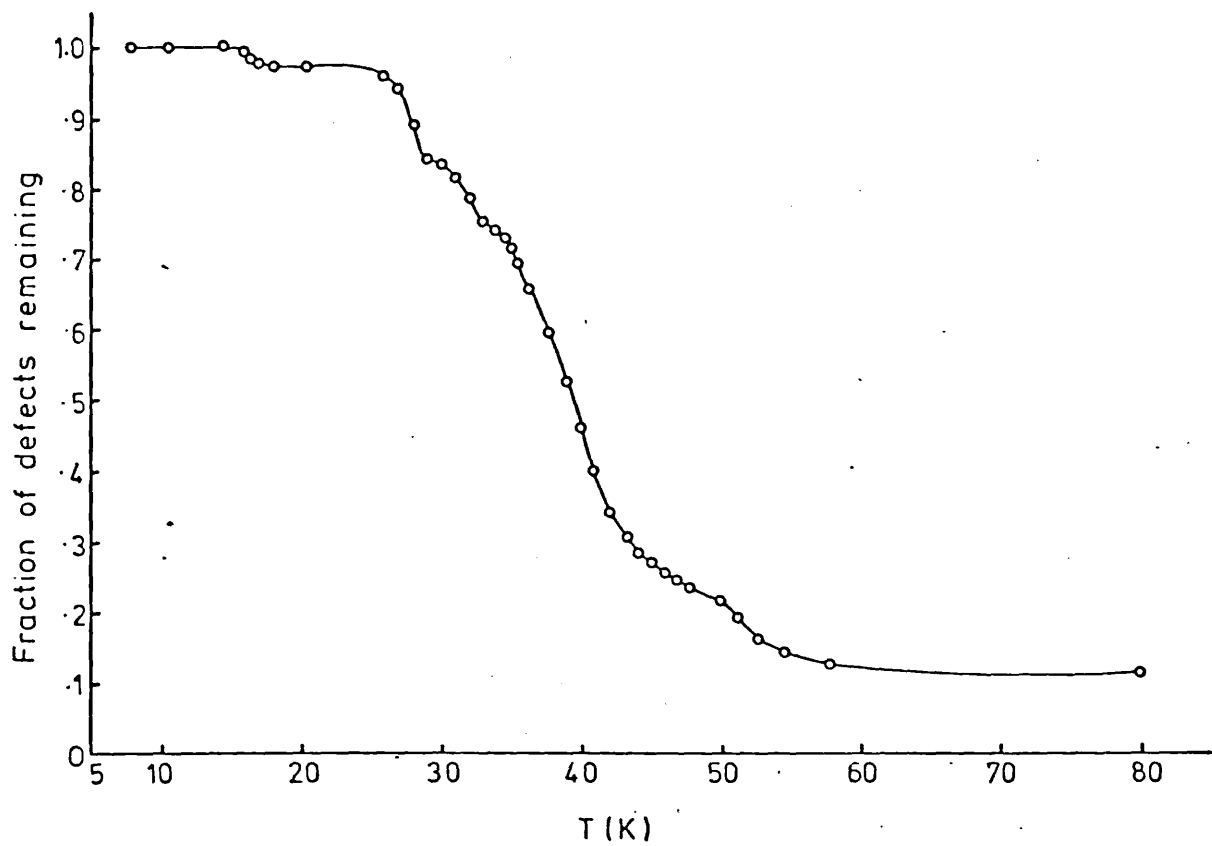
Figure 1.4.1   The annealing of defects in copper after irradiation
with 1.4 MeV electrons at 8K (after Corbett et al, 1959)

for. It was concluded that the presence of dislocations was the cause of the low yield stress values.

Electron microscopy has subsequently confirmed the existence of dislocations in metals. From the considerations of section 1.3.4.1 it is apparent that they exist in non-equilibrium concentrations. It is generally believed that dislocations are introduced into crystal matter as a consequence, of imperfect crystal growth. For instance, in the condensation of atoms from the vapour to the solid state it may be impossible for them to find their right positions quickly enough, thus initiating dislocation lines. The presence of small stress fields existing in the lattice may then substantially multiply the dislocation population through the Frank-Read mechanism (Frank and Read, 1950).

1.4 DIFFUSION

1.4.1 A Transport Mechanism for Defects

In a defected lattice where an inhomogeneous defect population exists the motion of defects is governed by Fick's law which states

$$J = - D \ (dn/dx) \qquad\qquad 1.4.1$$

where J is the number of defects crossing unit area of plane per second, D is the diffusion coefficient and dn/dx is the concentration gradient normal to the plane. When the defect concentration gradient becomes zero, transport activity due to this influence will cease. A second equation following on from equation 1.4.1 (see for instance Cahn, 1965) is given by

$$dn/dt = D \ d^2n/d \ x^2 \qquad\qquad 1.4.2$$

This equation is readily identified as Fourier's equation describing the problem of heat flow. The analogy with the defect problem outlined above is obvious - both problems are concerned with homogenisation.

The movement of point defects is achieved by the jumping of

interstitials or vacancies into neighbouring atomic sites. It is also generally believed that dislocations move or climb by the migration of vacancies or interstitials to them (Read, 1953). This jumping process is known as diffusion.

The stress fields supplying the energy to move atoms around are usually not very high and so on their own are not particularly good motivators for diffusion. A more important influence is temperature. Before diffusion can occur the defect must have enough energy to overcome its binding forces (the energy of migration). if v is the frequency of oscillation of the defect and E_m^r the energy required to allow the rth defect to jump from its stable position then the number of jumps, p, made in one second is given by

$$p = v \exp(- E_m^r/kT) \qquad 1.4.3$$

where $\exp(-E_m^r/kT)$ is the Maxwell-Boltzmann probability that an oscillation will have the energy E_m^r. Using equations 1.4.1 and 1.4.3 the diffusion coefficient is given by

$$D = v a^2 \exp(-E_m^r/kT) \qquad 1.4.4$$

Because of the exponential nature of equation 1.4.4 diffusion is dramatically influenced by increases in temperature. In fact the heating up of crystals is the standard way of annealing out defects.

1.4.2 Isochronal Annealing

Isochronal annealing plays an important role in the study of defects. Consider the case of non-equilibrium defects introduced as a result of plastic deformation. The types of defect species present are characteristic in the sense that their formation and migration energies are likely to be different. Consequently, the different types will anneal out at different temperatures. This migration activity can be observed by carrying out an isochronal anneal. Briefly, the isochronal anneal is performed by raising the deformed crystal in intervals to

successively higher temperatures. At each temperature the crystal is measured for defectiveness; for example by measuring the stored energy in the lattice or its electrical resistivity(see section 1.6). Whenever a defect species disappears a change should be registered. The resulting recovery curve can give valuable information on the migratory temperatures of each species and allows an attempt at identifying the likely nature of the species through an assessment of their migratory energies. Figure 1.4.1 shows the recovery curve of defects in copper produced as a result of electron-irradiation as obtained by Corbett et al (1959) measuring changes in electrical resistivity.

1.5 GENERATION OF NON-EQUILIBRIUM DEFECT POPULATIONS

The generation of defects due to plastic deformation and particle bombardment has important implications for technology. For this reason, and the fact that these defect production techniques bear direct relevance to this thesis, they shall be discussed below.

1.5.1 Plastic Deformation

1.5.1.1 Stress-Strain Relationships

When a crystal is subjected to elastic stress the strain fields last only for as long as the stress is applied and obey Hooke's law. The onset of plastic deformation occurs when the applied stress produces permanent strain fields and distortion. The general stress-strain curve for a polycrystalline metal is illustrated in figure 1.5.1a.

The initial stage of the graph OA corresponds to elastic behaviour and is linear in accordance with Hooke's law. At the point A the yield stress is reached and plastic flow sets in. This normally occurs for low strains - the highest yield strains observed are $\simeq 0.5\%$. The second stage of the curve AB corresponds to plastic behaviour. If the stress applied were suddenly released at·the point C the metal would recover elastically to the point D retaining the strain indicated at this point. For subsequent stresses the elastic flow follows the path

Stress

τ_c

τ_y

A

C

B

D
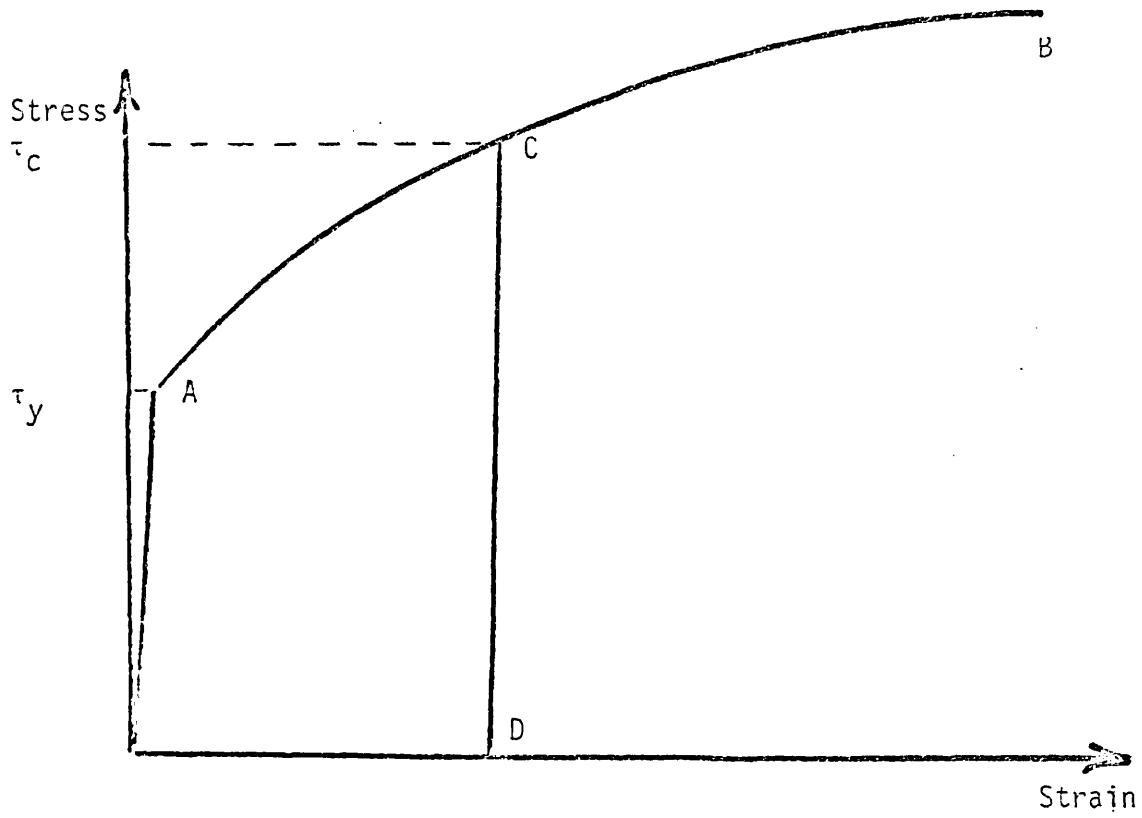
Strain

a)   The stress-strain curve of a polycrystalline
metal under tension

Stress

III

II

I

τ_c
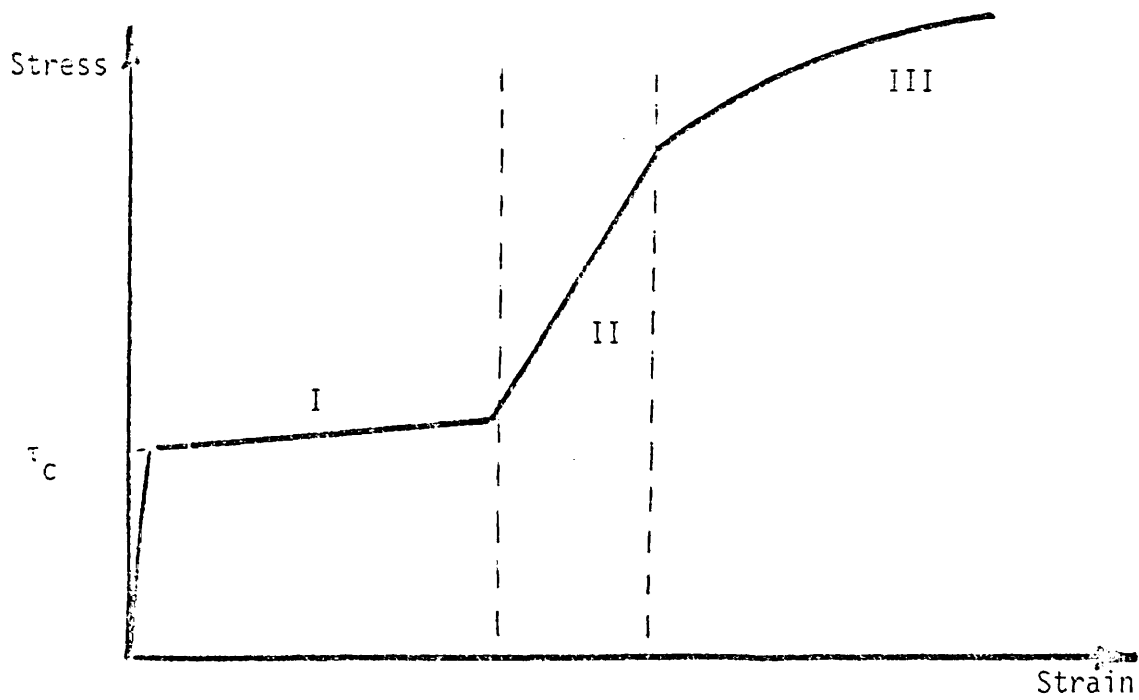
Strain

b)   Typical stress-strain curve for a single
crystal metal

Figure 1.5.1

DC and plastic flow is now achieved for a stress τ_c where $\tau_c > \tau_y$. It appears that the metal has a greater resistance to plastic deformation. This phenomenon is due to work-hardening and will be discussed below.

1.5.1.2 Work-Hardening

The phenomenon of work-hardening can be best interpreted by a consideration of the stages of deformation characterising a single crystal. The polycrystal complicates matters since it consists of an array of randomly oriented single crystals. Figure 1.5.1b illustrates the stress-strain relationship for a single crystal. The curve has been traditionally split up into three work-hardening regions - stages I, II and III repsectively. The precise profile of the curve and the relative significance of each stage is determined by the crystal structure. For instance, stage I in hcp structures will persist up to strains of 100-200% before stage II becomes active whereas stage II is reached by about 5-20% strain in fcc metals.

Qualitatively, the work-hardening process may be described as follows. When a metal is plastically deformed the shear stresses introduce dislocations and point defects. Initially slip is confined to one plane and so dislocations produced on parallel planes can move with relative ease. The shallow slope defined in figure 1.5.1b for stage I illustrates this and is also known as the easy glide region. As the stress is increased more damage is produced. Dislocation densities can rapidly multiply due to increased point defect debris through the Frank-Read mechanism. At a certain stage dislocation lines become cross-slipped and the intersection of different dislocations becomes possible. This dramatically impedes dislocation motion and so much higher stresses are needed to continue the deformation. This description can account for the higher stresses required to achieve further strain. It is also desirable to quantitatively explain the nature of the stress-strain relationships. Various theoretical models have been proposed but at the present time no one model enjoys universal acceptance.

One school of thought is based on the long-range stress fields

associated with dislocations. The stress field can be shown to vary as 1/r (Cottrell, 1953) where r is the radial distance from the dislocation core. Taylor (1934) developed a long range work-hardening theory by considering the average distance between dislocations and the stresses they imposed. By considering the extra stress to achieve plastic flow to be equal to the maximum internal stress he obtained

$$\sigma = Gb\,\rho^{\frac{1}{2}}/2 \qquad\qquad 1.5.1$$

where G is the rigidity modulus, b the Burger's vector and ρ the dislocation density. This relationship has been experimentally verified by Levinstein and Robinson (1964) on single crystals of silver. However, Young (1962) has obtained results on copper single crystals that conflict with the functional form of equation 1.5.1. Taylor then related ρ to the strain by assuming that every dislocation produced travelled a distance d before its motion was obstructed and that d was independent of the applied stress. The strain E could, therefore, be defined as ρdb and substituting in equation 1.5.1 arrived at the expression

$$\sigma = \frac{G}{2\pi}(bE/d)^{\frac{1}{2}} \qquad\qquad 1.5.2$$

This equation predicts a parabolic relationship between the applied stress and the resulting strain. Most polycrystalline metals obey a parabolic relationship (see figure 1.5.1a).

Stages I and II in figure 1.5.1b are both linear and Seeger has attempted to fit models to both these regions by considering long range mechanisms. Seeger et al (1961) obtained a linear stress-strain model for stage I by assuming that dislocation pile up did not occur. For the case of copper their theoretical estimate for the slope of the curve agreed favourably with experimental data. Stage II was also considered (Seeger, 1957; Seeger et al, 1957) using the same approach as for stage I with the difference that dislocations were assumed to pile up. Again, good agreement was found with experimental data. Finally, stage III was interpreted in terms of screw dislocation cross-slip. This had the effect of decreasing the work-hardening rate

because the cross-slip process relaxed the high stress fields associated with dislocation pile ups.

Short range work-hardening theories have also been considered. Long range theories assume that average distances between dislocations produce appreciable stress fields (for $\rho \sim 10^{15}$ m^{-2} average spacing is about 1000 Å). Short range theories assume effective defect interactions to be significant only over a few atomic distances. Such theories mostly assume that resistance to dislocation motion is due to the presence of debris left in the wake of other dislocations. Gilman (1962) has proposed that debris consists of dislocation dipoles and that these can be generated at dislocation jogs. As the stress is increased so is the debris, and so deformation becomes increasingly more difficult. Debris may also consist of vacancies and small dislocation loops (Kuhlmann-Wilsdorf, 1962). They believe that the interaction of the debris with the moving straight dislocation forces it to become crooked and eventually to become tangled. Such a mechanism can severely inhibit plastic flow.

1.5.1.3 Point Defects Produced by Plastic Deformation

Evidence for the existence of point defects produced by plastic deformation may be found in the open literature (e.g. Broom, 1954; Schilling, 1970). An important question to pose is how the generation of point defects varies as a function of the dislocation density. Blewitt et al (1955) measured the change in electrical resistivity for copper single crystals extended at 4K and then again for recovered copper at room temperature for a series of applied stresses. They proposed that the defects recovering at 20°C were vacancies, and showed that for both dislocations and vacancies the change in resistivity associated with them was proportional to the square of the stress. They concluded that the vacancies and dislocations were generated by a similar process. Pry and Henning (1954) found that the concentration of point defects was determined by the existing number of dislocations as a result of resistivity measurements on deformed copper wires.

Clearly, experimental evidence suggests that the presence of dislocations is responsible for the existence of point defects. A

popular theory attempting to account for these observations proposes that point defects are created by the non-conservative motion of dislocation jogs that may exist on screw dislocations as a result of dislocation cutting mechanisms. This mechanism would be expected to become important only when slip on more than one plane occurred. Evidence to support this view has been brought to bear by Masima and Sachs (1928a, b). They showed that the resistivity of α-brass single crystals remained almost constant when slip was confined to one plane, whereas when multiple slip came into play a marked increase in the resistivity occurred. It is not clear at this stage whether the point defects produced are of a vacancy or an interstitial nature. Cottrell (1957) has concluded that only interstitials can be formed as a result of dislocation cutting on the grounds of geometrical considerations. However, Seeger (1958) proposes that, in principle, equal numbers of both types should be generated. An experiment performed by Takamura et al (1962), estimating interstitials to be 10-20% of the total point defect concentration, would tend to favour the Cottrell theory.

Experimental evidence shows that the resistivity change due to deformation can be related to the strain through the general relation

$$\Delta\rho = AE^n \qquad\qquad 1.5.3$$

where A is a constant and n the exponent of the strain E. Most workers in the field have found values of n varying between 1 and 1.5. Since theory shows that the electrical resistivity is linearly proportional to the point defect concentration, C, it follows on from equation 1.5.3 that

$$C = \alpha E^n = \beta\sigma^m \qquad\qquad 1.5.4$$

where σ is the shear applied stress, and α and β constants, and m the exponent of σ.

1.5.2 Radiation Damage

1.5.2.1 Creation of Point Defects and Small Defect Clusters

When a crystal is bombarded with energetic particles (e.g. neutrons and electrons) energy will be transferred to the lattice as a result of their collisions with atoms. If in one collision enough energy is imparted to an atom to overcome its binding forces it will suffer a displacement and a vacancy-interstitial pair will be created. If the interstitials created have sufficient energy they, too, will displace other atoms and a collision cascade will occur. Such a sequence of events is illustrated in figure 1.5.2. To begin with there will be an equal number of vacancies and interstitials existing in the lattice. However, as will be seen later, this will not remain the case for long. If temperatures are high enough vacancies and interstitials will become mobile eventually meeting and so mutually annihilating. The rate of recombination of vacancy-interstitial pairs is governed by their jump frequencies and, since the ability to jump is dependent on thermal activity, recombination will be enhanced by increases in crystal temperature. Even at low temperatures where temperature-dependent diffusion mechanisms effectively do not operate a certain amount of annealing can occur if vacancies and interstitials are sufficiently close to each other. In this case the local strain fields associated with each defect will produce a potential gradient between the two providing enough attractive force to recombine them overcoming the binding forces that lock them to their stable positions. This mechanism will become significant for high doses of bombardment where there is a higher probability of finding interstitials and vacancies near to each other.

Mobile vacancies may meet up with others forming agglomerates of vacancies. These vacancy clusters, if not too large, are preferred because their configurational energies are less than the energy required for the same number of vacancies present in isolation (e.g. see Thompson, 1969). In the case of interstitials clusters do not generally form because of the very high strain energies that would be associated with the surrounding lattice. However, planar interstitial clusters may exist. These may be thought of as an extra plane of

O = Vacancy defects

● = Interstitial defects

—— = Ion tracks
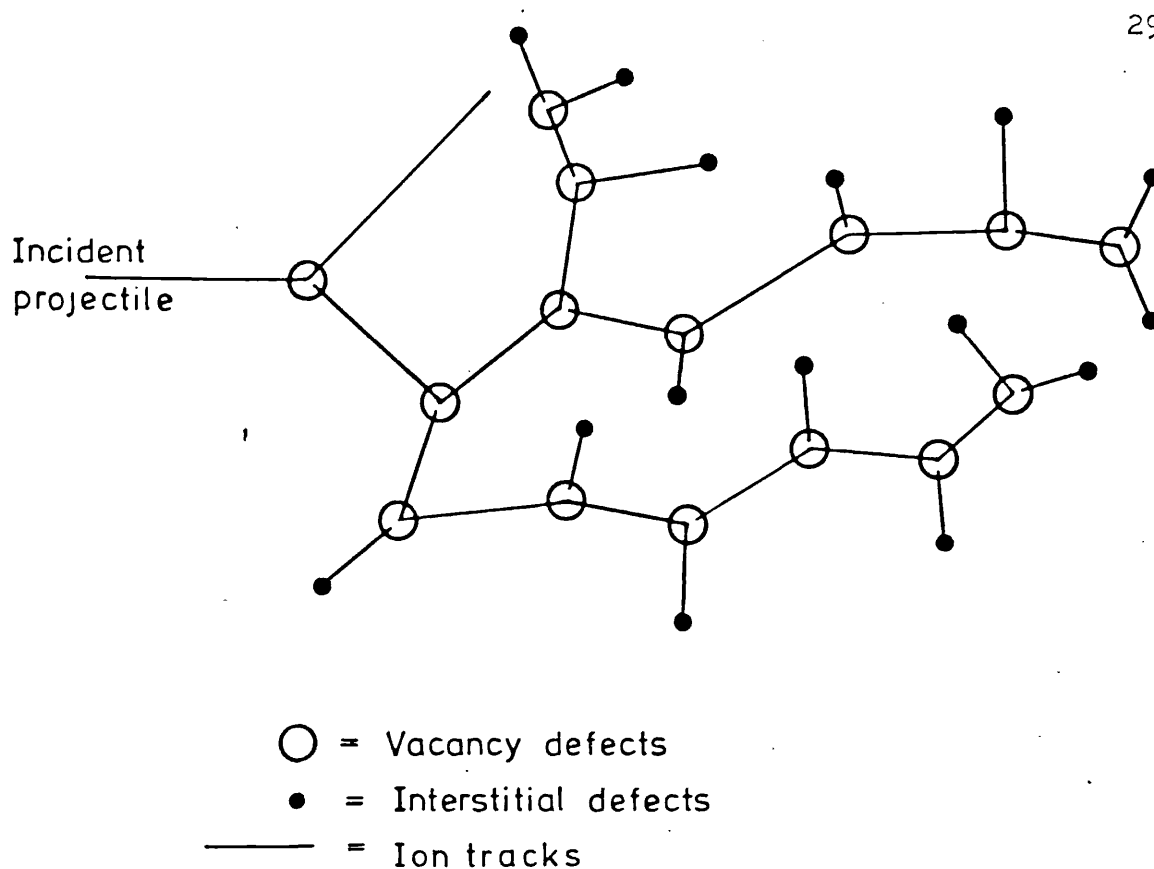
Figure 1.5.2   A displacement collision cascade (Courtesy A E Hughes, 1975)
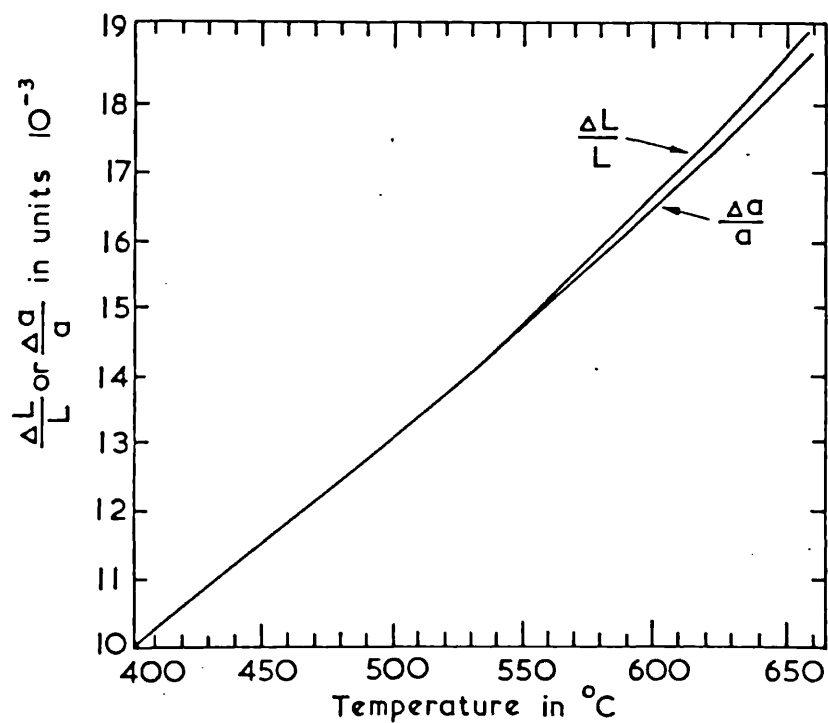
Figure 1.6.1   The change in macroscopic length and lattice parameter for a sample of aluminium as a function of temperature (after Simmons and Balluffi, 1960)

atoms, the periphery of which may be considered to be a looped edge dislocation.

In all irradiations taking place at room or at higher temperatures all the above mechanisms may operate since, for some metals, the temperature range at which vacancies and interstitials are mobile is well below room temperature. In general mobility temperatures for interstitials are in the range 50-100K (e.g. Walker, 1962). It is expected that interstitials become mobile before vacancies since they act under the influence of a greater driving force due to the greater stress fields they exert in their locality.

1.5.2.2 Large Defect Clusters and Voids

It is energetically favourable for small vacancy clusters to live in an irradiated crystal lattice. This is apparent from the expression relating the energy of formation of a cluster to that of a vacancy that emerges from a consideration of the rigid continuum model (Thompson, 1969). One obtains

$$U_f^{nv} = n^{2/3} U_f^v \qquad 1.5.5$$

where U_f^v is the formation energy for a vacancy and
U_f^{nv} the formation energy for a cluster of n vacancies.
However, after a certain critical size, due to surface energy considerations, a lower configurational energy can be achieved if the cluster collapses into a planar type. Planar clusters produce vacancy or interstitial loops depending on whether the cluster results in the removal or the addition of an extra atomic plane. As a consequence of such arguments it was expected that the only kinds of defects present in an irradiated crystal would be small defect clusters or dislocation loops, and that large defect clusters (voids) could not possibly exist. Experimental evidence, however, proved this exception to be false.

From measurements of volume expansions of fuel cladding samples taken from the Dounreay fast reactor in 1966 it was discovered that large spherical cavities were present. It was expected that the

swelling associated with the samples would be small because any changes in macroscopic size due to the presence of interstitial and vacancy loops would tend to cancel each other out. Rather dramatically, swelling of several percent occurred and voids in diameter of up to 100 nm were seen to be present. Since then electron microscope work has been extensively carried out on irradiated metals, and has confirmed that, under the right conditions, voids can be formed (e.g. Cawthorne and Fulton, 1966).

It is now generally believed that voids are nucleated because of the existence of impurity gas atoms in the lattice. For instance, helium nuclei can be produced by neutron irradiation of the host material and impurities within it by (n, α) relations. Helium is relatively insoluble in a metal lattice and so will seek out regions of large open volume. Vacancy clusters will, therefore, act as sinks for the helium. Correspondingly an excess pressure will be built up inside the cluster thereby opposing the tendency for surface tension to make it collapse. The result is a stabilisation of the cluster which can then grow in size.

The growth of voids will depend on the flux of vacancies diffusing towards them. If there is an equivalent flow of interstitials to them recombination processes will prevent the vacancies from coalescing with the voids to make them grow. However, it is thought that the vacancy population is in excess of the interstitial because dislocations tend to be more efficient sinks for interstitials than for vacancies. This viewpoint seems sensible when one considers the greater attractive force that exists between interstitials and dislocations due to the higher stress fields associated with the interstitials. The resulting imbalance in vacancy-interstitial population allows a net flux of vacancies to the voids and, thus, void growth occurs.

The rate of growth of voids depends on temperature. When the temperature exceeds a critical value, though, thermal emission of vacancies will become important and the process of void shrinkage will set in (Petersen et al, 1974).

1.6 CONVENTIONAL METHODS OF DEFECT DETECTION

The presence of defects in a crystal lattice will perturb the nature of the microstructure. Also, their presence will affect the properties of the crystal as a whole. Any attempts to study lattice defectiveness will, therefore, revolve around observations of changes in 'micro' and 'macro' properties. Historically, the macro-properties have been generally studied by measuring the increased stored energy and the changes in electrical resistivity associated with the defects. The study of micro-properties are more sophisticated in practical technicality, and involve the interaction of some 'defect sensor' with the microscopic defect locality. An ideal defect sensor should provide information on the nature of the defect and its location within the crystal. Therefore, the study of micro-properties is potentially more useful than macro-studies. However, macro-studies have been important historically and so this section shall be devoted to a brief discussion of both types. Finally, the limitations of such studies shall be discussed leading naturally onto a discussion of positrons as potentially useful defect sensors.

1.6.1 Macroproperties

1.6.1.1 Stored Energy

The presence of defects increases the stored energy of the lattice. When this stored energy is released it will be given up as heat thus increasing the temperature of the crystal. The measurement of such increases in temperature should, therefore, provide information on the lattice defectiveness (e.g. see Thompson, 1969). Meechan and Sosin (1959) performed such experiments on electron-irradiated copper and estimated the interstitial formation energy to be 2.8 eV. This result agrees favourably with theoretical predictions.

1.6.1.2 Electrical Resistivity

Imperfections in a lattice will obstruct electron motion through the mechanism of scattering. Phonons and defects will both act as imperfection centres. However, scattering due to phonon activity is

negligible at low temperatures and so defect populations will be the only cause of resistivity changes. It can be shown for a metal that the resistivity associated with scattering due to the presence of r defect types is given by

$$p = \frac{mV_f}{qe^2} \sum_r C_r \sigma_r \qquad 1.6.1$$

where C_r and σ_r are the concentration and scatter cross-section for the rth type of defect respectively, m and e the rest mass and change of the electron, V_f the electron Fermi velocity, and q the number of free electrons per atom. Equation 1.6.1 shows the effect on the electrical resistivity at low temperatures for different species and concentrations to be simply additive. Hence, the defectiveness of the crystal is directly related to the resistivity measured at low temperatures.

Many experiments to evaluate point defect formation and migration energies have used the technique of measuring changes in resistivity at low temperature. For instance, Corbett et al (1959) have obtained a recovery curve for defects in copper produced by electron-irradiation at 8K (see figure 1.4.1).

1.6.1.3 Macroscopic Changes in Crystal Dimensions

When a Schottky defect is formed the displaced atom goes to the surface (figure 1.2.1). When enough Schottky defects are created an extra layer of atoms will be formed on the surface, thus increasing the macroscopic dimensions of the crystal. The Schottky defect concentration, n/N, can be related to the fractional changes in macroscopic length, $\Delta L/L$, and atomic spacing, $\Delta a/a$, by the relation

$$\frac{\Delta L}{L} - \frac{\Delta a}{a} = 1/3 \; (n/N) \qquad 1.6.2$$

where n is the number of Shottky defects and N the number of atoms in the crystal.

Figure 1.6.1 shows the results obtained by Simmons and Ballufi (1960) for thermally generated defects in aluminium. By obtaining the defect concentration they evaluated the formation energy of a Schottky defect to be 0.75 eV.

1.6.2 Microstructural Determination

1.6.2.1 X-ray Diffraction

Diffraction occurs when waves passing through a lattice have wavelengths comparable with the lattice spacing. Under these conditions there is substantial interaction between the travelling wave and the micro-structure - a condition necessary for a defect sensor. Using the relation $\lambda = hc/E$ for electromagnetic radiation where E is the wave energy, h Planck's constant and c the velocity of light, the wavelength λ for X-rays of E = 10 keV is about 1.24 Å. This, of course, is comparable with atomic spacing. The angles of diffraction for the waves falling on a lattice of spacing d are given by Bragg's law

$$2d\sin\theta = n\lambda \hspace{3cm} 1.6.3$$

Where θ is the angle of diffraction and n an integer. The spacing d can be determined by two similar diffraction techniques. The Laue method is shown in figure 1.6.2a. A single crystal is stationary in an X-ray beam of continuous wavelength. Bragg diffraction occurs for those values of λ that satisfy equation 1.6.3. Analysis of the resulting photographic film can evaluate d. A second method (the powder method), figure 1.6.2b, is slightly different in that the crystal used is polycrystalline and the radiation monochromatic. This is more convenient since single crystals do not have to be specially prepared. The resulting diffraction patterns occur as the result of many planes possible for diffraction provided by the crystal grains. Again the lattice spacing may be evaluated.

Local regions of defectiveness will be sensed because of perturbations in diffracted ray intensity caused by distortions in the lattice structure.

Figure 1.6.3   Electron microscopy of a dislocation
                (Courtesy A E Hughes, 1975)

Figure 1.6.2   Laue and powder diffraction
                techniques (Courtesy A E Hughes,
                1975)

(a) Laue method

(b) Powder method
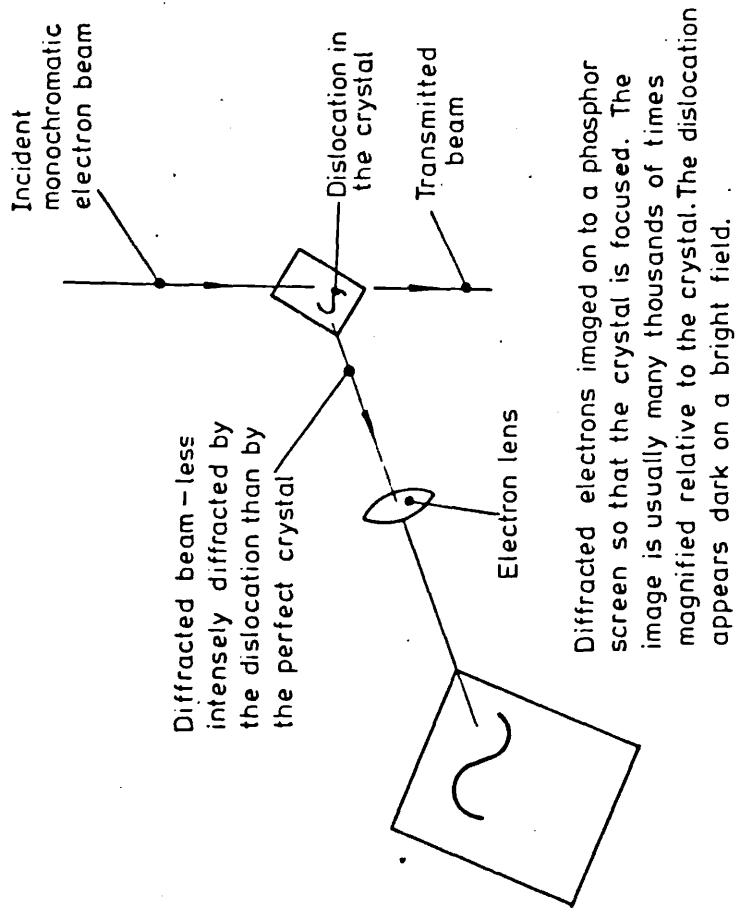
1.6.2.2 Electron Microscopy

Electrons with energies 100-200 keV have wavelengths comparable with atomic spacing and so can be diffracted by the microstructure. The electron microscope works on the principle that in regions of distorted lattice the Bragg diffraction conditions will be different to that of the perfect lattice. This will either result in stronger or less intense diffracted waves. The scattered electrons are captured at the receiving end of the apparatus where they can make imprints on photographic film (or phosphor screens) and trace out areas of darkness and brightness corresponding to the distribution of defects seen in the scanned part of the crystal. Large defects, such as dislocations and voids, can be observed in this way. Figure 1.6.3 shows how a dislocation is scanned using electron microscopy.

Electron microscopy is, to date, an extremely important tool used in the study of defects. It has been used, for instance, extensively to estimate dislocation densities in defected materials and has also evaluated void distributions in irradiated metals.

1.6.3 Limitations of Conventional Techniques

If a stored energy techique is employed to indicate the presence of defects then only when they have annealed out will the defects have been sensed. This is unfortunate since the defect configuration inside the lattice will have been changed or eliminated as a result of the experiment. Since the process is irreversible the original defect configuration will have been lost forever. The type of defect species should, in principle, be identified by a stored energy experiment because the energy released at a particular annealing stage will be characteristic of the formation energy required to form it. However, stored energy experiments on their own do not offer information on the concentration of defects present and so the energy per defect cannot be evaluated, thus ensuring that the defect species cannot be identified.

The concentration of interstitial-vacancy pairs can at least, in the case of irradiation damage at low temperatures, be theoretically calculated from the irradiation energy and dose-rate. Hence, one could

estimate the formation energy of the annealing species by dividing the total released energy by the number of defects present. A similar approach could be used in the case of electrical resistivity measurements where a resistivity change per interstitial-vacancy pair could be evaluated. This is fine when one knows the concentrations present and is sure that no migration processes have occurred. However, for most kinds of damage produced at room temperature all sorts of defects 'occur and theory cannot estimate the types and their individual concentrations. The 'macro' measurements of stored energy and resistivity cannot in these circumstances identify the types and their concentrations. The macro-measurements merely provide signals describing the general defectiveness within the lattice.

Electron microscopy has the ability to distinguish between different types of large defects as a consequence of the imagery provided by the diffracted electrons. For instance, it can distinguish between line dislocations, different types of dislocation loops, and voids. However, it lacks the necessary resolution to see point defects. Also, it is easy to appreciate that electron microscope observations cannot be performed on some samples in situ - e.g. a test-piece in a chamber at liquid helium temperatures being irradiated with neutrons!

An ideal defect detection technique will be sensitive to both point and extended defects, have the ability to distinguish between all possible types of species and assess their concentrations, will not change the state of the lattice as a result of interaction, and will also be relatively easy to handle. Although the attributes of a positron as a defect sensor are far from perfect they do offer hope as a more versatile tool in defect study than any of the techniques discussed above have been.

1.7 DEFECTS AND POSITRONS

The distortion and stress fields that are set up around the vicinity of a defect cause a re-arrangement of the atoms thereby modifying the potential fields between them. Such changes perturb the electron energy states thus causing changes in electron momentum

distributions. Electron densities will also be affected around defect areas so as charge neutrality can be restored. Assuming each type of defect to be unique then the identification of these defects should, in principle, be achieved by monitoring the electron environment around them.

In a metallic lattice open volume defects, such as vacancies and dislocations, are areas of reduced positive ionic charge. Since positrons have positive charges, they will be attracted to these areas preferentially to the rest of the lattice matrix, and will become trapped in them as a consequence of the attractive binding energy. Before the inevitable positron-electron annihilation (chapter 2) positrons will be highly localised in the defect region, thus able to sense the defect electron environment. The gamma rays emitted as a consequence of positron annihilation with electrons at the defect will possess an intrinsic rest mass annihilation energy modified by the motion of the electron positron pair through the Doppler effect. Thus gamma rays can provide information on the electronic momentum distribution structure of the defect and, also, the energy state of the positron trapped in it. If this information can be extracted from the gamma rays then the defect can be characterised.

Over the past ten years positron annihilation has been used extensively to study defects. Berko and Erskine (1967) performed one of the first experiments on plastically deformed aluminium and from the analysis of the angular-correlation distribution obtained concluded that gamma characteristics in the deformed lattice were dramatically different from those obtained on an undeformed, annealed aluminium sample. Positrons can also provide information on the electron density in the region of an open volume defect as a consequence of the slightly reduced electron populations that occur to the restoration of charge neutrality. This results in a slight increase in the mean life of a positron. MacKenzie et al (1967) observed that in a number of metals the mean life of the positrons increased reversibly with increasing temperature. This was attributed to positron trapping at equilibrium populations of vacancies.

If positrons interact with all open volume defect species in a

deformed sample, then in one single measurement information is essentially obtained on the character of all the defects present through the modulations of the gamma rays. The problem is then one of analytical extraction of such information. Positrons do not create damage as a result of their interaction in the lattice and so test-pieces can be used over and over again. Also, conventional positron sources can be relatively inexpensive and easy to use. It appears that the use of positrons in defect study is desirable because many of the criteria outlined in section 1.6.3, concerning the usefulness of defect sensors, may be potentially realised. However, some limitations in the use of positrons must also be described here. Positrons will not in general tend to become trapped at interstitial or some impurity type defects because of the positive charge they exert. Small perturbations in the electronic structure due to the presence of a positron will ensure that the gamma ray will never portray the true character of the defect electron environment it represents. It is obvious that these limitations conflict with the ethos of the ideal defect sensor. Such short-comings should not, however, dissuade the use of positrons in applications where it is potentially invaluable.

The nature of positron annihilation in metals depends on the properties and behaviour of positrons and electrons in the solid state. Accordingly, chapter 2 will be devoted to such a discussion.

C H A P T E R   2   :   E L E C T R O N S   A N D   P O S I T R O N S   I N   M E T A L S

2.1 EXISTENCE OF POSITRONS IN NATURE

Following the failure of the newly formed Quantum Mechanics developed by Schrödinger and Heisenberg in the ninteen-twenties to predict the spin of the electron, Dirac (1928) adapted the theory to include the elements of Einstein's theory of Special Relativity. The consequences were dramatic - in addition to predicting the electron spin, the Dirac formulation also predicted the existence of negative energy electron states suggesting particles of positive electronic charge and electronic mass. A consideration of Special Relativity yields the following expression for the total energy, E, of a relativistic particle

$$E = \left\{ p^2 c^2 + m_0^2 c^4 \right\}^{\frac{1}{2}} \qquad\qquad 2.1.1$$

where p and m_0 are the momentum and rest mass respectively, and c the velocity of light. Hence, applied to electrons in orbit around the atomic nucleus, the distribution of energy states will extend positively from $m_0 c$ to $+ \infty$ and negatively from $-m_0 c$ to $- \infty$ (figure 2.1.1). However, the absence of experimental evidence to suggest a positive particle of the mass of the electron led to the belief that there must be some error in the Dirac formulation. Attempts by others were made to modify the formula so that either the negative energy states could be effectively removed from the final solutions or, at least, the negative energies construed to be proton states. Such attempts failed (for a review see Hanson, 1963). Thus, with the original formula still intact Dirac (1930a) finally postulated his 'hole-theory'. This stated that in the absence of an external field all negative energy states would be filled and, therefore, no transitions to them could take place (and so could not be observed). However, in the presence of a field supplying an energy greater than $2m_0 c^2$ a negative energy electron could be raised to a positive energy state leaving a 'hole' in the negative state continuum. The

'hole' (known as the positron) would behave like a positively charged particle containing a positive energy and momentum. If an electron with positive energy were to jump into the 'hole' an energy $2m_0c^2$ would be released in the form of photons (figure 2.1.1), such a process effectively annihilating the electron and the positron.

The great boost for the Dirac theory came in 1932 when Anderson (1932) observed the existence of a positive particle with a mass equivalent to that of the electron by studying cosmic radition with a Wilson Cloud Chamber. However, only one track (that of the positive particle) was seen. Later, using more skilful cloud chamber detection techniques, Blackett and Occhialinin (1933) confirmed the results of Anderson. They observed pairs of tracks emanating from a single point, the tracks of each pair possessing equivalent curvatures of opposite sense. Analysis confirmed that the tracks were due to positrons and electrons. In addition, they concluded that it was 'most probable' that the electron-hole pair was created by a collision process. This was the convincing experiment that supported Dirac's Hole theory (and the possibility of pair creation), and confirmed that the particle discovered by Anderson was, indeed, the same one predicted by Dirac - namely, the positron.

2.2 ELECTRON-POSITRON ANNIHILATION

2.2.1 Modes of Annihilation

The process of electron-positron annihilation must obey all the laws of conservation - i.e. total energy, momentum, electric charge and parity. With such considerations in mind Akhiezer and Beristetski (1965) were able to determine various ways in which the annihilation process would occur. Figure 2.2.1 illustrates four modes of annihilation and they are represented by Feynman diagrams. For slowly moving pairs conservation of momentum demands that at least two bodies be involved in the process. In the case of non-photon and one-photon annihilation the presence of other bodies such as electrons or nuclei are required in order for the recoil momentum to be absorbed. In the two-photon annihilation mode each photon will carry a momentum $\sim m_0c$ (section 2.3). Since this quantity is orders of magnitude

E

ELECTRONS WITH POSITIVE ENERGY

$m_o C^2$

$-m_o C^2$

ALL STATES
OCCUPIED

HOLE

ALL STATES
OCCUPIED

ELECTRONS WITH NEGATIVE ENERGY
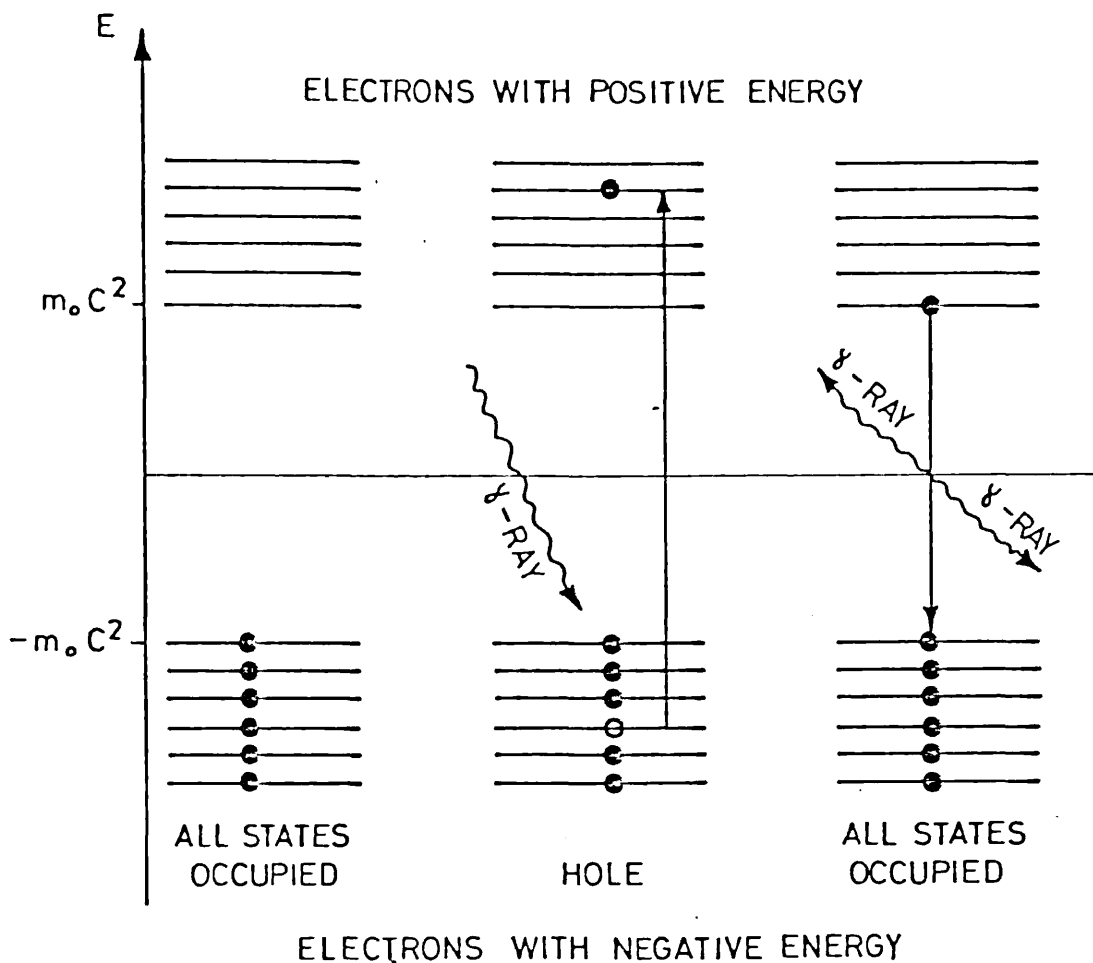
Figure 2.1.1.   Schematic representation of the "Hole-Theory"

(a)   (b)   (c)   (d)
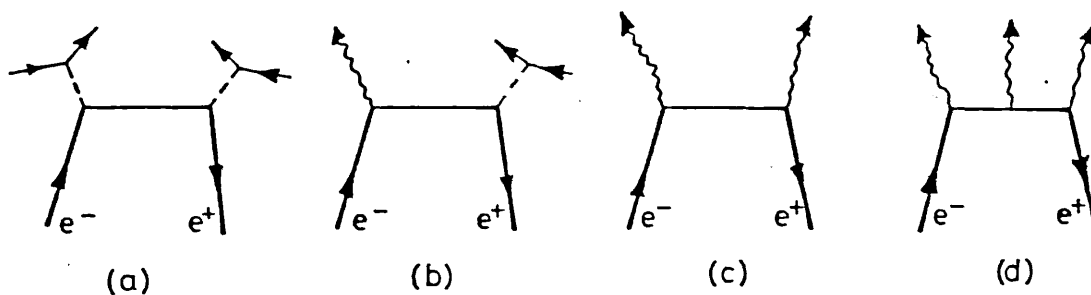
Figure 2.2.1.   Various Modes of Positron Annihilation
a) Non-Photon   b) One-Photon   c) Two-Photon
and d) Three-Photon Annihilation

larger than the electron-positron pair momentum (typically of order 10^{-3} m_0c) conservation of momentum requires that the two photons are emitted in opposite directions with a very small angular departure from collinearity. In three photon annihilation the photons can be emitted in various directions relative to each other, and each gamma can carry energies between zero and m_0c^2.

The relative cross-sections, σ_n, for annihilation producing n photons are found to be related by

$$\sigma_1/\sigma_2 \simeq \alpha^4 \qquad \text{and} \qquad \sigma_3/\sigma_2 \simeq \alpha \qquad\qquad 2.2.1$$

where (= $e^2/\hbar c$ = 1/137) is the fine structure constant. The cross-section for non-photon annihilation is much smaller than that for single-photon annihilation. Thus, the above expressions show that 2-photon emission is the dominant mode of electron-positron annihilation.

2.2.1.1 Positronium

In some circumstances it is possible for a free positron to become bound to an electron to form the atom positronium (Ps). Positronium formation is found in substances possessing complex molecular structure (Wallace 1960, Goldanski 1968). In the ground state óf Ps there are two possible spin configurations. These are known as the singlet ^1S (para-Ps) and the triplet ^3S (ortho-Ps) and give rise to total spins of zero and unity respectively. By considering conservation of charge parity in the annihilation process it is found that the para-Ps decays to give an even number of photons and the decay of ortho-Ps produces an odd number of photons (see West, 1974). It is clear that the dominant modes of decay will be due to 2 and 3 photon annihilation. It is found that the free para-Ps and ortho-Ps lifetimes in isolation are 125 psec and 140 nsec respectively. In practice the ortho-Ps decay is only slight because there are more rapid interactions involving this state with the surrounding lattice which terminate the ^3S state before its natural annihilation time. The formation of Ps in metals has been

shown by Ore and Powell (1949) to be unfavourable. Essentially, the conduction sea of electrons present in metals tend to prevent positrons from becoming bound to single electrons. To date, the presence of Ps in metals has not been observed.

2.2.2 Thermalisation of Positrons

When a positron is injected into a metal lattice interactions with its surroundings causes it to lose energy. The basic mode of interaction involves collisions with electrons. The most commonly used positron sources (e.g. Na^{22}, Cu^{64}) emit positrons having maximum energies of the order of 0.5 MeV. Since electrons in the lattice possess energies of typically only a few eV any collision between a positron and electron will (by conservation of energy and momentum) result in the positron losing about half its energy for each collision. This process is allowed if the energy imparted to the electron is sufficient to activate it into higher non-occupied electron states. Assuming that the mean free path between collisions is of the order of a lattice spacing, it is easy to show (using elementary classical mechanics) that the positron energy reduces to a few eV in about 10^{-15} sec (West, 1974). However, the positron has not yet achieved thermal energies (~ 0.025 eV). The ability for positrons of energy ~ 1 eV to lose energy by electron interactions will now depend on the availability of unoccupied electron states around these energies. For metals most of these states are occupied and so the process of positron energy loss will be slowed down. In fact, further energy loss will depend on phonon interaction. Lee-Whiting (1955) has calculated that positrons will thermalise in 3×10^{-12} sec, thus indicating that the majority of the time will be spent losing energy in the range 1 eV to ~ 0.025 eV. If positron lifetimes are longer than 10^{-12} sec (section 2.3.1) then positrons will annihilate in the thermalised condition.

2.3 FEATURES OF TWO-PHOTON ANNIHILATION

Section 2.2 has established that the most probable mode of annihilation is via two-phonon emission. Accordingly, the following discussion shall be devoted to this.

2.3.1 Positron Lifetime

Dirac (1930b) derived an expression for the relativistic cross-section for two-photon annihilation resulting from the interaction of a free positron and a stationary electron by summing over all spin directions:-

$$\sigma = \frac{\pi r_0^2}{\gamma + 1} \left\{ \frac{\gamma^2 + 4 + 1}{\gamma^2 - 1} \log_e \left\{ \gamma + (\gamma^2 - 1)^{\frac{1}{2}} \right\} - \frac{\gamma + 3}{(\gamma^2 - 1)^{\frac{1}{2}}} \right\} \quad 2.3.1$$

where $\gamma = (1 - v^2/c^2)^{\frac{1}{2}}$, v is the velocity of the positron and $r_0 = e^2/m_0 c^2$ is the classical electron Bohr radius. At low positron velocities equation 2.3.1 can be reduced to

$$\sigma = r_0^2 \, c/v \quad 2.3.2$$

Hence, the annihilation probability is given by

$$\Gamma = v n_e = \pi r_0^2 \, c n_e \quad 2.3.3$$

where n_e is the number of electrons per unit volume. Equation 2.3.3 shows that the positron lifetime ($1/\Gamma$) is proportional to the electron density and so any experiment capable of measuring this quantity (section 2.3.1.1) will offer information on the electron environment seen by the positron at the instant of annihilation. An estimate of the order of magnitude of the positron lifetime in metals can be derived from equation 2.3.3. The electron density, n_e, is given by $N_0 \rho Z/A$ where ρ is the density of the metal, A the atomic weight, Z the valence number of electrons and N_0 Avogardro's number. For the case of aluminium equation 2.3.3 predicts a lifetime of 750 psec. However, experiment yields the value 165 psec. Clearly, the theory has over-estimated the lifetime. This occurs because the positron perturbs its surroundings in such a way as to increase the electron density due to the electron-positron attractive field. Attempts have been made to account for the electron-positron interaction in the estimation of

lifetimes. The work of Bhattacharyya and Singwi (1972) has considerably improved the agreement between theory and experiment.

Typical values for positron lifetimes in metals lie in the range 100-500 psec (Weisberg and Berko 1967, Hautojarvi et al 1970, McKee et al 1972). Hence, positrons spend the majority of their life in the thermalised state and annihilate as thermalised positrons since the thermalisation time is of the order of 25 psec.

2.3.1.1 Lifetime Measurement

Since changes in lattice structure cause changes in electron density, defects can be monitored if such changes can be sensed. Due to the consequences of equation 2.3.3 for two-photon annihilation, positron lifetime measurements can be used to study defect structure. A brief discussion of the so-called 'lifetime' technique will be included here.

The technique rests on the ability to measure the time difference between the birth of a positron and its subsequent annihilation. This necessitates the use of the isotope Na^{22} which conveniently emits a 1.28 MeV gamma ray at the same time (within 10 psec) as a positron is emitted. Detection of such an event can, therefore, mark the birth of a positron, and the detection of the subsequent annihilation gamma indicates its death. The circuitry required to achieve this is seen illustrated in figure 2.3.1. The timing discriminators are used to process the pulses from each detector so that they are converted into standard pulses of short duration, thus facilitating time measurement. The Time-to-Amplitude converter (TAC) produces a pulse whose amplitude is proportional to the time interval between the detection of the 1.28 MeV gamma ray and the corresponding annihilation photon. The energy selection coincidence part of the system consists of two pre-amplifiers, two main amplifiers, two single channel analysers and a coincidence unit, and is used to isolate relevant coincidence events. When such events occur the Gate is opened and the amplitude of the pulse in the TAC digitised and sent to the multichannel analyser (MCA). In this way a spectrum of different lifetimes can be recorded. Analysis of such spectra can yield average lifetimes for positrons

SOURCE

DETECTOR

SAMPLE

DETECTOR

TIMING
DISCRIMINATOR

TIMING
DISCRIMINATOR

DELAY

PRE-AMP

TIME-TO-
AMPLITUDE
CONVERTER

PRE-AMP

AMPLIFIER

MULTI-
CHANNEL
ANALYSER

AMPLIFIER

SINGLE
CHANNEL
ANALYSER

GATE

SINGLE
CHANNEL
ANALYSER

COINCIDENCE
UNIT
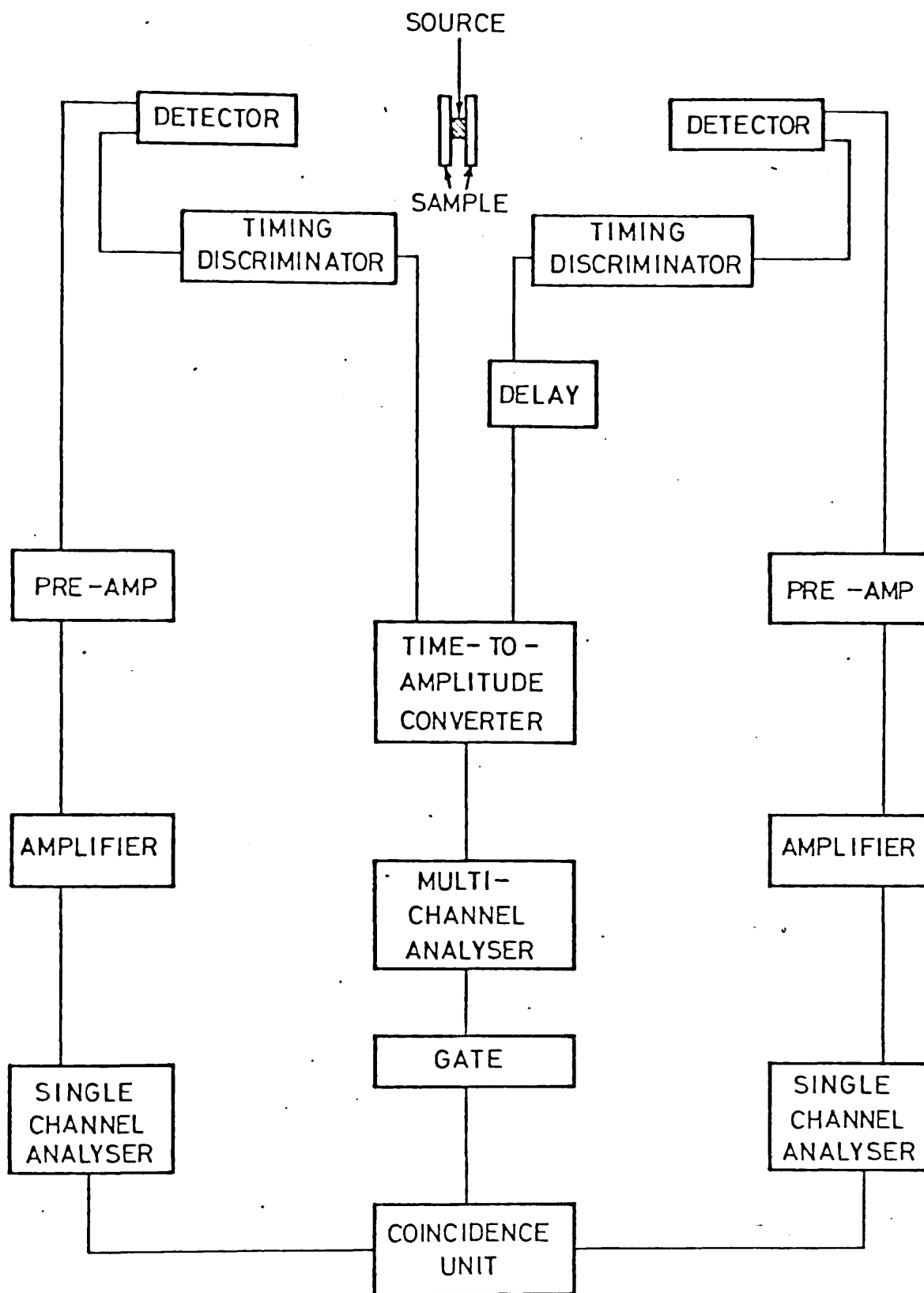
Figure 2.3.1   A typical lifetime spectrometer

annihilating in free and defected lattices (e.g. kirkegaard and Eldrup (1972).

.Of course, the apparatus gives rise to experimental error and so the stored spectrum in the MCA may be regarded as the convolution of the true lifetime distribution with the resolution function of the apparatus. The time resolution can be determined from the full-width-at-half-maximum (FWHM) of the coincidence curve of Co^{60} which emits two prompt coincidence gamma rays. Typical lifetime spectrometers are capable of measuring lifetimes of a few hundred picoseconds.

2.3.2 Angular Correlation of Annihilation Photons

Consider the motion of an electron-positron pair before annihilation. The momentum of the pair, $\underline{p}$, is given by

$$\underline{p} = \underline{p}^+ + \underline{p}^- \qquad 2.3.4$$

where $\underline{p}^+$ and $\underline{p}^-$ are the positron and electron momenta respectively. Since the positrons are thermalised before annihilation ($E \sim 0.025$ eV) and typical electron energies in the lattice are of the order of a few eV, equation 2.3.4 reduces to give $\underline{p} \sim \underline{p}^-$. When the electron-positron pair annihilates the total energy, E, released is

$$E = 2m_0c^2 + E_K + E_B \qquad 2.3.5$$

where m_0c^2 is the rest mass of each particle, and E_K and E_B the total kinetic and potential energies of the electron-positron pair respectively. Since the positrons are not bound (i.e. $E_B = 0$) and E_K (~ 10 eV)$<< m_0c^2$, equation 2.3.5 reduces to $E \stackrel{\simeq}{=} 2m_0c^2$. In accordance with conservation of momentum it is required that

$$\underline{p}_1 + \underline{p}_2 = \underline{p} \sim \underline{p}^- \qquad 2.3.6$$

where $\underline{p}_1$ and $\underline{p}_2$ are the momentum values for each photon. However, $\left| \underline{p}_1 + \underline{p}_2 \right| = 2m_0c$ and $2m_0c >> \left| \underline{p}^- \right|$. Hence, equation 2.3.6

requires that the photons travel in opposite directions with a small angle departure (millirads) from collinearity, each photon having an energy $\sim m_0c^2$ and momentum $\sim m_0c$. A vector diagram representing the annihilation event is seen in figure 2.3.2. Resolving the momentum into the x, y and z directions one obtains

$$p_x = p_2 - p_1 \cos \theta \cos \phi$$

$$p_y = p_1 \cos \theta \sin \phi \qquad\qquad 2.3.7$$

$$p_z = p_1 \sin \theta$$

Since θ and ϕ are small, equations 2.3.7 reduce to

$$p_x = p_2 - p_1 = (h\nu_2 - h\nu_1)/c$$

$$p_y = m_0 c \phi \qquad\qquad 2.3.8$$

$$p_z = m_0 c \theta$$

using $p_1 \sim p_2 \sim m_0c$. Equation 2.3.8 shows that distributions in ϕ and θ measure the transverse components of the $e^+ - e^-$ pair momentum distribution in the y and z directions respectively. Hence, an experiment capable of measuring the annihilation probability as a function of ϕ (or θ) will be reflecting directly the momentum distribution of the electron-positron pair in the direction y (or z). It is easy to see that an annihilation probability distribution can be obtained which is, essentially, a symmetrical curve centred at θ = zero mrad with m_0c $(-\theta)$ = $m_0c(\theta)$. In particular, the measured annihilation probability will reflect the electron momentum distribution in the lattice if the positron momentum is negligible. Such experiments are important because (as in the case of lifetime measurements) they provide a means of monitoring defect structure. Accordingly, angular correlation experimentation will be briefly discussed below.
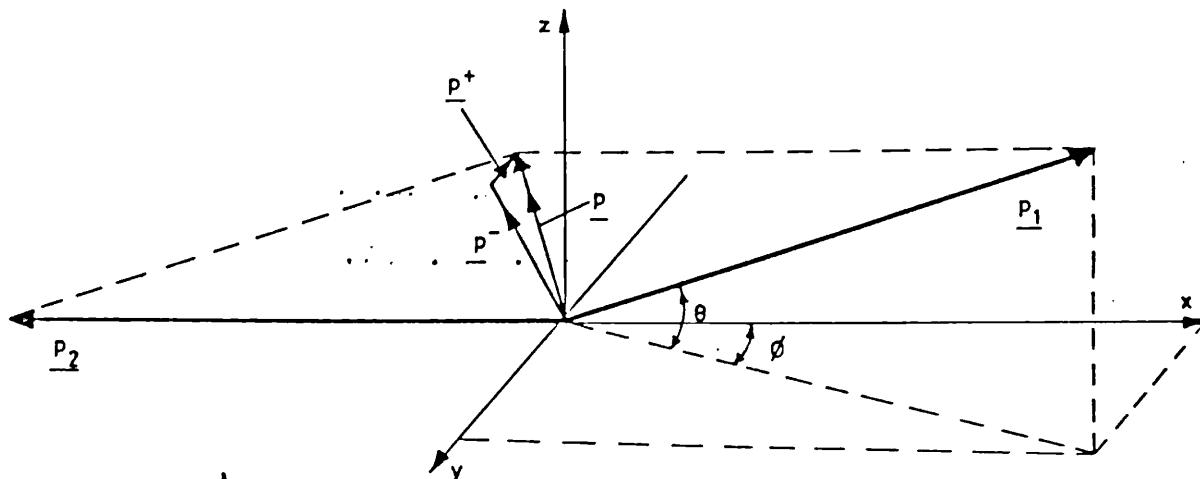
Figure 2.3.2   Vector diagram to illustrate angular correlation of
two-photon annihilation radiation
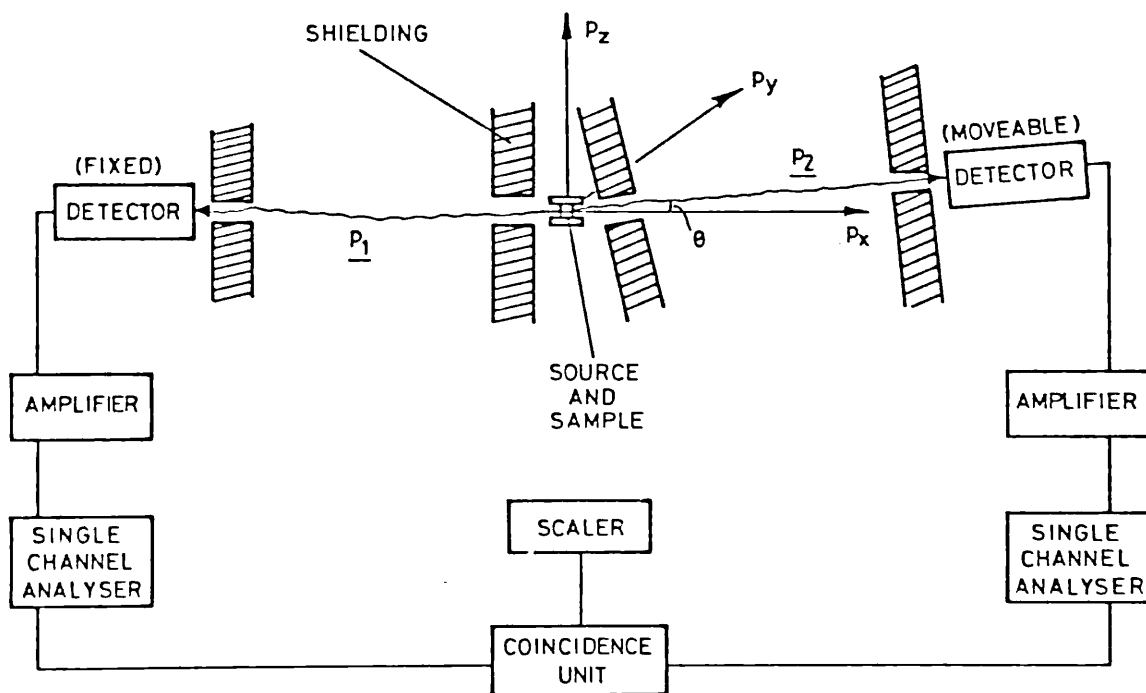
Figure 2.3.3   A typical angular correlation spectrometer

2.3.2.1 Angular Correlation Measurement

Figure 2.3.3 illustrates a typical angular correlation apparatus. Basically, the system consists of two detectors (one of which is moveable) and electronic coincidence circuitry. Departures from two-photon collinearity are observed by measuring the coincidence count-rate as a function of the position of the moveable detector. In order to resolve the p_z component of the annihilating pair the so-called 'long-slit' geometry is normally employed - i.e. the detectors are shielded in such a way as to present only a long, narrow line of visibility (across the detector) to the annihilation photons. If $\rho(\underline{p})$ is the momentum distribution of the annihilating pairs then the annihilation probability $N(\theta)$ at space ordinate θ will be given by

$$N(\theta) = N(P_z) = \int_{-}^{+} \rho(\underline{p}) \, dp_x \, dp_y \qquad 2.3.9$$

since for a specific θ the detector slit accepts an array of annihilation events in the x,y plane.

In order to achieve good angular resolution it is necessary to use large detector-source distances (typically ~ 2 m) and to use slits as narrow as is practicable. However, improved resolution is necessarily obtained at the expense of a reduced count-rate. In order to achieve a compromise between these two competing parameters experiments are usually run with angular resolutions in the range 0.5-1 millirad. Such resolutions are certainly sufficient to resolve angular distributions in metals which, typically, have widths in the range 10-20 millirads. A recent development is seen in the use of 2-dimensional, multi-counter detectors (e.g. Berko and Mader, 1975). The moveable, long-slit detector is now replaced by a multi-detector in the z,y plane (each counter defining a unique θ, ϕ). Hence, in accordance with equations 2.3.8, the system can resolve both the z and y components of the $e^+ - e^-$ pair momentum. Also, compared to the long-slit system, 2-dimensional systems enjoy much more rapid accumulation of data.

The use of angular correlation experiments has greatly assisted the study of electronic structure in metals, particularly in the field of Fermi surface topology (e.g. Danaghy and Stewart 1967, Mijnarends 1969, and McLarnon and Williams 1977). A detailed account of the development of the angular correlation technique is given by Dekhtyar (1974).

2.3.3 Doppler-Broadening of Annihilation Radiation

The total energy shared by the two photons is given by

$$h\nu_1 + h\nu_2 = 2h\nu_0 = 2m_0c^2 \qquad\qquad 2.3.10$$

Hence, using equation 2.3.8

$$p_x = \frac{2}{c}\left\{h\nu_2 - h\nu_0\right\} = \frac{2}{c}\left\{h\nu_0 - h\nu_1\right\} = \frac{2}{c}\Delta E \qquad\qquad 2.3.11$$

where ΔE is the Doppler shift in the energy of the emitted photons, and is caused by the momentum of the electron-positron pair in the direction of emission. Equation 2.3.11 shows that the Doppler-shifted energy distribution reflects the e^+ - e^- pair momentum distribution and, therefore, yields essentially the same information as the angular correlation distributions. From equation 2.3.11 it is clear that the Doppler-broadened energy distribution is a symmetrical curve centred at m_0c^2, with a half-width ΔE. Such a curve is also known as the Doppler-boradened lineshape. The kinetic energy of the e^+ - e^- pair (from equation 2.3.11) may be defined by

$$E_K = \frac{2(\Delta E)^2}{m_0c^2} \qquad\qquad 2.3.12$$

Using equation 2.3.12 it is seen that an electron with energy 10 eV will provide a Doppler shift, ΔE, of 1.6 keV.

2.3.3.1 Measurement of Doppler-broadened Photon Energies

The measurement of Doppler-broadened energy distributions has been the experimental approach adopted in this study. Accordingly, a detailed description of the 'Doppler-broadening technique' is to be found in chapter 3.

Unfortunately, Doppler-broadening systems do not offer the same, high degree of resolution that angular correlation systems provide. From equation 2.3.12 it has been shown that a 10 eV electron produces a Doppler shift of 1.6 keV and this turns out to be of the same order of magnitude as the instrumental resolution function - 1 keV FWHM for the best present day systems. In contrast, angular correlation systems provide angular resolutions of ~ 0.5 mrad for distributions having widths of 10 mrad (equivalent to $\Delta E \sim 1.6$ keV). Clearly, the resolving power of the Doppler system is approaching a value about an order of magnitude lower than that for angular correlation.

However, Doppler-broadening studies are popular because of the faster rate at which data, comparable to that offered by angular correlation, can be collected - in the same time it takes to produce one angular correlation curve using long-slit apparatus (~ 2 days) it is possible (assuming 2 hrs per run) to collect 24 Doppler lineshapes of comparable statistics. The instrumental smearing, bad as it is, does allow changes in the lineshape (due to lattice structure changes) to be observed, thus qualifying it for a valuable role in the monitoring of defect structure variations. Also, the detailed study of electronic momentum distributions is possible if suitable deconvolution techniques are applied to remove the instrumental smearing. Dannefaer and Kerr (1975) have applied such techniques to Doppler annihilation lineshapes and have found good agreement between the Fermi energies evaluated from the resulting deconvoluted lineshapes and those evaluated from corresponding angular correlation distributions.

2.4 ANNIHILATION IN THE PERFECT LATTICE

2.4.1 Theoretical Descrption of Annihilation Lineshapes

Of fundamental importance in the field of solid-state physics is

the ability to predict theoretically the electronic structure of metals in perfect and defected lattices. It is also of great interest to predict the behaviour of positrons in the perfect and defected lattice. In positron studies such theoretical work relies heavily on exploiting opportunities to compare predicted e^+ - e^- momentum distributions with those observed experimentally - i.e. observed data provide useful 'feedback' to the theoretician in his attempts to construct mathematical models. A convenient starting point for such interplay is provided by the expression (e.g. see West, 1974)

$$\Gamma_r(\underline{k}) = \frac{r_o^2 c}{(2\pi)^3} \left| \int d^3\underline{x} \exp(-i\underline{k}\cdot\underline{x}) \psi_r(x) \psi_+(x) \right|^2 d^3\underline{k} \qquad 2.4.1$$

where $\Gamma_r(\underline{k})$ is the probability per unit time that a positron in the state $\psi_+(x)$ will annihilate with the rth electron in the state $\psi_r(x)$, the emited quanta having resultant momenta defined by wavevector $\underline{k}$. Essentially, equation 2.4.1 describes the annihilation probability (given in real space by $\psi_r(\underline{x}) \psi_+(\underline{x})$) in momentum space by use of the Fourier transform. The total annihilation rate, Γ, summed over all photon momenta and possible electron energy states is, thus, given by

$$\Gamma = \sum_r \int \Gamma_r(\underline{k}) \, d^3\underline{k} \qquad 2.4.2$$

Hence, by constructing appropriate wavefunctions for electrons and positrons, equations 2.4.1 and 2.4.2 afford evaluation of the pair momentum distribution and positron lifetime respectively.

Since electrons and positrons are quantum mechanical particles, their dynamical behaviour may be described by means of the Schrodinger equation (the wave equation adapted to describe particle dynamics in terms of energy). For a particle of mass m and total energy E, the Schrodinger equation may be expressed as

$$\left\{ -\frac{\hbar^2}{2m} \nabla^2 + V(\underline{r}) \right\} \psi(\underline{r}) = E \psi(\underline{r}) \qquad\qquad 2.4.3$$

where $\psi(\underline{r})$ is the particle wave function and $V(\underline{r})$ the potential it experiences at position $\underline{r}$. Solution of equation 2.4.3 for a known $V(\underline{r})$ can yield the so-called eigenfunctions (wavefunctions) and corresponding eigenvalues (energies) of the possible particle states.

Equations 2.4.1 and 2.4.3, therefore, represent the basis for computing e^+ - e^- momentum distributions. Unfortunately, for many applications the solution of the Schrodinger equation is very difficult and sometimes impossible unless quite wild approximations concerning the description of the physical conditions are made. Such difficulties are particularly acute in present-day attempts to describe the electronic structure of defects (section 2.5.1). The next section is devoted to a brief review of how e^+ - e^- momentum distributions for annihilations in the perfect lattice may be calculated.

2.4.2 Annihilation with Valence Electrons

Owing to the positive charge on the metallic ions, positrons will spend much of their time in the region between ion cores where they will sample substantial numbers of conduction electrons. Thus, a significant fraction of annihilations can be expected to occur with these electrons. Since the positron momentum is negligible the e^+ - e^- momentum distribution can, essentially, be described by that of the electron.

The free electron momentum distribution can be derived from the solution of equation 2.4.3 under the conditions that $V(\underline{r})$ is zero (i.e. no electron interactions with the medium) and that the electron wavefunctions are taken to be plane-wave in nature ($\psi(\underline{r}) \sim \exp(i\underline{k}.\underline{r})$ and satisfy the Bloch conditions for lattice periodicity. It is relatively straightforward to show that (e.g. kittel, 1976).

$$E_F = \frac{\hbar^2}{2m} \left\{ 3\pi^2 \frac{N}{V} \right\}^{2/3} \qquad\qquad 2.4.4$$

where N is the number of electrons in a crystal of volume V, m the mass of the electron ad E_F the Fermi energy. If n is the total number of electrons possessing energies up to E, then equation 2.4.4 gives

$$n = \frac{V}{3\pi^2} \left(\frac{2mE}{\hbar^2}\right)^{3/2} = \frac{V}{3\pi^2} \left(\frac{p}{\hbar}\right)^3 \qquad 2.4.5$$

where $E = p^2/2m$. If $\rho(\underline{p})$ is the density of states for momentum $\underline{p}$ then

$$\rho(\underline{p}) = \frac{d}{d\underline{p}} \int_0^p \rho(\underline{p}) \ d\underline{p} = \frac{dn}{d\underline{p}} = \frac{V}{\pi^2\hbar^3} p^2. \qquad 2.4.6$$

Evidently, the momentum distribution for free electrons is parabolic. The distribution is cut off at the Fermi momentum, p_F, where the Fermi-Dirac electron occupancy function goes to zero. However, in reality, electrons undergo scattering events in the medium because their wavelengths are comparable to the lattice spacing. Hence, a perturbing potential $(V(\underline{r}) \neq 0)$ will be experienced by the electrons. Even though such scattering events will tend to modify the valence electron distribution from that describing the 'ideal' free electron case, a parabolic distribution is often quite adequate to describe it.

Typically, angular correlation curves appear to consist of two parts - a sharp profile sitting on top of a shallow, broader profile. Successful fits of an inverted parabola to the 'sharp' profile have shown that this distribution is due to annihilations with valence electrons (e.g. Stewart 1957, Gustafson et al 1963). The broader distribution, however, could not be explained in terms of valence electron annihilations and, as shall be seen below, has been attributed to the core states.

2.4.3 Annihilation with Core Electrons

Berko and Plaskett (1958) were among the first to fit computed

e^+ - e^- momentum distributions to experimental angular correlation curves. They considered the metals Cu and Al. They described (in accordance with equation 2.4.1) the e^+ - e^- momentum distribution for $2(2l + 1)N$ core electron states of angular momentum l for N atoms in the crystal as

$$\rho_l \, (\underline{p}) = 2N \sum_{m=-l}^{l} \int_{crystal} N^{-\frac{1}{2}} \, \psi^+ \, \frac{R_l}{r} \, Y_l^m \, exp(-i\underline{p}.\underline{r}) \, d\underline{r} \qquad 2.4.7$$

where m is the magnetic quantum number and the core-electron wavefunctions are considered to be tightly bound in orbit and are described in terms of the product of the spherical polar functions i.e.

$$\frac{R_l}{r} \, Y_l^m = \frac{R_l}{r} \, P_l^m \, exp(im\phi) \left\{ \frac{2l + 1}{4\pi} \, \left\{ \frac{(l - m)!}{(l + m)!} \right\} \right\}$$

$N^{-\frac{1}{2}} \, \psi_+$ is the normalised positron wavefunction.

The positron wavefunction was evaluated by employing the Wigner-Seitz method. Essentially, this method allows solution of the positron wavefunctions in the vicinity of the core electrons by constructing an imaginary sphere around the core region. This sphere is, in fact, the Wigner-Seitz cell (Kittel, 1976) approximated to a sphere of radius r_s and has been evaluated for metals. Since the potential seen by the positron inside the cell is spherically symmetrical the 'radial' Schrodinger equation can be solved subject to the boundary conditions $d\psi_+/dr = 0$ at $r = r_s$ where $\psi_+ = R_+/r$ and R_+ the radial component of the complete positron wavefunction. This equation is of the form (expressed in atomic units, e=h=m=1)

$$\frac{d^2R}{dr^2} + 2 \left| E - V(r) \right| R_+ = 0 \qquad 2.4.8$$

V(r) was taken to be the potential due to a positive ion together with a potential due to a uniform charge of electrons. The positron-electron exchange potential was not considered. Equation 2.4.8 was

integrated out and the function R_+ determined for the positron ground state ($\underline{k}$ = 0). Equation 2.4.7 could then be evaluated. To allow for some core states that existed outside the Wigner-Seitz cell, a further computation was performed to evaluate the e^+ - e^- momentum contribution from these states. Since the positron wavefunction was not evaluated for $r > r_s$ the value of the average $\psi_+(r)$ inside the cell was used for this region. Their results showed that for the innermost core electrons the integral in equation 2.4.7 approached zero - a result to be expected since the positron-electron overlap is small due to the positive ionic charge.

In the case of Al the calculated core distribution was seen to fit extremely well to the observed broad distribution. They concluded that the broad distribution was basically due to annihilations with core electrons. The calculated distributions also agree quite well for Cu, thus indicating core electron annihilations. However, in this case the theory overestimated the M shell contribution. It was decided that this was possibly due to the inaccuracy of the positron wavefunction defined at the M shell electron vicinity outside the Wigner-Seitz cell.

Subsequent work by various workers have shown that the broad, core electron distribution can be approximated by a Gaussian shape (e.g. Gustafson et al 1963, Arias-Limonta and Varlashkin 1970). West et al (1967) performed calculations similar to that of Berko and Plaskett on bismuth and mercury and concluded that the broad distribution was due to core electron annihilation. They, also, could approximate the shape of these distributions to a Gaussian. However, they found that, even though reasonable agreement was found, the calculated distributions decreased more slowly than the observed ones. This was considered to be due to inadequacies in the modelling (e.g. neglection of electron-positron interaction and use of the tight binding free atom orbital approximation.)

2.5 ANNIHILATION IN THE DEFECTED LATTICE

2.5.1 Determination of Defect Electronic Structure

Much theoretical work has been performed with a view to describing

the electronic structure of defects. To date, the precise
determination of such structure of various types of defects has not
been fully realised. All too often, the numerical solution of the
Schrodinger equation in the vicinity of a defect becomes a task of
great complication because of the awkward geometrical conditions
brought about by the disruption of perfect lattice periodicity. Also,
the construction of a suitable $V(\underline{r})$ (in equation 2.4.3) for an electron
in a defected region has been a source of great difficulty.

In principle, the problem can be reduced to one requiring the use
of perturbation theory - i.e. evaluate the perturbed electron states
(brought about by the presence of the defect) in terms of the
unperturbed states using a suitable perturbing Hamiltonian. The
perturbation approach has been used in so-called 'pseudo-potential'
theory (Harrison 1966) where, in order to aid computation, actual
physical potentials are replaced in the mathematical formulation by
'effective' (pseudo) potentials. Pseudo-potentials are made
artificially weak, thus validating the perturbation approach. Another
method involves the use of solid-state scattering theory (Singhal and
Callaway 1979, Baraff and Schluter 1979). However, most of these
approaches have only been applied (some quite successfully) to simple
vacancy-type defects and are only capable of describing valence
electron defect structure.

Manninen et al (1975) were successful in fitting a computer
angular correlation curve to an experimentally observed one obtained by
Kusmiss and Stewart (1967) for the annihilation of positrons in
aluminium vacancies. They constructed valence electron wavefunctions
at a vacancy in aluminium by use of the Jellium model. In this method
the metal is described by a uniform background charge together with an
interacting electron gas, and the vacancy is approximated as a
spherical hole in the background. The total energy of the electronic
system was expressed as a function of the electron density (Kohn and
Sham 1965).

Little success has been enjoyed in applying the above-mentioned
techniques to the problem of the dislocation. Among other things, it
is extremely difficult to construct a realistic model for the atomic

configuration around the core. It is clear that data provided by positron annihilation has an important part to play in facilitating theoretical modelling and, thereby, encouraging greater understanding of the behaviour of electrons (and positrons) in defected lattices.

2.5.2 Positrons at Defects

2.5.2.1 Positron Momentum

As has been discussed in section 1.7, positrons experience an attractive binding force at open volume defects, thus causing their wavefunctions to become localised around such regions. An important consequence of localisation is an increase in the positron momentum as predicted by the Uncertainty principle ($\Delta x \Delta p \sim \hbar$) where Δx and Δp are the uncertainties in the positron position and momentum respectively.

The positron at a defect can, ideally, be considered to exist in a square potential well of depth V with a corresponding binding energy (E_B) and kinetic energy (E_T) such that $V = E_B + E_T$. The kinetic energy in the 'trap' (or zero-point energy) directly reflects the positron momentum, and so measurements (or theoretical predictions) of this quantity should, in principle, provide information on the nature of the defect. For instance, a point defect might be expected to cause greater localisation than, say, a dislocation since in the latter the positron is effectively free to move along the direction of the dislocation line. Thus, for a given metal, the zero-point energy might be greater for a vacancy than that for a dislocation. The magnitude of the zero-point energy will depend on how effective the defect is as a positron trap. Shallow potential wells will be expected to cause less effective positron localisation with concomitant decrease in zero-point energy.

The magnitude of the positron momentum at defect sites has been estimated by various workers. For instance, Hautojarvi (1972) considered the angular correlation curve for positron annihilation in heavily deformed aluminium and assumed that the recorded events were mainly due to annihilations in dislocations. By smearing a parabolic component (to represent valence electrons) with a Gaussian function

(to represent positron zero-point motion) and fitting the convoluted distribution to the experimental curve, a value of 0.73 eV was evaluated for the kinetic energy of the positron in the bound state. Similar work was performed on Doppler-broadened lineshapes for vacancies in Cd by Rice-Evans et al (1979), and obtained a zero-point energy of 0.4 eV. Hodges (1970) and Hodges and Stott (1973) evaluated effective trapping potentials for vacancies in a series of metals using various theoretical approaches, and found values varying between 0.19 eV (Cs) and 0.72 eV (Al), and so suggesting zero-point energies of the same order of magnitude.

It seems that the momenta of thermalised positrons increase by an order of magnitude when trapped at defects. In any serious analysis of angular-correlation or Doppler-broadened lineshapes the positron momentum should now be considered since it contributes significantly to the centre-of-mass motion of the annihilating pair.

2.5.2.2 Positron Trapping at Defects

The annihilation behaviour of positrons in a defected lattice may be described by the 'trapping model' introduced by Brandt (1967) and Connors and West (1969). In this model the mode of positron annihilations are described by the rate equations:-

$$\frac{dn_f(t)}{dt} = -\lambda_f n_f(t) - \sum_j \mu_j C_j n_f(t) + \sum_j \lambda_{Dj} n_j(t) \qquad 2.5.1$$

for a system of j types of defect (trap) where

$n_f(t)$ = the number of free positrons at time t

$n_j(t)$ = the number of trapped positrons at time t in defect type j

λ_f = the annihilation rate in the perfect lattice (untrapped state)

λ_j = the annihilation rate in the jth trapped state

λ_{Dj} = the detrapping rate from the jth defect to the free state

C_j = the concentration of trap j

μ_j = the trapping rate for the jth type of defect.

Since the binding energies for positrons in defects are of the order of ~ 1 eV, the detrapping rate, λ_{Dj}, is usually considered insignificant. Equations 2.5.1 then yield solutions

$$n_f(t) = n_f(0) \exp(-t/\tau_0)$$

$$n_j(t) = \frac{\tau_0 \tau_j \mu_j C_j}{\tau_0 - \tau_{j_i}} n_f(0) \exp(-t/\tau_0) + \left\{ n_j(0) - \frac{\tau_0 \tau_j \mu_j n_f(0)}{\tau_0 - \tau_j} \right\} \exp(-t/\tau_j)$$

$$2.5.2$$

where $1/\tau_0 = 1/\tau_j + \sum_j \mu_j C_j$.

The probability that an annihilation will occur at defect type j is given by $\lambda_j n_j(t)$. Hence, the total annihilation rate in defect j will be given by

$$P_j = \int_0^\infty \lambda_j n_j(t) \, dt \qquad 2.5.3$$

Similarly, the total probability for annihilations in the free state will be given by

$$P_f = \int_0^\infty \lambda_f n_f(t) \, dt \qquad 2.5.4$$

whence

$$P_j/P_f = \frac{\lambda_j \int_0^\infty n_j(t) \, dt}{\lambda_f \int_0^\infty n_f(t) \, dt} \qquad 2.5.5$$

Substituting the solutions $n_j(t)$ and $n_f(t)$ (equation 2.5.2) in equation 2.5.5 one obtains

$$P_j/P_f = \mu_j C_j / \lambda_f \qquad 2.5.6$$

Finally, using the relation $Pf + \sum_j p_j = 1$ (i.e. all positrons eventually annihilate)

$$P_j = \mu_j C_j / (\lambda_f + \sum_j \mu_j C_j)$$ 2.5.7

Eqaution 2.5.7 expresses the probability that a positron will annihilate in the' defect type j, and is also popularly referred to as the 'trapped fraction'.

2.5.2.3 Relating Observed Annihilation Characteristics to the Trapping Model

It is often convenient in positron annihilation experiments to define a parameter $\bar{F}$ describing some aspect of the observed events through the relation

$$\bar{F} = \sum_i F_i P_i$$ 2.5.8

where F_i is the characteristic value for F in the ith type of annihilation mode, P_i the probability of occurrence of the ith mode, and $\bar{F}$ the average value of F for all possible modes. Thus, equation 2.5.8 provides an important link between measurable observables and the morphology of the lattice since P_i is given by equation 2.5.7. In other words, measurement of $\bar{F}$ can provide information on the defect concentration C_j and the trapping rate μ_j, the nature of which depends on the physical characteristics of the lattice (section 2.5.2.4).

An example of a real, physical parameter that can be ascribed to equation 2.5.8 is the mean lifetime, $\bar{\tau}$, of positrons observed from lifetime experiments. Equation 2.5.8 becomes

$$\bar{\tau} = \sum_i \tau_i P_i$$ 2.5.9

where τ_i is the positron lifetime in the positron state i. In the

case of Doppler-broadening experiments one can define a parameter S (defined and discussed in chapter 4). Essentially, S is the number of events in a central region of the Doppler lineshape normalised by the total number of events under the line, and has the property that $S = \sum_i S_i P_i$ where S_i is the characteristic value of S for annihilations in the ith mode. S can be re-defined as $S_f P_f$ + $\sum_j S_j P_j$ where subscript f denotes annihilations in the free state and j for those in defect traps. Hence, using equation 2.5.7 one obtains

$$S = S_f \left\{ 1 - \sum_j \left\{ \mu_j C_j / (\lambda_f + \sum_j \mu_j C_j) \right\} \right\} + \sum_j S_j \left\{ \mu_j C_j / (\lambda_f + \sum_j \mu_j C_j) \right\}$$

$$2.5.10$$

To illustrate an application of 2.5.10 consider the case of thermally generated vacancies in a lattice. Using equation 1.2.4 (A = exp(S_{re}/k)), equation 2.5.10 reduces to

$$C_v = \frac{(S - S_f)\lambda_f}{(S_v - S)\mu_v} = A \exp(-E_f^v/kT) \qquad 2.5.11$$

where subscript v denotes a vacancy. Thus, if μ_v is considered constant, an Arrhenius plot of the left-hand-side of equation 2.5.11 versus T produces a straight line with slope $-E_f^v/k$ from which the formation energy E_f^v may be determined.

The nature of the trapping rate must now be considered. in the above example, the trapping rate was considered to be independent of temperature. This may not necessarily be so. In order to obtain correct values of formation energies it is important to apply the correct trapping rate. Since the rate ultimately depends on the mobility of positrons to the defect site, effects such as positron scattering may be significant. Scattering effects increase as a function of temperature and, so, would be expected to give the trapping rate a functional dependence on temperature. The trapping rate is discussed below.

2.5.2.4 Positron Trapping Rate

The rate at which positrons are trapped can be considered to be dependent on two criteria - firstly, the time taken to reach the trap after initial injection into the lattice, and, secondly, the time taken to make the transition to a bound state (i.e.'jump-into' the trap) once it has arrived at the defect boundary. The first mechanism will, clearly, depend on the scattering cross-section that the lattice presents to the positron. The second mechanism can be treated quantum mechanically by the use of Fermi's Golden Rule. In the transition to a trapped state the positron releases the trap binding energy to the medium. There are two possibilities - the released energy produces either electron-hole pairs or phonon excitations, or even a combination of both. Quantum mechanically, the rate of transition will be governed by the initial population of thermalised positron states, the density of unoccupied states for the excited electrons and positrons, and the positron-defect Coulomb potential. If the positron current to the trap is equal to, or greater than, the Golden Rule transition rate then the trapping rate is simply governed by the quantum mechanical mechanism (transition-limited). However, if the positron current cannot compete with the transition rate, the trapping rate will now be dependent on the positron mobility through the lattice (i.e. diffusion-limited). Two approaches can, therefore, be applied to the problem of the trapping rate - classical diffusion and quantum mechanical approaches.

The Golden Rule approach is expected to give no temperature dependence (Hodges, 1974) for positron trapping at small defects (i.e. those which produce positron wavefunction ranges small compared to thermalised positron wavelengths. Diffusion models have been deduced by various workers (e.g. Connors and West 1969, Frank and Seeger 1974). However, although most diffusion theories predict temperature dependence, universal agreement has not been established on the functional dependence of the trapping rate.

Nieminen et al (1979) proposed a theory for trapping at voids in metals and found that at low temperatures ($\sim 4K$) the trapping was transition-limited and strongly temperature dependent with a cross-over to diffusion-limited and weakly temperature dependent behaviour at high

temperatures ($\sim$ 400K). Bergersen and McMullen (1977) considered positron trapping at dislocations. They concluded that the trapping rate was transition-limited at low temperatures and found electron-hole production to be the dominant form of positron-lattice interaction prior to trapping. From this they could conclude that the trapping rate was, essentially, temperature independent in the range 80K-300K. Rice-Evans and Hlaing (1976) performed measurements on deformed copper and showed that the trapping (presumed mainly to be due to dislocations) was temperature-independent in the range 73K-323K. Nieminen and Laakkohen (1979) considered a theoretical model based on the Golden Rule for trapping at vacancy clusters. For physically viable ranges of potential well widths ($<$ 10 Å) and binding energies ($>$ 1 eV) they found the trapping rate to be independent of temperature. Measurements by Mantl et al (1978) were made on neutron-irradiated copper, nickel and aluminium. They concluded that trapping at single vacancies was temperature independent in the range 4K to 250K. However, marked temperature dependence was found for positrons trapped at small vacancy clusters and for voids in aluminium specimens.

To date, theory and experiment do not provide a cohesive account of the nature of positron trapping. However, from the brief review discussed above it seems that trapping at vacancies and dislocations at low temperatures is not temperature dependent. It is clear that much more work is required to resolve the question of the temperature dependence.

2.6 DEFECT SENSING VIA ANNIHILATION CHARACTERISTICS

As has been indicated in previous sections, the presence of defects perturbs the electronic structure of the perfect lattice. In the perfect lattice the positron is free to move around, and can sense both core and valence electrons. Figure 2.6.1(a) illustrates schematically a Doppler-broadened lineshape for a perfect lattice and shows how the lineshape is composed of these two types of electron states. The broader (Gaussian) distribution corresponds to annihilations with the higher momenta core electrons and the narrow (parabolic) to that of the lower momenta valence electrons. When open-volume defects are introduced to the lattice the positrons become

$$|\Delta E_{max}| = m_o c^2 \cdot \frac{v_F}{2c}$$

I

ΔE

I

ΔE

γ-ray Counts

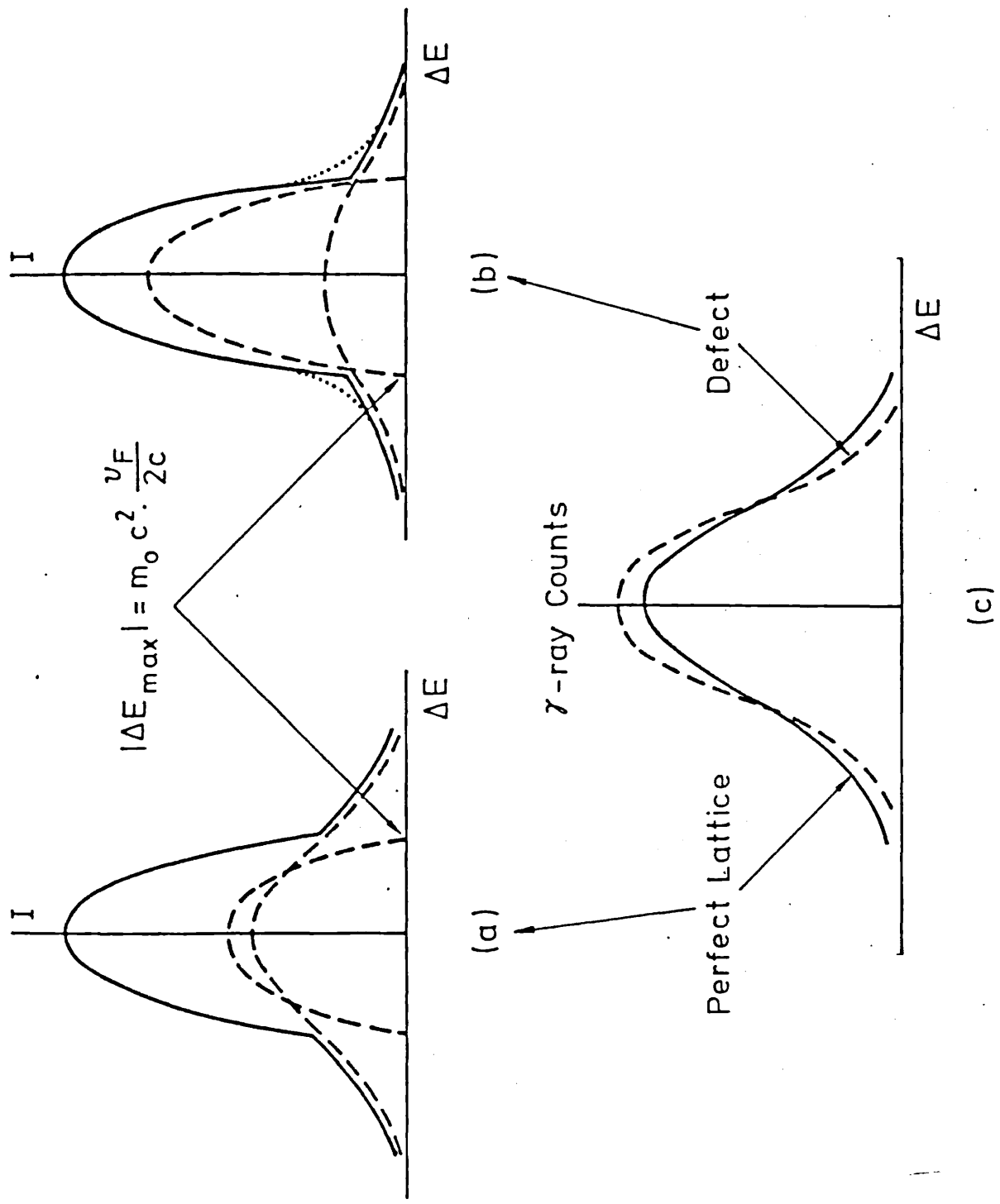(b)

Defect

(a)

Perfect Lattice

(c)

ΔE

Figure 2.6.1 Schematic Representation of Narrowing of Annihilation Lineshape due to Presence of Defects.

trapped in these regions as discussed in section 2.5. One consequence of positron trapping at open-volume defects is that the positron lifetime increases because of the reduced electronic charge. Lifetime measurements can, therefore, provide useful information on the defectiveness of the lattice.

Due to positron localisation at the defect, the wavefunctions are less able to penetrate the core electron regions of the surrounding lattice. Also, the Fermi velocities of valence electrons in the locality of the defect are reduced because of the smaller force they experience owing to the absence of the positive ionic charge. In fact, from equation 2.3.12 the Fermi velocity, v_F, produces a valence electron Doppler energy shift of $(v_F/2c)m_0c^2$. For the above reasons, the positrons tend to annihilate with more valence electrons (Figure 2.6.1(b)), and the width of the resulting distribution becomes narrower. Because different defects induce different perturbations on the perfect electron momentum distribution, they will give rise to experimental curves of varying shapes and widths. Hence, by defining these curves in terms of their shape (and width) defect structure can be monitored (chapter 4), and in some cases 'characterised'.

Chapter 4 also describes how the lineshapes for annihilation in the perfect lattice may be analysed in terms of parabolic and Gaussian components to represent the valence and core electrons respectively. This analytical regime has been extended to the defected lattice (for want of definition of the true 'shapes' of defected electron distributions), with the addition of a smearing component to represent the positron zero point motion. Attempts are made to characterise defects in terms of the parameters derived from such fitted components.

CHAPTER 3 : EXPERIMENTAL APPROACH

3.1 DETECTION AND COLLECTION OF ANNIHILATION PHOTONS

3.1.1 Doppler-Broadening Spectroscopy System

A Doppler-broadening system, illustrated in Figure 3.1.1, has been employed to study lineshapes resulting from positron annihilation. The system is composed of a Philips Ge(Li) solid state detector of sensitive volume 72 cm^3, a Harwell kandiah pulse processor, and a Canberra multichannel analyser (model 8100). The Kandiah pulse processor incorporates an opto-electronically controlled pre-amplifier, amplifier, analogue-to-digital converter (ADC), and a digital gain- and zero-stabiliser unit.

Essentially, incident radiation falling on the sensitive area of the detector produces a number of electron-hole pairs, the concentration of which is proportional to the energy expended by the radiation. Accordingly, charge pulses are collected at the detector electrodes whose amplitudes are proportional to the energy of the incident annihilation photons. These pulses are subsequently amplified. Pulses from the main amplifier are then sent to the ADC where their amplitudes are digitised in a linear fashion. The stabiliser has been incorporated to counter the effects of electronic drift caused by noise in the detector and the processing electronics. In order to achieve this the gamma ray line Hf_{181} (481 keV) is collected concurrently with the annihilation line and its centroid position determined by the stabiliser. A range of 16 channels on either side of the peak is monitored and any changes in the centroid position causes an error signal to be generated. Such signals produce changes in the amplifier gain so that the original centroid position can be restored. Finally, the digitised information is stored in the multichannel analyser (MCA). The MCA has a total memory capacity of 4096 channels with the ability to store 10^6-1 counts per channel. Figure 3.1.2 illustrates a typical annihilation lineshape collected by the system.
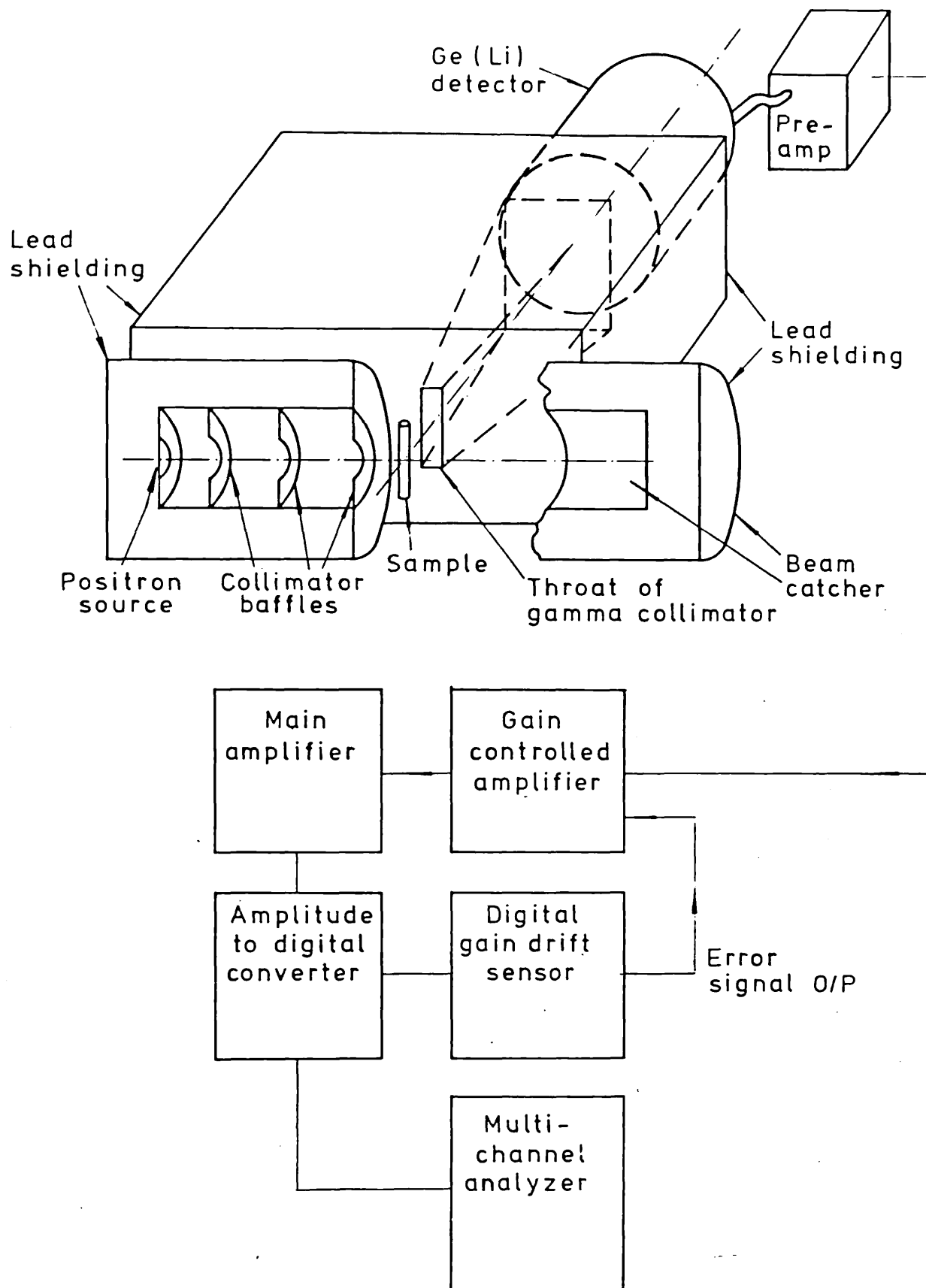
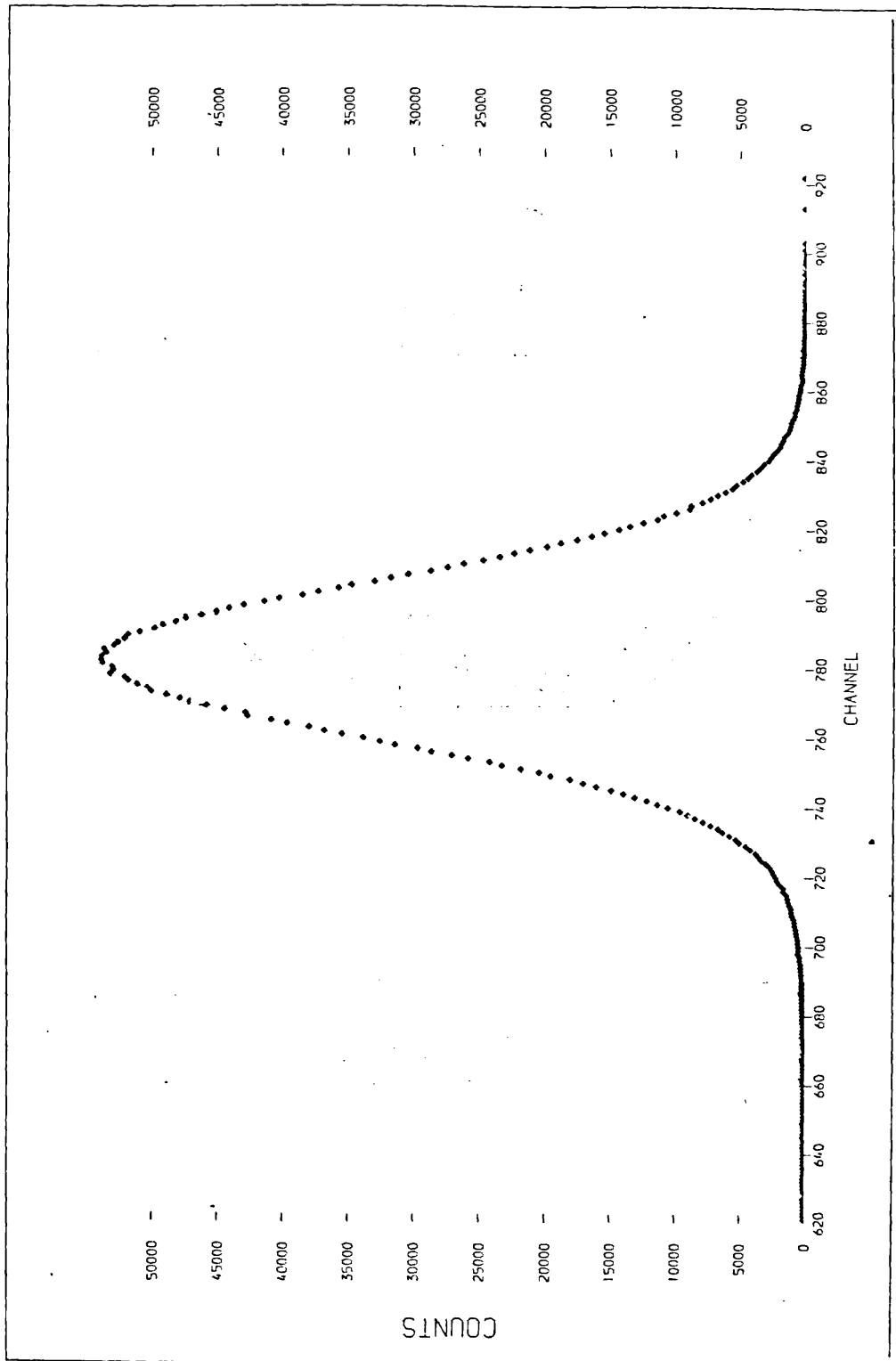Figure 3.1.1 Layout of Doppler-Broadening System

Figure 3.1.2   A Typical Annihilation Lineshape

Recently (August 1980), a new pulse processor (Harwell unit NM8841) and ADC and stabiliser (Harwell unit NM8871) have been installed to replace the original Kandiah system. The new ADC has a maximum resolution of 16K channels and the stabiliser controls to within $\pm$ 1% of the ADC energy dispersion. Figure 3.1.3 is a photograph of the complete Doppler-broadening system.

3.1.2 Energy Characteristics of Spectroscopy System

3.1.2.1 Energy Calibration

In order to achieve the best detailed energy lineshape (i.e. a lineshape defined by the maximum number of channels), it is necessary to operate at the highest energy dispersion obtainable with the ADC. Bearing this in mind the ADC was set to the maximum resolution of 16K channels. The MCA has four separate memories each of capacity 1024 channels. Thus, in order to store the desired energy range in any one memory, the first 9472 channels were offset by the use of a digital back bias unit. The energy dispersion of the system was determined by computing the centroid positions of both the monitor and annihilation lines in terms of channel number. Knowing the energy difference between the Hf^{181} and annihilation lines the energy dispersion was evaluated as 50 eV/channel.

When operating at such high dispersions it is inevitable that, for a given count-rate, the statistics in each channel will be relatively poorer. This poses a problem for the analysis of 'difference curves' (chapter 4) where high noise levels may smear out any detail. However, the use of 'smoothed' difference curves (e.g. running integrated difference curves described in chapter 4) permits the employment of such dispersions since the statistical noise per channel can be dramatically reduced.

Originally, experiments performed on the Harwell Doppler system were carried out with the desired energy range defined over a small range of 256 channels. This posed problems in the fitting of unprejudiced curve-fits to the lineshapes due to their 'sharpness' (Coleman et al, 1976). Another reason for operating at high
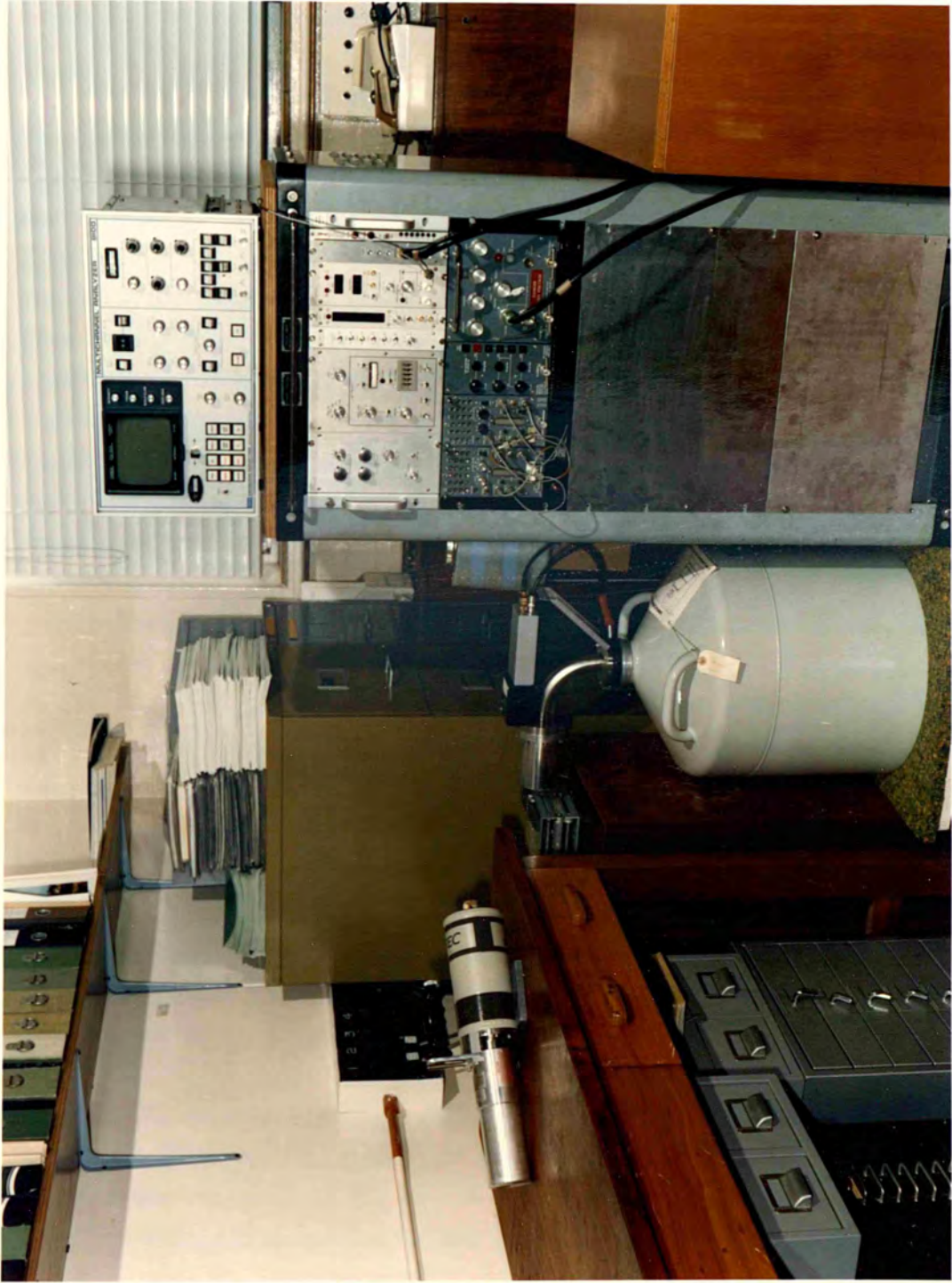
Figure 3.1.3
Doppler – Broadening Spectroscopy System.

dispersions, when positron work was initiated at Harwell, was to reduce the sharpness of the lines, hence encouraging successful performance in curve-fitting.

3.1.2.2 Energy Resolution

The ability of the spectroscopy system to resolve an energy, E, may be derived by the resolving power $E/\Delta E$, where ΔE is known as the resolution of the system and represents the error associated with the measurement of the energy E. Thus, the resolution of the overall spectroscopy system ensures that the true energy distribution of the annihilation photons is never stored in the MCA. The smearing of the true energy distribution is due to a number of effects. The statistical nature of the generation of electron-hole pairs for an incident particle of a given energy, together with the small leakage current in existence across the sensitive layer, are the main contributors to the resolution in the detector itself. Also, impurities and defects in the detector crystal can act as trapping centres from which recombination of charge carriers (produced by incident radiation) can occur adding to the detector resolution. The subsequent electronics is a further source of inherent resolution due to the array of components it contains. It is, therefore, desirable to keep the electronic circuitry required to a minimum. It is unfortunate that the stabiliser unit employed to minimise line-drift (hence line broadening), by its very existence, contributes a small amount to the overall resolution. however, the use of the stabiliser is justified since it prevents more broadening than it introduces. The resolution of the system is also a function of count-rate. Generally, the resolution degrades as the count-rate is increased due to the increased probability of pulse pile-up.

If the true energy distribution of annihilation photons is to be retrieved from the measured distribution then it is necessary to measure the response of the system to a mono-energetic gamma ray so that the measured distribution can be deconvoluted. The ideal response function will be recorded simultaneously with, and at the same energy as the annihilation photons. Clearly, this is not possible. However, a good approximation to the ideal reoslution can be obtained by

measuring, independently, the response of the system to the gamma ray line Sr^{85} which has an energy close to the annihilation line (514 keV). In all experiments performed the response of the Sr^{85} line was measured and the count-rate matched to that of the annihilation spectrum. The resolution (full width half maximum) of the system, for a count-rate of 250 Hz, is 1.44 keV at the Hf^{181} energy (481 keV). Such resolution is sufficient for detecting changes in the annihilation profile without resorting to deconvolution, thus enabling changes in lattice morphology to be observed. Although such information is extremely useful, detailed analysis of momentum distributions can only be achieved if the instrumental smearing is removed from the observed lineshapes.

3.1.3 Data Collection and Analysis

Data from the MCA was read out, via a Canberra 8531 magnetic tape controller, onto Pertec 7820/9, 7" reel, 9 track magnetic tape. When data collection was complete the Pertec tape was submitted for analysis on the Harwell IBM 370 computer. Two stages of computation were performed; firstly, the transfer of data onto master storage tape and, secondly, the analysis of lineshapes. Analysis of spectra is discussed in chapter 4.

After analysis on the IBM 370 the Pertec tape was submitted to the University of London Computer Centre and further analysis performed on the CDC 7600 computer. Prior to curve-fitting analysis the Pertec raw data was reformatted (to be compatible with CDC 7600 programming) and then copied onto master storage tape. All jobs on the CDC 7600 were run from the Bedford College Computer Terminal.

3.2 POSITRON SOURCES

Positron emitters commercially avaialble at the present time include Na^{22}, Cu^{64}, Ge^{68} and Co^{58}. For Doppler-broadening studies the ideal positron emitter will have the following properties:

(a) high intensity of positron decay,

(b) long half-life,

(c) absence of gamma decays above the annihilation energy that contribute to background under annihilation line,

(d) suitably high positron energies so as to achieve necessary penetration in test samples,

(e) ease of penetration.

An overall consideration of such factors renders Na^{22} the most popular choice. However, in this study, three of the above sources have been employed. The relatively high energies (1.89 MeV) of positrons emitted from Ge^{68} has made this source suitable for remote-source studies (section 3.3). Studies at elevated temperatures have necessitated the use of both Na^{22} and Cu^{64} (section 3.4).

When a positron beam enters a metal its intensity (N/N_0) attenuates according to the exponential law (Siegbahn, 1965)

$$N = N_0 \exp(- \frac{\mu}{\rho} x) \hspace{3cm} 3.2.1$$

where $\frac{\mu}{\rho}$ is the absorption coefficient and x the penetration distance. The absorption coefficient is a function of the maximum positron energy. Consideration of equation 3.2.1 shows generally that, for metals, a penetration depth of 2-3 μm can be responsible for 3-6% of the total annihilation contribution. This, of course, is important to consider when preparing sample-source 'sandwich' arrangements. The finite thickness of the source, and any material enclosing it, will provide a non-genuine contribution to the lineshape. Depending on the source arrangement, source contributions may be as high as 16% of the total intensity (e.g. Dave and LeBlanc, 1978). Estimates of effective maximum positron penetration ranges may be derived from equation 3.2.1 by, say, evaluating x for a positron beam intensity of 1%. Maximum positron penetration distances are dependent on sample density and maximum positron energy (e.g. Segre, 1953). For instance, typical

distances for Na^{22} positrons (E = 0.55 MeV) are in the range
100-250 µm. Pentration depths for the higher energy Ge^{68} positrons
may be as high as 1000 µm. Therefore, test samples with widths greater
than 1 mm are suitable for positron study with either of these two
sources.

3.3 EXPERIMENTAL TECHNIQUE FOR ROOM TEMPERATURE MEASUREMENT

3.3.1 Remote Positron Source Method

The use of a beam of positrons from a remote source, made to fall
incident on a test sample, has been the technique adopted for studying
annihilation events at room temperature. the general lay-out of the
positron beam apparatus is seen in Figure 3.3.1. Basically, a Ge^{68}
positron source is positioned in a positron beam collimator assembly of
which the collimator baffles are made of brass. The test sample is
made to sit at a point directly in view of the positron beam at which
subsequent annihilations take place. The Ge(Li) detector is positioned
at right angles to the direction of the positron beam and annihilation
gammas emerging from the sample are able to enter the detector mouth.
Beyond the sample and directly opposite the positron collimator, a lead
beam stopper is positioned so as practically all positrons entering it
are stopped and forced to annihilate in the lead. In such an
experimental arrangement it is easy to see that annihilation events,
other than those coming from the sample, can find their way to the
detector and, thus, contribute to the resulting lineshape. In order to
minimise such events (section 3.3.1.1) the detector is suitably
shielded with lead so that the resulting lineshapes are predominantly
composed of genuine, sample events.

3.3.1.1 Minimisation of Spurious Events seen by Detector

Apart from annihilations occurring in the sample, the existence of
the positron beam across the width spanning the positron collimator and
beam catcher ensures that annihilation events occur in the brass
collimator baffles, the volume of air in front of the detector, and
also in the beam catcher. The detector can be protected from much of
this annihilation activity by using the shielding arrangement shown in

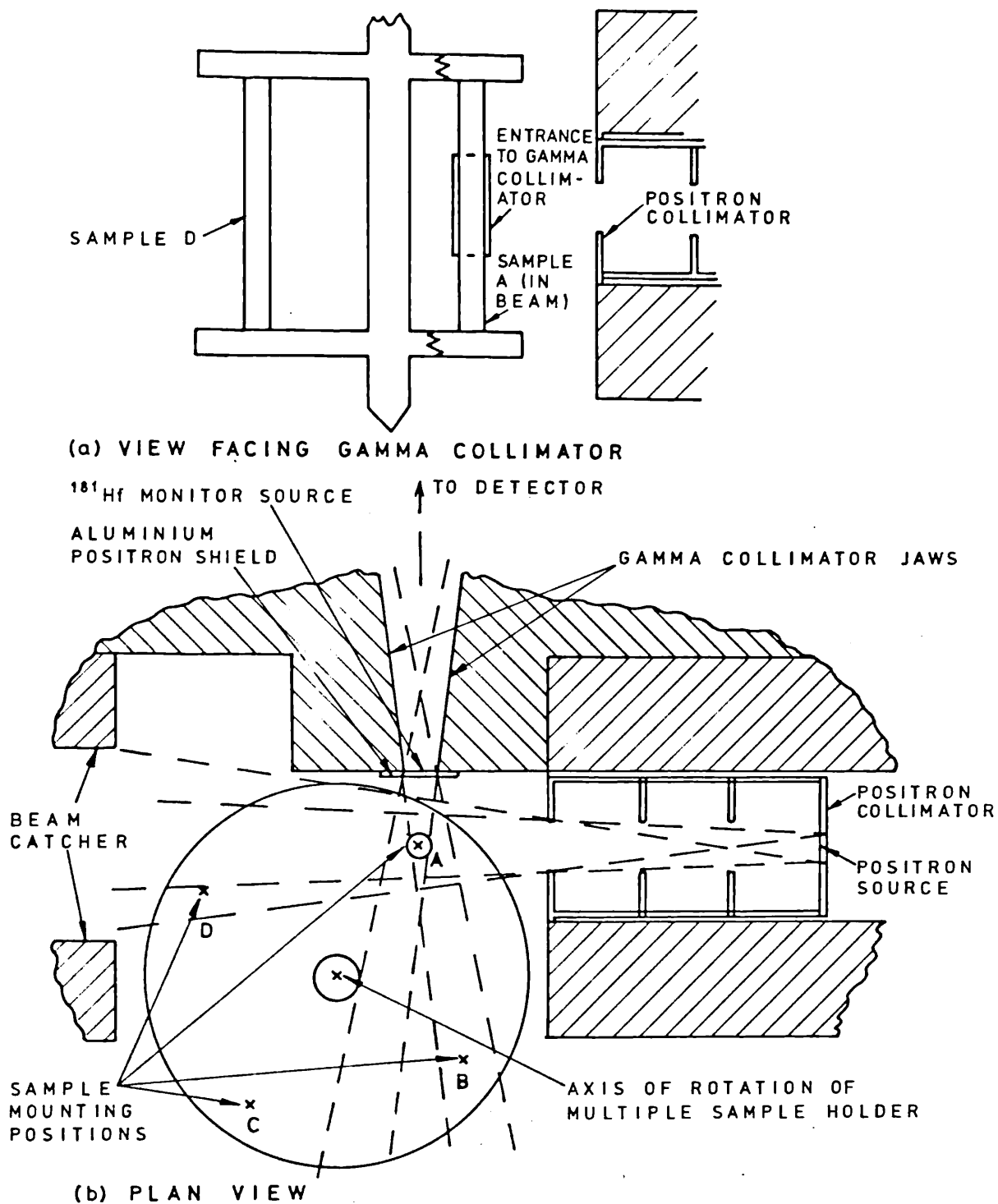(a) VIEW FACING GAMMA COLLIMATOR

(b) PLAN VIEW

Figure 3.3.1 Arrangement of Positron and Detector Collimators with Rotary Sample Changer

Figure 3.3.1(b). A wedge-shape collimator is cut in the lead directly in front of the detector giving dimensions 7 mm wide by 20 mm high at its throat. This restricts the field of view of the detector to the sample area only. Figure 3.3.2 is a photograph of the detector and positron beam collimator arrangement, and shows more clearly the detector shielding and gamma collimator. The cylindrical samples are fatigue test pieces.

Of course, a percentage of positrons scattered off the sample, and from the air surrounding it, can enter the collimator giving rise to detectable annihilations occurring in the collimator itself. Such events have been significantly reduced by introducing an aluminium absorber ($^1/16$" thick) over the collimator throat (Figure 3.3.1(b)). This has the effect of forcing all scattered positrons entering the throat to annihilate in the absorber. The restricted area of the throat reduces the cross-section for gamma detection. Such events have been estimated to contribute between 5-8% to the total collected counts. The Hf^{181} monitor source is mounted on the aluminium absorber.

3.3.2 Rotary Sample Changer

The analysis of differences in lineshapes, due to changes in sample morphology, demands that changes in experimental conditions be kept to an absolute minimum. In order to encourage the collection of lineshapes under identical electronic and geometrical conditions a special rotary sample changer has been developed (Figure 3.3.1(b)). It can be seen that, at any one time, only one sample is directly in front of the beam. The design of the holder is such that a high degree of symmetry is imposed on the overall geometry. Samples A, B, C and D (Figure 3.3.1(b)) are mounted at rim positions 90° apart from each other, and the complete holder assembly is suitably placed in front of the detector collimator. Figure 3.3.1(a) illustrates the view facing the gamma collimator.

When accumulating data on a group of four samples over a long period of time it is desirable to match electronic conditions so that differences between lineshapes due to electronic drift can be reduced.
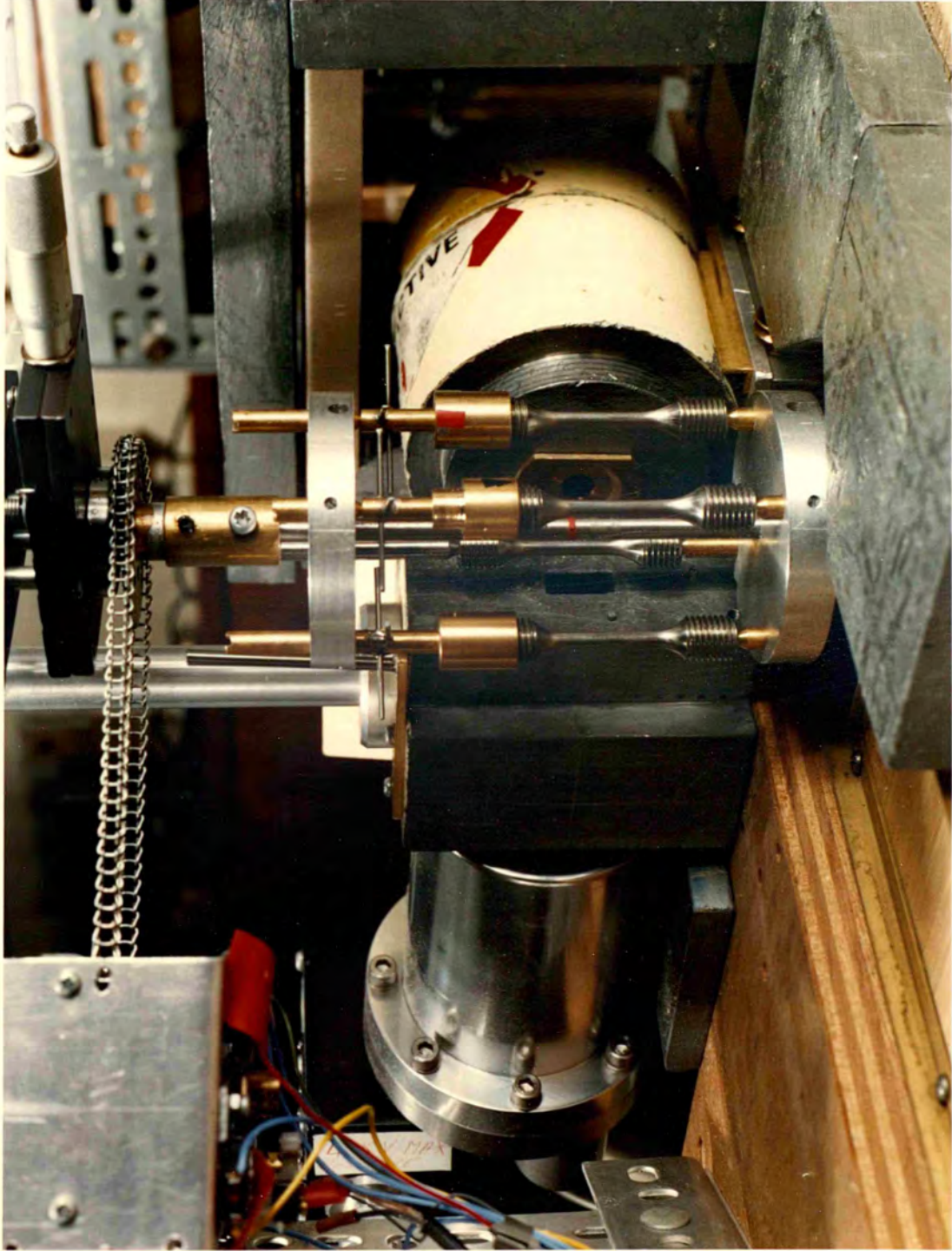
Figure 3.3.2
Arrangement for Detection and Positron Beam Collimation.

This can be achieved by collecting data on each sample for a series of relatively short intervals as opposed to a longer, continuous fixed period of time. Hence, the holder has been automated (Coleman et al, 1978) so that every 30 minutes it rotates by 90°, thereby positioning the next sample in front of the detector and positron beam. With such an arrangement each sample is placed in the beam several times during the course of a complete run. The use of digital logic circuitry allows the events collected for each sample to be routed to a separate memory in the MCA.

3.3.3 Sample Geometry for Remote Source Method

To study mechanical damage it is important to design test samples that can be easily deformed. Since the chosen method to produce such damage was by cold-rolling the samples employed were flat, rectangular slabs (unlike the cylindrical pieces shown in Figure 3.3.2). Also, in order to minimise the signal-to-noise ratio of annihilation detection the sample dimensions should be comparable with those of both detector collimator and positron beam divergence. Accordingly, the test samples were cut to the nominal dimensions 1 cm x 4 cm x 2 mm. For a rectangular slab geometry optimum conditions are achieved by positioning the slab face at 45° to the axis of the positron collimator (Figure 3.3.3(b)). In order to reduce the number of scattered positrons entering the detector collimator the incident slab face is positioned away from the detector. In order to position the slabs in the rotary sample changer triangular notches on each end of the slabs were cut out (Figure 3.3.3(a)) so that they could be slotted into specially prepared brass locating pins.

As indicated in section 3.3.2 it is important to keep experimental conditions constant. For instance, changes in sample width can significantly alter the positron beam scatter cross-section and so change the intensity of the spurious annihilation contribution. A preliminary experiment was performed in order to assess the effects of small changes in sample width. Ten samples of 5N purity copper (Johnson Matthey) were cut to the nominal dimensions quoted above but with the average sample widths varying as illustrated in Figure 3.3.3. All samples were then annealed for 8 hours at 900°C. The positron
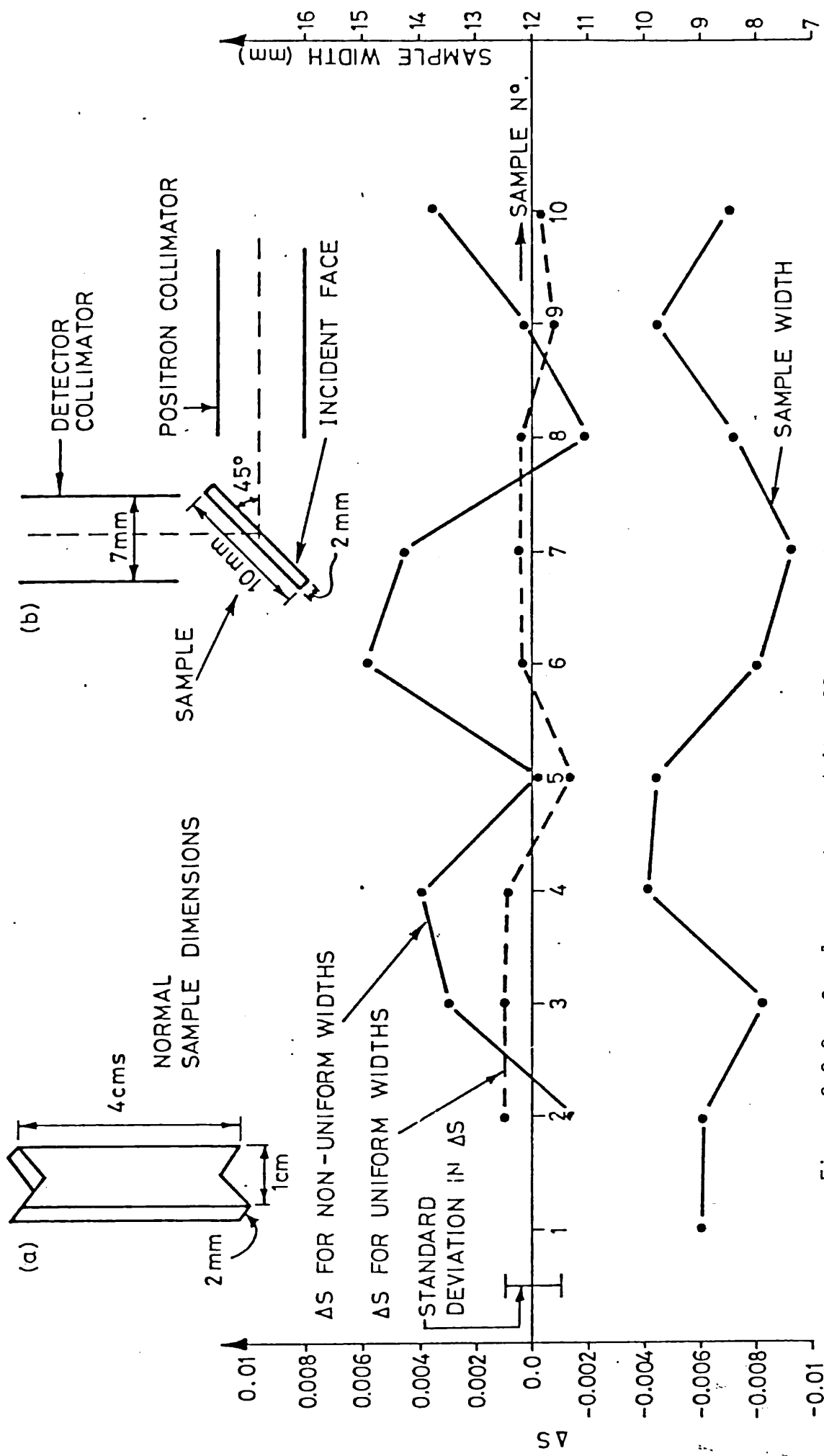
Figure 3.3.3   Sample geometry and its effect on positron characteristics

parameter S (defined and discussed in chapter 4) was measured for each sample. This parameter is dependent on the intensities of all modes of annihilation events entering the detector. For a series of samples with identical lattice morphology changes in S (ΔS) should, within statistical error, be non-existent. Figure 3.3.3 shows that ΔS (sample 1 is taken as the reference) varies significantly in the case of non-uniform widths whereas when samples are machined by lathe to produce uniform widths the variation lies within statistical error. It was concluded that changes in S were caused by differing spurious annihilations resulting from variations in sample width. The experiment shows that a standard deviation of 0.9 mm in width over a sample batch can cause significant changes in lineshape positron parameters. Consequently, all samples prepared for remote source experimentation were machined to exactly the same dimensions.

3.3.4 Mechanical Deformation of Samples

All samples employed for remote source measurement were compressed to various strains with the use of a rolling mill (Sir James Farmer Norton and Co. Ltd.) available at Harwell (Bldg. 35, Metallurgy Division). Swelling of sample dimensions was confined to the direction of rolling (i.e. along sample length) and, thus, ensured that the original sample width could be retained.

3.4 EXPERIMENTAL TECHNIQUE FOR MEASUREMENTS AT ELEVATED TEMPERATURES

3.4.1 Sample-Source Sandwich Method

All positron measurements carried out above room temperature were performed in a specially built furnace. For practical simplicity, the remote source arrangement was abandoned in favour of the conventional sample-source sandwich approach. Samples were normally prepared using an aqueous solution of $Na^{22}Cl$ (supplied by The Radiochemical Centre, Amersham). Drops of $Na^{22}Cl$ were deposited on one of the sandwich sample 'twins' and then left to evaporate, thus leaving a solid layer of Na^{22} Cl. Typical activities attained in this way were usually about 80 μCi. The sample-source sandwich was then made by placing the uncontaminated sample on its twin, and the resulting

assembly wrapped well in metal foil.

Since the melting point of NaCl is 801°C, experiments requiring measurements above this temperature were performed with the use of Cu^{64} sources. These were copper foils (~ 2 μm thickness) neutron-irradiated in the Harwell DIDO reactor by the Radioisotope Production Unit.
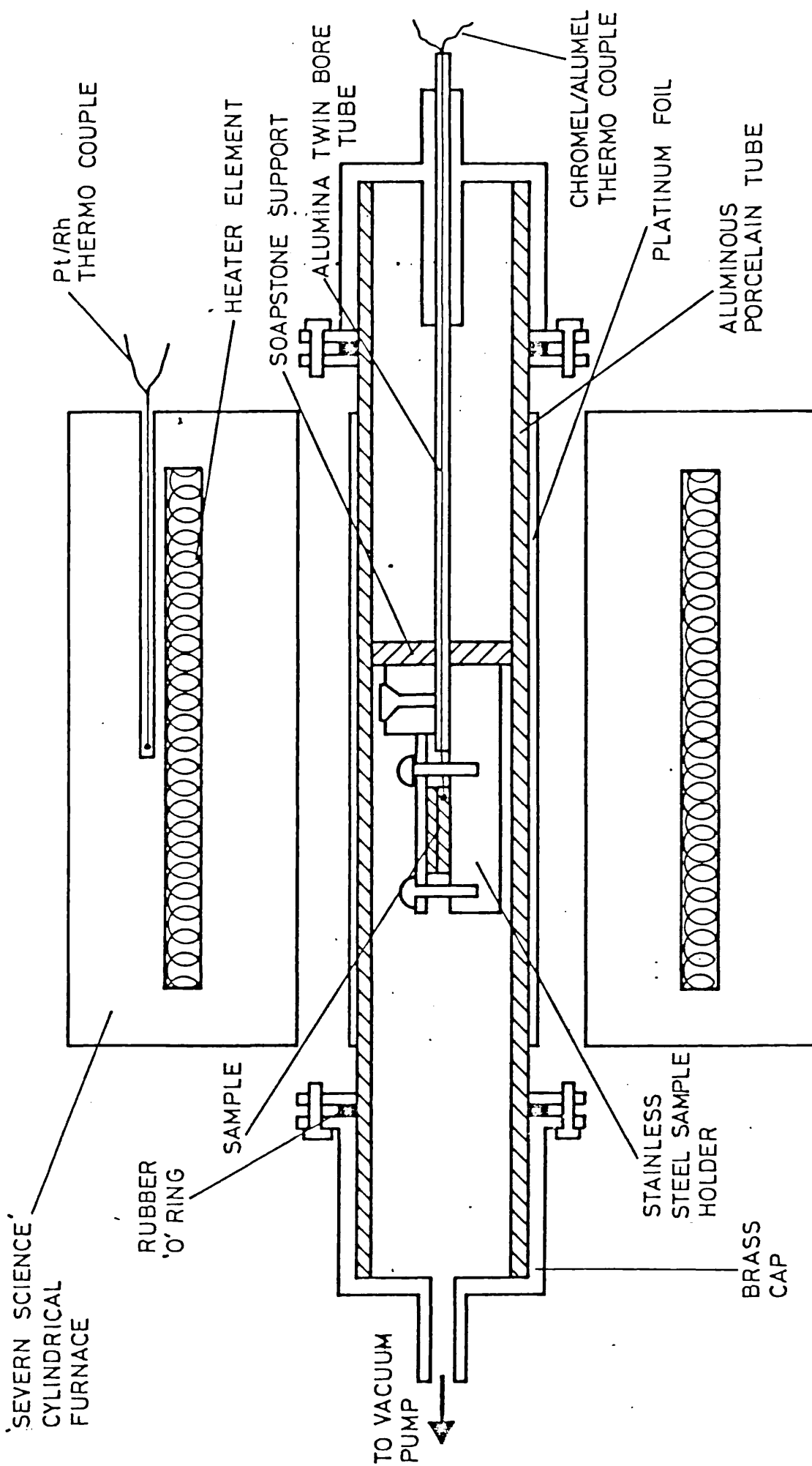
3.4.2 Apparatus for High Temperature Experimentation

3.4.2.1 High Temperature Furnace

Figure 3.4.1 illustrates the way in which an aluminous porcelain tube, nominal bore 22.5 mm (supplied by Thermal Syndicate Ltd.), has been adopted for high temperature use. Thermocouple leads (chromel/alumel) are fed through to the stainless steel sample holder via an alumina twin-bore tube. The weight of the stainless steel holder is supported by the soapstone block which ensures that it does not droop to make possible contact with the porcelain tube wall. Brass-caps are screwed on at each end and, with the use of 'O' rings, provide good vacuum seal. Originally a nichrome heater wire was wound directly around the tube, and the complete assembly placed in an aluminium box filled with glass wool to provide good thermal insulation. Such a furnace design works well up to a temperature of about 500°C (e.g. Chaglar, 1978). Above this temperature, however, the insulating behaviour of aluminous porcelain was found to break down. Consequently, heater element a.c. voltages appeared across the thermcouple wires since they were now in contact with the element via aluminous porcelain, alumina twin-bore tube and sample holder. In an attempt to prevent such action a layer of 'high purity' alumina ($\sim \frac{1}{4}$" thick) was sprayed around the tube before the element was wound on. Unfortunately, the treatment proved unsuccessful.

The problem was finally solved by employing a commercial furnace (Severn Science Ltd.) capable of reaching 1200°C. The porcelain tube was now positioned inside this, and no physical contact was made with the furnace body. However, induction currents appeared on the thermocouple wires at about 500°C, but these were subsequently removed

Figure 3.4.1   High Temperature Furnace

with the use of an earthed platinum foil wrapped around the porcelain tube.

3.4.2.2 Vacuum Pump

To prevent oxidation of samples at elevated temperatures a diffusion pump was employed to evacuate the furnace tube and, in this way, vacuums of 10^{-6} torr could be achieved.

3.4.2.3 Heater Supply and Temperature Control

A temperature controller unit (Eurotherm Ltd.) was used to supply the power to the furnace heater element. Due to the excessive time delay between error signal and heat transfer to sample it was impossible to control the sample temperature by use of the sample thermocouple without serious overshoot occurring. Instead, a Pt/Rh thermocouple was attached to the Kanthal element windings in the furnace and control performed on this. Although not the ideal arrangement, temperature could usually be controlled to an accuracy of $\pm$ 1°C.

3.4.3 Problems Encountered in the Use of Na^{22}Cl at High Temperatures

3.4.3.1 Contamination

Contamination will certainly occur if the sample sandwich is heated above the melting point of Na^{22}Cl - liquid Na^{22}Cl will leak out and contaminate the holder assembly. However, contamination was encountered at temperatures well below this limit. At first this was attributed to bad temperature control due to the induced a.c. currents on the thermocouple wire on the original furnace design. However, when this problem was solved, and many contaminated tubes later, it became clear that contamination was due to the presence of the vapour phase of Na^{22}Cl.

Figure 3.4.2 shows the variation in total integrated annihilation counts collected in a given time (count-rate) as a function of

Figure 3.4.2   Significance of gaseous $Na^{22}Cl$ as a function of temperature
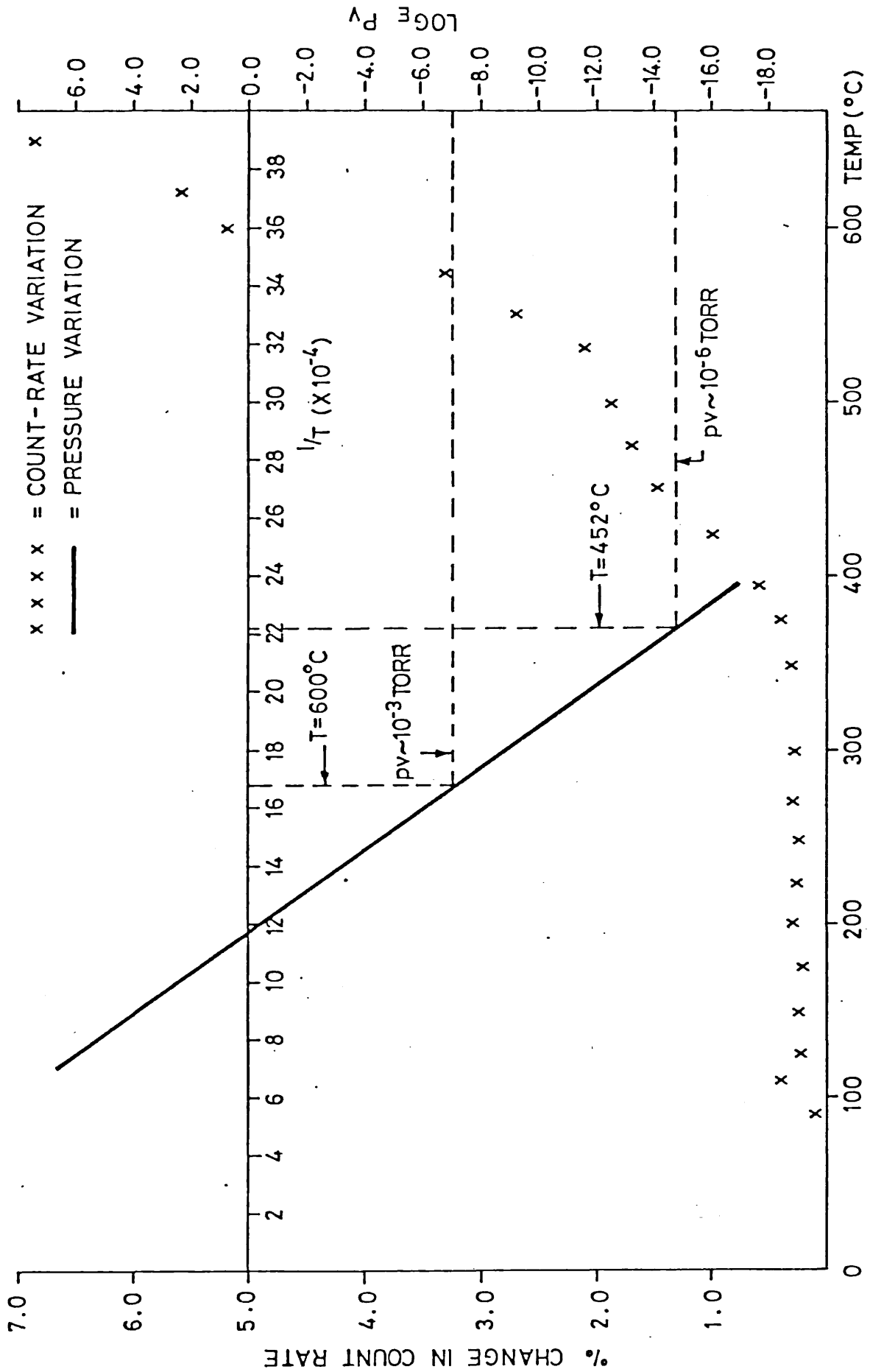
temperature for an isochronal anneal of copper (chapter 5). For a typical lineshape consisting of about 10^6 counts the fluctuation in count-rate will be $\sim 0.1\%$. Figure 3.4.2 shows that the variation in count-rate up to 400°C is compatible with this figure. However, above this temperature the count-rate increases and is no longer compatible with statistical error. It was concluded that the increase was due to the presence of a significant concentration of gaseous $Na^{22}Cl$ which, therefore, generated a higher cross-section for annihilation detection.

To test this theory data available on vapour pressures as a function of temperature for liquid NaCl were extrapolated to approximate the vapour pressures for $Na^{22}Cl$ below its melting point. The vapour pressure of a solid is given by the relation

$$P_v \ \alpha \exp(-E_v/kT) \qquad\qquad 3.4.1$$

where T is the temperature of the solid and E_v the energy of vaporisation. Figure 3.4.2 illustrates the extrapolated plot and shows that at 450°C the vapour pressure is comparable with the vacuum pressure ($\sim 10^{-6}$ torr). This, of course, is the stage at which the pumping action will cause the vaporised $Na^{22}Cl$ to be driven out of the sandwich and so contaminate the surroundings. It seems the vapour pressure extrapolation confirms the count-rate evidence - i.e. contamination will occur in the temperature region 400-450°C.

3.4.3.2 Alternative Techniques

Clearly, if the $Na^{22}Cl$ sandwich configuration is to operate successfully at high temperatures methods must be sought to confine the area of $Na^{22}Cl$ vapour activity. Various techniques have been employed to date - e.g. deposition of metal ions to cover source deposit by d.c. evaporation or ion-beam sputtering, electron beam welding, and ion-implantation. All these methods had to be ruled out for reasons of time, expense and practicality. However, an unsuccessful attempt was made at sealing in the source by depositing

over it a layer of carbon ($\sim$ 1000 Å) by d.c. evaporation. The usual sandwich geometry was then attained by placing on top of the active sample its twin counterpart. Before heating up the assembly the upper sample was removed and checked for activity - contamination had occurred. Unfortunately, the crystal structures of carbon and $Na^{22}Cl$ are not easily matched and so it was relatively easy to destabilise the carbon/$Na^{22}Cl$ interface by friction.

Electron beam welding had to be ruled out on the grounds that the high temperatures applied in the process would anneal out damage in deformed samples. In fact, sources sealed by metal deposition or ion-implantation, and used in the sandwich configuration, normally have to be supported by an electron beam weld so as to reduce the inevitable source escape associated with diffusion at higher temperatures ($\sim$ 700°C) e.g. Fluss and Smedskjaer, 1979, Herlach and Maier, 1976. Hence, the use of these methods would not be suitable for deformed samples at temperatures above 700°C.

3.4.4 Concluding Remarks

Due to the problems discussed in section 3.4.3 isochronal experimental studies were carried out by limiting the maximum temperature of operation to 400°C. The use of a Cu^{64} source for such studies was rejected since its short half life ($\sim$ 12 hrs) would necessitate interrupting an experimental run every few hours to replace the source. An experimental run performed over a period of a week would, therefore, require 6 or 7 samples (expensive), would extend the duration of the run to uncomfortable lengths, and would mean a continuous change of experimental conditions. The use of Cu^{64}, however, has been employed for high temperature work where only a few hours experimentation is required.

Positron work at high temperatures is not easy. Apart from the practical problems discussed above associated with 'in-situ' sources, such experimentation (if not handled carefully) can also constitute health risks. The use of heated sources is not the most desirable approach to adopt.

The loss of source integrity associated with in-situ measurements at high temperatures must, surely, make the possibility of using remote source methods more attractive. Remote source experimentation, to date, has not been favoured. However, such methods would offer a 'cold' positron source and avoid the problems associated with 'hot' ones. In fact, Burton and Huang (1978) have discussed and employed the use of a remote, Na^{22} source in conjunction with a high temperature furnace. They did not, though, consider details of photon collection. By incorporating the principles of gamma collimation and detection discussed in section 3.3, and by using the Burton and Huang furnace arrangement, it would not be beyond the bounds of possibility to build a good, workable remote source, high temperature assembly. With a growing interest in high melting-point metals for use in modern day technology, the use of remote source systems in high temperature positron studies should be seriously considered.

91

CHAPTER 4 : L I N E S H A P E   A N A L Y S I S

4.1 INTRODUCTION

To understand the nature of positron annihilation in matter it is important to relate characteristics of the observed lineshape to the lattice morphology. Various approaches have been adopted. For instance, since the lineshape is a reflection of the electron momentum distribution, attempts can be made to decompose it into specific mathematical profiles based on the theoretical predictions of band theory calculations (chapter 2). In other words, the lineshape is made to fit a specific mathematical model the parameters of which can provide information on the absolute physical characteristics of the electron environment encountered by the positrons. This approach has been adopted by a number of workers in the field (e.g. Dlubek and Brummer, 1977; Jackman et al, 1974; Barshay et al, 1974b; Rice-Evans et al, 1976).

Another approach is to devise lineshape parameters that are, essentially, model independent. Such parameters merely describe the profile or shape of the line, yet can be tremendously powerful in indicating changes in lattice structure. An example of such a parameter is the S-value (introduced by MacKenzie et al, 1970) and is discussed in section 4.2.1. Although the S-value, and one or two other lineshape parameters, have been successfully employed for many years, little work has been done on devising other shape parameters capable of exploiting more exhaustively the shape of the line and, thus, the information it has to offer. There is also a clear need to devise so-called 'defect-specific' parameters such as the R-parameter introduced by Mantl and Trifthauser (1978). These parameters offer the prospect of characterising individual defect types. Such parameters would be exceedingly useful for studying the defect types present, and defect mechanisms involved in, say, mechanically deformed samples.

The purpose of this thesis is to study both defect and positron behaviour in metals by employing the two approaches discussed above - i.e. model -dependent and -independent approaches. An attempt will

be made to highlight the pros and cons for each type. Also, the use of 'running-integrated-difference' curves to study defected lattices will be discussed, with emphasis placed on the 'defect-specific' parameters derived from such curves. Accordingly, this chapter outlines the principles involved in each type of analysis.

4.2 A MODEL INDEPENDENT APPROACH

4.2.1 The S-Parameter

Figure 4.2.1 illustrates how the S-parameter may be defined - it is the number of counts in the region AB normalised by the total integrated count of the line. With an increasingly defected sample, more positrons will annihilate with conduction electrons, thus causing the lineshape to narrow. This will be registered as an increase in the value of S. If N is the total integrated count of which a fraction P_i annihilate in the ith mode, then the number of counts in the region AB will be $\Sigma_i S_i P_i N$, giving

$$S = \sum_i S_i P_i N/N = \sum_i S_i P_i \qquad 4.2.1$$

where S_i is the characteristic value for S when all positrons are annihilating in the ith mode. This definition is useful, since the observed value of S can be related to the concentration of defect traps in the lattice via the 'trapping' model (chapter 2).

Equation 4.2.1 shows that changes in S are dependent on the types of defect present and their relative concentrations. Hence, although such a parameter is extremely valuable for monitoring changes in defect structure, it cannot characterise the nature of a defect unless all positrons annihilate at it.

The statistical error in the measured value of S is given by approximately $1/\sqrt{N}$ where N is the total count in the line (section 4.2.4). The computation of S is discussed in Section 4.2.5.

$$S = \frac{\text{Counts in region AB}}{\text{Total counts}(N)}$$

$$\sqrt{\frac{\delta S^2}{S}} \simeq \frac{1}{\sqrt{N}}$$

$$\sim \frac{1}{10^3} \quad \text{For } N = 10^6$$
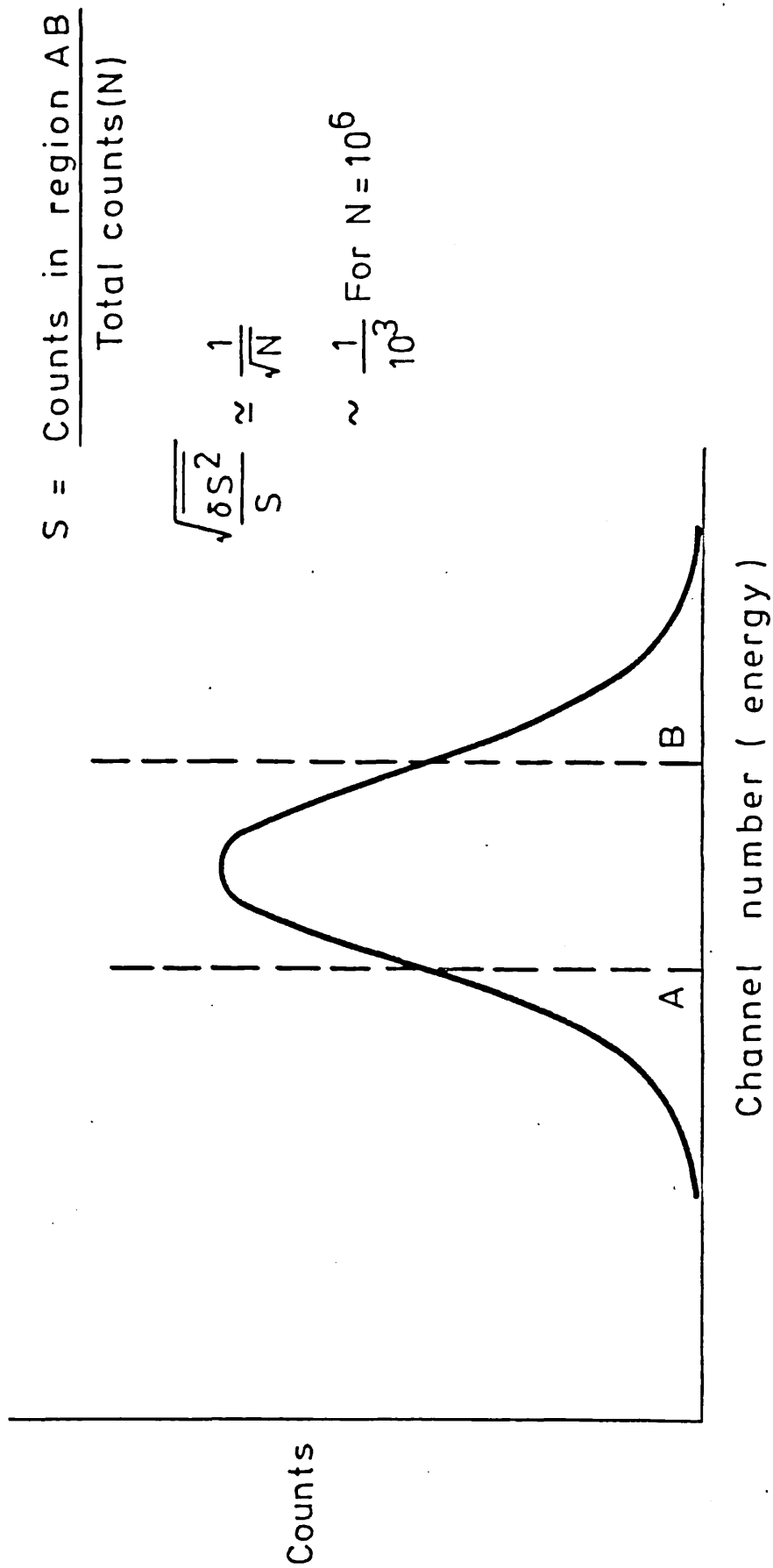
Counts

Channel number (energy)

Figure 4.2.1   Definition of the S-Parameter

4.2.2 Running Integrated Difference Curves

Following changes in annihilation lineshapes can be facilitated by working directly with the difference profiles obtained by subtracting one lineshape from another. Under favourable circumstances the profile of the difference curve can characterise a specific defect (e.g. Gauster, 1976). Figure 4.2.2(a) illustrates how the lineshape of a sample has narrowed due to fatiguing, and figure 4.2.2(b) shows the difference profile, $D(E)$, resulting from a channel by channel subtraction of the reference line from the deformed line. These profiles also have the advantage that, in a batch of runs performed under identical experimental/geometric conditions, the inevitable spurious contribution collected will be removed from the difference profile as a consequence of the subtraction. However, when small changes in lineshape are monitored by the use of difference curves the statistical noise becomes important, and figure 4.2.2(b) shows the scatter involved in such a profile. The noise will become even more significant when the line is collected at a higher energy dispersion, thus producing results of high uncertainty in any attempt to analyse the profile. Clearly, the statistical noise must be minimised. A simple, effective way of achieving this is by transforming the difference profile into a running integrated difference profile (Coleman, 1979). Briefly, if $D(I)$ is the normalised difference in channel I then the running integrated difference for channel N is defined as

$$I(N) = \sum_{I=1}^{N} D(I) \hspace{3cm} 4.2.2$$

The resulting profile is illustrated in figure 4.2.2(c). It is immediately obvious that after a few integrations over a few channels the counts accumulated in each channel of the running integrated difference (RID) curve have generated statistics good enough to dramatically suppress the noise.

In a defected lattice the electron momentum profile $X(p)$ may be defined by the normalised distribution
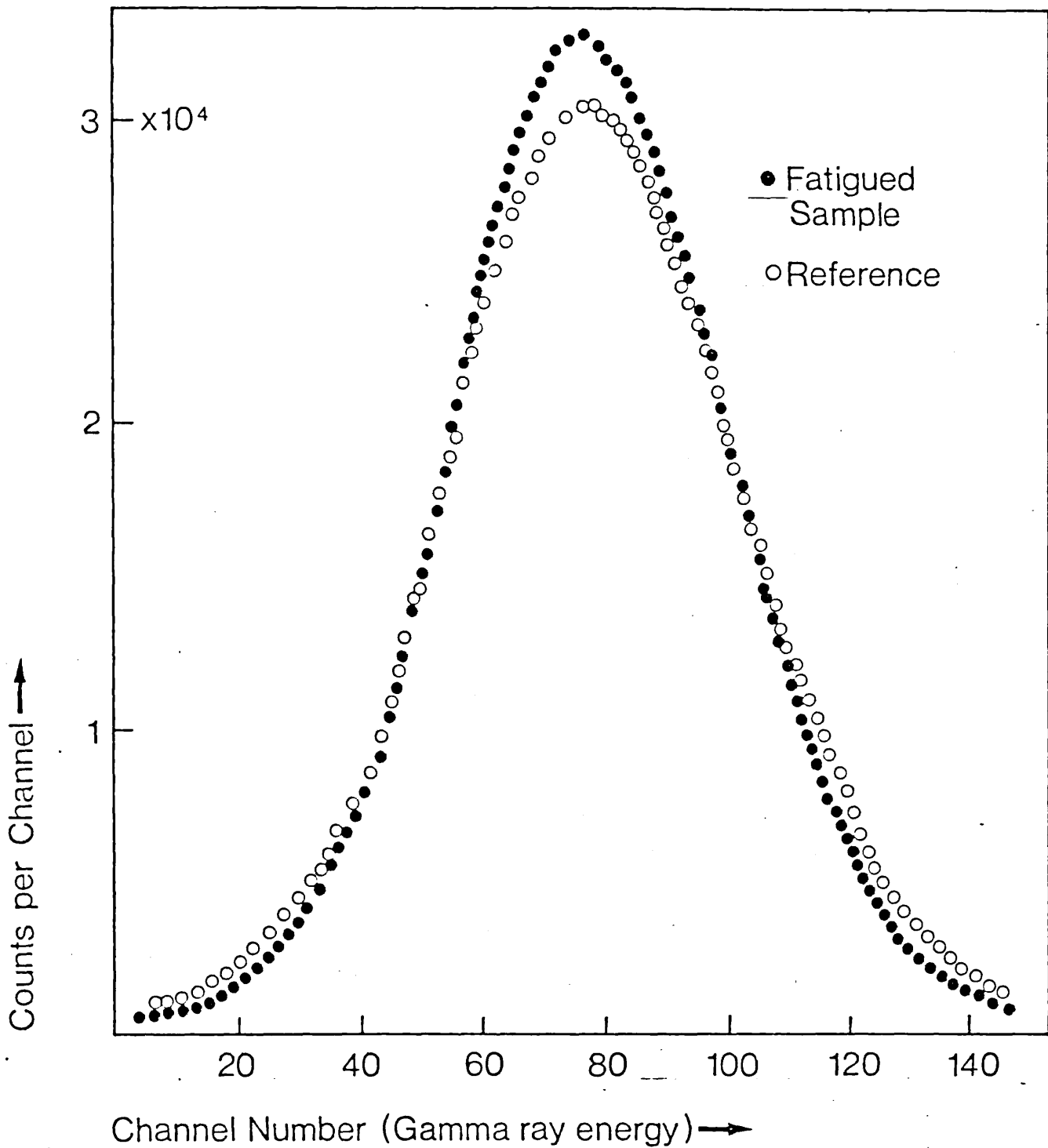
Figure 4.2.2(a)   Change in Annihilation Lineshape due to Fatigue
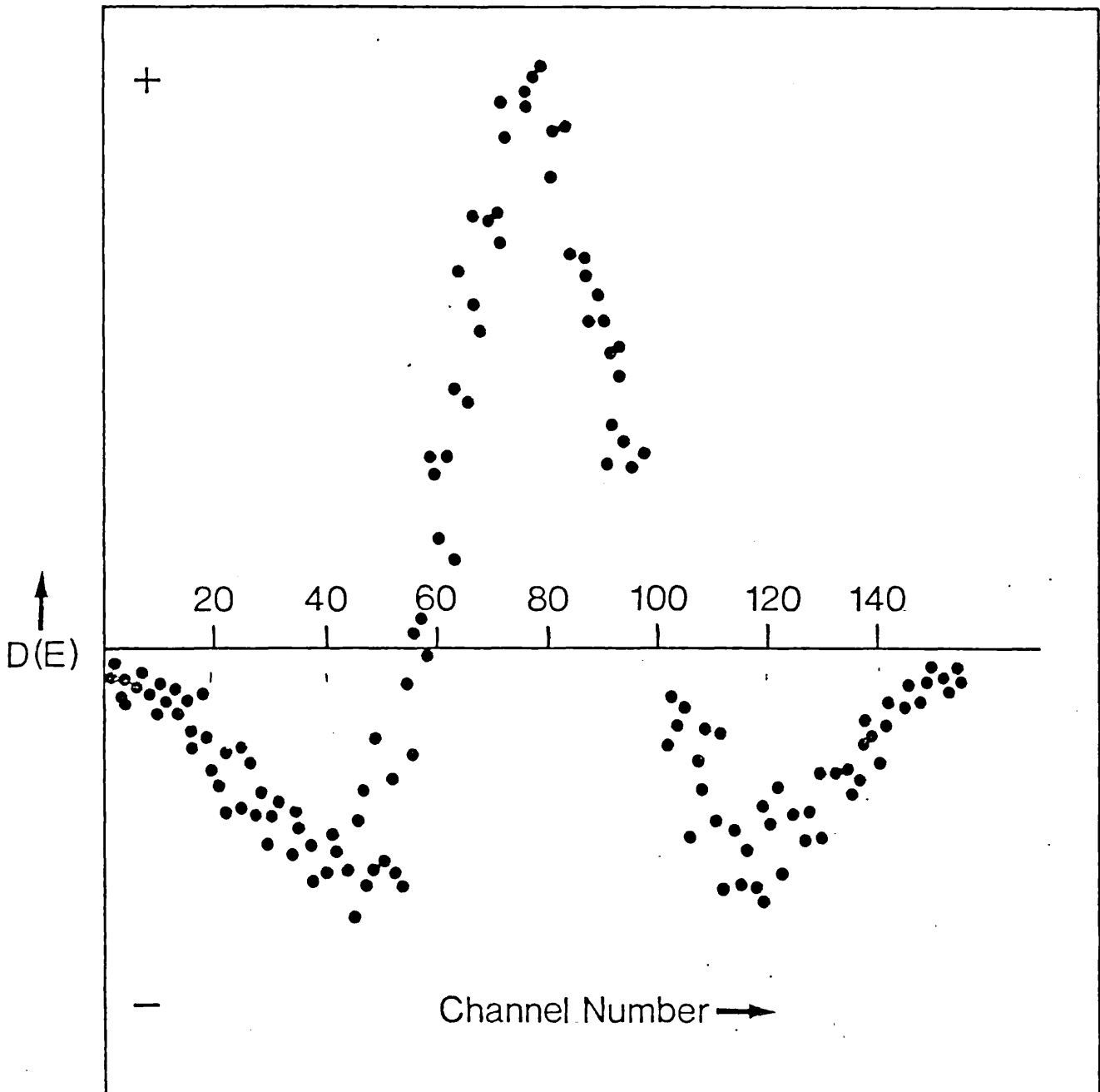   damaging.

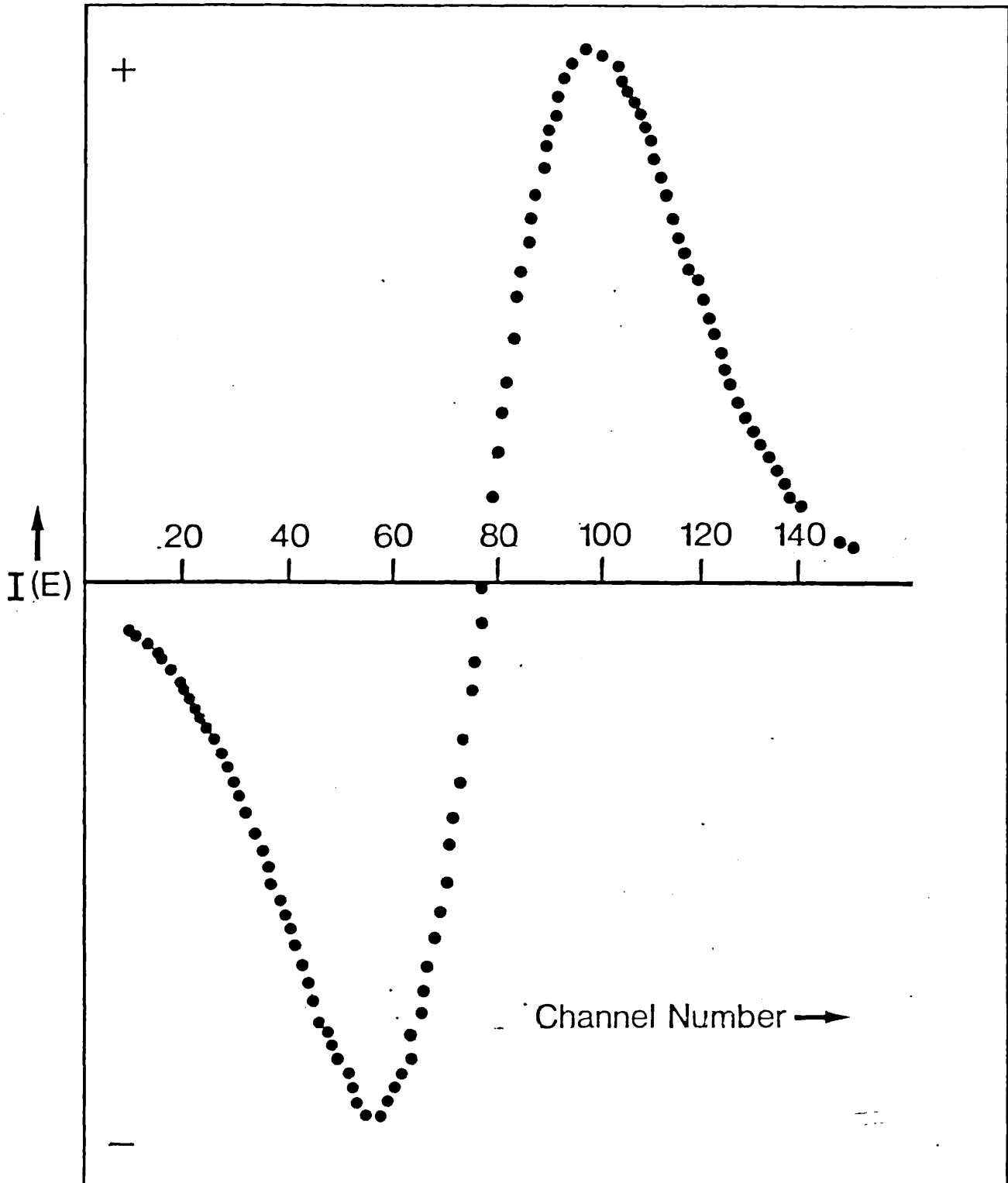Figure 4.2.2(b) Difference Spectrum Generated from Reference and Fatigued Lineshapes

Figure 4.2.2(c)   Integrated Difference Spectrum I(E) Generated
from Difference Spectrum D(E)

$$X(p) = \sum_{j=0}^{n} \left\{ \alpha_j f_{vj}(p) + \beta_j f_{cj}(p) \right\} \qquad 4.2.3$$

where n = number of defect types

$f_{vo}(p)$ = conduction electron distribution in the perfect lattice

$f_{vj}(p)$ = conduction electron distribution at the jth type of defect

$f_{co}(p)$ = core electron distribution in the perfect lattice

$f_{cj}(p)$ = core electron distribution at the jth type of defect

and $\qquad \sum_{j=0}^{n} (\alpha_j + \beta_j) = 1.$

In the case of positron trapping at defects, and the resultant localisation of the positron wavefunction, the momentum of the positron becomes significant. Hence, the experimental profile for the annihilation lineshape due to a defected sample may be represented by the normalised distribution

$$F(p) = \sum_{j=0}^{n} \left\{ \left\{ \alpha_j f_{vj}(p) + \beta_j f_{cj}(p) \right\} * \left\{ p_j(p) \right\} \right\} * R(p) \qquad 4.2.4$$

where $p_j(p)$ is the positron momentum distribution for the jth type of defect and R(p) is the response function of the experimental system. The symbol * denotes a convolution. Equation 4.2.4 shows that the experimental lineshape profile depends on the shape of each individual electron and positron profile. As different defects induce different perturbations in the perfect electron distribution one can expect a unique momentum profile for each defect type, j. Also, it is likely that the positron momentum profile will be different for each type of defect trapping centre. Hence, if the response function remains unchanged during the course of an experimental run, changes in lineshape profile will be dependent only on positron and electron

profile changes. It will now be shown that if only the concentrations of all defect traps present in a sample change in the same proportions, then the 'shape' of the resulting RID curve will remain constant.

From equation 4.2.4 let

$$\sum_{j=1}^{n} \left\{ \alpha_j f_{vj}(p) + \beta_j f_{cj}(p) \right\} * p_j(p) = \gamma_1 f_t(p)$$

where $f_t(p)$ represents the resultant electron-positron momentum profile due to all defect environments, and γ_1 is a constant proportional to the total trapped fraction of positrons in n types of defect. Also,

$$\left\{ \alpha_0 f_{vo}(p) + \beta_0 f_{co}(p) \right\} * p_0(p) = p_1 f_f(p) = (1 - \gamma_1) f_f(p)$$

where $f_f(p)$ is the $e^+ - e^-$ momentum distribution for annihilations in the free state, and p_1 proportional to untrapped positrons. If the sample now changes to give a different trapped fraction (defined through γ_2), the following difference profile is obtained

$$D(p) = \left\{ \gamma_1 f_t(p) + (1-\gamma_1) f_f(p) \right\} - \left\{ \gamma_2 f_t(p) + (1-\gamma_2) f_f(p) \right\}$$
$$= (\gamma_1 - \gamma_2) \left\{ f_t(p) - f_f(p) \right\} \qquad \qquad 4.2.5$$

Translating the momentum parameter, p, to channel number, I, and using equation 4.2.2, the difference profile in equation 4.2.5 becomes the RID profile

$$I(N) = (\gamma_1 - \gamma_2) \sum_{I=1}^{n} \left\{ f_t(I) - f_f(I) \right\} \qquad \qquad 4.2.6$$

Equation 4.2.6 shows that the shape of the RID profile is independent of the trapped fraction of positrons, and will only change

if the individual e^+ - e^- momentum profiles change. Hence, changes in shape will occur only when one or more defect types either appear or disappear. Equation 4.2.6 also holds for the case when only one defect trap is varying in its concentration (see Appendix 1). The next section describes how 'defect-specific' shape parameters can be derived from the RID curves.

4.2.3 Defect-Specific Parameters

Coleman (1979) has defined the following RID curve parameters:
BR - the width of the curve between the two maxima
CR - the curvature at the peaks
MlR - the centroid of the profile
SR - the peak-to-peak amplitude of the curve.

Apart from SR, all the above parameters may be classified as 'defect-specific'. Clearly, for a given distribution of n defect types, the value of SR increases as the trapped fraction increases, the RID profile remaining constant if the presence of the same n defect types persists in the same proportions. In fact, if $\sum(V)$ is the running integrated count up to channel V and $\sum(U)$ the running integral up to channel U, where U and V represent the lower and upper boundaries respectively of the region AB in figure 4.2.1, then

$$\sum(V) - \sum(U) = S_C - S_R = \Delta S \qquad 4.2.7$$

where S_C is the S-value for a defected sample and S_R that for a reference sample (annealed). Equation 4.2.7 shows that the maximum value of ΔS is given by the maximum value of $\sum(V) - \sum(U)$ and this occurs when $\sum(V) - \sum(U) = SR$. Hence, the parameter SR possesses the best statistics for any definition of ΔS since it represents the maximum value that ΔS can attain by considering any choice of channel boundaries U and V.

Finally, another shape parameter, $\Delta M_2/\Delta S$, has been devised and used. The second moment, m_j, of the e^+ - e^- momentum profile

for the jth defect is proportional to the trapped fraction, μ_j, of positrons annihilating in the jth mode, and is equal to M_2 (the observed lineshape second moment) if all positions are trapped at the jth defect. Using this fact, and equation 4.2.1 one obtains

$$S = \sum_{j=1}^{n} \mu_j S_j \quad \text{and} \quad M_2 = \sum_{j=1}^{n} \mu_j m_j \qquad 4.2.8$$

where S_j and m_j are constants characteristic of the defect type j. Coleman (1979) shows that if, in a sample containing n defect types, only the trapped fraction μ_j varies then

$$\Delta M_2 / \Delta S = (m_0 - m_j)/(S_0 - S_j) \qquad 4.2.9$$

where ΔM_2 and ΔS are the changes in M_2 and S, respectively, associated with the change in trapped fraction μ_j, and S_0 and m_0 the characteristic values associated with annihilations in the free state. Clearly, under such circumstances, $\Delta M_2 / \Delta S$ does not depend on the total trapped fraction and will characterise the defect that is varying. However, $\Delta M_2 / \Delta S$ will vary if more than one defect type varies in its trapped fraction.

A description of the computation performed for RID curve and shape parameter analysis is given in section 4.2.5.

4.2.4 Statistical Error Analysis for Lineshape Parameters

Two classes of events are described by the distribution illustrated in figure 4.2.1 - annihilation events either fall inside or outside the region AB. Thus, the probability for events to fall inside the region may be described by a Binomial distribution whose standard deviation, σ, will be given by

$$\sigma = \sqrt{N(1-p)p} \qquad 4.2.10$$

where N is the total count in the line and p the probability in one event of falling inside the region AB. Since S is a fraction defining the counts in AB, its associated error, σ_S, will, therefore, be given by

$$\sigma_S = \sigma/Np = \sqrt{N(1-p)p}/Np = 1/\sqrt{N} \qquad 4.2.11$$
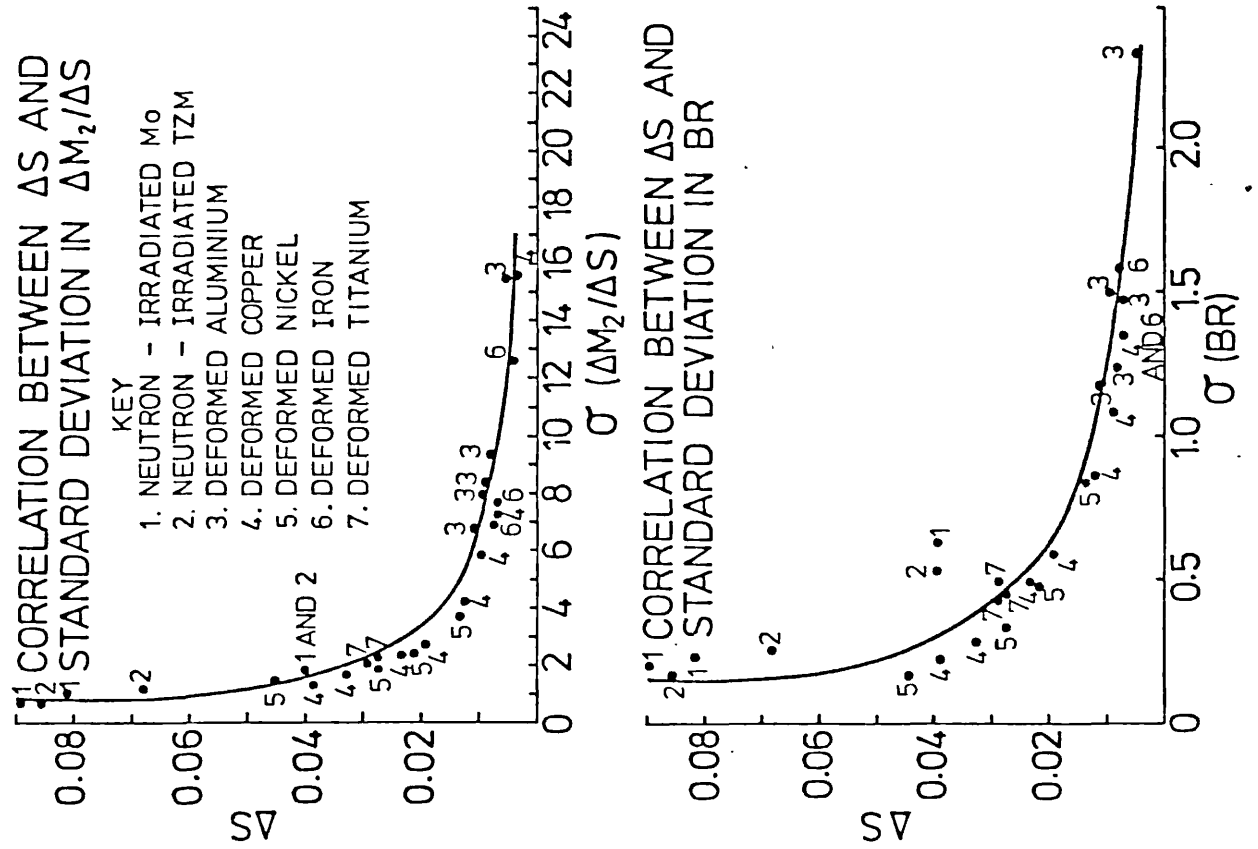
for p $\sim$ 0.5 and where Np is the mean of the Binomial distribution. For a typical line shape consisting of 10^6 counts, $\sigma_S = 0.001$.

An estimate may also be made of the error involved in the second moment of the annihilation lineshape. By considering it to be Gaussian in nature, the error in M_2 is found to be $1/\sqrt{2N}$ (e.g. Coleman et al, 1976). In reality, however, the annihilation lineshape is not Gaussian and so the above expression is only a crude approximation. It is extremely difficult to theoretically determine statistical uncertainties in parameters of non-Gaussian shapes.

Estimates of errors in RID curve parameters (including $\Delta M_2/\Delta S$) were, therefore, derived by using the Monte-Carlo technique. Essentially, for each experimental lineshape, a series of 15 random spectra were generated and subsequently analysed in the normal way. The standard deviation for each shape parameter could then be evaluated. The computer program specially written for this analysis is listed in Appendix 3.

Figure 4.2.3 shows the variation in standard deviation for the shape parameters $\Delta M_2/\Delta S$, CR, BR and M1R as a function of the value ΔS. All points on the graphs are representative of individual measurements taken for different samples with differing defect concentrations. The reference measurement in each case was provided by the annealed state of the metal concerned. It is seen that larger values of ΔS give smaller uncertainties in the shape parameters. This is to be expected since the larger values of ΔS produced RID curves of larger amplitude, thus reducing the significance of the noise. A continuous line has been drawn through the points in each graph so as, for any value of ΔS, an estimate of the uncertainty in the parameters can be made. The fractional error in the computer Monte Carlo standard

Figure 4.2.3   Variation of standard deviation, σ, for shape parameters as a function of the parameter ΔS

KEY
1. NEUTRON – IRRADIATED Mo
2. NEUTRON – IRRADIATED TZM
3. DEFORMED ALUMINIUM
4. DEFORMED COPPER
5. DEFORMED NICKEL
6. DEFORMED IRON
7. DEFORMED TITANIUM

CORRELATION BETWEEN ΔS AND STANDARD DEVIATION IN ΔM₂/ΔS

CORRELATION BETWEEN ΔS AND STANDARD DEVIATION IN M1R

CORRELATION BETWEEN ΔS AND STANDARD DEVIATION IN BR

CORRELATION BETWEEN ΔS AND STANDARD DEVIATION IN CR

deviations is given by $\sqrt{N}/N$ where N is the number of spectra used in the calculation - 16 spectra give rise to 25% error - and this should be added to the errors defined in Figure 4.2.3. Unfortunately, the statistical correlation associated with CR is not good - as is evident from the scatter in the standard deviations seen in figure 4.2.3. This is thought to be due to errors associated with the curve-fitting of an analytical function (section 4.2.5) to the RID peak profiles from which CR is calculated. Hence, variations in CR as a defect-specific parameter should not be taken too seriously.

4.2.5 Computational Description of Lineshape Analysis

The main computer program for lineshape analysis, CFCANPY, has been developed by Coleman (Coleman et al, 1978). A brief account of its operation is given here. Before shape parameters are derived all annihilation lineshapes have their backgrounds removed. This is performed in two stages. Firstly, the program evaluates an average value for the high-energy background in a predefined region above the annihilation peak, and this is then extrapolated linearly under the line. A second background contribution considered to be proportional in any channel to the downward-running-integral for that channel (the running integral taken from the high energy side to the low energy side) is next evaluated. The downward-running-integral for each channel is weighted by a constant of proportionality experimentally determined so that its value at the edge of the line on the low energy side matches the low energy background level. This second background profile provides a simple way of generating a smooth, continuous profile capable of simulating Compton scattering. Other methods, based of multi-parameter curve-fits have been considered by Jorch and Campbell (1977). However, since they found only small improvements to the fitting of a spectral line by inclusion of a so-called multi-parameter 'step-function', the method above is justified as a simple, workable alternative.

The program then computes the S-parameter by considering six inner regions AB (in figure 4.2.1) defined by the input data file to CFCANPY. The program places the mid-point of the first inner region three channels below the centroid position, calculates the S value and then repeats the operation five more times using the remaining inner

regions, moving up one channel at a time. A quadratic function is then fitted to the six S-values and an optimum S derived by computing the function maximum. The program then proceeds to calculate the second, third and fourth moments of the annihilation profile using the first moment as a reference.

Finally, the program determines the RID curve parameters discussed in section 4.2.3. The program normalises each lineshape, adjusts the centroid of the reference line to that of the comparison line, subtracts one from the other, and generates the RID curve. The centroid position M1R is determined directly from the RID profile. The parameters CR, BR and SR are then computed by least-squares fitting an analytical function to the maximum and minimum of the RID curve - usually over the top and bottom 30% of the curve. The analytical function consists of the difference between two similar Lorenzians symmetrically displaced about the common centroid of the component annihilation lines.

4.3 A MODEL DEPENDENT APPROACH

4.3.1 Representation of Annihilation Lineshape for a Defect-Free Lattice

In a perfect lattice the electron momentum distribution may be described by equation 4.2.3 using the j=0 terms only. The terms $\alpha_0 f_{vo}(p)$ and $\beta_0 f_{co}(p)$ must now be formalised to represent analytically the conduction and core electron states. Since the conduction and the core electron momentum distributions in a perfect lattice can be characterised by parabolic and Gaussian distributions respectively (chapter 2) the following expression has been used to describe an ideal lineshape (i.e. one devoid of experimental smearing)

$$X(p) = A\exp\left\{-(p-\bar{p})^2/2\sigma_G^2\right\} + B\left\{1 - (p-\bar{p})^2/2\sigma_p^2\right\} \text{ for } |p-\bar{p}| < \sigma_p\sqrt{2}$$

and

$$X(p) = A\exp\left\{-(p-\bar{p})^2/2\sigma_G^2\right\} \text{ for } |p-\bar{p}| > \sigma_p\sqrt{2} \qquad 4.3.1$$

where A and σ_G represent the height and width parameters of the Gaussian, and B and σ_p the height and width parameters of the parabola. However, experimental smearing has to be taken into account and if positrons annihilating in the free state have negligible momenta compared to the electrons equation 4.2.4 becomes

$$F(x') = \int_{-W_R}^{+W_R} \left\{ A\exp\left\{ -(x' - x)^2/2\sigma_G^2 \right\} + B\left\{ 1 - (x' - x)^2/2\sigma_p^2 \right\} \right\} R(x)dx$$

4.3.2

where the substitution $p-\bar{p} = x$ has been made, $R(x)$ is the value of the response function for electron momentum x, and the convolution integral is over with width, $2W_R$, of the response function $R(x)$. The fitting of the above function to an observed lineshape can provide useful information about the electronic structure. For instance, estimates of Fermi energies and the proportion of conduction to core electrons can be determined.

4.3.2 Representation of Annihilation Lineshape for a Defected Lattice - Complete Positron Trapping

When positrons become trapped at defects their wavefunctions become localised causing their kinetic energies to become comparable with those of the electrons (chapter 2). An attempt has been made to assess the magnitude of the positron motion at a defect site by smearing the electron momentum distribution with a positron component. Since the defect environments cause small perturbations on the perfect electron configurations they may still be approximated by the superposition of a Gaussian and parabola. The positron momentum distribution has been made to smear the electron distribution via the experimental response function, and if all positrons annihilate at a single defect type then, using equations 4.2.4 and 4.3.2, the lineshape may be described by

$$F(x") = \int_{-W_R}^{+W_R} \left\{ A\exp \left\{ -(x"-x')^2/2\sigma_G^2 \right\} + B \left\{ 1 - (x"-x')^2/2\sigma_p^2 \right\} \right\} \int_{-W_p}^{+W_p} R(x'-x)p(x)dx$$

4.3.3

where $p(x)$ is the positron distribution whose width is defined over the limits $\pm W_p$.

If the motion of the positron is approximated to a harmonic oscillator in its ground state within the defect trap then its wavefunction will be Gaussian (e.g. Semat and Albright, 1971). A Fourier transform to momentum space will, therefore, generate a Gaussian momentum profile. Accordingly, the positron component $p(x)$ has been approximated by a Gaussian distribution. The width of the positron component will give a measure of the positron zero-point energy above the bottom of the trap. It is seen from Appendix 2 that the zero-point energy is given by the expression

$$E_p = 3 \left(\frac{4\sigma^2}{m_0 c^2} \right)$$

4.3.4

where σ is the standard deviation of the convoluting positron distribution and $2m_0 c^2$ the $e^+ - e^-$ rest mass energy. This is useful since the value of E_p can indicate the effectiveness of different defect types as positron traps. Also, the positron zero-point energy may be used to characterise a particular defect in a manner similar to the defect-specific parameters discussed in section 4.2.3.

4.3.3 Monitoring Defect Structure Using Model Dependent Approach

By fitting the sum of a parabola and Gaussian to an annihilation lineshape derived from a perfect lattice, the fit parameters of these functions can be used to characterise electrons in the perfect state. In a similar manner, the lineshape recorded as a consequence of complete positron trapping at defects can be fitted to a Gaussian and

parabola the fit parameters of which will be characteristic of the electronic structure at the defect sites. In addition (as seen in section 4.3.2) the positron component smeared in with this electron distribution will be characteristic of the positron behaviour at the defect sites. Hence, other lineshapes characteristic of partial positron trapping at defects can, in principle, be fitted by mixing the two sets of functions defining the two extreme situations (i.e. zero and complete positron trapping). In such cases only the heights of the electron functions need to be varied by the least-squares minimisation routine (section 4.3.4) and so a direct value of the positron trapped fraction can be obtained by simply evaluating the intensity of the trapped Gaussian and parabolic components. One can try to make the fitting routine more adventurous by defining a series of Gaussian/parabola electron and positron components to represent a series of defect types that may be described by the lineshape. Again, as in the case of a single type of defect, each electron and positron distribution would have to be separately determined and then a floating of all their heights could be performed in the fit. This, of course, would be better than performing fits on undetermined functions where all of the parameters would then have to be varied. Such fittings normally result in failure because the least-squares iteration routine cannot handle such large numbers of floating parameters. Even when the widths of the functions have been pre-determined, thus reducing the number of floating parameters required, the decomposition of the momentum profile into too many components reduces the intensity of each one. If the profile is too shallow then noise problems will probably cause the minimisation routine to fail. Hence, the fitting of functions should be confined to just a handful of components if the approach is to be employed successfully.

In this study, the fitting of annihilation lineshapes has been confined to just one Gaussian and parabola to define the electron states with the inclusion of a positron smearing component where necessary. Due to difficulties encountered in minimising the fits when a positron component was included it was decided that it would not be feasible to carry out fittings involving the mixture of two sets of Gaussian/parabola functions in the way discussed above. Such difficulties are considered later in the treatment of results.

However, fitting just one Gaussian and parabola can be useful in monitoring the way in which defect structure is changing. An increase in the parabola intensity (producing a corresponding decrease in the Gaussian intensity) will normally indicate an increase in the defect population. Also, the goodness-of-fit of the final function (defined by χ^2/ν) can provide information on the defect structure. The goodness-of-fit is defined by the relation

$$\chi^2/\nu = \frac{1}{(N-r-1)} \sum_{i=1}^{N} \left\{ \frac{(f(x_i) - y_i)^2}{y_i} \right\} \qquad 4.3.5$$

where $f(x_i)$ is the value of the fitted function to the observed count y_i at channel x_i, N the number of channels fitted, and r the number of fit parameters. For instance, sudden increases in the value of χ^2/ν above that which is considered definitive of a good fit may indicate that the positron traps are becoming quite deep, thus enhancing the positron component in the momentum profile. Such characteristics are discussed in the treatment of results.

4.3.4 Computational Description of Lineshape Analysis

Details of the main analysis computer program are seen in Appendix 4. Prior to lineshape fitting all backgrounds are removed. Pre-determined ranges on either side of the annihilation peak are defined and a 4-degree polynomial least-squared fitted inside them. With the polynomial coefficients defined by such a fitting procedure the program proceeds to generate the background under the peak itself. Figure 4.3.1 illustrates a typical background profile simulated under the peak by using a polynomial.

The program then proceeds to call the main fitting NAG subroutine E04FBF (based on the Harwell routine VA05A). This function minimises the sum of squares, S, given by the expression

$$S = \sum_{i=1}^{N} \left\{ y_i - \sum_{j=1}^{m} f_j(x_i, \alpha_1, \alpha_2, \ldots\ldots \alpha_n) \right\}^2 \qquad 4.3.6$$
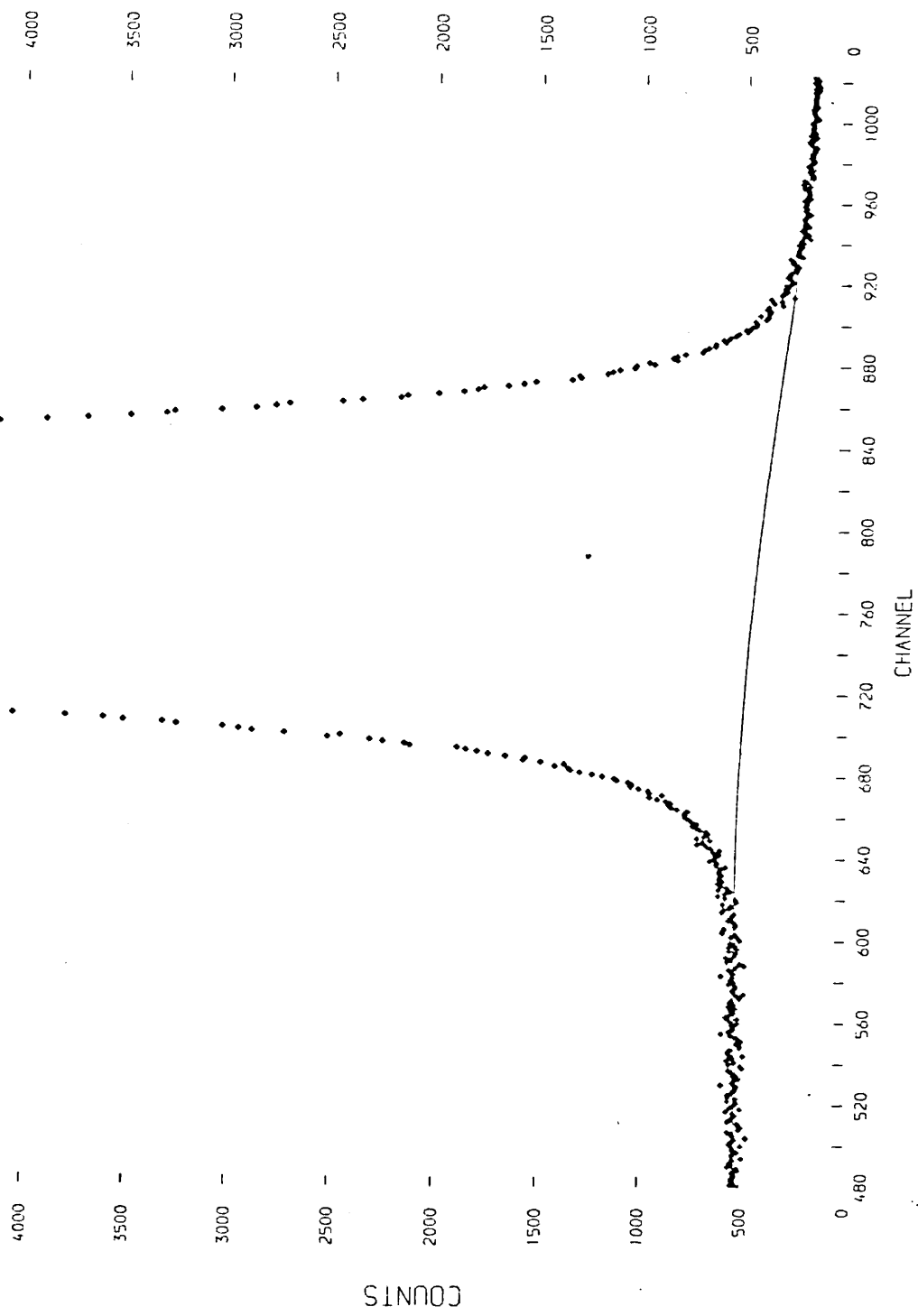
Figure 4.3.1   Simulation of the Background Under the Annihilation Line by Use of a 4-Degree Polynomial
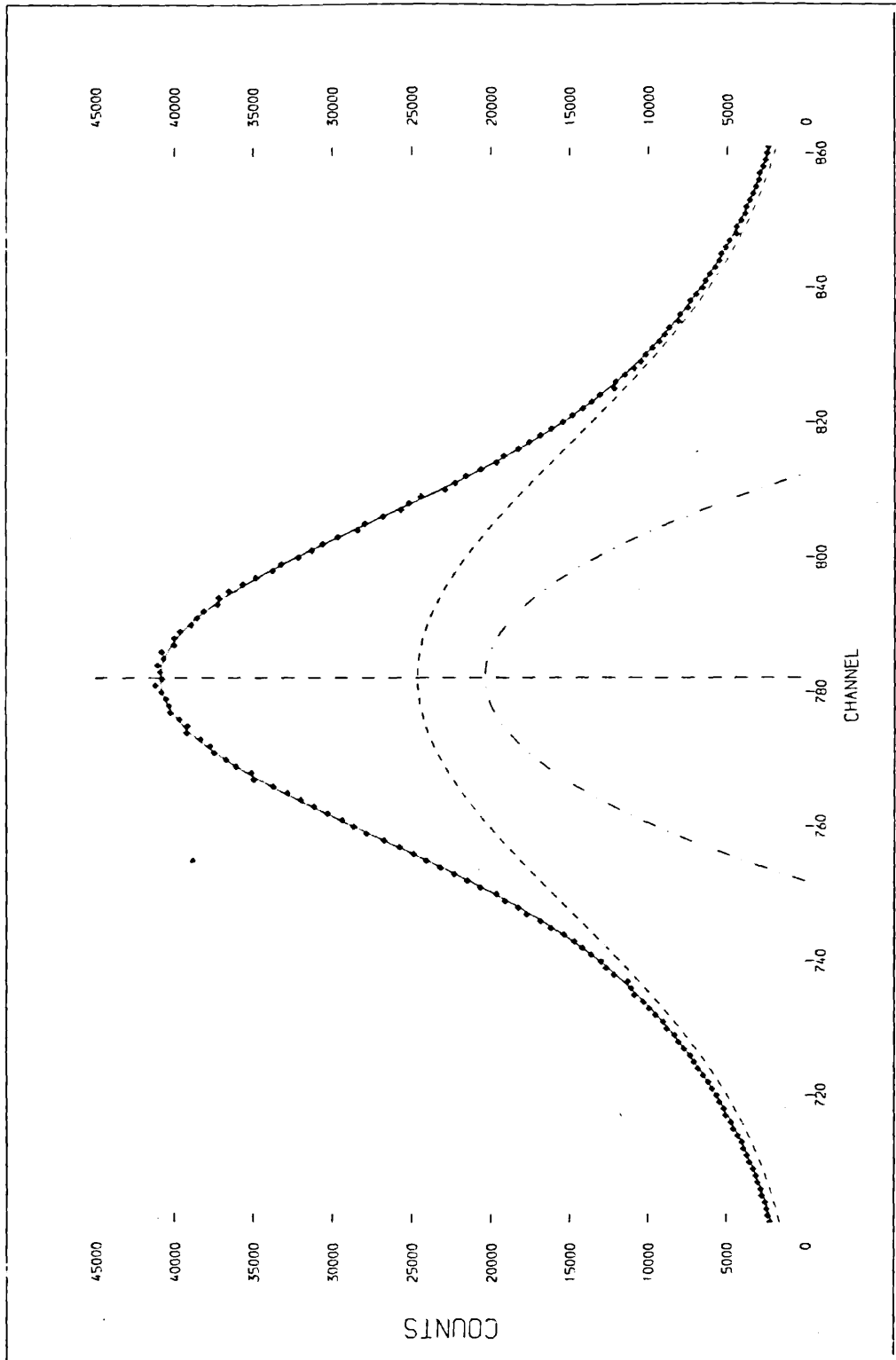
Figure 4.3.2   Model-Dependent Fitting for the Annealed State of Copper
--- Gaussian, -·-· Parabola, ——— Fit to Data

where m are the number of functions, $f_j(x_i, \alpha 1, \alpha 2, \ldots\ldots\alpha_n)$
the value of the jth function at channel number x_i, y_i the observed
value at channel x_i, and $\alpha_1, \ldots\ldots \alpha_n$ the fit parameters. In
the fitting of a superposition of a Gaussian and a parabola five
parameters have been allowed to float. These are parabola width and
height, Gaussian width and height, and the common centroid of the two
functions. Initial guesses are first supplied to the routine and a
trial Gaussian and parabola generated. The instrumental resolution
function is then normalised before it is made to perform a convolution
on the trial function. The routine proceeds to minimise S by varying
the values of the fit parameters in small, uniform steps defined by the
user, thus generating new trial functions. The process is iterated
many times until a minimum is found for the sum of squares. Figure
4.3.2 illustrates the fitting of a parabolic and Gaussian component for
the annealed state of copper.

A positron distribution may be smeared into the resolution
function by generating a normalised Gaussian whose standard deviation
is supplied by the user. The smeared resolution function is then used
in the fitting procedure until a minimum is reached. The cycle can be
repeated several times by supplying positron components of varying
widths. The optimum electron and positron functions are determined by
those which give the best fit to the data as judged by the smallest
achieved value of χ^2/ν.

CHAPTER   5 :   D E F E C T S   I N   M E C H A N I C A L L Y
D E F O R M E D   C O P P E R

5.1 INTRODUCTION

Over the past decade, copper has been extensively studied with a
view to understanding the properties of defects - and the mechanics of
their formation - produced by various modes of deformation. Amongst
the various techniques employed over this period of time (e.g.
electrical resistivity and stored energy measurements, and electron
microscopy) the positron annihilation method has emerged as an
established state-of-the-art tool (e.g. MacKenzie et al 1970, Hinode et
al 1977, Wampler and Gauster 1978, Eldrup et al 1981).

To date, many questions remain unanswered. For instance, the
exact nature of the defect populations present in mechanically deformed
copper at room temperature is not known. Almost fifty years after
Taylor's paper of 1934, a universal work-hardening theory has still not
been established. In particular, the relationship between the
dislocation density and the point defect population is not known, and
such shortcomings severely restrict an understanding of the processes
of point defect generation in mechanical deformation.

The ability to understand defect structure through the use of the
positron annihilation technique (PAT) depends on a knowledge of the
types of open-volume defects that are likely to trap positrons. For
instance, since the phenomenon of positron trapping in mechanically
deformed nickel was first observed by Dekhtyar et al (1964), it has
always been generally believed that dislocations are mainly responsible
for the trapping of positrons in mechanically deformed metals.
Nowadays, however, this view is no longer held with such universal
acceptance (e.g. Eldrup et al 1981). Clearly, it is important to
establish whether or not positrons become trapped at dislocations since
the interpretation of PAT data will depend on this.

In an attempt to shed light on the areas discussed above, the
experimental programme outlined in section 5.2 was carried out.
Briefly, in order to assess the nature of defects in mechanically

deformed copper, annihilation radiation characterising vacancies (generated thermally) was compared to that derived from the as-deformed state through the use of model-dependent and -independent analytical methods (chapter 4). In order ot test for point defect recovery, an isochronal anneal performed on deformed copper was monitored with defect-specific 'shape' parameters. Finally, in an attempt to understand the nature of work-hardening, annihilation events were measured and analysed as a function of deformation strain.

5.2 EXPERIMENTATION AND RESULTS

5.2.1 Generation of Thermal Vacancies

Two polycrystalline copper slabs (7 mm x 40 mm x 2 mm) were cut from a 5N purity copper sheet supplied by Johnson Matthey and Company. After annealing treatment both samples were cold-rolled to 15% strain and, afterwards, etched in dilute nitric acid. They were ultimately made to sandwich a Cu^{64} foil (2.5 μm thickness) irradiated in the Dido reactor (AERE Harwell) to give a total activity of $\sim$ 650 μCi. The sandwich was then placed in the furnace and measurements commenced after good vacuum conditions had been achieved. Since the Cu^{64} source has a half-life of $\sim$ 12 hrs, the detector count-rate was kept constant by appropriately moving the furnace nearer to the detector after the completion of each run. Also, since the experiment was performed over a three day period, a new Cu^{64} foil was inserted between the copper slabs at the start of each day. Each run lasted for 4×10^3 s to give, approximately, 10^6 counts in the annihilation line.

Figure 5.2.1 illustrates the chronological order of the experiment and shows the parameter S plotted as a function of temperature. The experiment allows for direct comparison between mechanical damage and vacancies in copper. The spectrum recorded for annealed copper at room temperature was used as the 'reference' for RID curve analysis.

5.2.2 Generation of Mechanically Deformed Copper

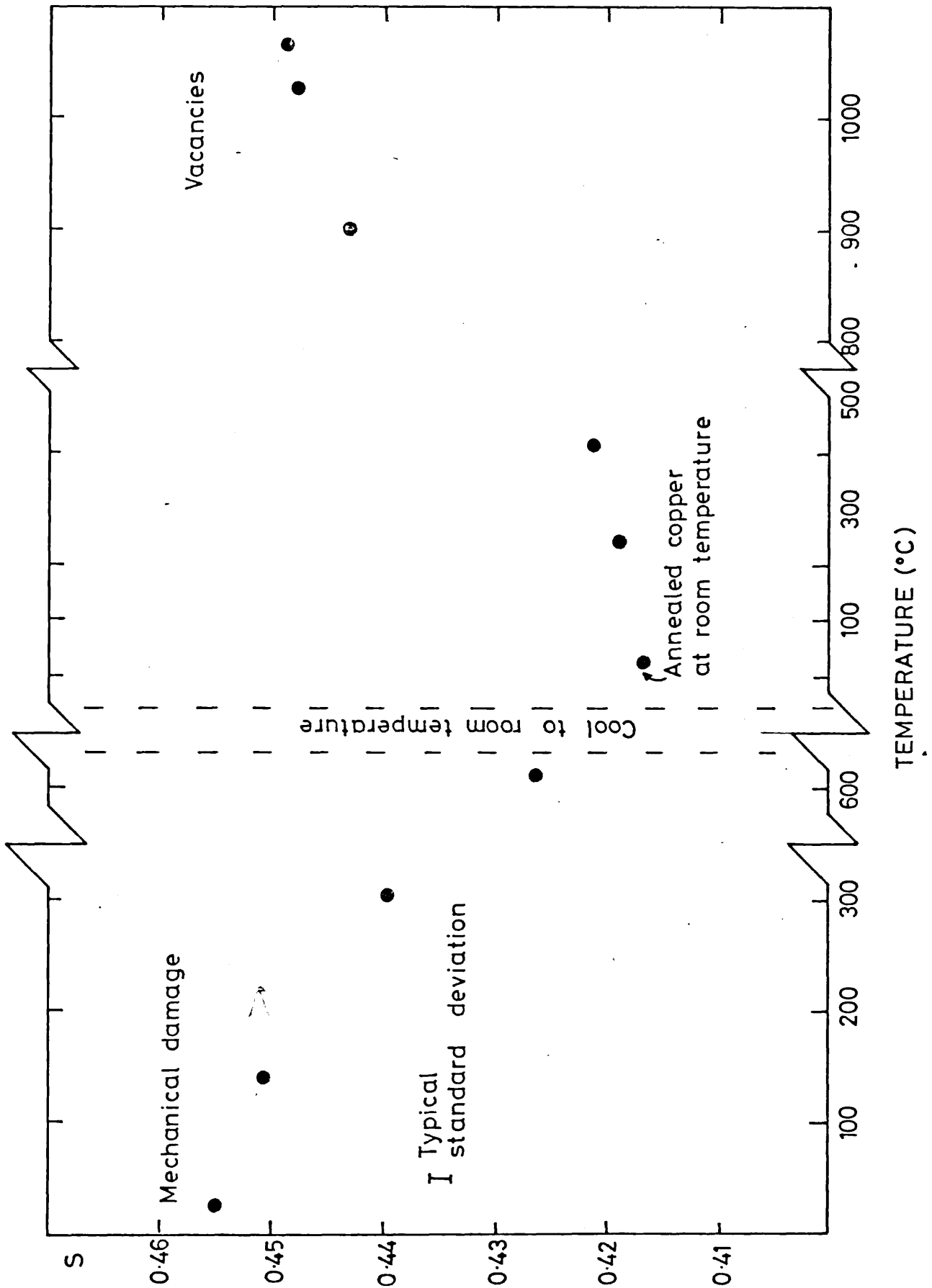Polycrystalline slabs of 5N purity copper (Johnson Matthey and

Figure 5.2.1   Variation of S as a Function of Temperature for Copper
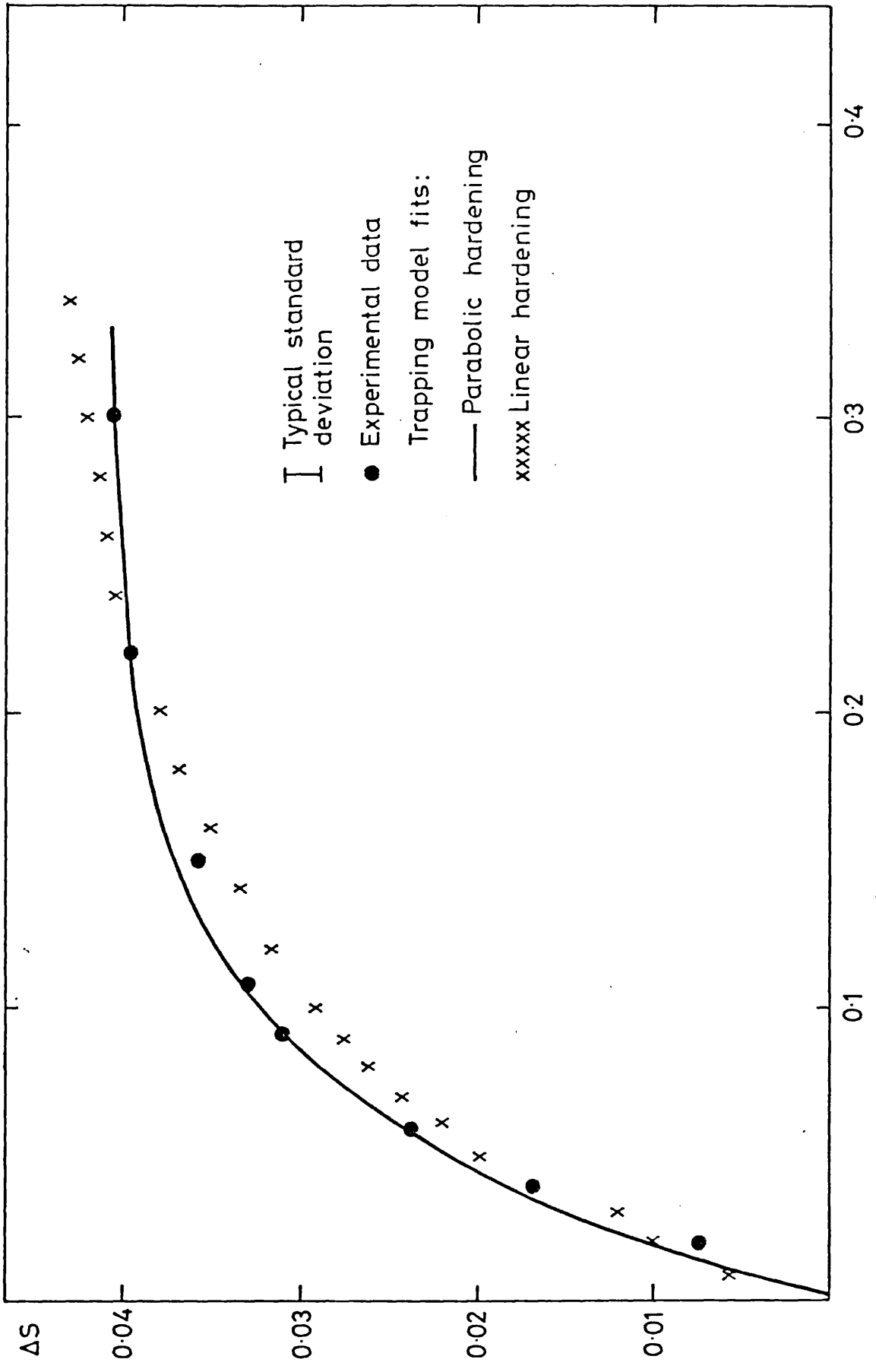   Initially Subjected to 15% Deformation Strain

Figure 5.2.2   Variation of ΔS as a Function of Deformation Strain for Copper

ΔS

0·04

0·03

0·02

0·01

STRAIN

0·1   0·2   0·3   0·4

Typical standard
deviation

Experimental data

Trapping model fits:
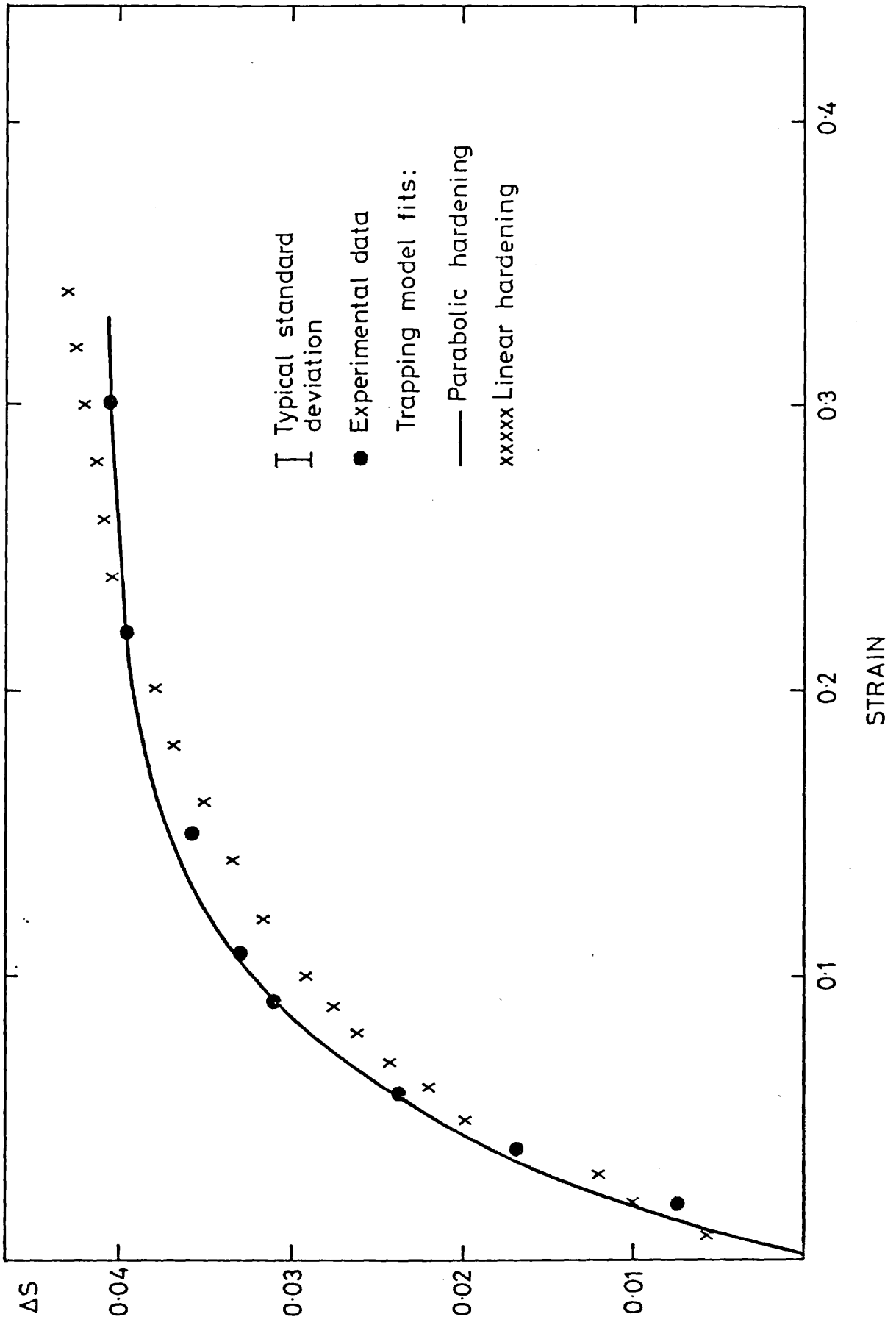
——— Parabolic hardening

xxxxx Linear hardening

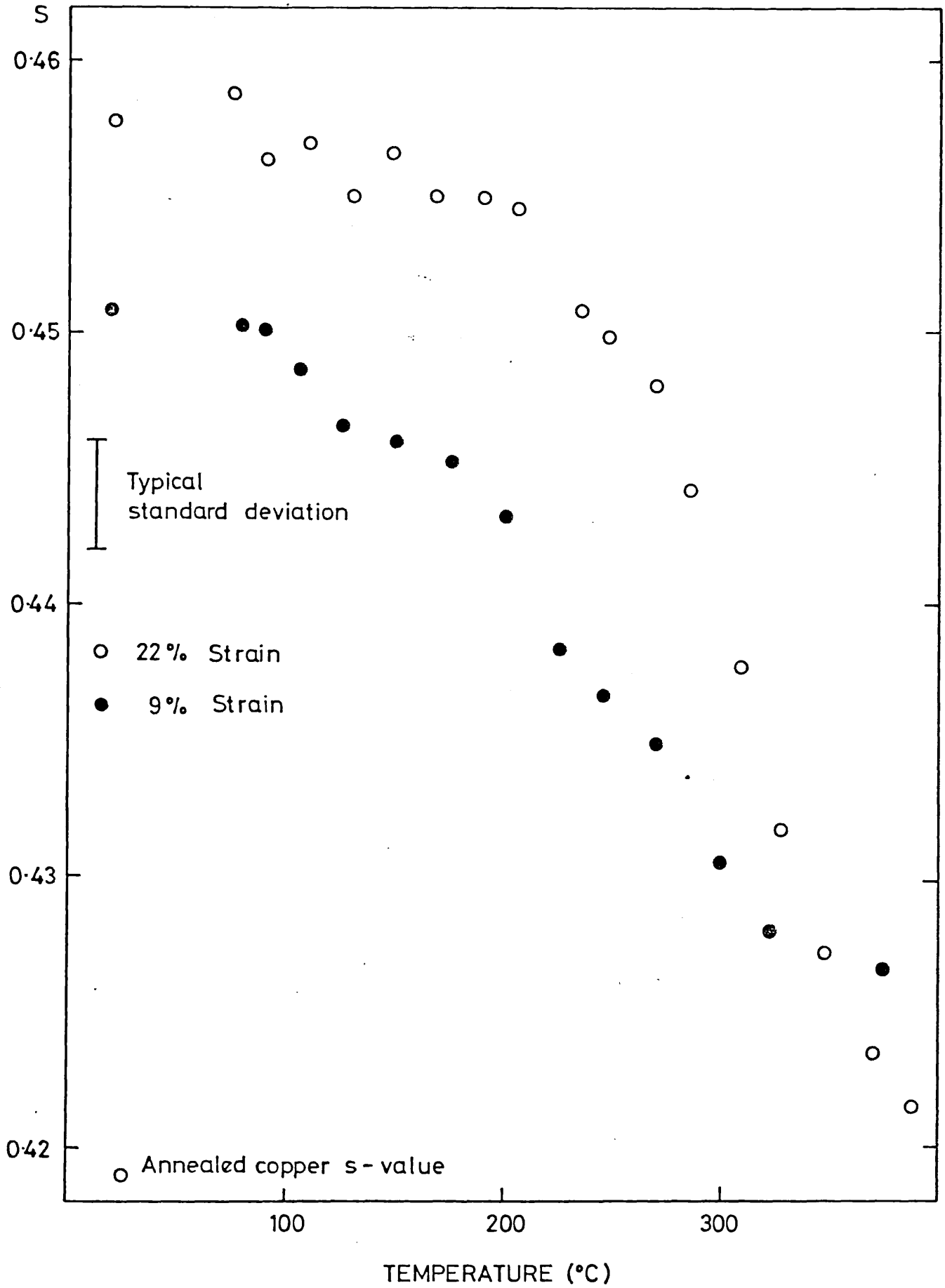Figure 5.2.2   Variation of ΔS as a Function of Deformation Strain for Copper

Figure 5.2.3   Isochronal Annealing of Deformed Copper

Company) and dimensions 40 mm x 7 mm x 2 mm were cold-rolled to values between 2% and 30% strain after suitable annealing treatments. Before rolling,the surfaces were lapped in order to obtain a surface variation in thickness of no greater than 0.1 thou. Before measurements were commenced, each slab was cleaned with acetone and distilled water in order to remove any surface dirt.

Measurements were performed using the 'remote-source' geometry approach (chapter 3) in which each slab was placed in front of a Ge^{68} positron beam. The selected energy range counted at a rate of 13550 counts/min and data collection was continued until about 3 x 10^6 counts were recorded for each annihilation spectrum. Figure 5.2.2 shows the variation in the parameter ΔS as a function of deformation strain.

5.2.3 Isochronal Annealing of Mechanically Deformed Copper

Two polycrystalline copper sandwiches, cold-rolled to 9% strain and 22% strain respectively, were prepared in a manner similar to that described in section 5.2.1. For these samples, however, Na^{22} was used as the positron source instead of Cu^{64}. In both cases, drops of an aqueous solution of $Na^{22}Cl$ were deposited on the 'twin' slab of each pair to give an activity of ~ 80 μCi. The sandwiches were placed in the furnace and measurements taken. Each run lasted for 3 x 10^3s to give ~ 1.3 x 10^6 counts.

Figure 5.2.3 shows the variation of S as a function of temperature for each sandwich. In the case of the sandwich deformed to 9% strain, measurements in excess of 400°C were performed but, unfortunately, spoilt by furnace contamination due to vaporised $Na^{22}Cl$ (chapter 3). Therefore, measurements taken at points higher than 400°C are not shown for this sandwich. After annealing, each sample was cooled to room temperature and a spectrum recorded in order to provide a reference spectrum for RID curve analysis.

5.3 DATA ANALYSIS AND DISCUSSION

5.3.1 Comparison of Thermally Generated Vacancies and Defect Species Encountered in Mechanically Deformed Copper

5.3.1.1 S-Parameter Analysis

Figure 5.2.1 shows the variation of S as a function of temperature. As expected, the value of S drops as the temperature of the deformed sandwich is raised, thus indicating the removal of defect damage. After heating to 610°C, the sandwich is cooled to room temperature and measurements continued by raising the temperature again. The positron response is now due to trapping at thermally generated vacancies in accordance with equation 2.5.11.

Of major interest is the comparison of the response of positrons trapped as positrons (generated near the melting point) to that of positrons at the defects in mechanically deformed copper. Inspection of figure 5.2.1 shows that there exists a significant difference in the S-values for these two cases. If complete positron trapping had occurred at only one predominant type of trap in both cases, then the S-values could be taken as characteristic of the defect traps available, and some conclusion reached as to the nature of the predominant trap' in deformed copper. However, S-value analysis is made complicated because of the possibility that more than one type of trap exists for positrons in the deformed case, and that 100% positron trapping conditions may not have bene achieved in both cases. In fact, figure 5.2.2 shows that saturation trapping conditions are not yet achieved for 15% strain. Hence, it is highly desirable to monitor positron response through the use of defect-specific parameters. Accordingly, RID curve analysis is discussed below.

5.3.1.2 RID Curve Analysis

The defect-specific RID curve parameters corresponding to the S-values in figure 5.2.1 are shown in figure 5.3.1(a)-(b). For obvious reasons, the S value for annealed copper at room temperature does not possess a complementary set of RID parameters ($\Delta S = 0$). Also, for
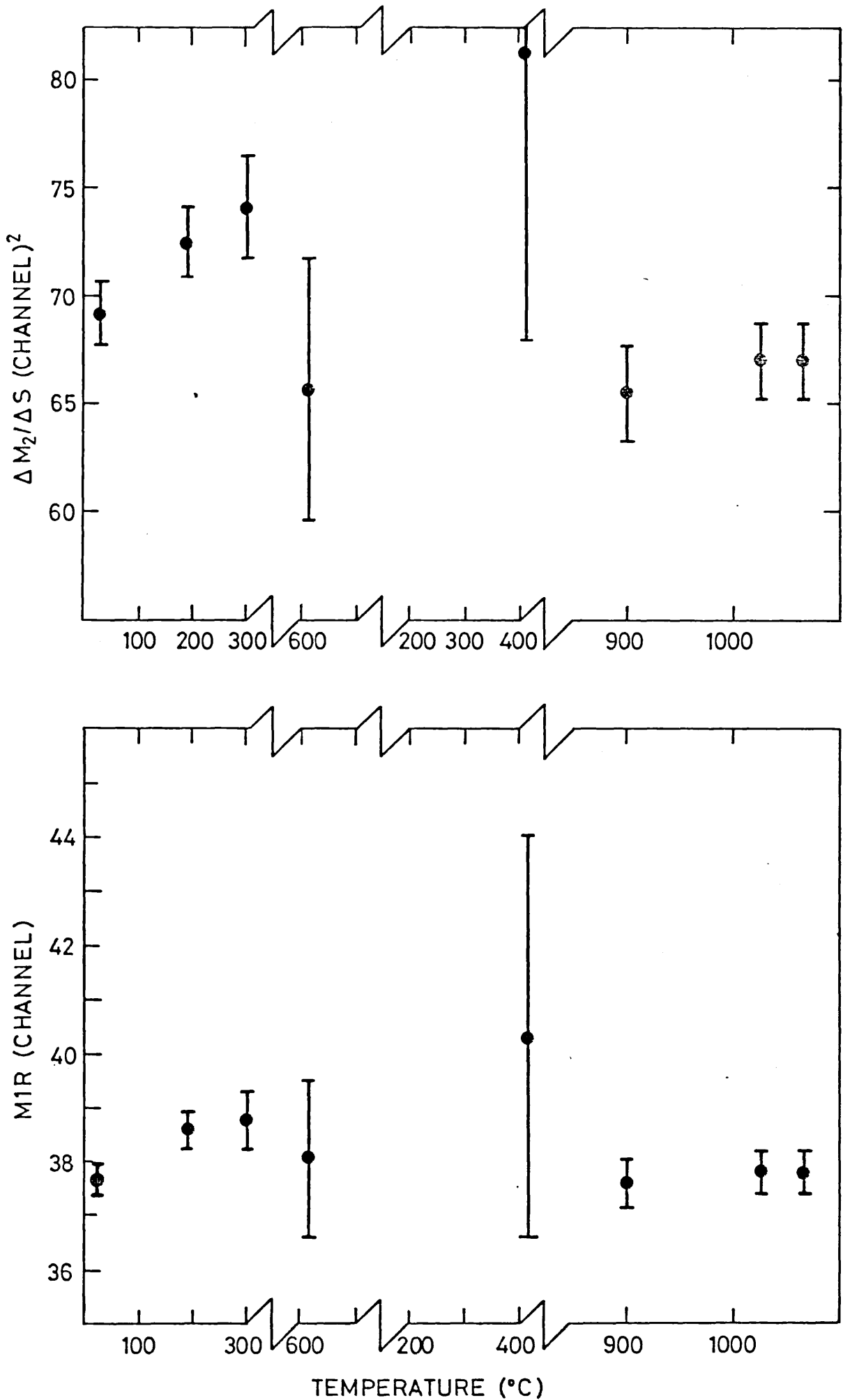
Figure 5.3.1.(a)   Variation of $\Delta M_2/\Delta S$ and M1R as a Function of Temperature for Copper Initially Subjected to 15% Deformation Strain
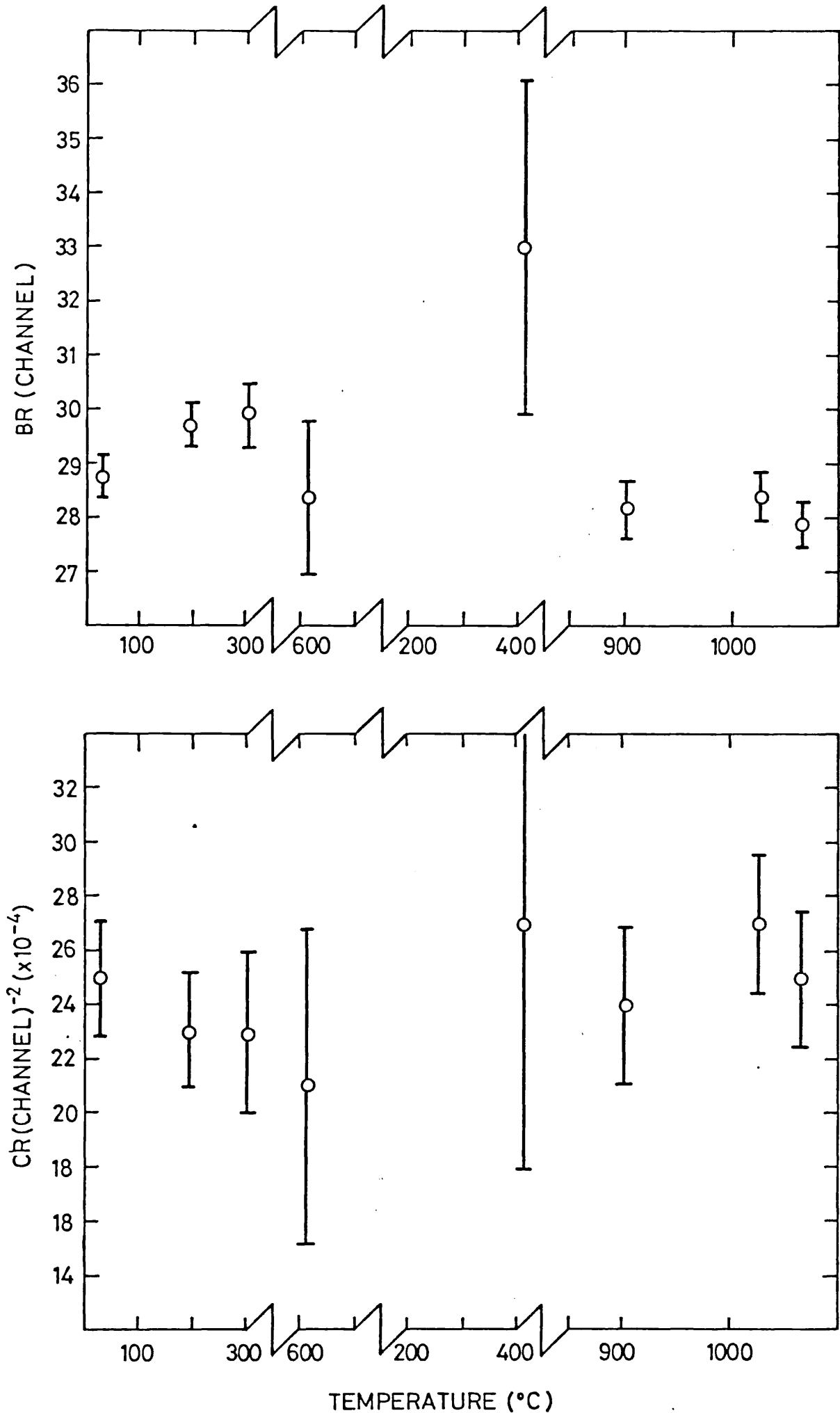
Figure 5.3.1.(b)   Variation of BR and CR as a Function of Temperature for Copper Initially Subjected to 15% Deformation Strain

convenience, the RID parameters corresponding to S at 236°C have been omitted because the errors associated with them require error bars extending beyond the bounds of the graphic scales. For reasons stated in chapter 4 (section 4.2.4) the CR parameter should not be taken seriously. However, it is included for the sake of completeness. It is also recalled that an extra 25% uncertainty (section 4.2.4) should be associated with all error bars indicated in the plots.

Two features become immediately obvious on inspection of figures 5.3.1(a)-(b). Firstly, defect-specific parameters offer some evidence of a change in 'shape' at 200°C, thus indicating a change in the nature of the defects responsible for trapping positrons. This is discussed more fully in section 5.3.2. Secondly, and more important to the discussion in this section, is the absence of significant change in the values of defect-specific parameters characterising annihilations in the as-deformed state and at vacancies. Thus, it appears that the positron traps in deformed copper are 'vacancy-like'. Similar findings have been reported by Mantl and Trifthauser (1978) using their defect-specific R parameter.

If it is thought that the predominant traps for positrons in deformed copper are dislocations, then initial reaction is one of surprise at the similarity of defect response expressed in figures 5.3.1(a)-(b) - one expects significant change in the positron response since dislocations are expected to provide shallower traps than vacancies. Undoubtedly, the defect-specific parameters at elevated temperatures for annealed copper characterise vacancies. It is, therefore, tempting to rush to the conclusion that the trapping centres for positrons in deformed copper are, also, vacancies. However, it is not known for sure whether vacancies (or vacancy clusters) exist in the deformed lattice and so, at this stage, it would be useful to list the most likely causes of positron trapping. Subsequently, an attempt is made to isolate the most probable cause. The following trapping modes may be operative:-

(i) positrons are predominantly trapped at vacancies

(ii) positrons are predominantly trapped at vacancy clusters

(iii)   positrons are trapped predominantly at dislocations with the possibility that electronic environments in dislocations and vacancies are similar, and positron behaviour is common to both

(iv)   positrons are trapped at points along dislocations (e.g. at point defects associated with dislocations, or at jogs and other irregularities along the dislocation line which may give rise to 'vacancy'like' positron characteristics).

For the purposes of this discussion, and in order to avoid confusion, the definition of positron trapping in dislocations is considered to mean the existence of a positron wavecloud extending along the entire length and breadth of the dislocation line.

Possibility (iii) can be rejected immediately. It is inconceivable to suggest that intrinsic physical differences do not exist between electron environments in vacancies and dislocations - the differing strain fields associated with each type will ensure that this is so.

Divacancies and vacancy clusters are expected to be stronger traps for positrons than monovacancies because of the removal of two or more positive ions. Theoretical calculations by Hautojarvi et al (1976) have shown that the lifetime of trapped positrons in vacancy clusters increase as a function of the cluster radius from a minimum in divacancies to a saturation value for clusters larger than ~ 12 Å radius. The concomitant behaviour in Doppler studies is narrowing of the annihilation line. Experimental evidence confirms this. For instance, Mantl and Trifthauser (1975) performed annealing studies on copper electron-irradiated below 10K. They observed a recovery stage at 230-280K and concluded that the recovery mechanism was the coalescion of monovacancies into three dimensional clusters. Compared to the reduction in linewidth caused by vacancy trapping, further dramatic narrowing of the lineshapes were observed during this stage. Wampler and Gauster (1978) observed similar findings through annealing studies of electron irradiated copper and copper possessing quenched-in vacancies.

In view of such findings, one would expect to find significant differences in the values of RID 'shape' parameters representing thermal vacancies to those in deformed copper if, in the latter case, clusters were present. Further evidence to suggest the absence of vacancy clusters in deformed copper is presented in section 5.3.2 where an isochronal recovery spectrum is considered. Hence, possibilty (ii) may be eliminated.

It is worthwhile pointing out at this stage that Mantl and Trifthauser (1978) arrived at similar conclusions by comparing the positron response in electron-irradiated copper, annealed to provide a population of vacancy clusters, to those observed in deformed copper. The responses were markedly different. However, the mechanical deformation response was similar to that observed in dislocation loops (obtained by suitable annealing of quenched-in vacancies) in another copper sample. They concluded that dislocations were responsible for trapping.

5.3.2 Isochronal Annealing of Mechanically Deformed Copper

Figure 5.2.3 shows the variation of the S-parameter as a function of annealing temperature for the two deformed sandwiches at 9% and 22% strain. As expected, the more heavily deformed sandwich possesses a higher S-value before annealing, thus indicating a higher concentration of defect species. Inspection of the S-variation for 9% strain reveals two temperature ranges (80-125°C and 200°C onwards) at which marked drops in S-value occur. For the case of 22% strain the first temperature range is not apparent. Most likely, this occurs because 22% strain imposes saturation conditions on positron trapping (figure 5.2.2) and, hence, S is insensitive to changes in defect concentration. However, the S drop in the region above 200°C is clearly seen. Both these ranges are indicative of recovery behaviour.

Evidence suggesting recovery behaviour in the range 200-250°C appears in the literature (e.g. Kopetskii et al 1974, Hinode et al 1977, Myllyla et al 1977). Apart from Myllyla et al, none of these authors present evidence for a recovery stage in the region 100-150°C. Disagreement exists as to the mechanisms responsible for recovery

at around 200°C. By studying deformed copper with the use of electron microscopy and electrical resistivity measurements, Kopetskii et al (1974) concluded that dislocation recovery processes occurred in this temperature range. Hinode et al (1977) studied the mean lifetime of positrons trapping in deformed copper. They rejected a vacancy cluster annealing mechanism at ∿ 200°C on the grounds that a long lifetime (similar to that expected for trapping in vacancy clusters and voids) could not be resolved from the lifetime spectrum. Also, release of monovacancies from impurity traps was thought not to be possible due to the high purity of the samples. They concluded that dislocation mechanisms were responsible for the recovery. Myllyla et al (1977) suggested that dislocation processes were responsible for recovery behaviour in the temperature ranges 100-150°C and 200-250°C. However, Saimoto et al (1974) concluded that submicroscopic defects (not including vacancies) were responsible for annealing behaviour. McKee et al (1974) also arrived at similar conclusions.

5.3.2.1 RID Curve Analysis

The variation of the RID defect-specific parameters corresponding to the S-variation in figure 5.2.3 for deofrmed copper at 22% strain is shown in figures 5.3.2(a)-(b). RID variations are not shown for 9% strain because at temperatures above 400°c furnace contamination spoilt the annihlation response to the annealed sandwich required for the 'reference' spectrum. Also, variations above 300°C are not shown because at such temperatures $\Delta S \rightarrow 0$ quite rapidly, and the large errors associated with the parameters make for near-impossible extraction of useful information.

5.3.2.1.1 Evidence /for against Vacancy Cluster Annealing

Section 5.3.1.2 has discussed how measurements of annihilation events occurring at vacancy clusters have provided positron characteristics dramatically and significantly different from those derived from mechanically deformed samples (where 'vacancy-like' trapping appears to occur). Hence, if clusters are present in deformed copper one expects to find convincing and significant changes in RID parameters at the point at which they anneal out. Supporting this
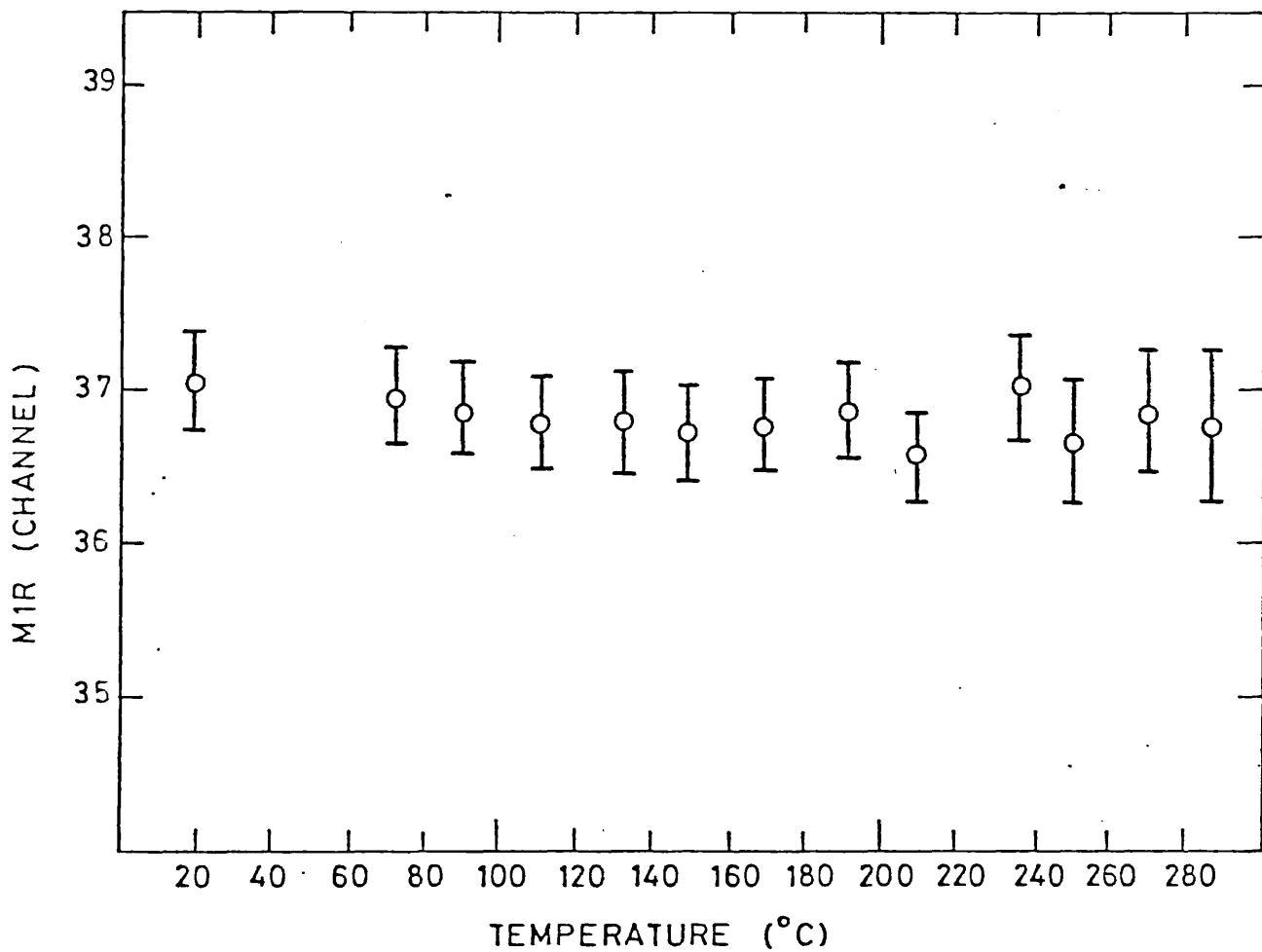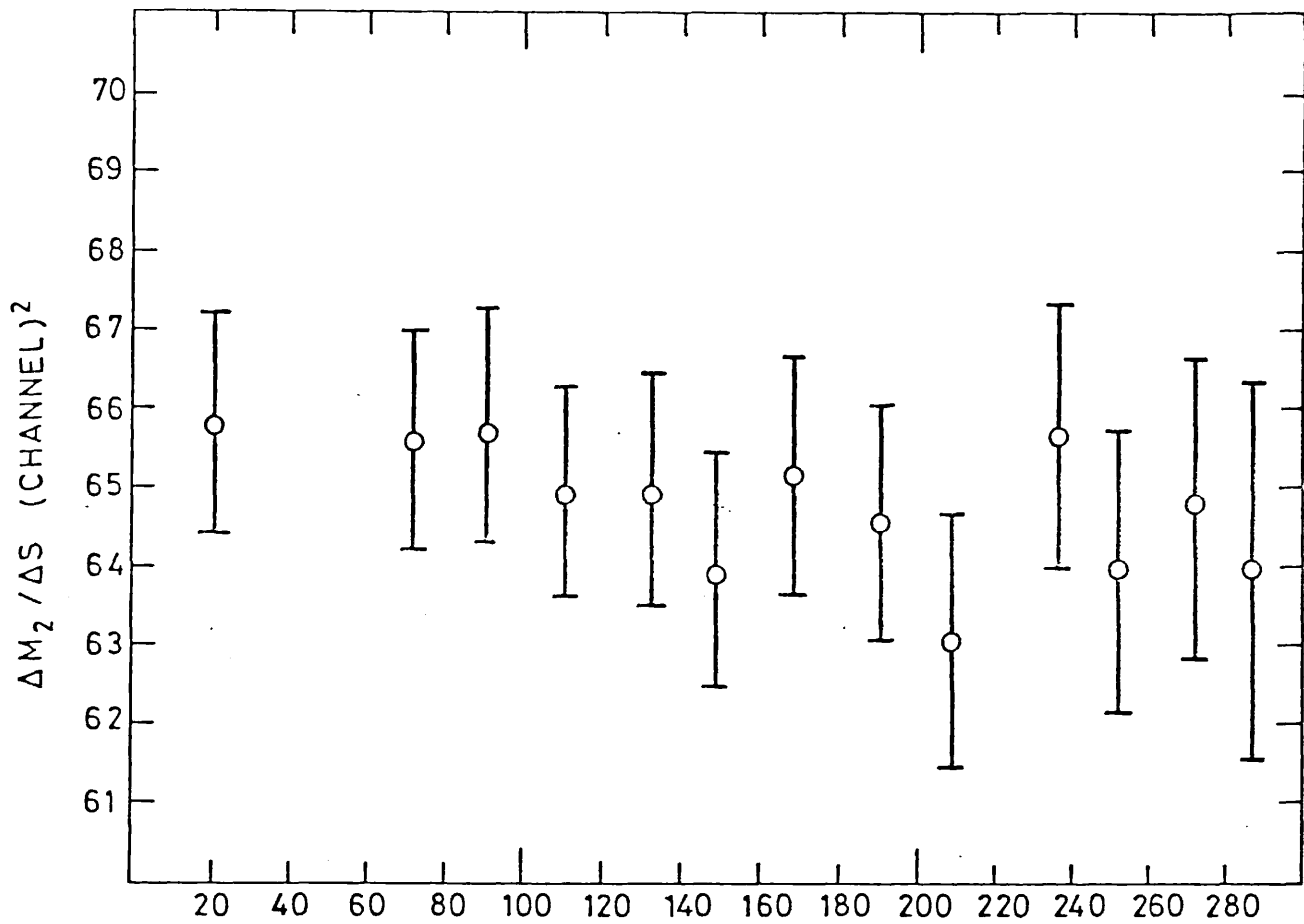
Figure 5.3.2.(a)   Variation of $\Delta M_2/\Delta S$ and M1R as a Function of Temperature for Deformed Copper (22% Strain)
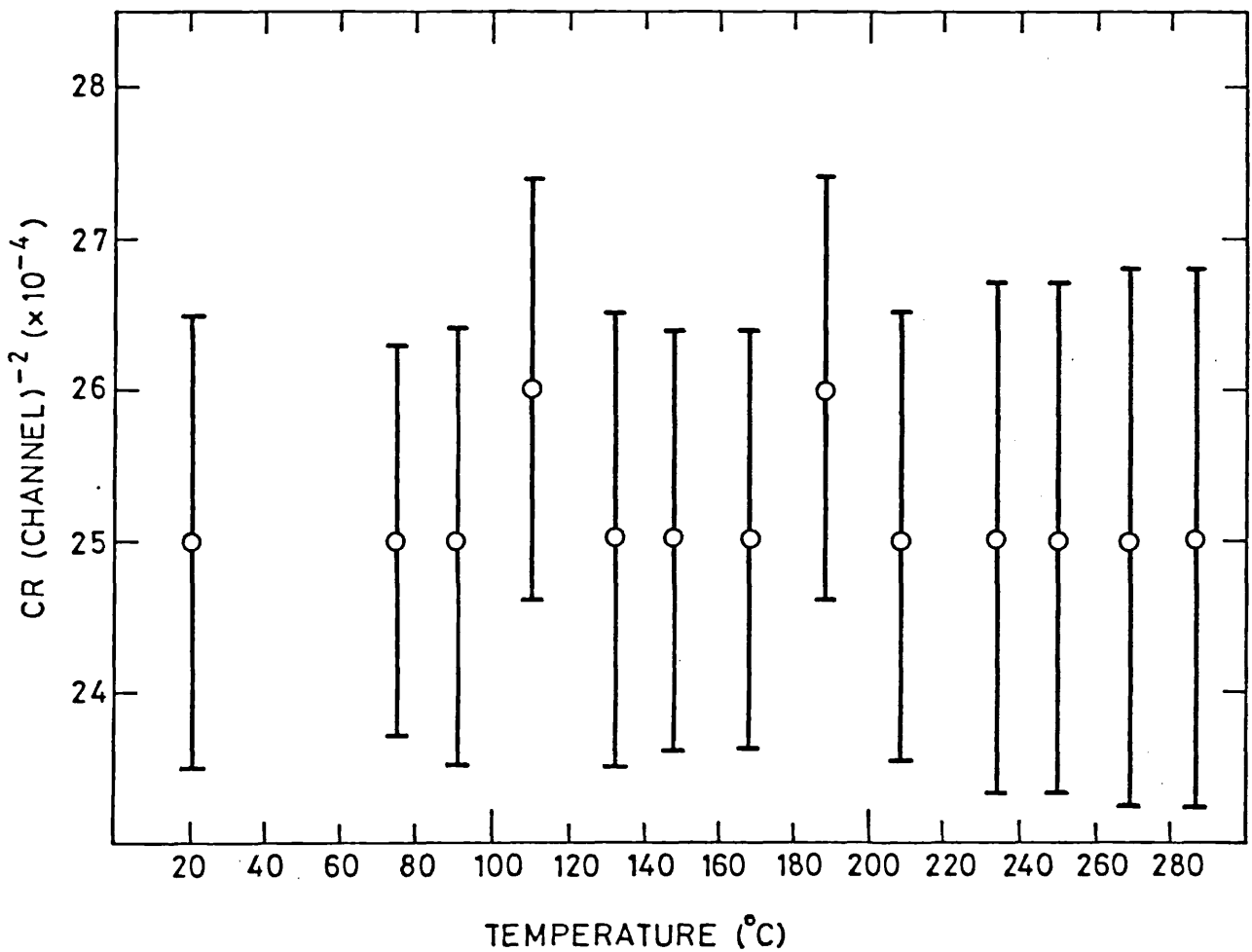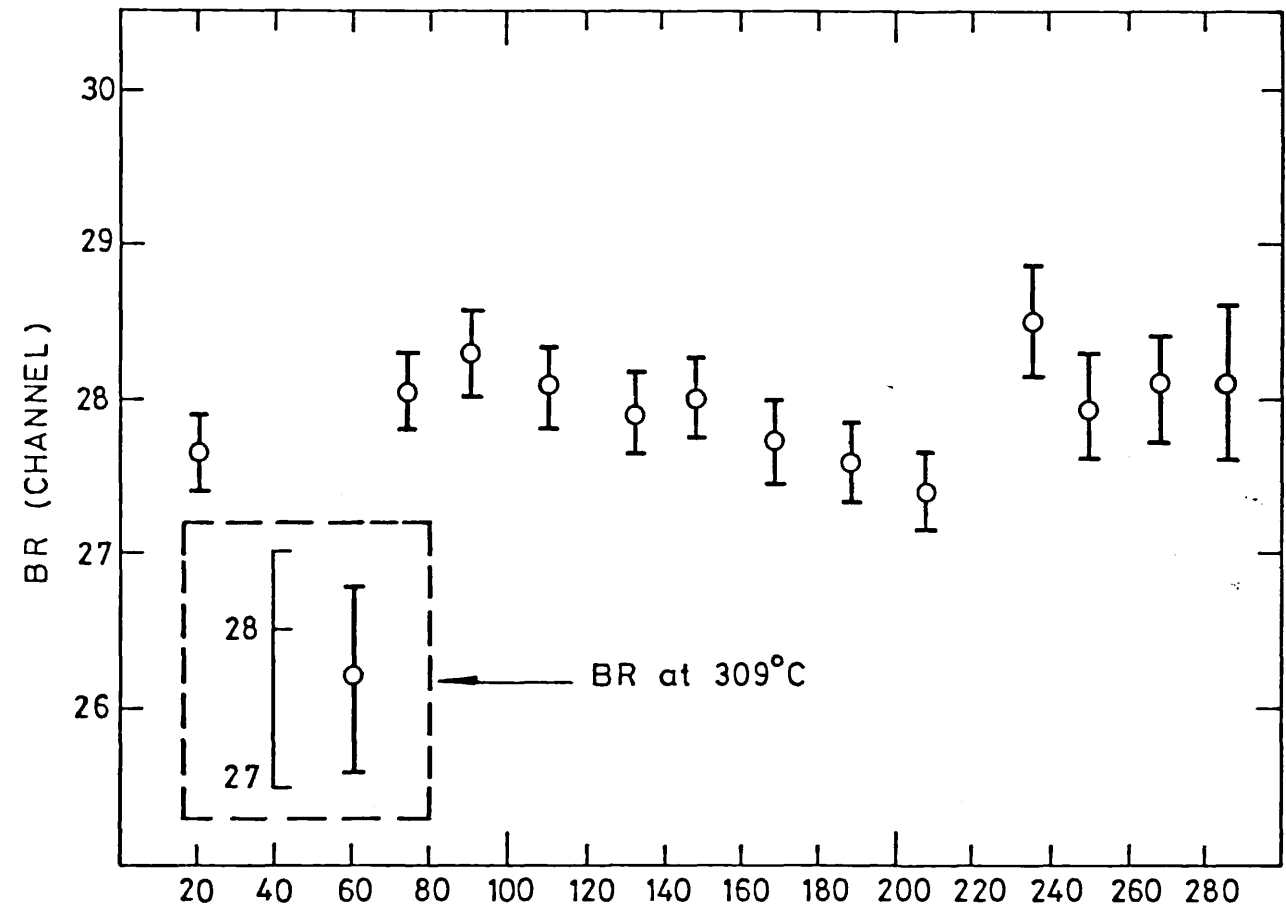
Figure 5.3.2.(b)   Variation of BR and CR as a Function of Temperature for
Deformed Copper (22%Strain)

expectation are the results of chapter 8 demonstrating marked and significant changes in 'shape' parameters characterising voids and dislocation loops in neutron-irradiated molybdenum.

Figure 5.3.2(a) shows that over the entire range 20-300°C no significant changes in the values of $\Delta M_2/\Delta S$ and M1R occur. Although the behaviour of BR in figure 5.3.2(b) is a little more interesting (section 5.3.2.1.2) this parameter does not offer evidence of the distinct 'shape' changes which one would expect to see if vacancy cluster annealing mechanisms were operative. Accordingly, this section reports no evidence of vacancy-clusters in the as-deformed state of copper.

5.3.2.1.2 Evidence for Vacancy Annealing.

As discussed above, changes in the shape-parameters $\Delta M_2/\Delta S$ and M1R in the range 20-300°C do not occur. However, the behaviour of BR is not quite so clear-cut to interpret. Clearly, the variation of BR offers structure that is not found in the variations of $\Delta M_2/\Delta S$ and M1R. For reasons discussed in section 5.3.2.2 (concerning the sensitvity of RID parameters) further discussion on 'shape' analysis in this section is confined to the BR parameter.

Statistically, one cannot place much faith in the idea that changes in BR (with respect to the as-deformed value) are occurring in the range 20-300°C. For instance, there are indications of change in the ranges 80-100°C and 200-220°C (incidentally, the ranges at which defect recovery is indicated by the S-variations in figure 5.2.3). The rather oscillatory behaviour of BR across the entire range would suggest that the changes at 80-100°C and 200-220°C are spurious. This argument is supported by the fact that BR at 309°C returns to the value associated with the as-deformed state. However, if the BR variation is studied more carefully, there appears to be a suggestion of a small steady increase over the entire temperature range. This point is worth making because similar behaviour has been found elsewhere. For instance, the annealing treatment of the sample deformed to 15% strain in figure 5.3.1(b) shows evidence of an increase in the value of BR at ~ 200°C. Also, Coleman (1979) finds evidence of a systematic increase

in the value of BR (though by no means confidently resolved as physically significant) during an isochronal annealing treatment of stretched copper. Such changes might be indicative of change in the nature of the defect trap. However, in the absence of any concrete evidence to the contrary, the value BR is taken to be constant over the entire annealing temperature range.

The latter recovery stage occurring at 200°C indicated by the S-variation in figure 5.2.3 may be attributed to recrystallisation since the more heavily deformed sample appears to return to the annealed state at a faster rate than for the less heavily deformed sample. This, of course, reflects the higher motivation (induced by the greater strain fields) for the more heavily deformed sample to return to the state of thermal equilibrium. Hence, if the positron response is sensitive to recrystallisation positrons must be trapped at dislocations in one way or another. The earlier recovery stage indicated by the S-variation in the range 80-125°c may be indicative of the following processes

(a) vacancy annealing

(b) dislocation re-arrangement.

Since positron characteristics at dislocations appear to be vacancy-like (as indicated by the absence of 'shape' change at the start of recrystallisation) possibility (a) could explain the measured observations - i.e. the vacancy positron traps annealing out in the range 80-125°C reduce the defect population (thus reduce the value of S) leaving the 'shapes' of momentum distributions unaltered as positrons are left to trap at dislocations. Alternatively, the observed behaviour of S and RID parameters might be explained by possibility (b). Myllyla et al (1977) performed isochronal annealing experiments on deformed copper samples and concluded that an observed recovery range in the range 100-150°C was due to polygonisation. This is the process by which dislocations haphazardly distributed at the grain boundaries re-arrange into agglomerates of parallel dislocation lines resulting in increased mean distance between dislocations. Hence, if distances between dislocations in the pre-polygonisation

state are large compared to the mean positron diffusion length, then polygonisation will reduce the porbability of positrons becoming trapped at dislocation sites. This will have the effect of reducing the S value.

It is clear that RID parameters cannot determine which (if any) of the interpretations (a) and (b) is correct and, hence, whether or not vacancies are present in the as-deformed state. In section 5.3.3 annihilation lineshapes are decomposed into their respective electron and positron distributions in an attempt to pursue the matter further. The results suggest that vacancies are not present in the as-deformed state.

5.3.2.2 Sensitivity of RID Curve Parameters

By nature of their definitions, the parameters $\Delta M_2/\Delta S$ and M1R are particularly sensitive to the shape of the RID curve flanks and, hence, to the shape of the higher momentum components of the annihilation line. However, for its definition, BR is dependent on the inner (lower) momentum components of the lineshape since the points of RID maxima occur around the Fermi energy region. Such differences may be the cause of inconsistency in parameter variation for the reasons now discussed.

Our results on deformed copper (figure 5.3.1) show evidence of change in defect-specific parameters at $\sim 200°C$. For this experiment a Cu^{64} source was used. Coleman et al (1978) studied the variation of $\Delta M_2/\Delta S$ in an isochronal annealing study of deformed copper and found evidence of change around 200°C. They used a Ge^{68} source. Our results in figure 5.3.2(a) show no change in $\Delta M_2/\Delta S$ and M1R at 200°C - a Na^{22} source was used. Mantl and Trifthauser (1978) performed an isochronal anneal on deformed copper using a Na^{22} source. They found no change in the value of the R-parameter in the temperature range embracing 200°C.

The R-parameter is, essentially, defined by $\Delta S_V/\Delta S_C$ where ΔS_V is the change in counts over a specified central region in the annihilation line, and ΔS_C represents the change in counts in a

defined outer region where positrons annihilate with core electrons only. Hence, the R-parameter is dependent on the shape of the high momentum regions in a way similar to $\Delta M_2/\Delta S$ and M1R.

In the absence of obvious differences in the nature and treatments of the copper samples, it is difficult to neglect a seemingly common denominator - the use of a Na^{22} source by Mantl and Trifthauser and ourselves, and the negative response of their R-parameter with our $\Delta M_2/\Delta S$ and M1R. It is rather likely that background radiation under the annihilation line will dominate in intensity the extreme, higher momentum components and that the true shape may be lost due to errors associated with background subtraction technqiues. This problem may be particularly acute with Na^{22} where (in comparison to Cu^{64} and Ge^{68}) an extremely intense background is present. Thus, it is extremely likely that changes in shape occurring in the flanks of the lineshape may not be sensed by R, $\Delta M_2/\Delta S$ and M1R. Schultz et al (1981) have made similar comments on the dangers of using parameters with added weight on the outer channels. Hnece, BR is probably a more sensitive RID parameter to use where noise dominates the higher momentum components.

5.3.3 Positron and Electron Momentum Distributions in Deformed Copper

5.3.1.1 Evidence for Positron Zero-Point Motion

In order to achieve greater understanding of the nature of traps in deformed copper it is useful to resolve both the electron and positron momentum distributions from the annihilation lineshape. The model adopted for the electronic distribution has been the superposition of an inverted parabola on a Gaussian to represent valence and core electron components respectively (chapter 4). The convolution of the electronic distribution with the instrumental resolution function is then fitted to the observed annihilation lineshape by least-squares analysis in order to find the best fit. Such analysis effectively removes instrumental smearing and thus, in principle, should allow differences in positron behaviour to be more clearly seen. This is in contrast to RID curve analysis where instrumental smearing is not removed. Table 5.3.1 shows the variation

in x^2/ν (goodness-of-fit) as a function of deformation strain, along with the Gaussian and parabola widths and parabola intensity for the data presented in figure 5.2.2.

Table 5.3.1 Results of model-dependent fitting to deformed copper

% Strain	Gaussian width (channel)	Parabola width (channel)	% Parabola	x^2/ν
0.0	49.13	30.21	27.7	1.095
1.96	48.33	30.06	29.2	1.168
3.95	47.25	30.41	31.5	1.869
5.84	46.78	30.27	32.8	1.727
9.09	44.98	29.77	32.9	1.883
10.74	45.30	30.08	34.5	2.497
14.92	45.31	30.34	35.3	2.822
22.14	44.23	29.63	34.2	2.945

Table 5.3.1 shows that increasing deformation has the expected effect of narrowing the line as exemplified through the general lowering of the Gaussian and parabolic widths. Concomitant with this is the systematic increase of the parabola percentage with strain. The parabola intensity of 27.7% for annealed, undeformed copper compares with 27.1% found by Jackman et al (1974a) using similar convolution techniques. Using equation 2.3.12 (chapter 2) and assuming negligible positron kinetic energy in the undeformed sample, the parabola width yields a Fermi energy of 8.9 eV. This compares with the value 8.1 eV found by Shizuma (1978) using deconvolution techniques. The theoretical value of the Fermi energy derived from the free-electron model is 7.00 eV.

In theory, the value x^2/ν (defined by equation 4.3.5) will be unity, if the statistics of the line are Poisson in nature, for a good fit. In practice, deviations from such a definitive vaue are likely to occur if the nature of the statistics are changed - e.g. spurious background contributions and computational errors introduced to the line as a result of background subtraction. It appears from table 5.3.1 that a good fit is obtained for the undeformed sample. However, a gradual worsening of fit accompanies increasing deformation. This is taken to be indicative of the presence of a significant positron momentum in the centre-of-mass distributin appearing as a result of positron trapping. Accordingly, attempts have been made to account for such a positron component in the fitting.

5.3.3.2 Convolution of Electronic Momentum Distribution by Positron Momentum Component

The way in which a Gaussian distribution of specified standard deviation has been used to convolute the electronic distribution to account for positron zero-point motion has been discussed in chapter 4 (sections 4.3.2 and 4.3.4). Figure 5.3.3 typifies the variation of x^2/ν as a function of the convoluting positron momentum component . It is clearly seen that the inclusion of such a component has the effect of improving the fit. Ideally, one expects to see a well defined minimum at the optimum width, σ, with a steep rise in x^2/ν occurring immediately therafter. Unfortunately, such ideal behaviour is not apparent and the worsening of x^2/ν after the minimum is a slowly varying function of σ. This behaviour is misleading because, even though the values x^2/ν do not suggest greatly worsened fits, the number of iterations required to obtain minimisation is greatly increased, thus suggesting that difficulties are encountered in the fitting.

In order to test for any effect that noise might have on the minimisation performance, lineshapes were made to undergo '9-point' binomial smooths, and the range over which fittings were performed in the high momentum wings of the line was varied. Also, to test for any effect that might be 'energy-dispersion dependent', the lineshapes were narrowed by 'doubling-up' adjacent channels, thus narrowing the width

to half the original dispersion. None of these effects altered the nature of the x^2/ν variation. The slow rise in the value of x^2/ν, together with increased difficulty in iteration, indicates that the routine may be trapped in an extremely shallow minimum in the 'Jacobian sum-of-squares' space - large variations in the trial fit parameters do not greatly increase the sum-of-squares. Certain conditions can exist for which minimisation becomes difficult. For example, Shizuma (1978) analysed annihilation lineshapes by the use of convolution techniques and reported problems in the fitting of two trail Gaussians under certain conditions, viz if one Gaussian was weaker than 10% of the intensity of the other, or if one of the Gaussians was narrower than half the width of the response function (in our analysis, the process of continued positron smearing successively decreases the width of the parabola).

Nonetheless, in our analysis, the minimisation routine has been able to recognise an optimum fit (defined by $\sigma = 10$ in figure 5.3.3). This is, accordingly, considered to be representative of the correct amount of positron smearing and of the true electronic structure. At $\sigma = 10$, the reduction in parabola width represents a fall in Fermi electron velocities of about 10%. This does not seem unreasonable. Using similar convolution techniques, Jackman et al (1974a) accounted for the positron zero-point energy in deformed copper by smearing in a Gaussian width 0.5 keV. It is pleasing to see that our minimum at $\sigma = 10$ provides an energy dispersion of 10 x 50 eV/channel = 0.5 keV.

5.3.3.3 Characterisation of Defects via e^+ and e^- Momentum Distributions

Figures 5.3.3-5.3.6 show the variation in x^2/ν as a function of σ for annihilations in deformed copper and in thermally generated vacancies. In all cases, the process of positron smearing has the effect of reducing the parabola width. Over the entire σ range, the Gaussian width increases only very slightly. From the values of the optimum σ and parabola width, the positron zero-point energy and Fermi energy respectively have been evaluated, and the results are presented in table 5.3.2. Also shown are the errors associated with each computed energy. These have been evaluated via consideration of the
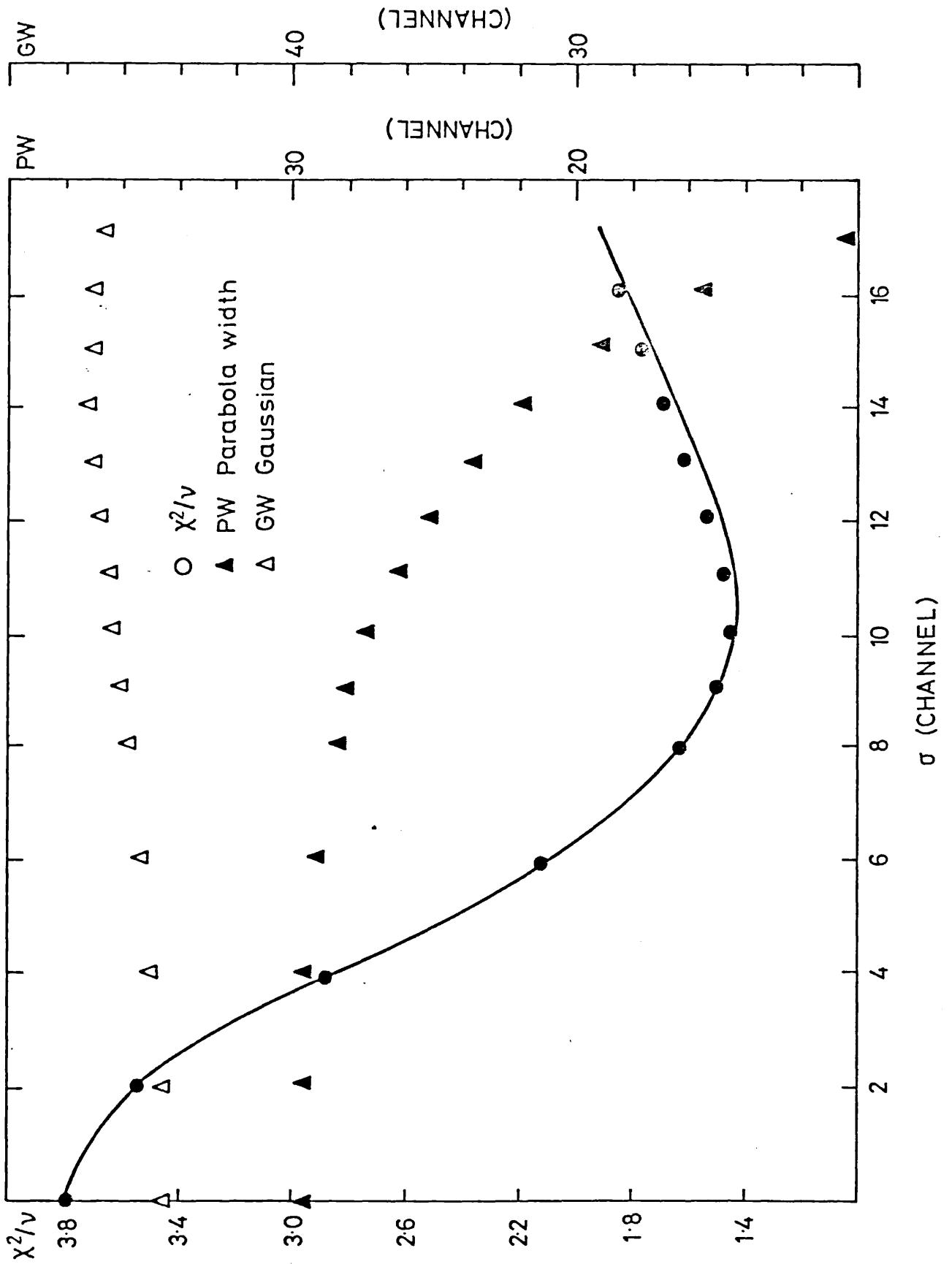
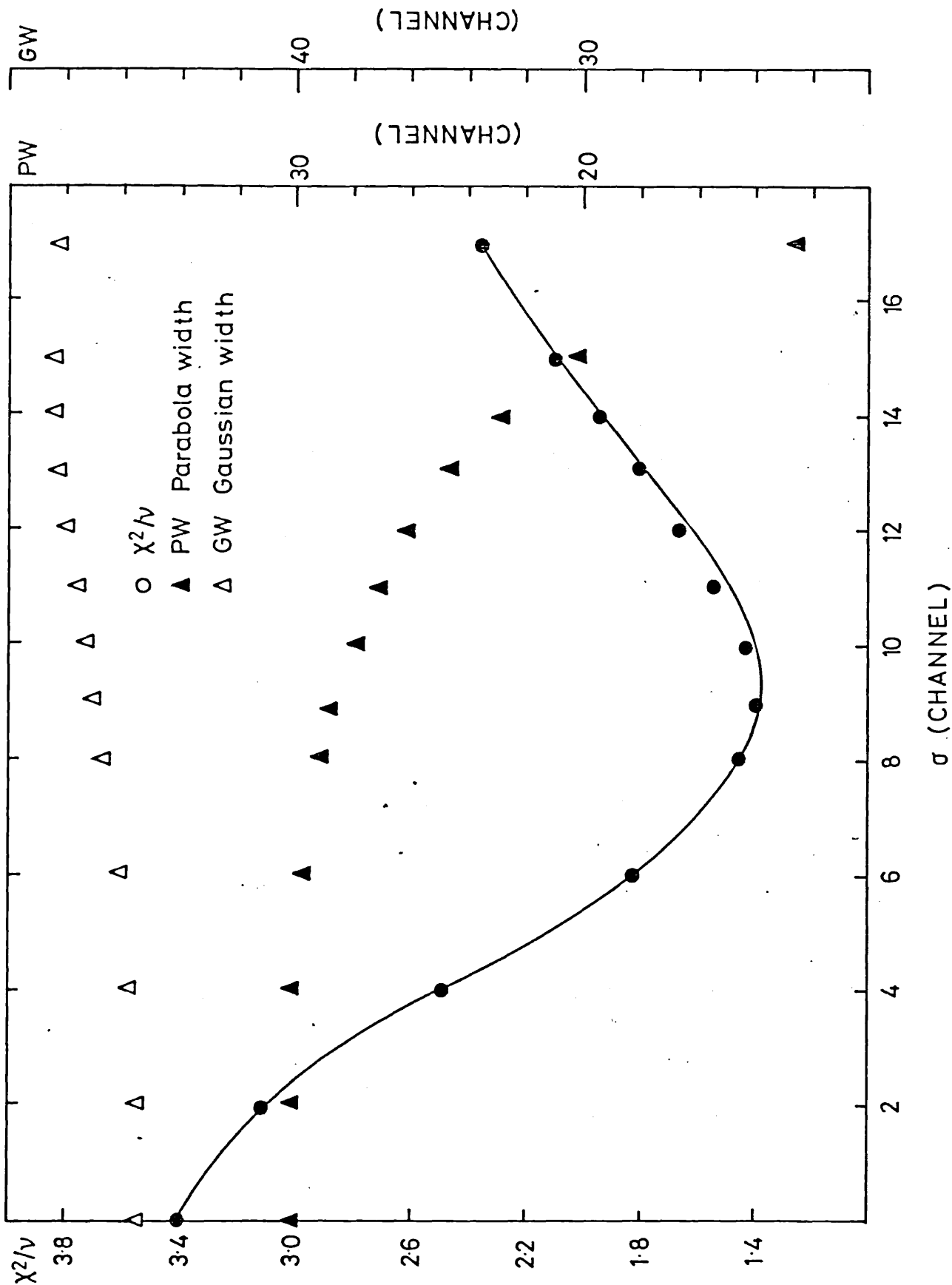Figure 5.3.3   Variation of χ^2/ν as a Function of σ for Copper Subjected to 22% Deformation Strain

136

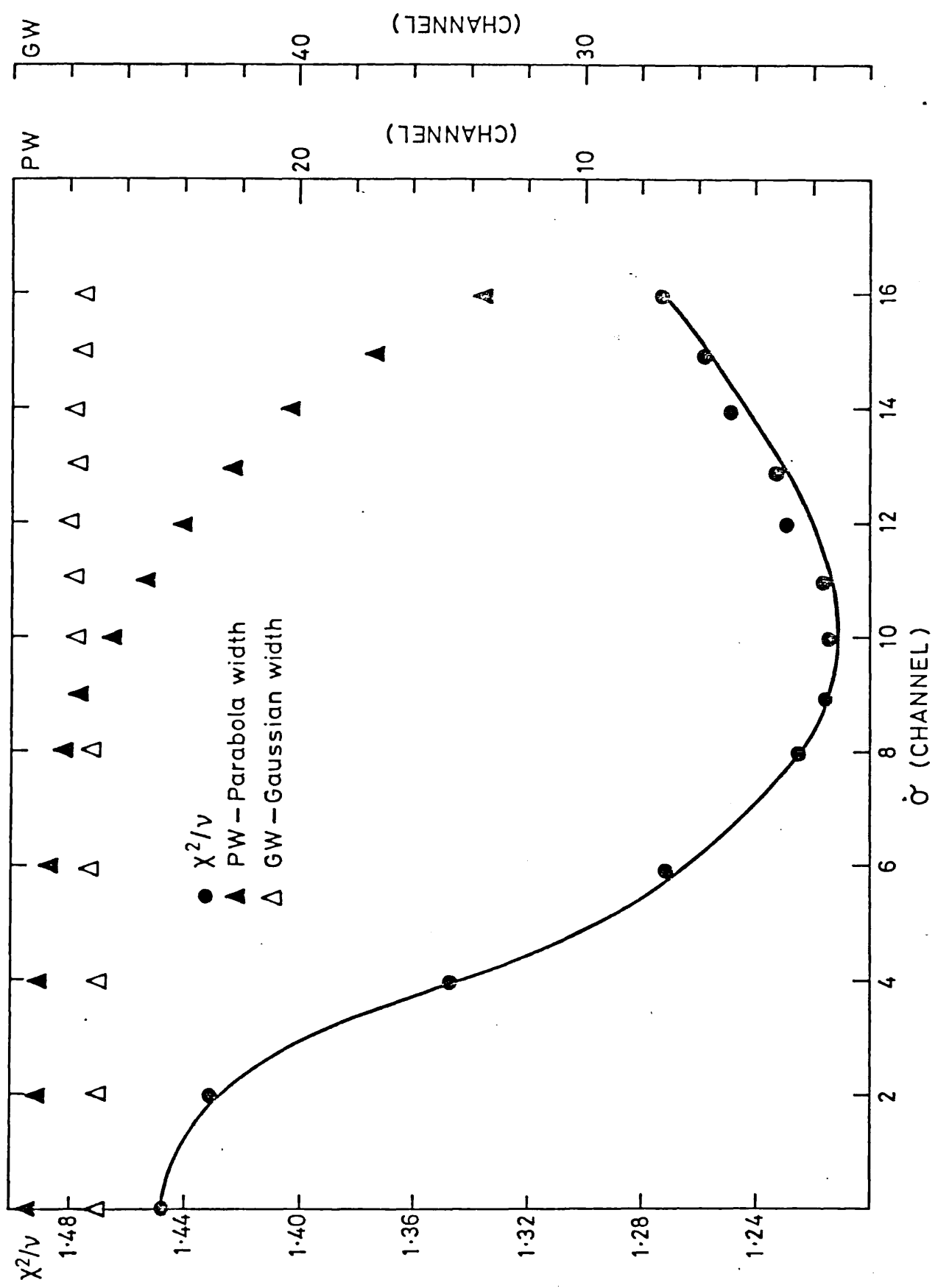Figure 5.3.4   Variation of χ^2/ν as a Function of σ for Copper Subjected to 15% Deformation Strain

Figure 5.3.5   Variation of χ^2/ν as a Function of σ for Copper Heated to $1025^{\circ}C$
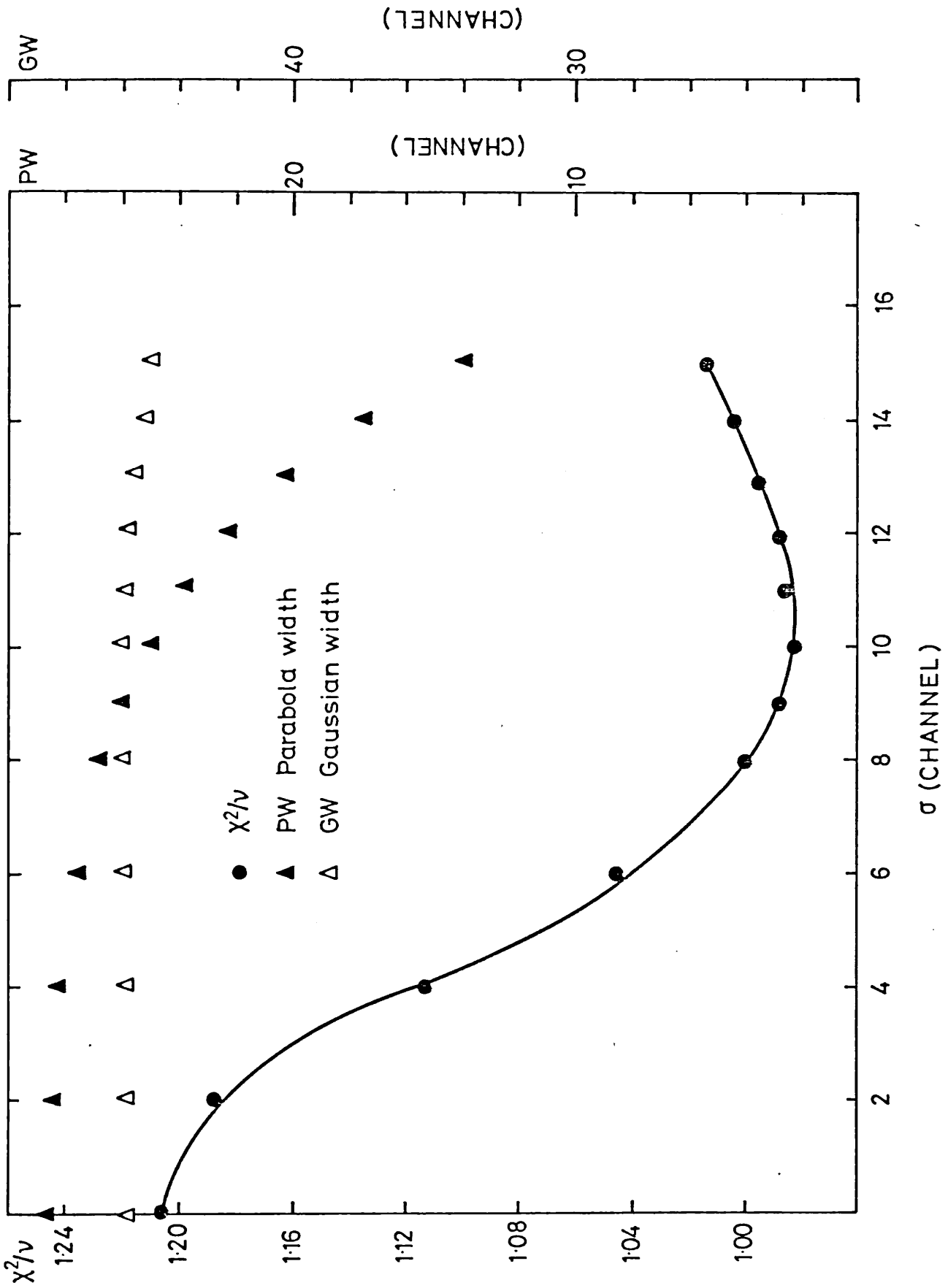
Figure 5.3.6   Variation of χ^2/ν as a Function of σ for Copper Heated to $1064^{\circ}C$

fractional error, $\sqrt{N}/N$, associated with the optimum x^2/ν where N is the number of points fitted by the annihilation routine. Clearly, the possible error spread associated with each value is quite large. However, in view of the consistency of the data, quite useful information can be extracted.

Table 5.3.2 Characterisation of Vacancies and Defects in Deformed Cu

Sample	Fermi Energy (eV) (66% confidence for error limits	Optimum σ	Positron Zero-Point Energy (eV) indicated below)
Undeformed	8.93 ± 0.05	-	-
15% strain	7.24 < 8.12 < 8.34	9	3.22 < 4.76 < 7.10
22% strain	5.54 < 7.40 < 7.89	10	3.95 < 5.87 < 9.62
1025°C	- < 6.87 < 8.23	10	1.35 < 5.87 < -
1064°C	- < 6.12 < 7.67	10	1.59 < 5.87 < -

The apparent similarity in the positron zero-point energy for both deformed copper and thermal vacancies is striking. With the exception of 15% strain, all samples provide a zero-point energy of 5.87 eV. One expects the magnitude of σ to be lower in the case of deformed copper if positrons are trapped at dislocations. Martin and Paetsch (1972) obtained theoretical estimates of the binding energies for positrons trapped in dislocations in Al by approximating the dislocation potential well to a cylinder (dimensions of length and breadth of dislocation core). Low binding energies were found (some of order kT) and the trapped positron wavefunction was not confined to the dislocation core. Quantum mechanically, one can idealise the positron interaction at a vacancy to that of a particle under the influence of a three-dimensionsal square-well (cubical box) potential. In a similar

manner, the positron interaction at a dislocation can be idealised to a particle confiend to an infinite three-dimensional rectangular potential (with same width and breadth as for vacancy case) and unbounded along the length. Solution of the ground-state wavefunction for both systems yields the relation $\bar{p}_d = 0.8 \ \bar{p}_v$
where $\bar{p}_d$ and $\bar{p}_v$ are the r.m.s. values of momentum at dislocations and vacancies respectively. Hence, for such idealised cases one would expect to find a minimum at $\sigma = 8$ for the case of deformed copper. Of course, in reality the positron experiences a finite attractive potential in the region of the defect and its wavefunction will spread over an area outside its immediate vicinity. However, one might expect to find roughly the same relation between $\bar{p}_d$ and $\bar{p}_{dv}$ in this more realistic case.

In the case of 15% strain the minimum value of σ occurs for 9 channels. Saturation conditions have not quite been achieved and so the overall amount of smearing would be less than for a fully saturated case. This might explain the shift in the minimum to a lower energy. Table 5.3.2 also illustrates the similarity in the values of zero-point energies for positrons trapped in vacancies at 1025°C and 1064°C. This, of course, is to be expected.

There appears to be more fluctuation in the values derived for the optimum Fermi energy than is the case for the optimum σ. For instance, the Fermi energy of 8.12 eV derived for 15% strain is higher than the value (7.40 eV) obtained for 22% strain. Again, this is probably reflecting the fact that 15% strain does not provide complete saturation trapping conditions, and so the Fermi energy is weighted towards the annealed value. Also, there are differences in Fermi energy for the cases of 1025°C and 1064°C which may be attributed to incomplete trapping - evidence in the literature supports this view (e.g. Rice-Evans et al 1976, Nanao et al 1977). Although at these temperatures the percentage of untrapped positrons may be quite small, our results would indicate that how sensitive the parabola width is to small changes in the trapping fraction.

However, table 5.3.2 does illustrate how the Fermi energies derived from the as-deformed samples are consistently and markedly

higher than those derived from vacancies. Thus, the results appear to provide the following physical interpretation of positron trapping in deformed copper. Firstly, similarity in optimum σ found for vacancies and deformed copper would indicate that the traps in the latter induce positron localisation similar to vacancies. Secondly, the higher Fermi energies associated with deformed copper suggests trapping sites of rather more +ve ionic charge/unit volume - dislocation cores would fit such a description. Thus, it appears that positrons are trapped at points (or jogs) along dislocation lines.

Other evidence exists to suggest that dislocations are responsible for positron trapping in deformed copper. For instance, McKee et al (1974) performed a trapping model fit on deformed copper data and evaluated a trapping rate higher than that found by McGervey and Trifthauser (1973) for trapping at vacancies. Clearly, if vacancies were responsible for trapping, oen would expect identical trapping rates. Such evidence would tend to confirm the suggestions of Doyama and Cotterill (1979). They stated that dislocations act as initial traps, and then positrons diffuse rapidly along the dislocations and finally get trapped at jogs or, perhaps, vacancies stabilised close to dislocations. Our results, though, would rule out the latter possibility.

Finally, consider the variation of x^2/ν as a function of σ for the annealed sample in figure 5.3.7. The original intention of this analysis was to show that the improvement of x^2/ν with the addition of positron smearing was not due to some idiosyncrasy of the computation. Hence, it was expected that x^2/ν would gradually worsen with the addition of smearing. Although the general trend of the curve is in contrast to those in figures 5.3.3-5.3.6, an extremely shallow minimum exists for σ = 2. For reasons discussed in section 6.3.1.3.2 this is attributed to trapping at dislocations. Furthermore, the observed trapping supports a theoretical model proposed by Smedskjaer (1980a) that trapping in well annealed samples can occur if positrons undergo point-like trapping at dislocations. This is also discussed in section 6.3.1.3.2.
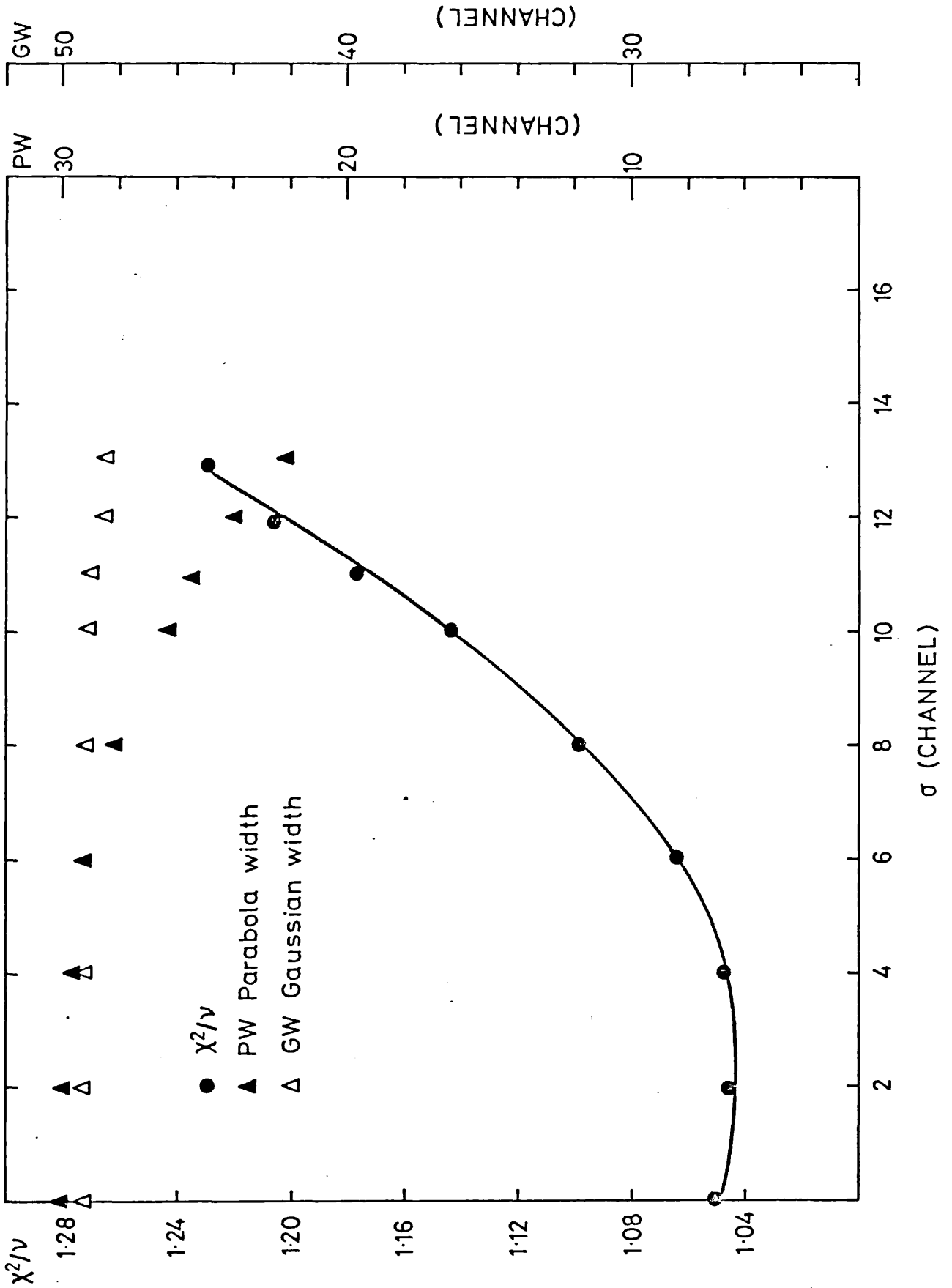
Figure 5.3.7   Variation of χ^2/ν as a Function of σ for Undeformed, Annealed Copper

5.3.4 Work-Hardening in Deformed Copper

Figures 5.3.8(a)-(b) show the variation of RID defect-specific parameters as a function of deformation strain corresponding to the data in figure 5.2.2. Over the entire range no changes in 'shape' are indicated. From the discussion of section 4.2.2 such positron response implies

(i) only one type of defect is available for trapping,

(ii) an assortment of traps are available and vary by the same proportions as a function of deformation

(iii) an assortment of traps are available but only one of them is varying its concentration.

On the basis of discussion in earlier sections, (ii) and (iii) can be rejected - dislocations seem to be the only traps present. The monitoring of defect-specific parameters as a function of strain is useful because, if more than one trapping type is present and their populations do not vary in the same proportions, the shape aprameters will vary. Such analysis would provide a useful insight as to the relative numbers of point defects produced as a function of strain in the cold-rolling process - e.g. a varying ratio of clusters to dislocations as a function of strain would indicate a varying population of vacancies produced during the deformation. Our analysis does not provide evidence of clustering in as-deformed samples and so, unfortunately, such insight cannot be gained. However, the fact that clusters are not formed might indicate that an excess of vacancies to interstitials are not generated during the deformation.

It is also of interest to assess the nature of the stress-strain relationship and the positron specific trapping rate into dislocations in work-hardened copper. Assuming a simple, two-state trapping model (i.e. annihilations at dislocations and in the free state) one can write using equations 2.5.7 and 4.2.1
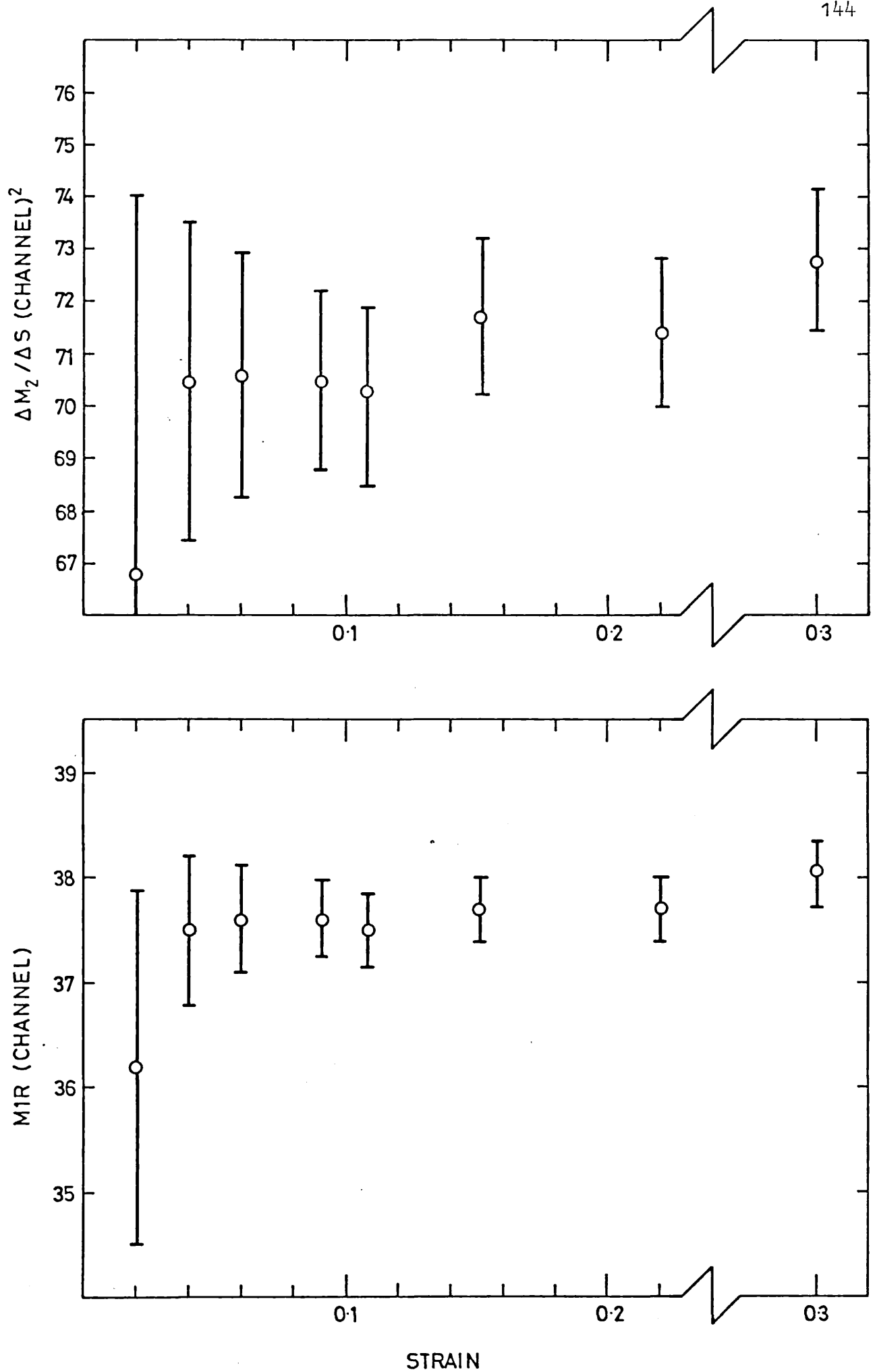
Figure 5.3.8.(a)   Variation of $\Delta M_2/\Delta S$ and M1R for Copper as a Function of Deformation Strain
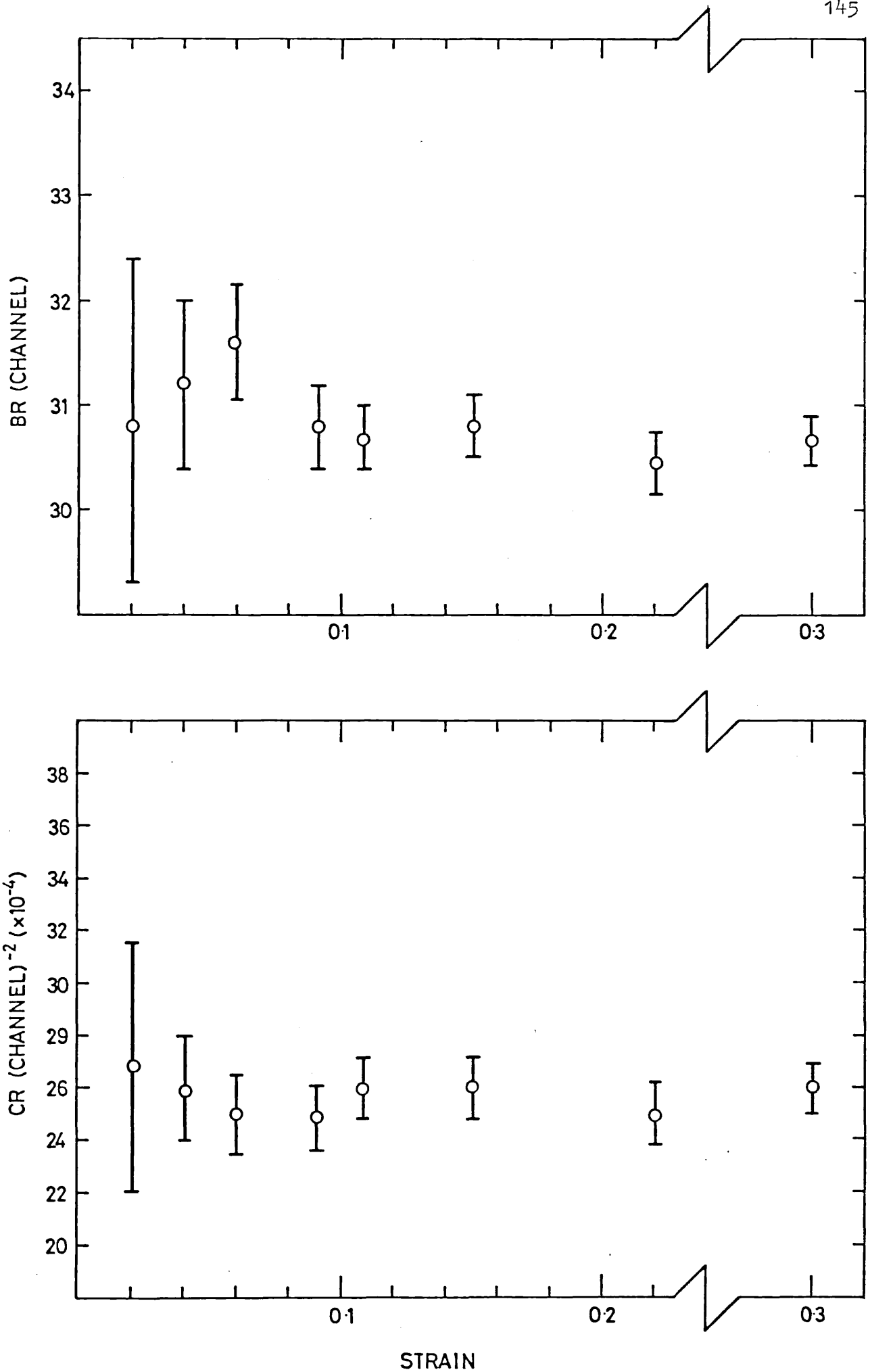
Figure 5.3.8.(b)   Variation of BR and CR for Copper as a Function of Deformation Strain

$$\frac{S - S_f}{S_d - S_f} = P_d = \frac{\Delta S}{\Delta S_d} = \frac{\mu C}{\lambda_f + \mu C} \qquad 5.3.2$$

where subscripts f and d represent annihilations in the free state and at dislocations respectively. The applied stress, σ, is related to the dislocation density, ρ, through the relation (equation 1.5.1)

$$\sigma \propto \rho^{\frac{1}{2}} \qquad 5.3.3$$

Now consider the two most likely forms of the stress-strain relationship:-

linear hardening	$\sigma \propto e$
parabolic hardening	$\sigma \propto e^{\frac{1}{2}}$

$$\qquad \qquad 5.3.4$$

where e is the strain. Substitution of equation 5.3.4 into 5.3.3 yields

$$\rho \propto e^n \qquad 5.3.5$$

where n = 1 for parabolic hardening, n = 2 for linear hardening. Since C in equation 5.3.2 refers to the fractional concentration of dislocations, it may be expressed by ρ/N where N is the number of atoms per cm^2 of surface. Hence, equation 5.3.2 may be re-written

$$\frac{e^n}{\Delta S} = \frac{N}{(\mu/\lambda_f)(\rho/e^n)\Delta S_d} + \frac{e^n}{\Delta S_d} \qquad 5.3.6$$

where ρ/e^n is the constant of proportionality defined by equation 5.3.5. In order to test for the most likely power of the strain, e, equation 5.3.6 can be rewritten to give

$$\log \left\{ \frac{1}{\Delta S} - \frac{1}{\Delta S_d} \right\} = \log k - n \log e \qquad 5.3.7$$

where

$$k = \frac{N}{(\mu/\lambda_f)(\rho/e^n)\Delta S_d} \qquad 5.3.8$$

Least-squares fits of equation 5.3.7 to the experimental data points in figure 5.2.2 were performed by guessing a value for ΔS_d. As dictated by the experimental data, two sensible guesses ΔS_d = 0.0410 and ΔS_d = 0.0420 were tried (the latter value considered to be an overestimate). The fits yielded

$$n = 2.16 \quad \text{for } \Delta S_d = 0.0410$$
$$n = 1.80 \quad \text{for } \Delta S_d = 0.0420$$

thus favouring the linear hardening relationship in equation 5.3.4. Accordingly, a fit of equation 5.3.6 to the experimental data was performed for n = 2. The fit yielded ΔS_d = 0.0417 and k = 0.0629 and is illustrated in figure 5.2.2. For comparison, a similar fit for n = 1 is also shown. This yielded ΔS_d = 0.0547. Clearly, the data favour a.linear hardening regime in the strain range 0-30%.

Finally, the specific positron trapping rate, μ, my be evaluated from equation 5.3.8 for the case of linear hardening (n = 2) by using the fit values k and ΔS_d. For the case of copper, N = 1.9 x 10^{15} cm^{-2}, λ_f^{-1} = τ_f = 130 ps (e.g. McKee et al, 1974). The value of ρ (3.75 x 10^{10} cm^{-2}) for 30% strain was taken from the work of Kopetskii et al (1974). Equation 5.3.8 then yields μ = 1.34 x 10^{16} s^{-1}, and compares with the trapping rate to dislocations evaluated by Johnson et al (1978) of 1.6 $\pm$ 0.4 x 10^{16} s^{-1} in copper deformed by bending. The trapping rate in copper was evaluated by McGervey and Trifthauser (1973) to be 1.37 x 10^{14} s^{-1}. In other words, the specific trapping rate to dislocations is about two orders of magnitude higher than that found for vacancies. The dislocation would be expected to possess a higher trapping rate than

vacancies because of the long range strain fields associated with it and, also, fo the availability of more continuous bound states for positrons at a linear defect than at a point defect (McKee et al, 1974). Since our data fit well to a dislocation trapping model, and the evaluated trapping rate appears to be substantially higher than that for vacancies, our fitting analysis would lend further support to the idea that positrons are, at least initially, trapped at dislocations in deformed copper.

5.3.5 Conclusions

This chapter has attempted to assess the nature of defects in deformed copper. It is suggested that vacancy clusters are not present in as-deformed copper. It is also suggested that positrons are trapped at dislocations. Resolving annihilation lineshapes into their respective e^+ and e^- momentum distributions provides an insight into the nature of positron trapping at dislocations, and suggests that they are trapped at a point along the dislocation core. The resulting localisation is similar to that for vacancies, providing a zero-point energy of 5.87 eV. A trapping model fit to experimental data favours a linear-hardening regime for deformed copper and provides a specific trapping rate to dislocations of 1.34×10^{16} s^{-1}.

CHAPTER 6 : DEFECTS IN MECHANICALLY
DEFORMED ALUMINIUM

6.1 INTRODUCTION

Amongst the first to study mechanical damage in aluminium were
Grosskreutz and Millett. (1969) and Hautojarvi et al (1970) using
lifetime techniques. They attributed the observed increase in mean
lifetimes to positron trapping at dislocations. However, as in the
case of copper, later work has shown that positron annihilation
characteristics in deformed aluminium are similar to those found for
vacancies (e.g. Cotterill et al, 1972), and such findings place doubt
on the suggestion that dislocations are the prime positron traps. The
types of defects actually present in deformed aluminium have still yet
to be determined unambiguously and the accumulation of much needed
'defect-specific' data is vital to this task. It is important to
establish whether positrons are sensitive to certain kinds of defects
(e.g. dislocations) since the interpretation of positron annihilation
data will depend on this. There is also a need in metallurgical
studies to 'characterise' individual defect types.

In an attempt to shed light on the areas discussed above, the
experimental programme outlined in section 6.2 was carried out.
Characterisation of defects was achieved through the use of the model-
dependent and -independent approaches (chapter 4) by analysing
lineshapes from individual defects in isolation - in particular,
vacancies, voids (or clusters) and dislocations. Vacancies were easily
produced through thermal generation. However, an attempt to produce an
isolated population of voids (or clusters) in aluminium through
neutron-irradiation was unsuccessful. ·Dislocations were produced in
aluminium by cold-rolling. Under favourable circumstances (i.e. the
absence of point defects in deformed samples) where dislocations are
the only defect population present, characterisation is possible if
positrons are, indeed, trapped at such sites.

In order to assess the nature of defects in deformed aluminium,
two experimental approaches were adopted. Firstly, the positron
response in cold-rolled samples was compared with that at thermally

generated vacancies, and, secondly, isochronal annealing performed in order to test for the recovery of any point defects that might be present in the deformed state. Unfortunately, due to 'teething' problems with the newly installed spectroscopy system (section 3.1.1) the isochronal annealing runs were spoiled due to line-drift and incorrect data collection. They have not, therefore, been used for serious analysis.

Finally, to assess how the presence of a significant proportion of impurities might affect the types of 'intrinsic' defects present in the deformed state, an identical experimental programme was performed on an aluminium alloy. Details of experimentation are given below.

6.2 EXPERIMENTATION AND RESULTS

6.2.1 Generation of Thermal Vacancies

Two polycrystalline aluminium slabs (20 mm x 10 mm x 2 mm) were cut out from a 5N purity aluminium sheet supplied by johnson Matthey and Company. After annealing at 550°C for 4 hours, both samples were cold-rolled to 21% strain and then etched in a 1% solution of NaOH. The aluminium slabs were then made to sandwich a Cu^{64} foil (2.5 μm thickness) irradiated in the Dido reactor (AERE) to give a total activity of $\sim$650 μCi. Positron measurements were then performed in the furnace in a way similar to that described in chapter 5 (section 5.2.1.).

Figure 6.2.1 illustrates the chronological order of the experiment and shows the parameter S plotted as a function of temperature. The experiment allows for direct comparison between mechanical damage and vacancies in aluminium. The spectrum recorded for annealed aluminium was used as the 'reference' for RID curve analysis.

6.2.2 Generation of Mechanically Deformed Aluminium and Aluminium Alloy

Polycrystalline aluminium slabs of 5N purity and dimensions 40 mm x 7 mm x 2 mm were cold-rolled to values between 1% and 35% strain,
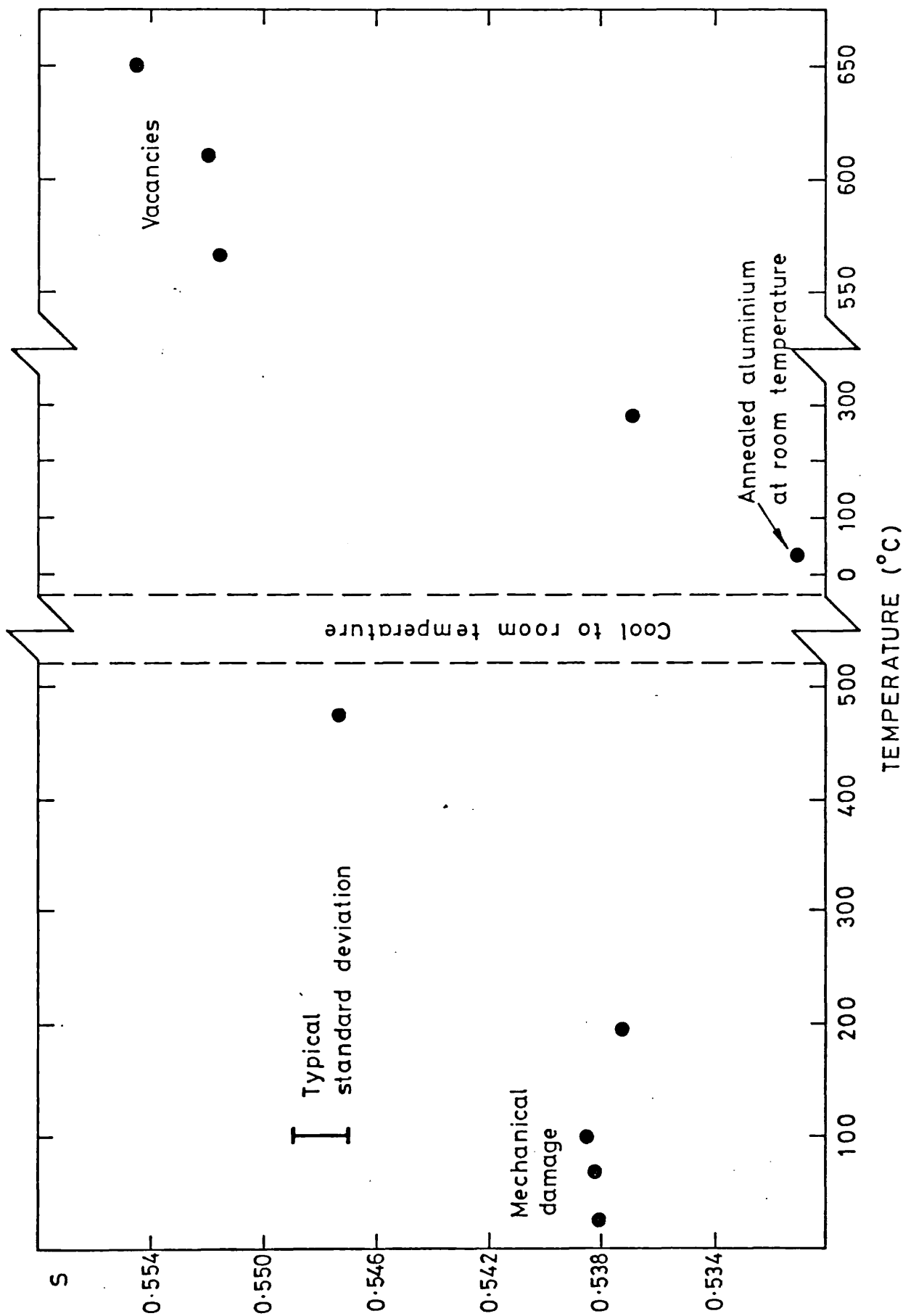
Figure 6.2.1   Variation of S as a Function of Temperature for Aluminium
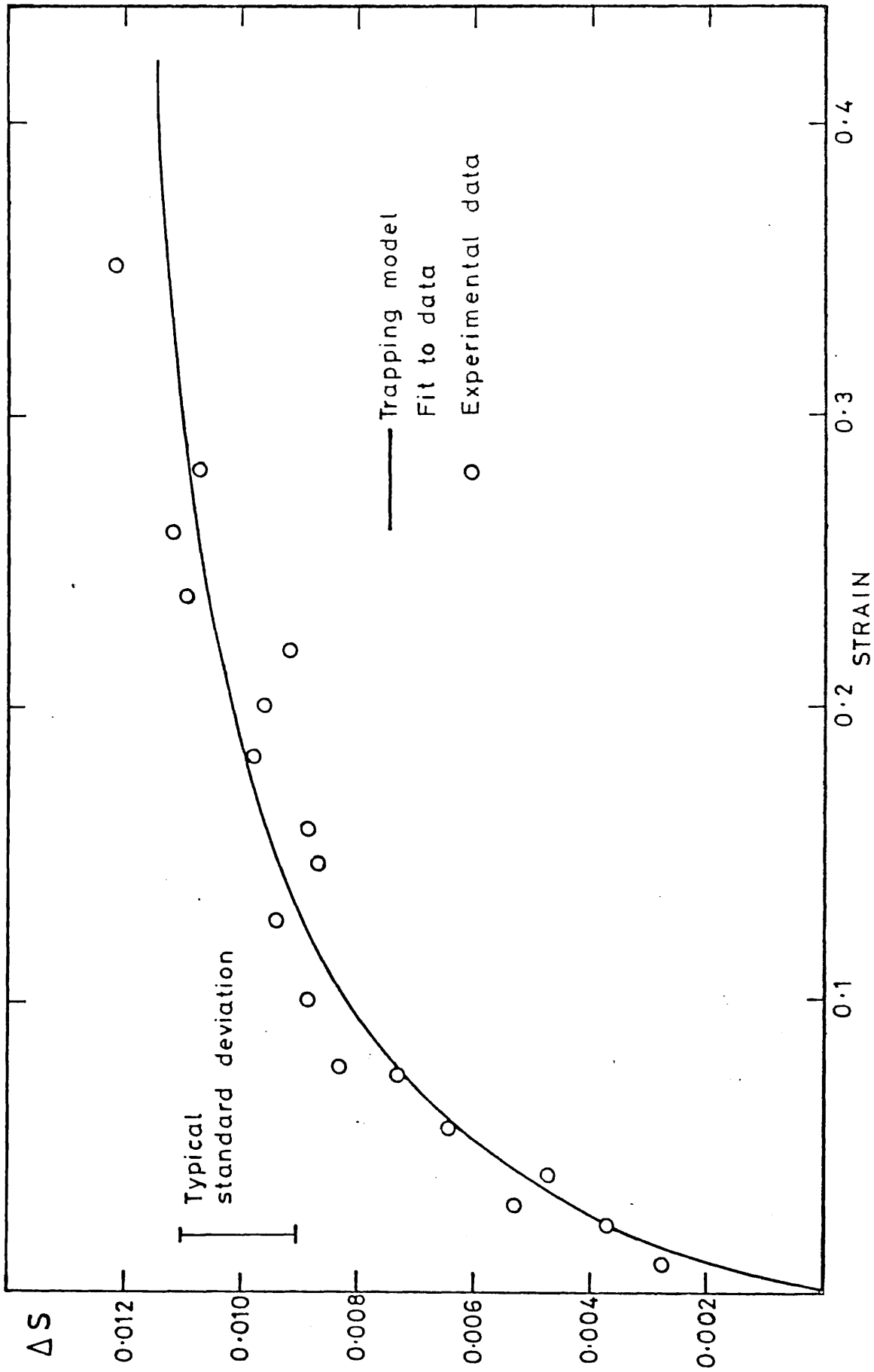Initially Subjected to 21% Deformation Strain

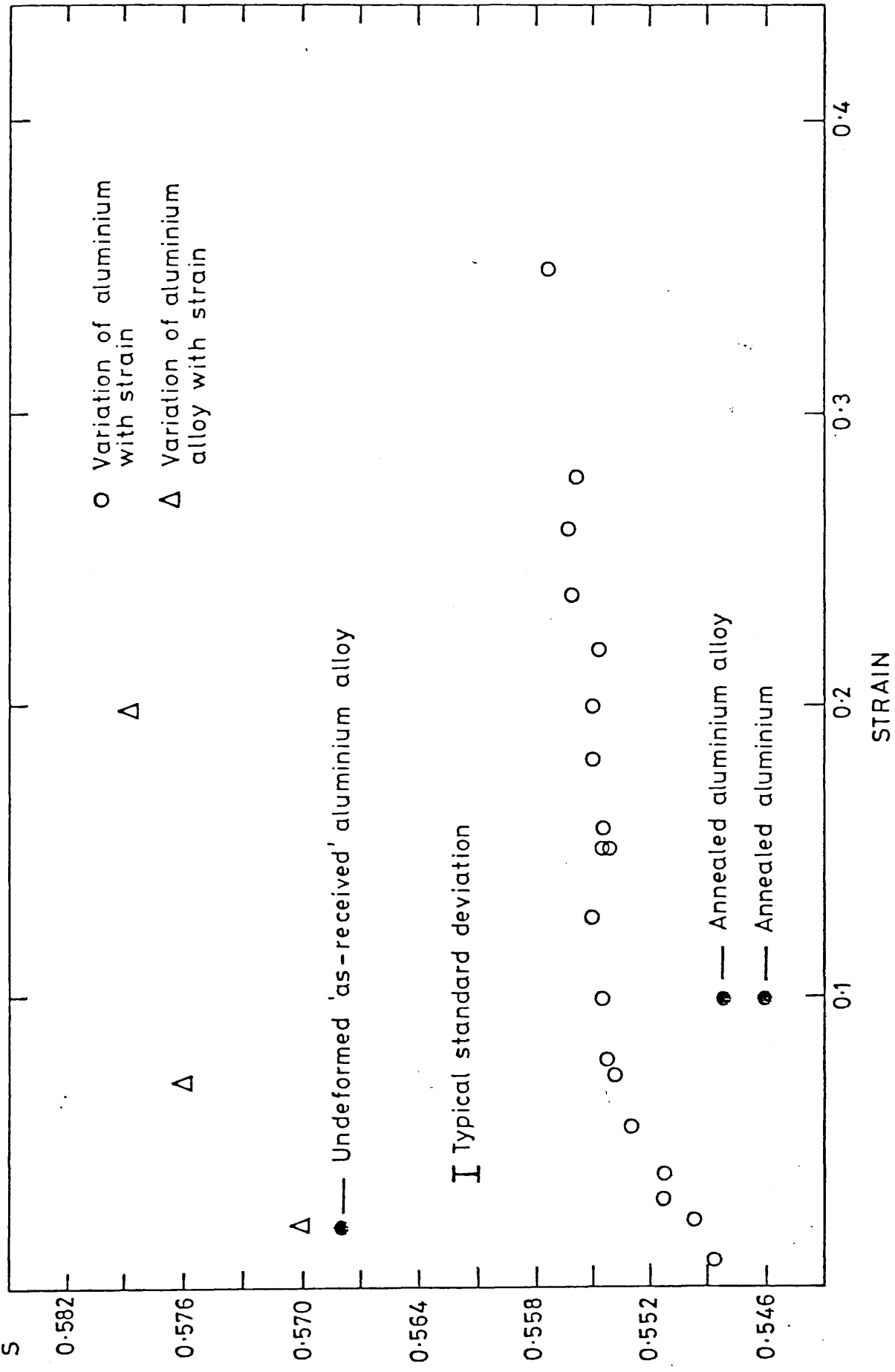Figure 6.2.2   Variation of ΔS as a Function of Deformation Strain for Aluminium

Figure 6.2.3   Variation of S as a Function of Deformation Strain for Aluminium and an Aluminium Alloy

after annealing at 550°C for 4 hours. Also, slabs of similar dimensions were cut out from a sheet of 'as-received' commercial aluminium alloy (2½% Mg) and, without annealing treatments, cold-rolled to strains of 2%, 7% and 20% respectively. An undeformed, unannealed slab was used as a 'reference'. In addition, an undeformed alloy slab, annealed at 550°C, was prepared for positron measurements.

Measurements were performed using the remote-source geometry approach (chapter 3). The selected energy range in the MCA counted at a rate of ∿10000 counts/min and, in the case of the aluminium slabs, data collection continued until 2.5 x 10^6 counts were recorded. In the case of the alloy 12 x 10^6 counts were recorded for each measurement. Figure 6.2.2 shows the variation of the parameter ΔS as a function of deformation strain for aluminium. Also, for reasons of comparison, the S-values for both aluminium and its alloy are plotted in figure 6.2.3 as a function of strain.

6.3 DATA ANALYSIS AND DISCUSSION

6.3.1 The Nature of Defects in Mechanically Deformed Aluminium

6.3.1.1 S-Parameter Analysis

Figure 6.2.1 show the variation of S as a function of temperature for aluminium initially deformed to 21% strain. It is interesting to note that the S-values for aluminium are markedly higher than those for other metals - e.g. the value 0.531 for annealed aluminium is to be contrasted with the value 0.417 for annealed copper in figure 5.2.1 (chapter 5). This, of course, reflects a markedly higher probability of annihilation with valence electrons. In fact, in the annealed state, ∿85% of positrons annihilate with valence electrons (section 6.3.1.3). This is unfortunate because changes in electronic structure, brought about by the presence of defects, may not be so easily seen if the enhanced probability of annihilation with conduction electrons at such sites is not much greater than that in the perfect lattice.

Figure 6.2.1 shows that the change in S (relative to the annealed state) for positrons trapped at vacancies is about 3 times that

associated with positrons at defects in the deformed state. Figure
6.2.3 show that a deformation strain of 20% allows saturation trapping
conditions to be approached. In fact, a 'trapping-model' fit (section
6.3.1.3) to the data is shown in figure 6.2.2, and indicates that $\sim$ 73%
of positrons are trapped at this strain. Hence, on this basis, the
saturation value for the deformed sample at 21% strain in figure 5.2.1
may be evaluated as 0.5407 which is still much lower than the observed
value of S for vacancies in the saturation region. Cotterill et al
(1972) compared the mean lifetime of positrons trapped in aluminium
deformed to 50% (where saturation conditions are known to exist) to the
saturation lifetime observed for vacancies, and found identical values.
Similarity in defect structure is also suggested in section 6.3.1.2
where RID defect-specific parameters show no differences in the 'shape'
of e^+-e^- momentum distributions between thermal vacancies and those
defects encountered in deformed aluminium. Hence, one expects
similarity in the corresponding saturation S-values. The large
difference in positron response in our S values could be explained if
some degree of recovery had occurred in the deformed sample, since this
would have the effect of lowering the S-value associated with the
deformed sample.

Evidence for recrystallisation of aluminium below room temperature
is found in the literature (e.g. Frois 1966, Nielsen and Petersen
1976). The deformed sample used for the experiment in figure 6.2.1 was
left for about 6 months at room temperature after cold-rolling before
measurements were taken, and a degree of recovery might, therefore,
have taken place.

6.3.1.2 RID Curve Analysis

Figures 6.3.1(a)-(b) show the variation in RID defect-specific
parameters as a function of temperature corresponding to the S-values
in figure 6.2.1. Apart from deformed aluminium annealed at 200°C, no
significant differences in RID parameters are seen for the cases of
positron trapping at vacancies and in the mechanically deformed state.
The change at 200°C probably indicates the return of the defected
lattice to the perfect state - Petersen (1978) performed isochronal
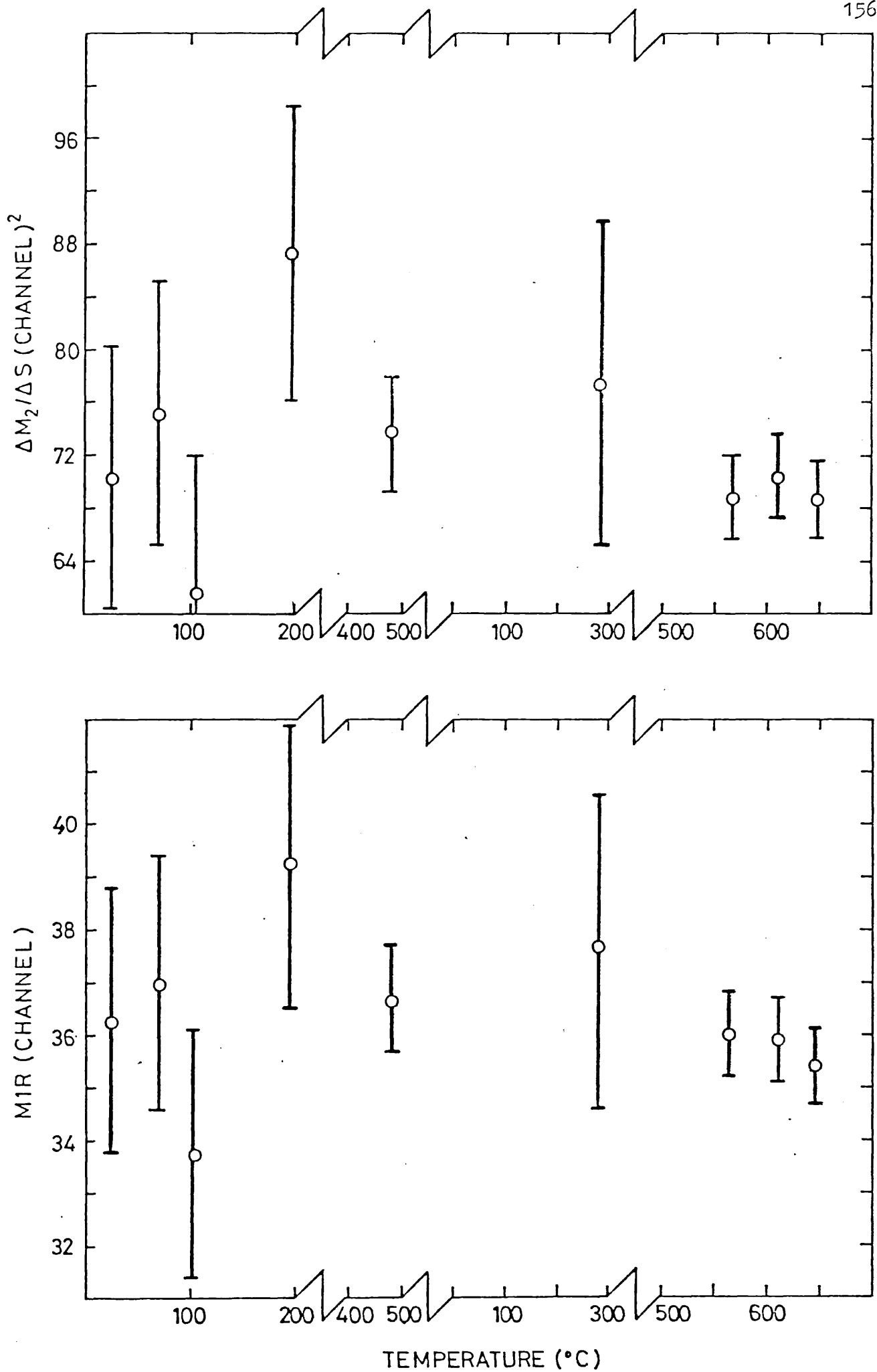anneals on aluminium samples deformed at room temperature to varying

Figure 6.3.1.(a)   Variation of $\Delta M_2/\Delta S$ and M1R as a Function of Temperature for Aluminium Initially Subjected to 21% Deformation Strain
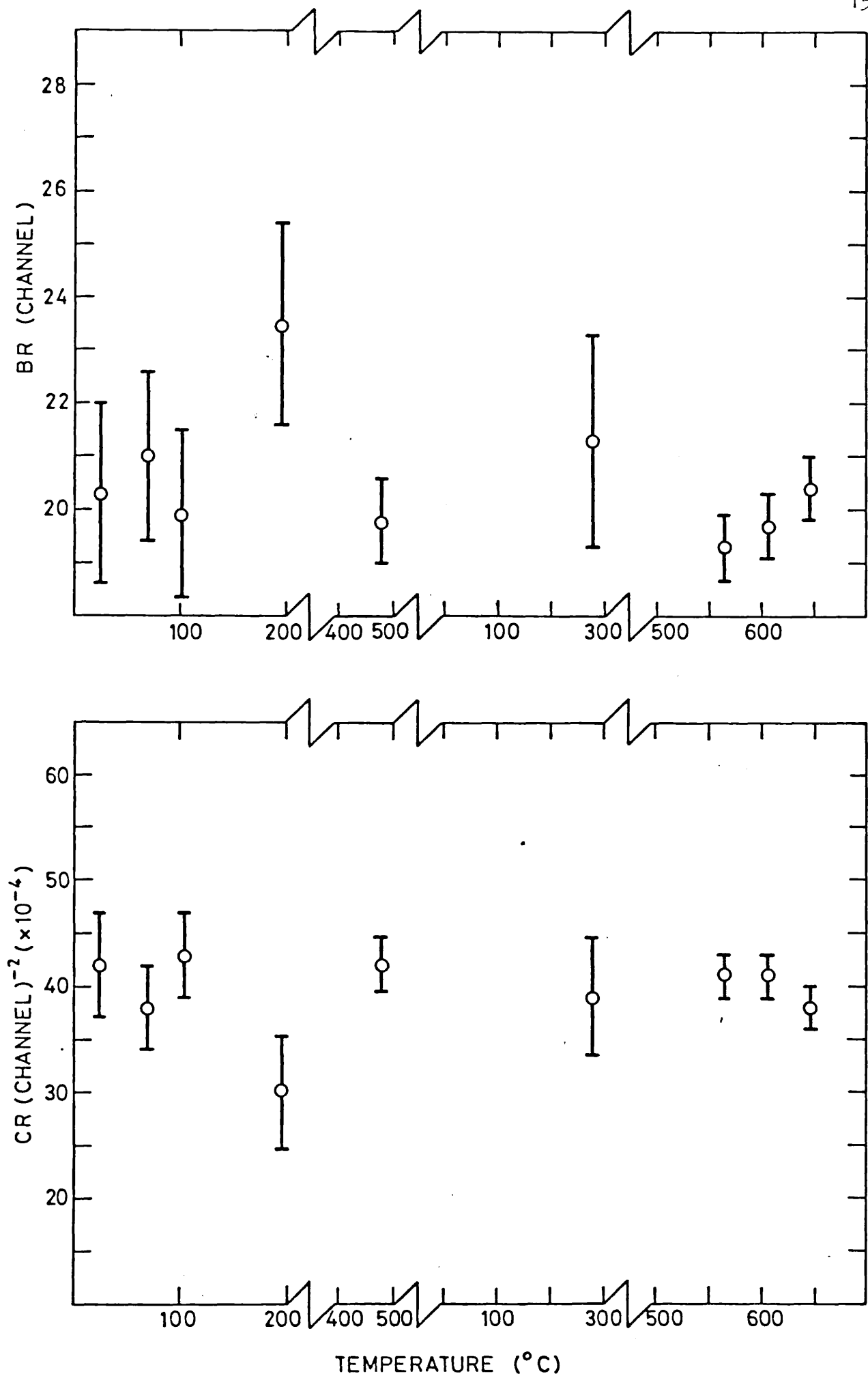
Figure 6.3.1.(b)   Variation of BR and CR as a Function of Temperature for Aluminium Initially Subjected to 21% Deformation Strain

strains and showed that complete recovery occurred in the region 150-250°C (although in the case of 48% strain, complete recovery was achieved by 100°C). It appears that, as in the case of copper, the similarity between vacancies and defects in deformed aluminium indicates a vacancy-like trapping centre for positrons in the latter. Hence, for reasons similar to those given in section 5.3.1, our results would indicate an absence of vacancy clusters in the deformed state at room temperature. The similarity in RID curve parameters for deformed aluminium and vacancies would support the theory that the saturated S-values for both cases should, indeed, be identical (section 6.2.1.1).

Evidence for vacancy clustering in aluminium samples containing non-equilibrium vacancy popultions produced as a result of quenching and irradiation appear in the literature. Wampler and Causter (1978) found evidence for vacancy clustering in aluminium containing vacancies quenched-in at 200K. Clusters were found to appear at an annealing temperature fo 250K, and then to coarsen into loops at around room temperature. Also, Alam et al (1979) found evidence of vacancy clustering for vacancies quenched-in at 230K. The annealing temperatures at which clusters appeared, and their coarsening to loops, were similar to those found by Wampler and Causter. No evidence appears in the literature suggesting the presence of clusters in mechanically deformed aluminium. However, even if clusters were formed during the cold-rolling process at room temperature, the evidence of the literature presented above would suggest that they would immediately change to loops. Petersen (1978) found no evidence for point defect recovery in isochronal anneals of aluminium deformed at room temperature. Also, if dislocation recovery is possible at or below room temperature, one would expect vacancy clusters (if produced during deformation) to recover at even lower temperatures since, in general, point defect activation energies are lower than those for dislocations.

As in the case of deformed copper, this section can find no evidence of a presence of vacancy clusters in deformed aluminium at room temperature. However, it should be pointed out that, compared with other metals, lineshape changes in aluminium are small and,

hence, errors, in RID curve parameters larger. This might have the effect of concealing real change.

6.3.1.3 Positron and Electron Momentum Distributions in Deformed Aluminium

6.3.1.3.1 Evidence for Positron Zero-Point Motion.

The results of model-dependent parabola/Gaussian fits to observed annihilation lineshapes for deformed aluminium showed a systematic worsening of x^2/ν (from 1.2 to 1.9) with increasing deformation. This was taken to be indicative of significant positron momenta in the deformed state.

In the case of the annealed, undeformed aluminium sample, the parabola width yielded a Fermi energy of 12.5 eV - the free-electron model predicts a Fermi energy of 11.63 eV. Using similar convolution techniques on Doppler broadened lineshapes, Jackman et al (1974b) derived a Fermi energy of 10.3 eV, whereas Hautojarvi (1972) obtained a value of 11.9 eV by fitting an angular correlation curve for annealed aluminium. Also, by angular correlation curve-fitting, Dlubek and Brummer (1977) derived the value 11.9 eV. These values illustrate the expected result that angular correlation fits are likely to yield more precise values than their counterpart Doppler lineshapes.

6.3.1.3.2 Characterisation of Defects via e^+ and e^- Momentum Distributions.

In the 'parabola/Gaussian' fittings (mentioned in section 6.3.1.3.1) the parabola percentage was found to decrease as a function of deformation strain. Clearly, this contradicts the observed behaviour of a systematic narrowing of the line indicating increased probability of annihilation with valence electrons (as exemplified by the S-parameter in figure 6.2.3). Similar behaviour was reported by El Khangi (1980) for 'Gaussian/parabola' fits to lineshapes representative of increasing concentrations of vacancies as a result of the heating of annealed aluminium up to temperatures near the melting point. This problem illustrates a case where the minimisation routine is unable to
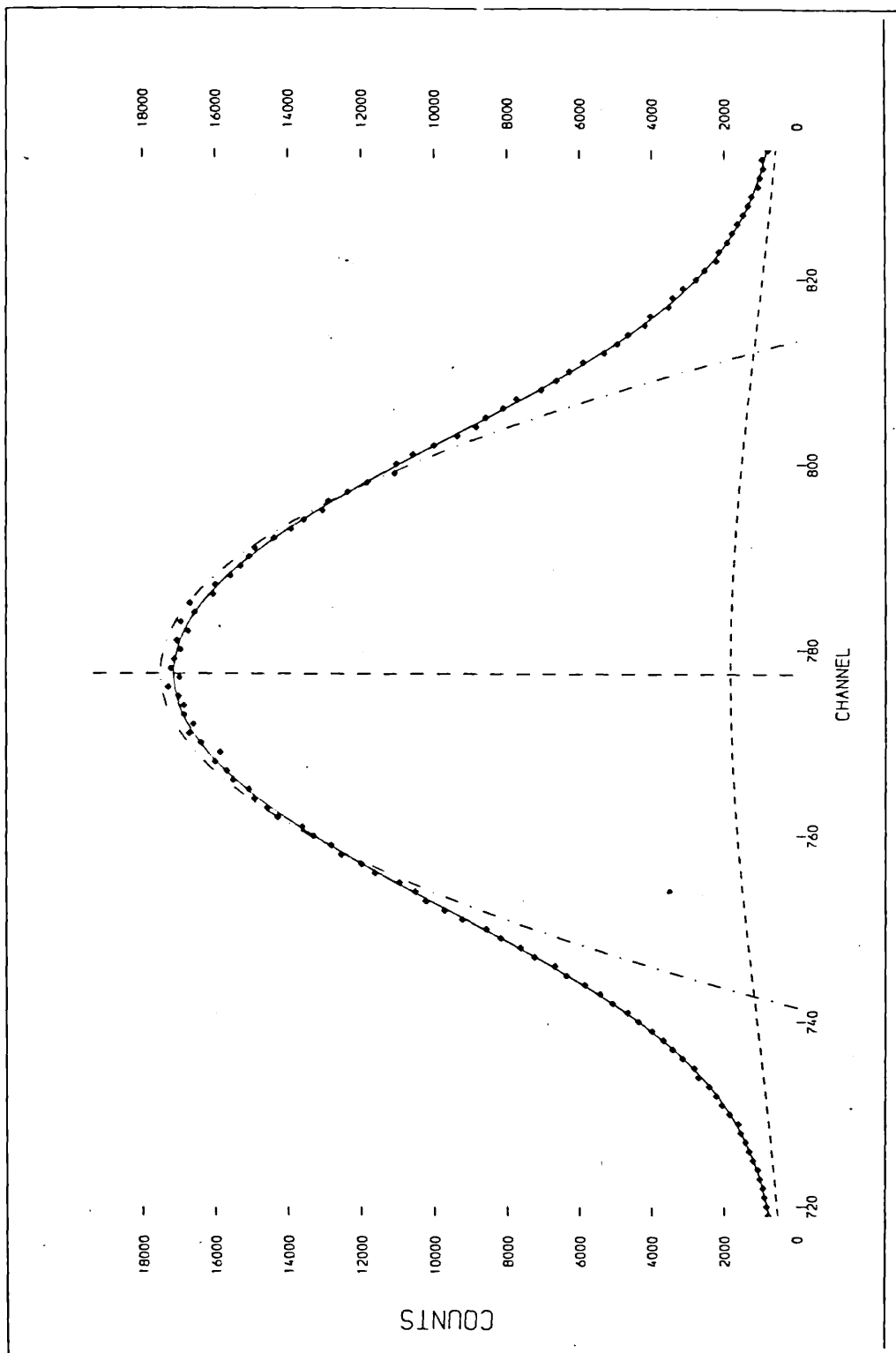
Figure 6.3.2   Model-Dependent Fitting for the Annealed State of Aluminium.
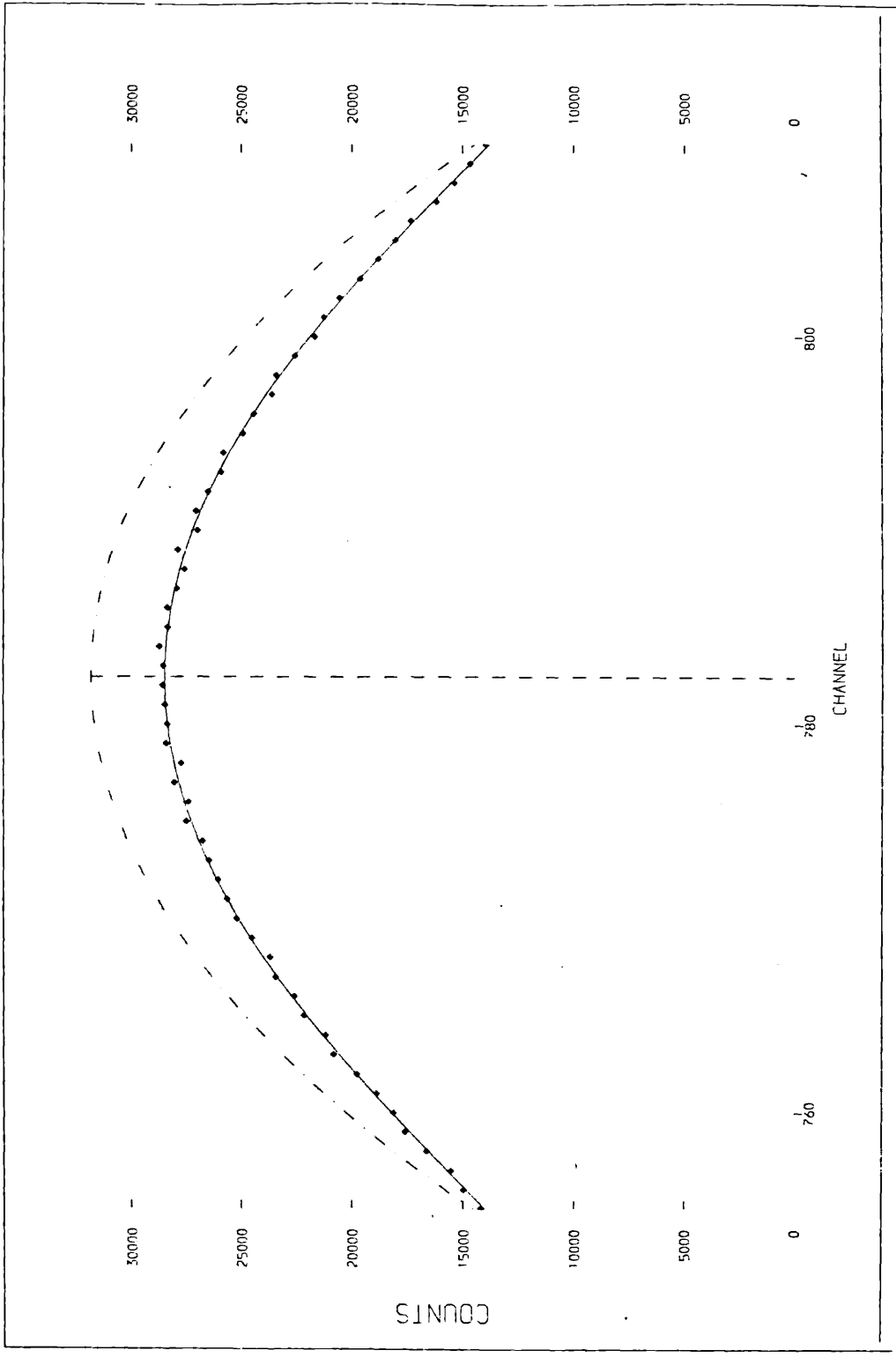----- Gaussian, ---·-· Parabola, ——— Fit to Data

Figure 6.3.3   Model-Dependent Fitting for the Annealed State of Aluminium.
-·-·-· Parabola,   ——— Fit to Data

cope, and give physically reasonable solutions, because the Gaussian component is only 16% of the total intensity (figure 6.3.2). Shizuma (1978) has discussed the breakdown in minimisation procedures when one of the two fitted components becomes comparatively low in intensity (section 5.3.3.2). As a consequence, the fitting of deformed aluminium lineshapes (where the 'true' Gaussian intensity is lower than 16%) with a parabola/Gaussian regime to represent the electronic distribution, plus a convoluted Gaussian positron momentum component, was unsuccessful.

In order to overcome these problems, only the upper half of annihilation lines were fitted by approximating the electron momentum distribution to that of a parabola only - thus avoiding the need to fit a shallow component. Since such a fitting is now only a crude approximation it should be stressed that calculated parameters (e.g. Fermi energies and positron zero-point energies) are not representative of the true physical values. However, the use of such an approximation allows some insight into the physical nature of the problem to be achieved since fits can now be successfully performed. In particular, differences in fit parameters characterising lineshapes derived from annihilations occurring at vacancies and in mechanically deformed aluminium, may be taken as indicative of differences in the defect electronic environment encountered by the positron. Figure 6.3.3 illustrates a parabola fit to the upper half of the annihilation lineshape for annealed aluminium.

Figures 6.3.4-6.3.7 show the variation in x^2/ν as a function of σ for annihilations in deformed aluminium (for samples in which saturation trapping conditions are suggested - figure 6.2.3) and in thermally generated vacancies. In all cases, the process of positron smearing has the effect of reducing the parabola width. From the values of the optimum, σ, and parabola width, the positron zero-point energy and Fermi energy, respectively, have been evaluated, and the results are presented in table 6.3.1.

Inspection of table 6.3.1 reveals three main features:-
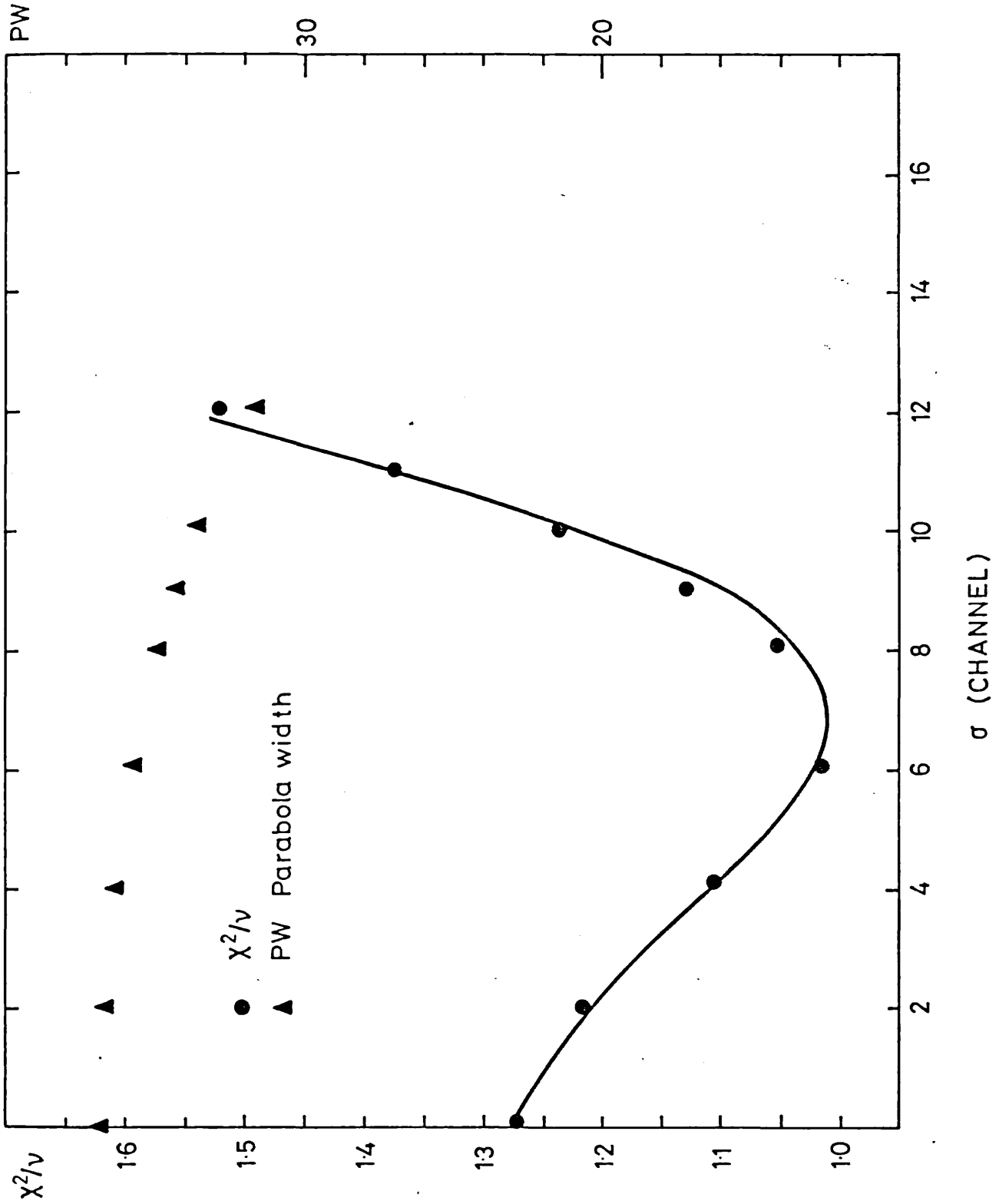
Figure 6.3.4   Variation of χ^2/ν as a Function of σ for Aluminium Subjected to 21% Deformation Strain
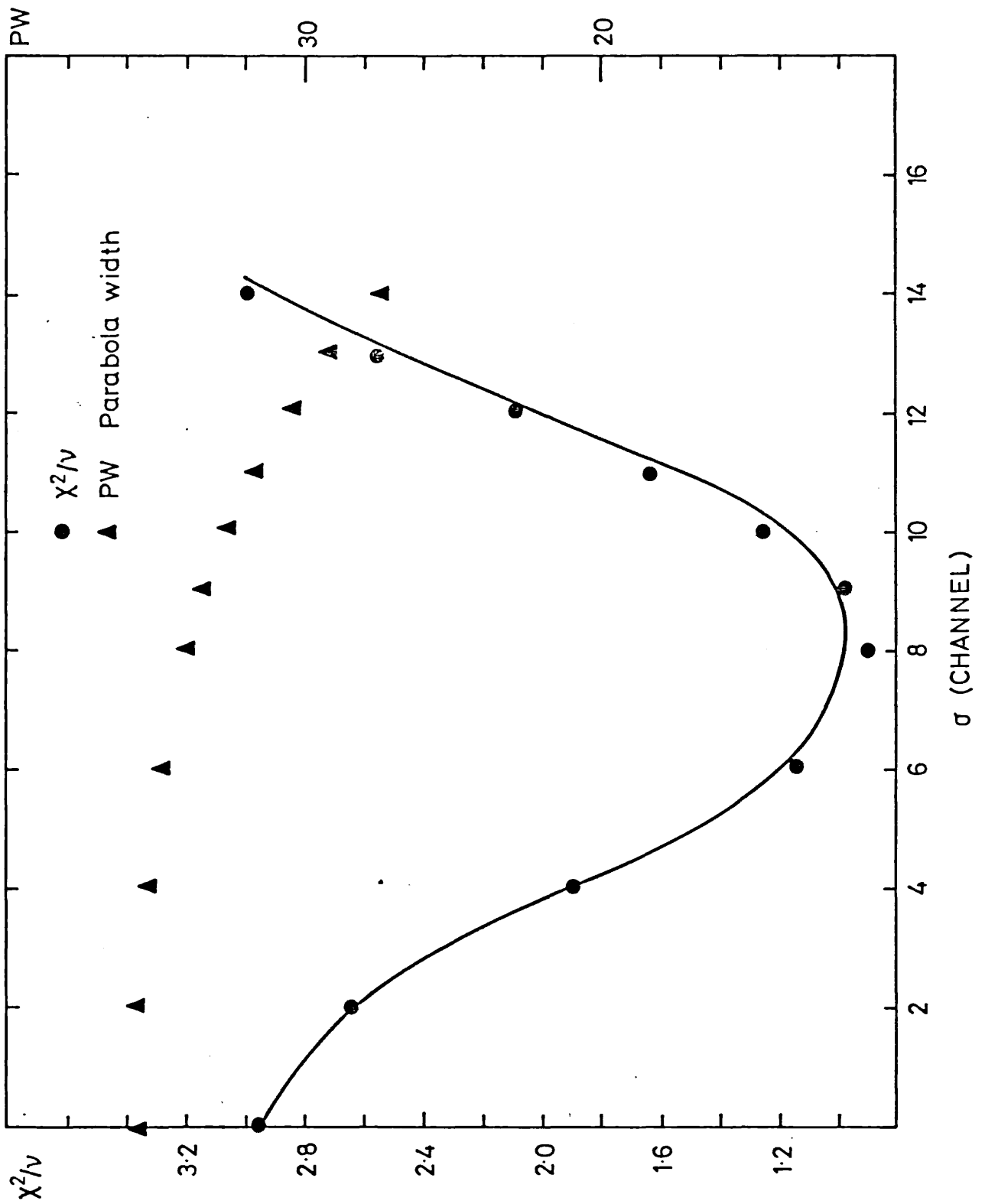
Figure 6.3.5   Variation of χ^2/ν as a Function of σ for Aluminium Subjected to 28% Deformation Strain
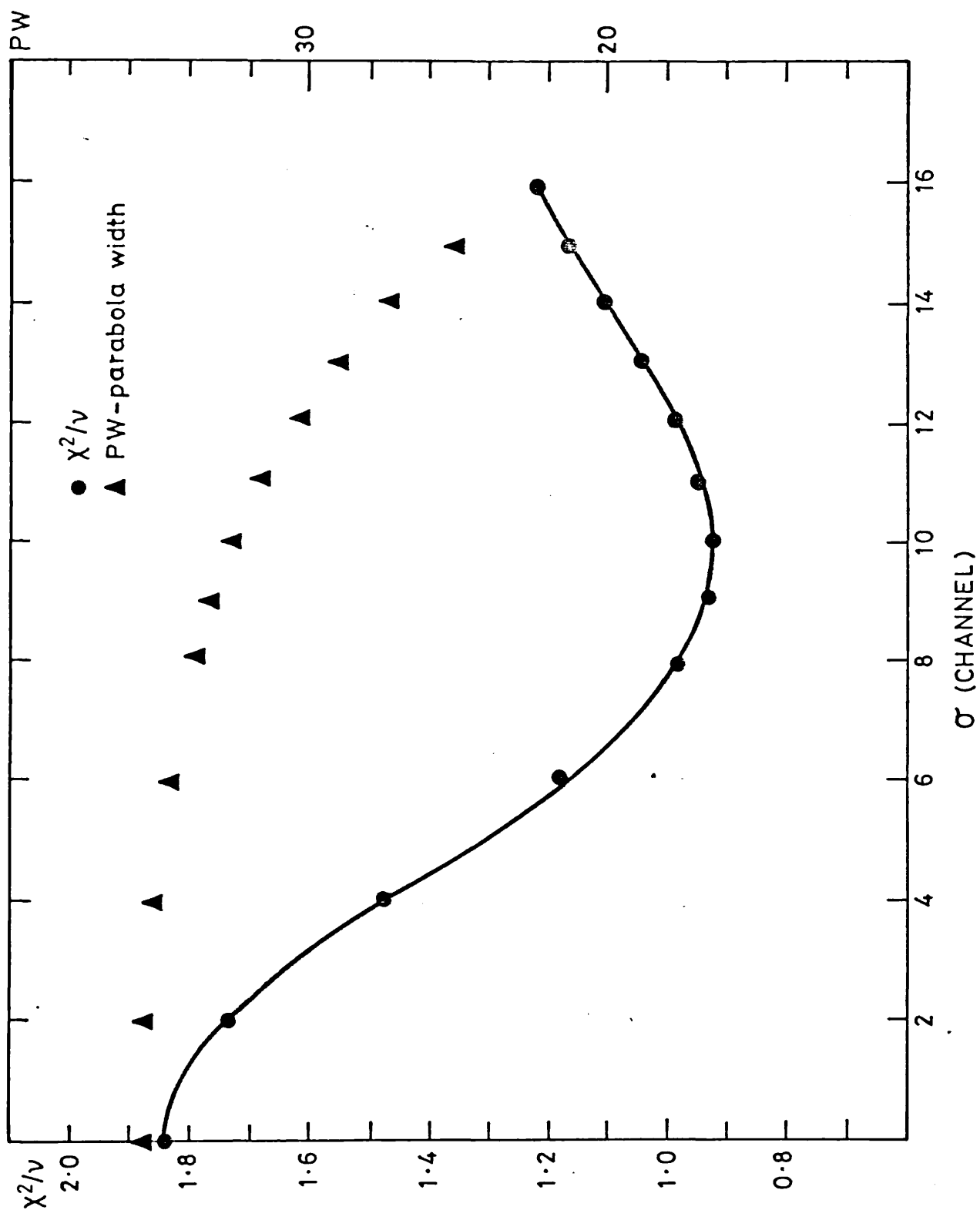
Figure 6.3.6   Variation of χ^2/ν as a Function of σ for Aluminium Subjected to 35% Deformation Strain
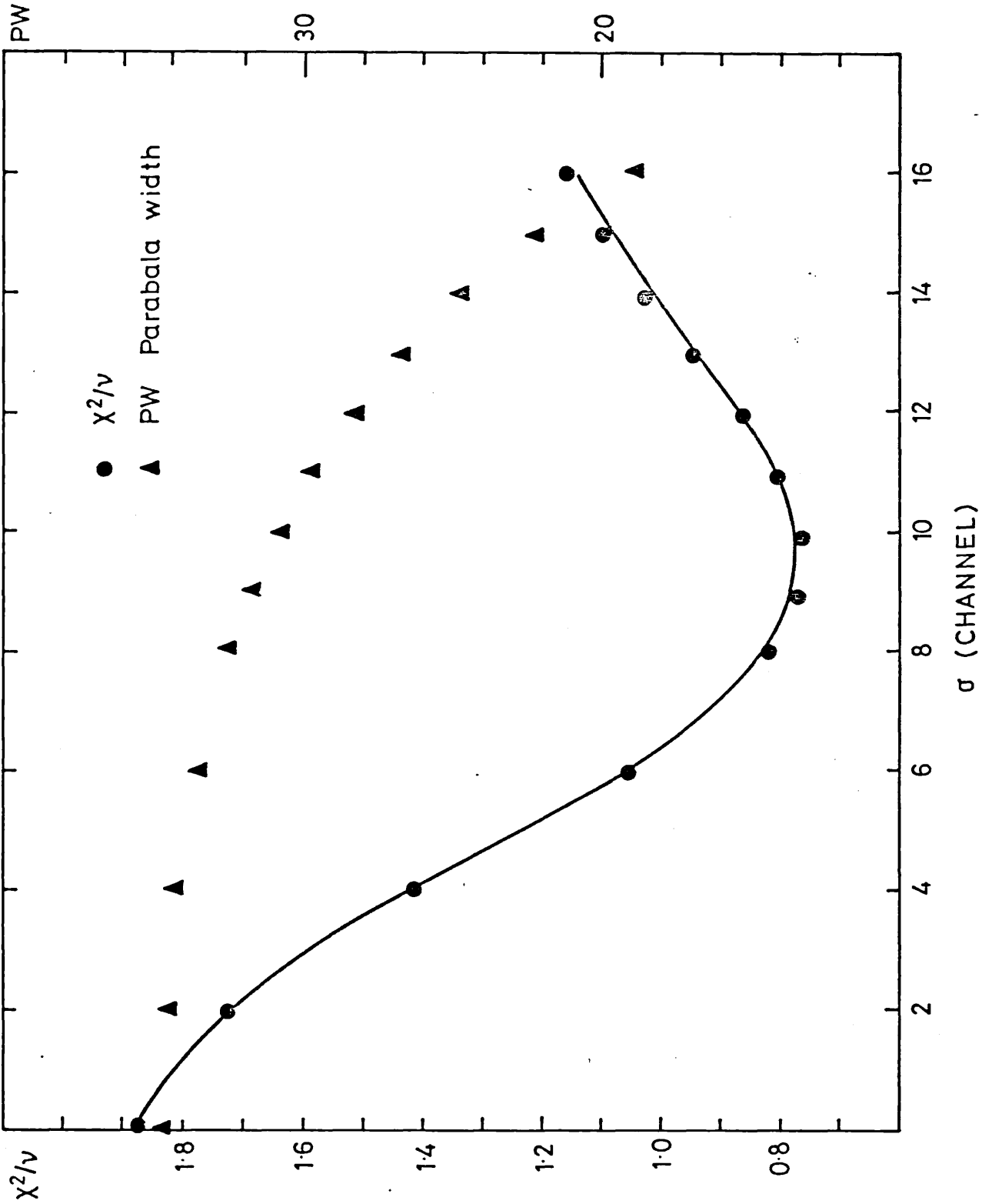
Figure 6.3.7   Variation of χ^2/ν as a Function of σ for Aluminium Heated to 647°C

Table 6.3.1   Characterisation of Vacancies and Defects in Deformed Al

Sample	Fermi Energy (eV) (66% confidence for error limits		Optimum σ	Positron Zero-Point Energy (eV) indicated below)	
Undeformed		13.56 + 0.05	-	-	
21% strain	11.45 < 12.61	< 13.21	6	0.69 < 2.13	< 5.19
28% strain	11.58 < 11.31	< 10.92	8	3.06 < 3.75	< 4.77
35% strain	8.92 < 10.40	< 11.31	10	3.57 < 5.87	< 8.73
647°C	8.12 < 9.34	< 10.66	10	3.39 < 5.87	< 8.19

(a)   the positron localisation (as indicated by σ) in deformed aluminium varies as a function of deformation strain

(b)   the localisation of positrons at defects in deformed aluminium at 35% strain is identical to the localisation for vacancy trapping (647°C)

(c)   Fermi energies for electrons encountered in the 35% strain sample appear to be higher than those found for electrons in the case of vacancy trapping (647°C).

If it is certain that saturation conditions exist (i.e. for practical purposes ∿90% trapping) in the strain range 20-35% then feature (a) is an important result. It implies that, if the trapping centres for positrons in deformed aluminium are dislocations, then increasing dislocation densities encourage more and more positron localisation at such defects. This would be explained by increasing concentrations of jogs and irregularities, found along the dislocation line, produced as a consequence of enhanced dislocation entanglement and interaction through the presence of higher dislocation populations - the positron would then preferentially trap at such points resulting

in more 'point-line' annihilation features.

However, due to the large errors associated with the data, the ΔS variation of figure 6.2.2 does not establish clearly whether saturation has been achieved by 20% strain. It can be argued that, since ΔS values found in the strain range 20-35% lie within about 2 standard deviations, saturation has been effectively achieved. However, because of the small changes seen in lineshapes due to deformation in aluminium, comparatively small changes in ΔS represent rather large variations in the percentage of trapped positrons. For instance, if one takes the saturated value ΔS, as defined by the best trapping-model fit in section 6.3.1.4, then the trapped percentage of positrons at 20% strain is evaluated as $\sim 73\%$. In other words, in the range 20-35% strain, $\sim 27\%$ more positrons have yet to be trapped. Hence, positron convolution at 21% and 28% strain would be performed incorrectly since partial trapping conditions exist - the positron component is now smearing both the broader (perfect) electron distribution and the narrower (defective) electron distribution. This would have the net effect of reducing the amount of positron smearing required, thus rendering the values of σ uncharacteristic of the 'true' localisation associated with the trap. Clearly, aluminium is a difficult metal to analyse unambiguously since statistical error is capable of swamping real, physical change.

Despite the statistical problems inherent in the strain range 20-35%, it would be difficult not to regard 35% strain as representative of effective saturation trapping conditions (the trapping-model fit indicates $\sim 92\%$ trapping). Hence, convolution analysis at 35% strain may be compared with the analysis for saturation trapping at vacancies. Features (b) and (c), referred to earlier in this section, are similar to those found for identical analysis on deformed copper (section 5.3.3.3) - i.e. the same positron zero-point energy (5.9 eV) is possessed by the positron for trapping in deformed aluminium and at vacancies (thus indicating a similar degree of localisation), and the electron Fermi velocities seen by positrons at vacancies are lower than those encountered at traps in deformed aluminium (thus indicating less +ve ionic charge/unit volume than for the traps in deformed aluminium). Accordingly, in a way similar to

that described in section 5.3.3.3, this section proposes that dislocations are responsible for positron trapping in deformed aluminium at room temperature, and that the positron is confined to a point along the dislocation line.

Regarding the authenticity of the values shown in table 6.3.1, it is seen that the Fermi energy derived for annealed aluminium (13.56 eV) is rather higher than that derived through the use of a 'parabola/Gaussian' fit to the data (12.5 eV), and, thus, even more removed from the value predicted by the free-electron model. This occurs because the parabola electron distribution superimposed on the Gaussian distribution (albeit extremely shallow) results in a small distortion of the overall 'true', physical shape from a perfect parabola. The minimisation routine compensates for this by generating a slightly broader 'fitted' parabola in order to simulate the 'true'. distribution and its overall width. Hence, the magnitude of the convoluting positron component σ at 35% strain may not be any different to the value that might have arisen from a successful 'parabola/Gaussian' fit.

Finally, consider the variation of x^2/ν as a function of σ for the annealed, undeformed aluminium sample in figure 6.3.8. This sample was annealed at a temperature of 550°C for 4 hours. It is seen that a definite minimum in the curve occurs at $\sigma = 4$. The average kinetic energy of the positron may be derived from the relation $E = 2\sigma^2/m_0c^2$. Using this expression it is seen that a free positron with thermal energy kT (= 0.013 eV) associated with one Cartesian direction would give rise to a positron momentum distribution of width $\sigma = 1.2$ channel. The observed minimum ($\sigma = 4$) gives rise to a mean kinetic energy of 0.16 eV (an order of magnitude higher than positron thermal energies). Thus, it appears that thermal effects do not provide an explanatin of the observed minimum and a degree of positron localisation at trapping sites is, therefore, indicated.

Smedskjaer et al (1980a) proposed a trapping mechanism for positrons at dislocations. They assumed low positron-dislocation binding energies ($\leqslant 0.1$ eV), and proposed that the positron is initially trapped at a dislocation only to make a further transition
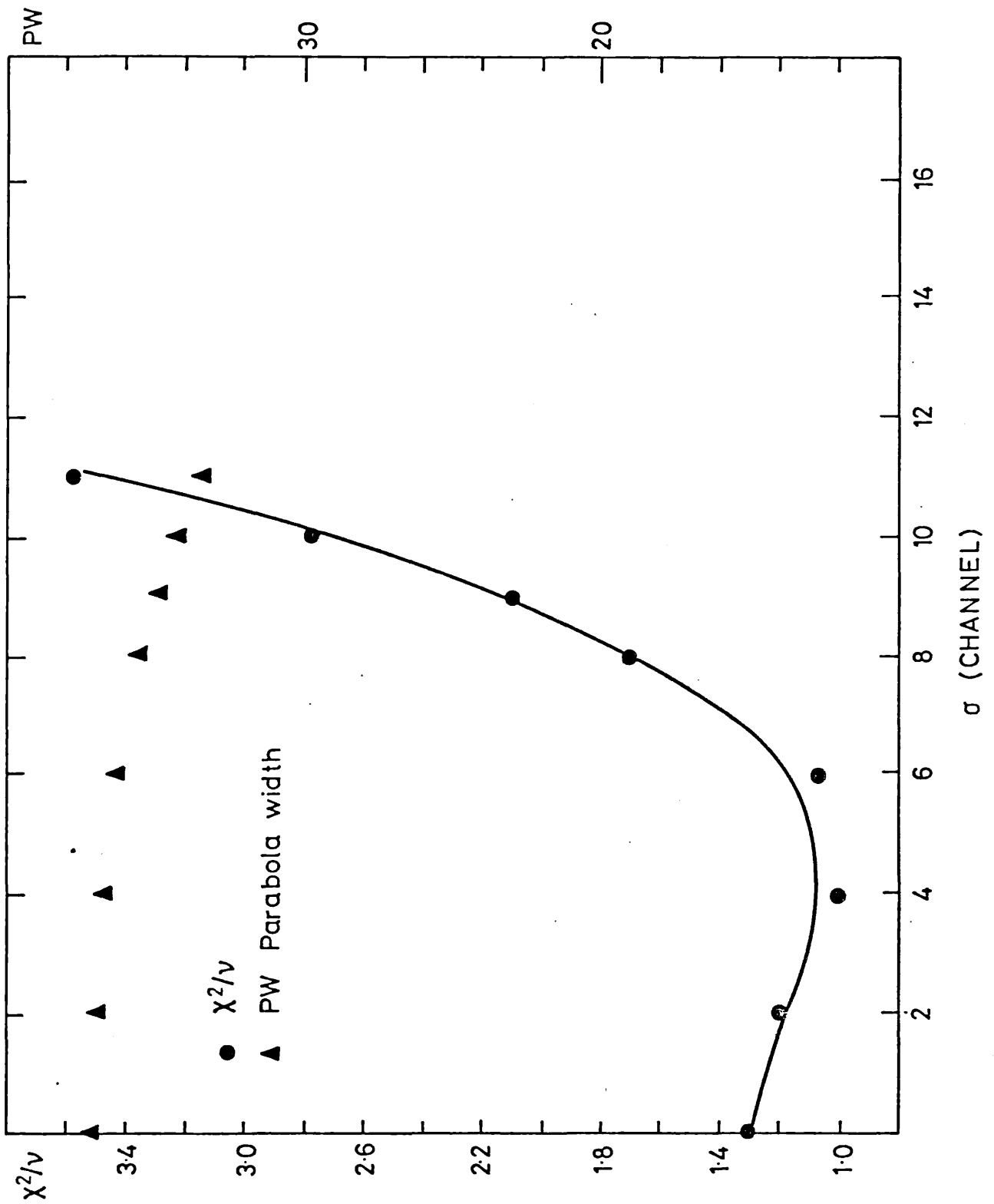
Figure 6.3.8   Variation of χ^2/ν as a Function of σ for Undeformed, Annealed Aluminium

to deeper 'point-defect like' traps (of binding energy a few eV) associated with the dislocation - this would then conform to the observations of experiment where vacancy-like features of positron annihilation are recorded in deformed metals. From such a model, they evaluated the mean lifetime of positrons $\bar{\tau}(t)$ in annealed aluminium (dislocation density 10^8 cm^{-2}) as a function of temperature T. They found that, depending on the values of the dislocation-positron binding energy, E_b, and the transition rate, η, from the initial dislocation trap to the associated point-defect trap (dependent on concentration of point-like defects associated with the dislocation) chosen in the model, various profiles $\bar{\tau}(T)$ in the range 0-300K were generated similar to those found experimentally in the pre-vacancy region for various metals (e.g. Rice-Evans et al 1978, Herlach et al 1977, Smedskjaer et al 1980b). In addition, they found that for some values of E_b and η, the calculated mean lifetime at room temperature was slightly higher (~ 2 ps) than that evaluated on the basis of 'perfect annihilation' (thermal expansion effects considered only). In other words, partial trapping in annealed aluminium at room temperature might be possible under certain circumstances (e.g. high η). Our results certainly support this, and show how sensitive the 'convolution technique' is to small departures from the mode of 'perfect' annihilation. MacKenzie et al (1970) also found that 25% of positrons are likely to be trapped in an undeformed, annealed, commercial aluminium alloy (6061). However, the extrinsic defects might have been responsible for most of this trapping. The implications of such findings are that it cannot be assumed that absolutely no trapping occurs in well-annealed samples.

6.3.1.4 Work-Hardening in Deformed Aluminium

Figures 6.3.9(a)-(b) show the variation in RID defect-specific parameters as a function of deformation strain. No significant shape changes are indicated, thus suggesting the presence of only one type of trap - presumed to be point-like traps at dislocations following the analysis of preceding sections. In an attempt to assess the stress - strain relationship for deformed aluminium, the data of figure 6.2.2 were fitted to the two-state trapping model with the use of equation 5.3.7 (chapter 5). As outlined in chapter 5, a fit of this equation
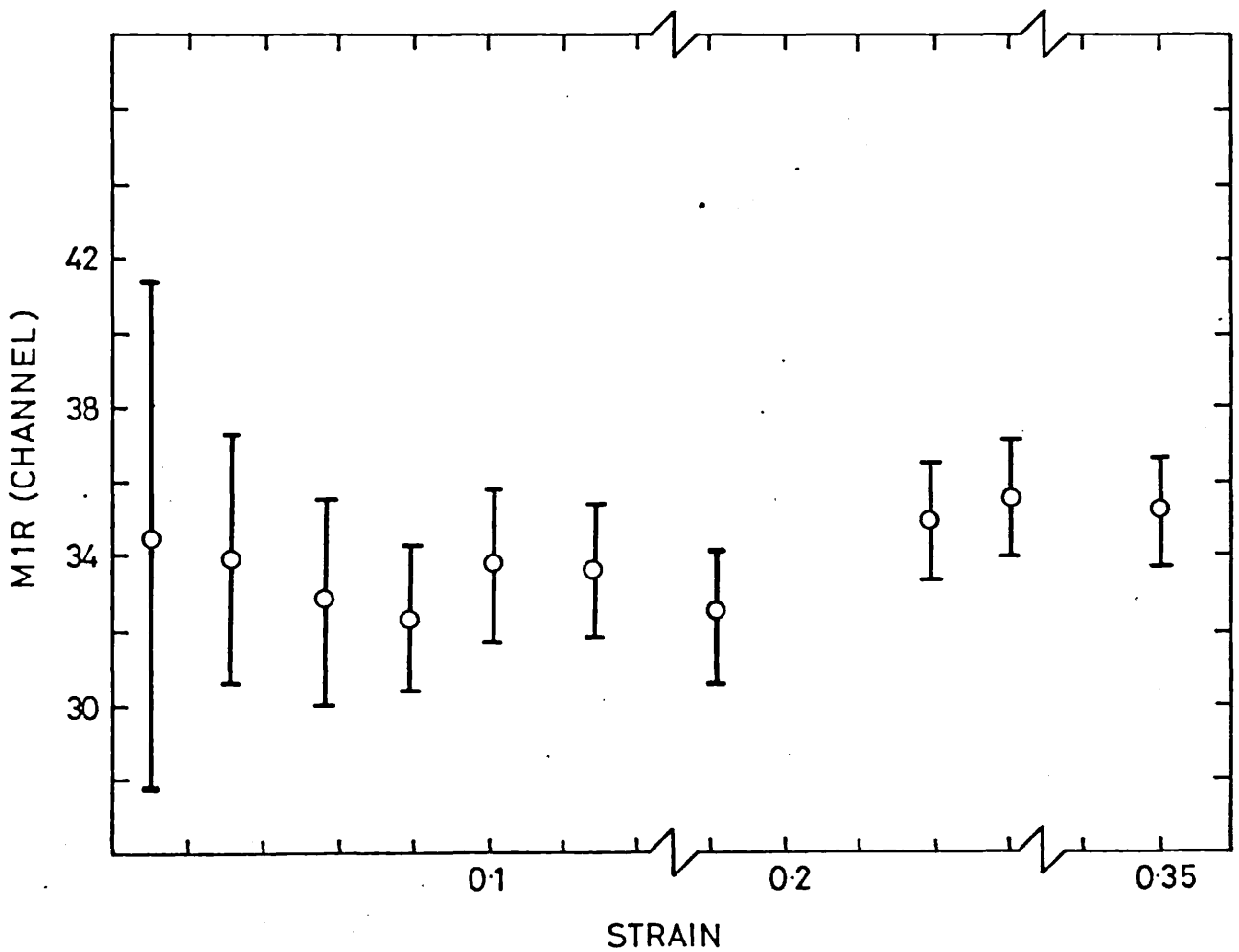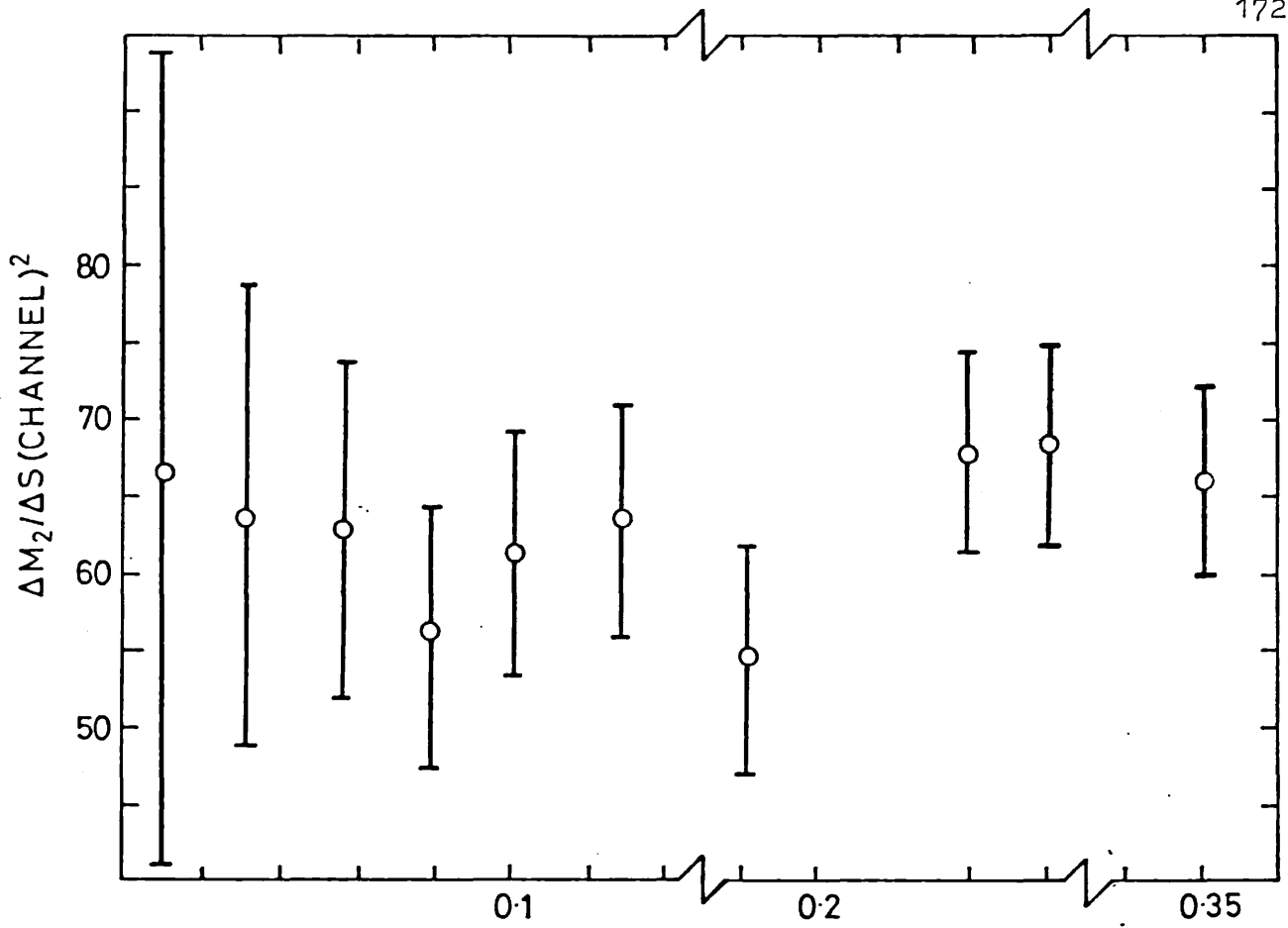
Figure 6.3.9.(a)   Variation of $\Delta M_2/\Delta S$ and M1R for Aluminium as a Function of Deformation Strain
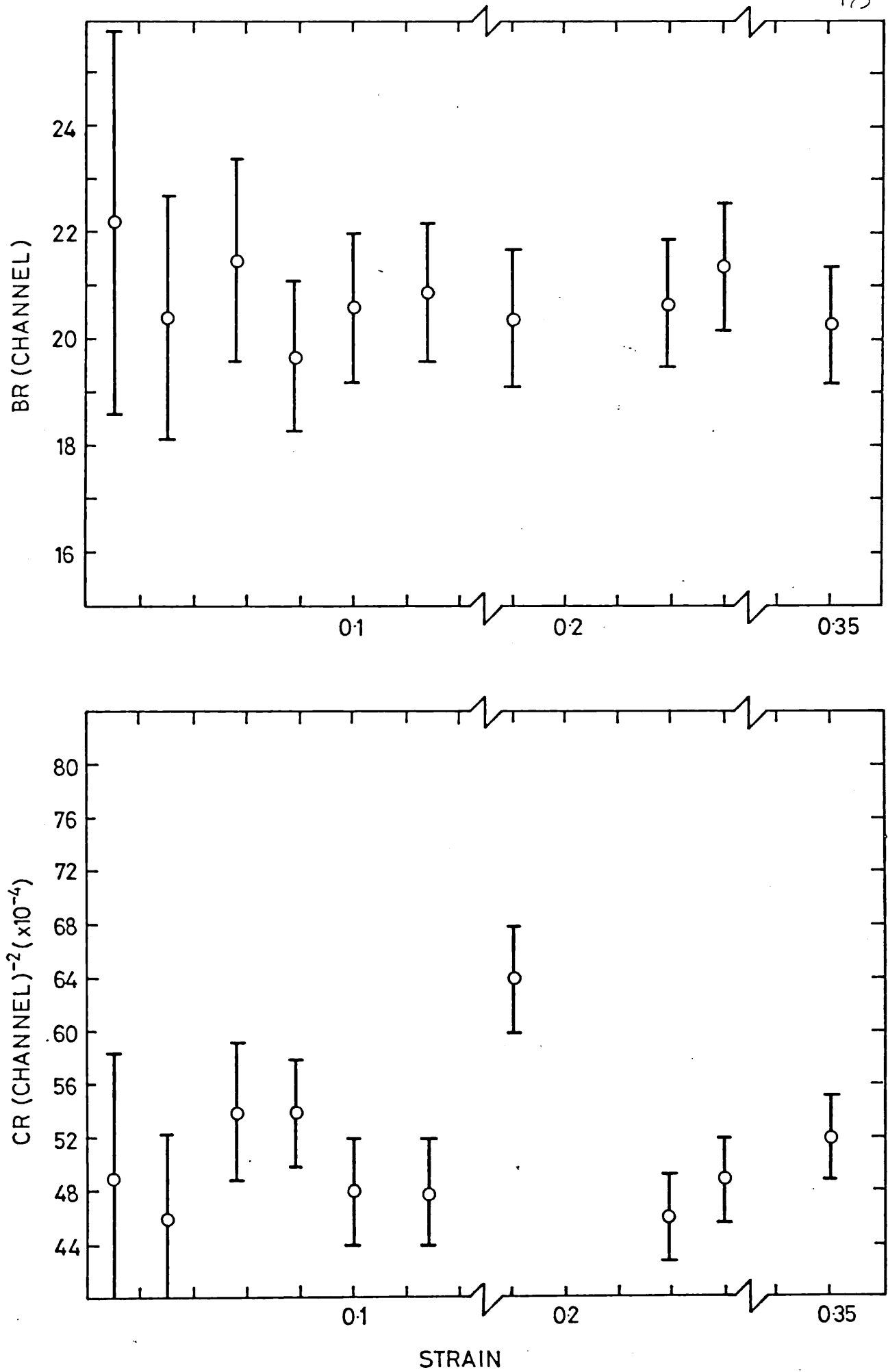
Figure 6.3.9.(b)   Variation of BR and CR for Aluminium as a Function of Deformation Strain

predicts the mode of work-hardening (i.e. linear or parabolic) and is defined by the value of the integer n. However, a guess for ΔS_d must first be supplied, and the scattered data of figure 6.2.2 do not provide an obvious value. Hence, a series of guesses were tried as indicated in table 6.3.2

Table 6 3 2   Predicting the Nature of Work-Hardening in Deformed Aluminium   .

Range of fit	Guess for ΔS_d	Fitted n
0-35% strain	0.013	0.97
"	0.0125	1.08
"	0.01225	1.18
0-28% strain	0.01208	1.04
"	0.0115	1.20

Two fit ranges (0-35% and 0-28%) were chosen in order to assess the effect of varying ΔS_d from 0.013 to 0.0115, such a ΔS_d variation considered to embrance a fair range of saturation limits in view of the errors in the data. Table 6.3.3 shows rather convincingly that a parabolic rather than a linear hardening regime is favoured since n ~ 1. Accordingly, equation 5.3.6 (with n = 1) was fitted to the data as shown in figure 6.2.2. This fit yields ΔS_d = 0.0131, and so would imply that $\sim 92\%$ of the positrons are trapped at 25% strain. Owing to a lack of knowledge of the dislocation density as a function of strain a trapping rate was not derived from the fit. In any case, because of the scatter in the data, the usefulness of such a result would be greatly diminished in view of the imprecision that would be associated with it.

6.3.2 The Nature of Defects in an Aluminium Alloy

Figure 6.2.3 shows the variation in S as a function of strain for a commercial aluminium alloy (2¼% Mg) in solid solution (i.e. the alloying agents exist on host lattice sites throught he process of direct substitution). It is seen that the value for S for an annealed alloy sample is comparable with that for the annealed state in pure aluminium. Hence, S measurement on the 'as-received', undeformed alloy shows that quite a sizeable fraction of positrons are trapped at defects. It is clear from the alloy S-parameter variation that saturation trapping conditions are approached by 20% strain. In fact, if a guess of 0.579 is made for the saturated value of. S, then, the trapped fraction of positrons annihilating in the 'as-received' undeformed sample may be estimated as ∿ 64%. This, of course, is not surprising because the 'as-received' sample has been deliberately work-hardened (in this case to a quarter of its total hardness) and so contains a population of dislocations and other defects associated with the impurity.

The most striking feature of figure 6.2.3 is the markedly higher value of S associated with the deformed alloyed metal. Clearly, since 20% strain is in the saturation region, such a finding indicates that a significantly different trapping site is operative in the deformed alloy - i.e. a trapping centre different in character to the dislocations found in the pure, deformed metal. Evidence for positron trapping at sites associated with alloying impurities is found in the literature. For instance, Wilkenfeld and John (1976) studied the lifetime of positrons in an aluminium structural alloy (Al-clad 7075 - T6). This alloy was 'precipitation-hardened'. They estimated that ∿ 80% of positrons became trapped in their 'as-received' undeformed sample of which only ∿ 25% of those were trapping at dislocations - the remainder annihilating at trap sites associated with precipitates.

Johnson et al.(1977) showed that positrons were sensitive to the process of aging (i.e. the growth of alloying precipitates occurring at a speicfied temperature as a function of time), and increases in the positron shape-parameter could be attributed to the increasing 'hardeness' of the alloy.

However, our alloy exists in solid-solution rather than as a distribution of precipitates. The following trapping centres may be effective:

(i)   single Mg ions

(ii) Mg ions situated at a point along a dislocation

(iii) Mg-vacancy or Mg-vacancy cluster complexes.

Possibility (i) exists because a Mg ion possesses +ve charge +2 as opposed to +3 for the aluminium ion. Thus, positrons might be attracted to these areas. In fact, Dupasquier et al (1980) showed that for a silute Al-Mg alloy (at 100 ppm and 1000 ppm) the substitutional Mg impurities were responsible for positron trapping. Trapping was found to increase with increased impurity content. However, such a possibility may be discounted here because of the similarity in the S-values depicting the annealed states of the alloy and the pure metal. In the annealed state the only defect sites are 'extrinsic' (i.e. impurities), and if these were strong trapping centres significant changes in S would be expected. The similarity suggests that, even if the Mg centres are capable of some degree of trapping, they are extremely weak traps and that the associated positron wavefunctions are essentially 'nearly-free' to sample the perfect lattice. Possibility (ii) seems improbable since point or extended trapping along the dislocation line would not be encouraged by the presence of extra +ve charge. However, the presence of Mg impurities might be capable of trapping vacancies and/or vacancy clusters produced by cold-rolling, and that the Mg-vacancy/Mg-cluster interaction is sufficiently strong to prevent migration of vacancies/clusters at room temperature. Dlubek et al (1980) performed measurements on the alloy Al-Mg (3 at.%) and concluded that positrons were trapped at Mg-vacancy pairs after quenching the alloy from 450°C to room temperature. Our ΔS-value for thermal vacancies in aluminium (0.024) is significantly lower than that for the alloy at 20% strain (ΔS = 0.031) - in fact the true ΔS-value for vacancies will be lower than 0.024 because of the temperature contribution to the measured value. Hence, it appears that clusters trapped at Mg sites may be the defects responsible for positron

trapping. Figure 6.2.3 shows that the alloy S-value increases as a function of strain and this could then be explained in terms of more vacancies (produced by deformation) becoming trapped at the available Mg sites, either going to those sites at which no vacancies exist, or to those which contain vacancy clusters and, thus, increasing their size.

Section 6.3.1 indicates that vacancies and vacancy clusters do not exist in aluminium deformed at room temperature. However, there is evidence of a vacancy cluster population in the deformed alloy. The implication of such a finding is that the presence of impurities in mechanically damaged metals is likely to affect the mechanics of point defect annealing and to alter the complexion of defect populations existing in the deformed state.

6.3.3 Conclusions

This chapter finds no evidence of a presence of vacancies or vacancy clusters in mechanically deformed aluminium at room. temperature. The defects responsible for positron trapping in the deformed state have been identified as dislocations via the use of 'model-dependent' analysis. The positron zero-point energy evaluated at dislocation traps (5.87 eV) has been found to be identical to that. for trapping at vacancy sites. This similarity in positron localisation implies that positrons are trapped at a point along the dislocation line. Also, dislocations and vacancies have been characterised through definition of their local electron momentum distributions, the latter giving rise to lower Fermi energies. · However, the nature of positron annihilation in deformed aluminium alloy is found to be dramatically different to that in the pure, deformed state, and the evidence suggests that vacancy clusters might be the predominant trapping sites. A trapping-model fit to deformed minimum data reveals a parabolic stress-strain relationship.

CHAPTER 7 : DEFECTS IN MECHANICALLY DEFORMED Ti Fe AND Ni

7.1 INTRODUCTION

This chapter seeks to assess the nature of the defect-types encountered in the mechanically deformed state for the metals Ti, Fe and Ni through the use of the model-dependent and -independent methods. The analysis performed on Cu and Al (chapters 5 and 6) compared annihilation characteristics derived from positrons trapped at defects in the deformed state to those derived from tapping at thermal vacancies in order to assess the nature of defects in the former. Unfortunately, it was not possible to perform similar analysis on Ti, Fe and Ni because of their higher melting points (beyond the maximum working temperature of our furnace) and, also, because of the problems encountered with 'hot' positron sources (section 3.4.3). Hence, analysis has been confined to mechanically deformed samples at room temperature and of subsequent isochronal annealing in the temperature range 25-400°C.

To search for point defect recovery in the above-mentioned temperature range, isochronal anneals performed on Ti and Fe were analysed with the use of RID defect-specific parameters. Due to lack of time, however, it was not possible to perform a further isochronal anneal on deformed Ni.

For all metals measurements were taken as a function of deformation, and those measurements giving rise to saturation trapping conditions were used for model-dependent analysis in order to assess the nature of the defect traps through evaluation of the zero-point energy. To assess the relationship between point defect concentration and dislocation density for each metal as a function of strain and, where possible, the nature of the stress-strain, work-hardening relationship assessed by fiting the 'trapping-model' to the observed data. Details of experimentation follow below.

7.2 EXPERIMENTATION AND RESULTS

7.2.1 Generation of Mechanical Damage in Ti, Fe and Ni

Nickel and iron polycrystalline slabs of 5N purity (Johnson matthey and Company) and dimensions 40 mm x 7 mm x 2 mm were cold-rolled to a series of deformation strains. Prior to rolling, all samples were suitably annealed - 12 hours at 900°C (nickel) and 8 hours at 850°C (iron). In addition, polycrystalline titanium slabs of 3N purity (Koch-Light) and dimensions 40 mm x 7 mm x 1.25 mm were cold-rolled to varying degrees of strain. Before rolling, annealing was performed at 700°C for 4 hours. All samples were lightly etched before commencing measurements.

Measurements were performed using the 'remote-source' geometry approach, collecting about 2×10^6 counts in the annihilation lineshapes for nickel and iron ($\sim 3 \times 10^6$ counts for titanium). Figure 7.2.1 shows the S-variation as a function of deformation strain for titanium. Figures 7.2.2 and 7.2.3. show the variation in ΔS as a function of strain for iron and nickel samples respectively.

7.2.2 Isochronal Annealing of Mechanically Deformed Ti and Fe

After suitable annealing and etching treatments, two Na^{22} sandwiches (~ 80 μCi) were prepared for experimentation for each of the metals titanium and iron. The dimensions of each slab constituting the sandwiches were identical to those in section 7.2.1. The first sandwich for each metal was kept in the annealed, undeformed state and used for the 'reference'measurements because complete recovery of the deformed sandwiches would not be attained by limiting temperature (i.e. 400°C) of the experiment and, hence, unable to represent the recovered state. The deformed Ti and Fe sandwiches were cold-rolled to strains of 30% and 10% respectively. The sandwiches were then placed in the furnace and measurements taken, each lineshape consisting of ~ 1.25 x 10^6 counts. Figures 7.2.4. and 7.2.5 show the variation in the S parameter as a function of annealing temperature for titanium and iron respectively.
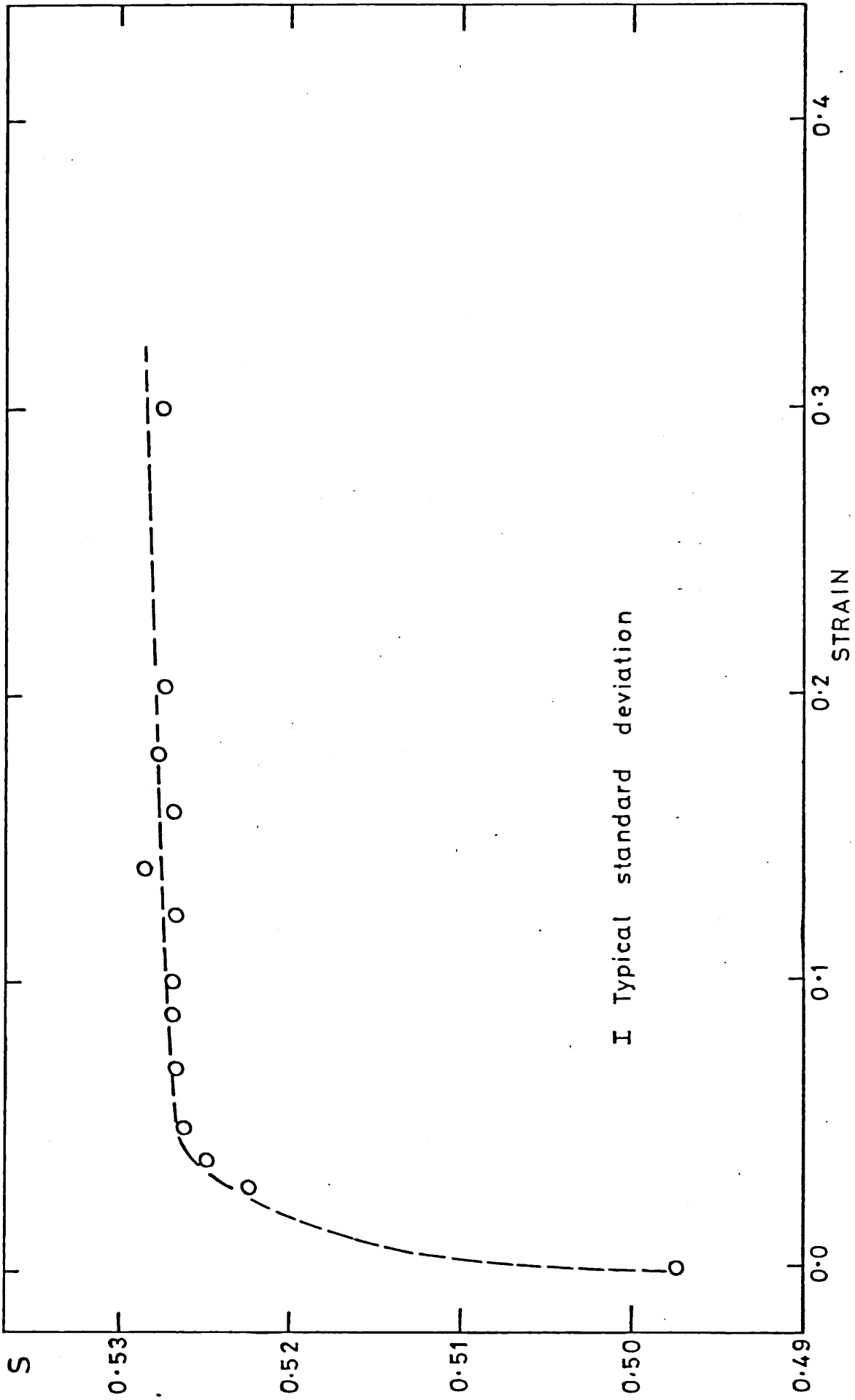
Figure 7.2.1   Variation of S as a Function of Deformation Strain for Titanium
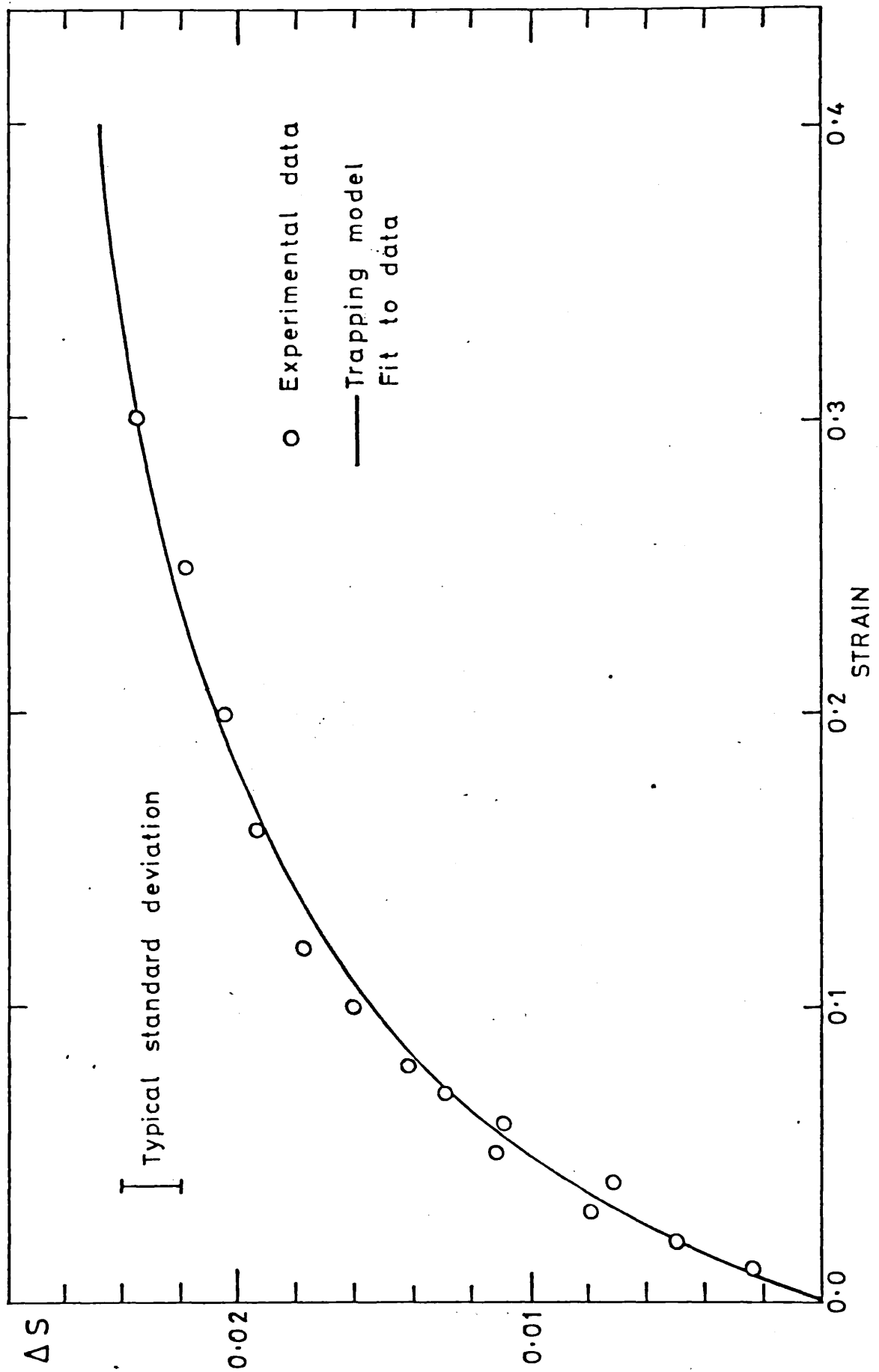
Figure 7.2.2   Variation of ΔS as a Function of Deformation Strain for Iron
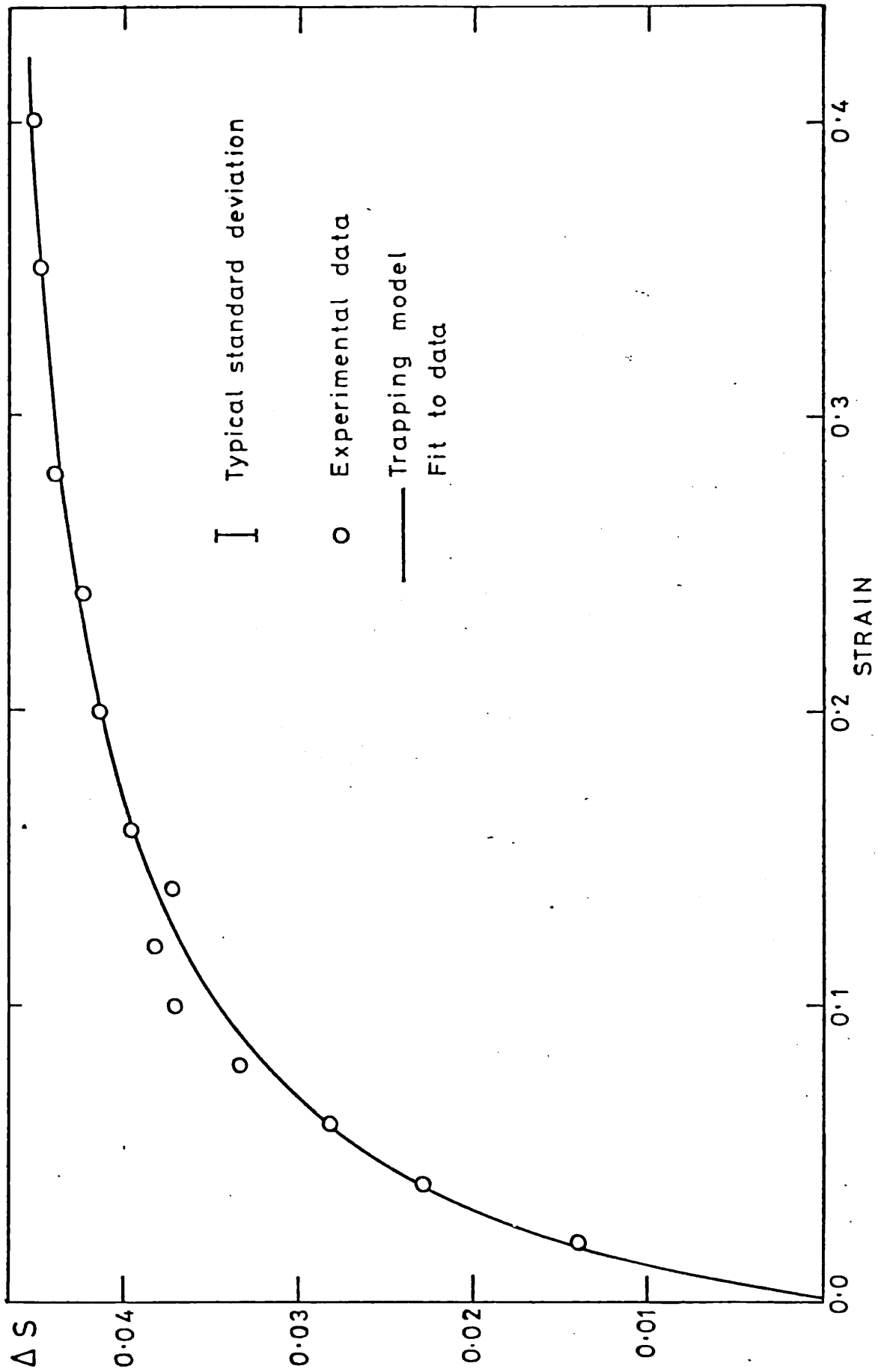
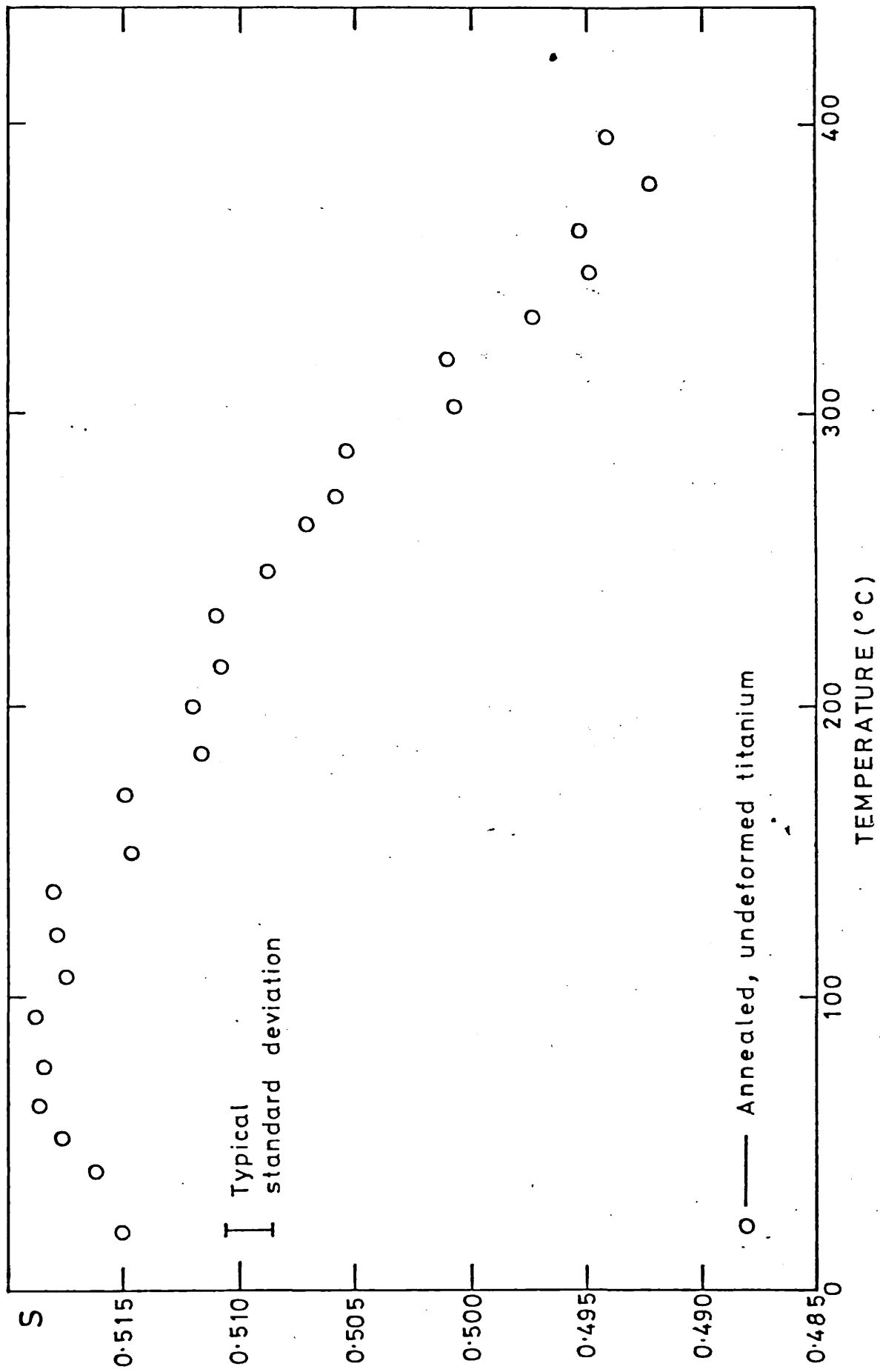Figure 7.2.3　Variation of ΔS as a Function of Deformation Strain for Nickel

Figure 7.2.4   Isochronal Annealing of Titanium Subjected to 30% Deformation
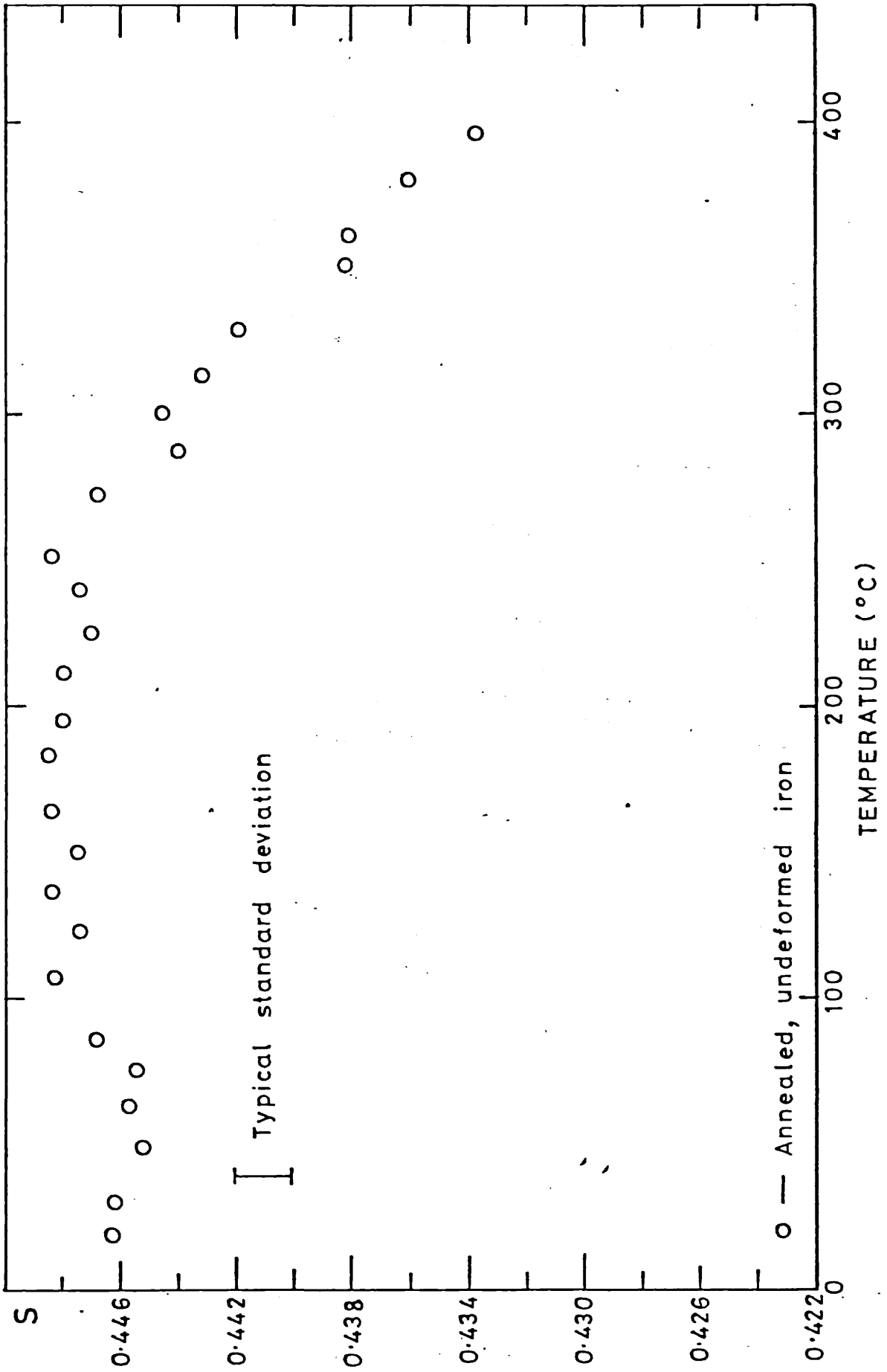Strain

Figure 7.2.5   Isochronal Annealing of Iron Subjected to 10% Deformation
Strain

7.3 DEFECTS IN MECHANICALLY DEFORMED TITANIUM

This section attempts to assess the defect-types present in deformed titanium. In particular, the presence of vacancies in the deformed state capable of trapping positrons is discussed in the light of other evidence suggesting that vacancies may not be effective traps. For instance, Hood et al (1976) performed experiments on annealed Ti by measuring the lineshape parameter L (equivalent to S) as a function of temperature T. They found no evidence of the usual 'S' variation in the L-T profile which is normally attributed to vacancy trapping and, instead, found two linear regions of differing slopes corresponding to the α and β phases of Ti. They concluded that vacancies did not trap positrons. However, in a later paper Hood et al (1979) discuss positron measurements on an electron-irradiated Ti sample and conclude that vacancies are capable of trapping positrons.

The next section seeks to determine whether positrons sense the presence of vacancies in deformed Ti and, hence, to establish the existence of an effective positron-vacancy interaction.

7.3.1 Isochronal Annealing of Mechanically Deformed Ti

Figure 7.2.4 shows the variation in S as a function of annealing temperature, and figures 7.3.1(a)-(b) show the corresponding variations in RID defect-specific parameters. The S-variation shows a gradual return to the annealed state from 100°C onwards. However, in the range 20-100°C a significant increase in the S value occurs. In principle, increases in S may be due to:

  (i) an increase in defect population,

  (ii) a change in the nature of the available trapping sites,

  (iii) a temperature effect.

  Possibility (i) may be ruled out since, in general, the effect of heating the lattice will motivate a return to thermodynamic equilibrium and, hence, decrease the defect population. Possibility (iii) may be

rejected on the basis of experimental results obtained by Hood et al (1976). As has been discussed earlier, they analysed the Doppler lineshape in annealed Ti as a function of temperature. In the range 20-100°C they found a change in the lineshape parameter of $\sim$ 0.1% and this was not attributable to the effects of any defect trap - a purely thermal effect. Our results show $\sim$0.8% change in the lineshape parameter in the same temperature region and, thus, cannot be explained through temperature effects alone. hence, possibilty (ii) provides the most likely explanation.

Possibility (ii) would be most likely explained by the coalescion of single vacancies into clusters followed by cluster annealing at $\sim$100°C leaving dislocations to be the only traps available from 100°C onwards. To support such an explanation, one would expect to see corresponding significant changes in the values of the RID parameters in figures 7.3.1(a)-(b). Bearing in mind that the indicated error bars have an extra 25% uncertainty associated with them (section 4.2.4) none of the RID parameters offer significant variations (greater than statistical error) in the range 20-100°C. It is seen that changes in $\Delta M_2/\Delta S$ and M1R (within statistical error) are less pronounced than those for BR and this probably reflects the greater insensitivity associated with the former two due to the reasons discussed in section 5.3.2.2.

RID curve behaviour does not provide absolute proof of changes in defect regime in the temperature range 20-100°C. Nonetheless, indications of change are seen and should not be ignored. It is seen in the case of BR that a definite move towards higher values occurs in the range 20-50°C, followed by a drop in value at $\sim$75°C and finally maintaining an average value in the range 100-250°C that is slightly lower than that associated with 20°C. This might be consistent with vacancies at $\sim$20°C coalescing into clusters at $\sim$50°C, followed by cluster annealing at $\sim$75°C. Similar but less pronounced behaviour is seen in $\Delta M_2/\Delta S$. However, it is difficult to see any clear cut variations in M1R.

Since the S-parameter has much greater statistical accuracy associated with it and definite, significant changes in S are revealed,
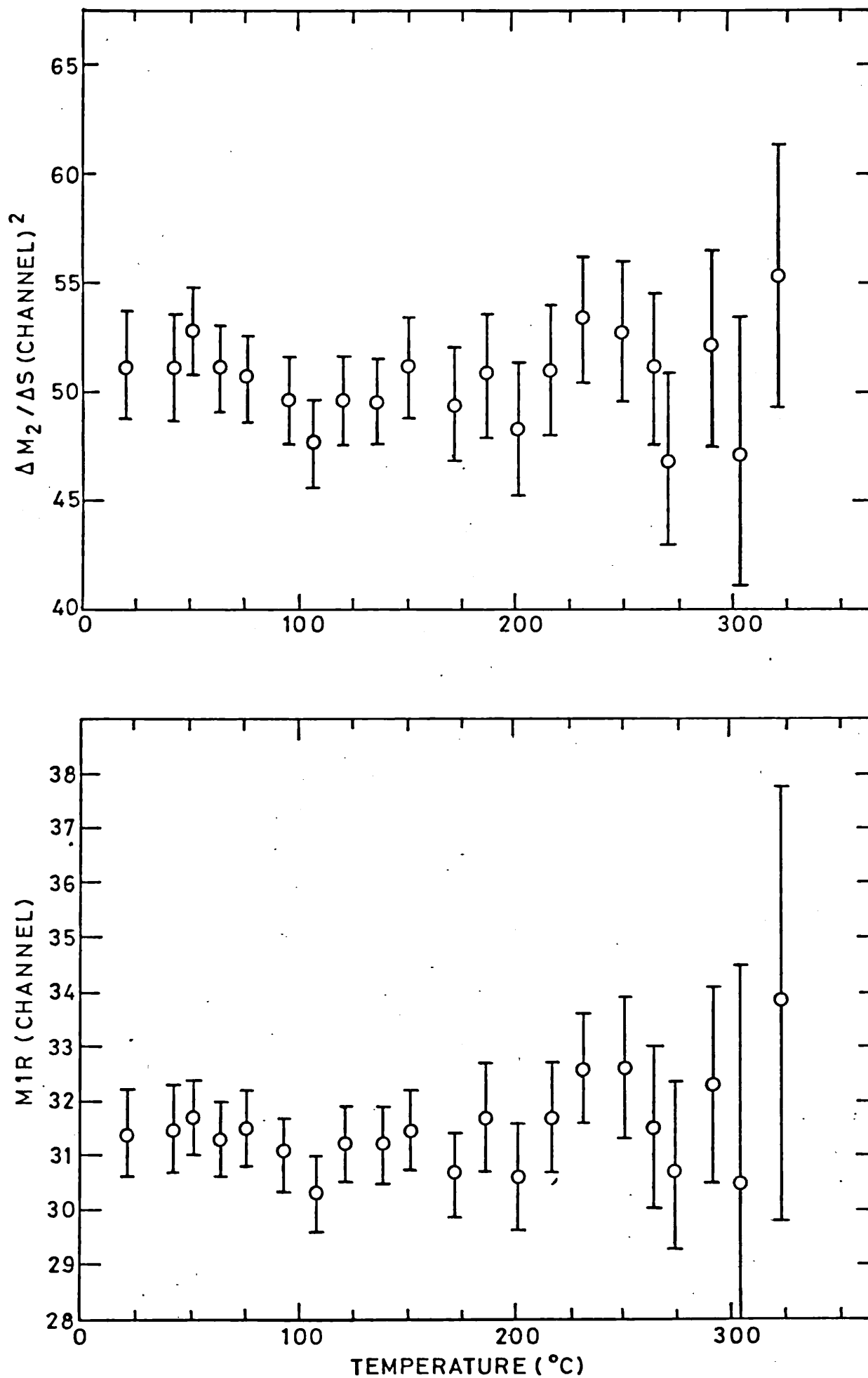
Figure 7.3.1.(a)   Variation of $\Delta M_2/\Delta S$ and M1R as a Function of Annealing Temperature for Titanium Initially Subjected to 30% Deformation Strain
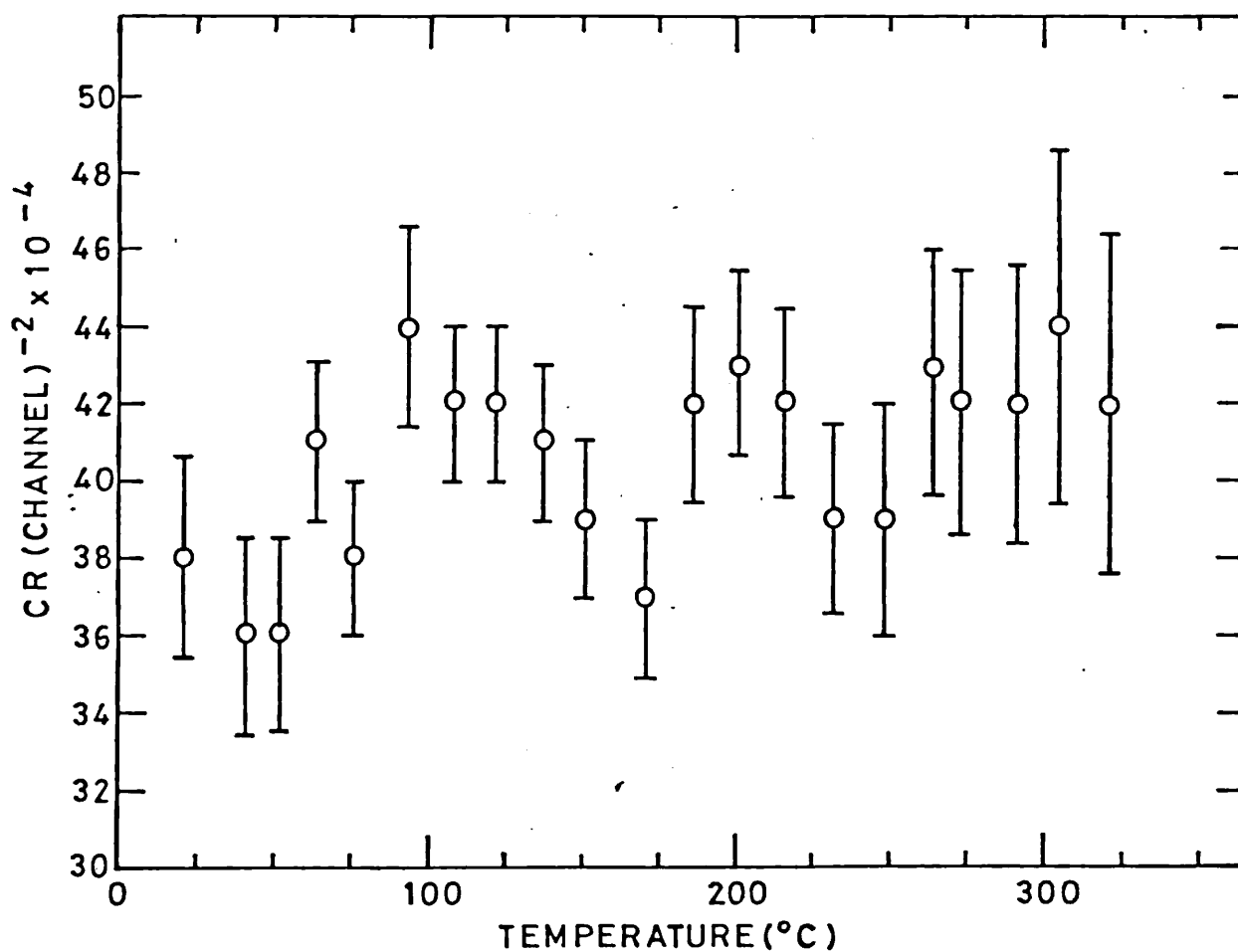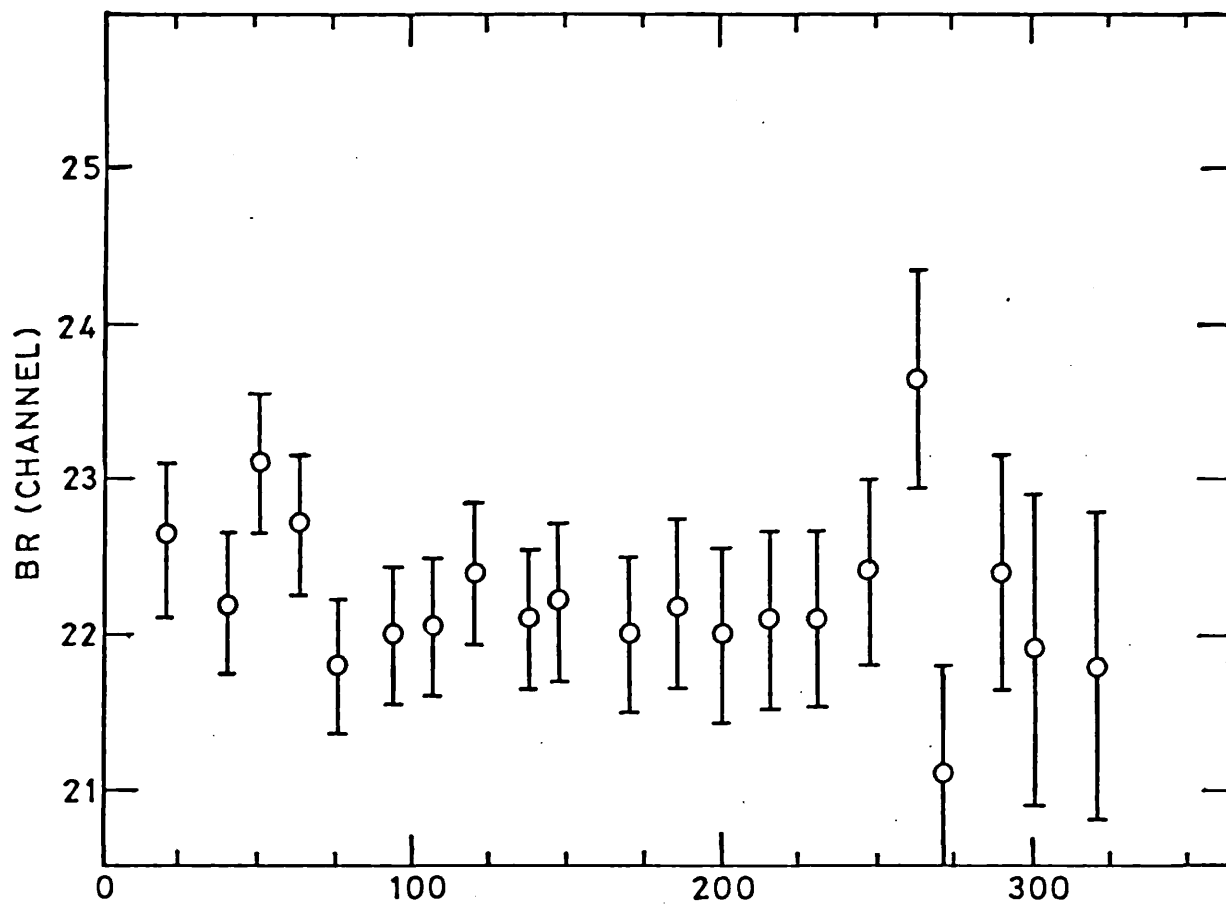
Figure 7.3.1.(b)   Variation of BR and CR as a Function of Annealing Temperature
                    for Titanium Initially Subjected to 30% Deformation Strain

this section concludes that some degree of clustering occurs in the region 20-100°C and proposes the presence of vacancies in the deformed state. Accordingly, evidence is provided of an effective positron-vacancy interaction.

7.3.2 Positron Response as a Function of Deformation Strain

The RID parameters in figures 7.3.2(a)-(b) corresponding to the S-variation shown in figure 7.2.1 remain constant throughout the indicated strain rnage. Since section 7.3.1 provides evidence of a presence of vacancies in deformed titanium, the possible trapping sites for positrons are vacancies and dislocations. If the assumption is made that both defect-types are trapping positrons the constancy of RID curve behaviour would imply a constant vacancy-dislocation concentration ratio as a function of strain. This, of course, would imply that the vacancy population is due to, and proportional to, the dislocation density and that the mechanism of vacancy generation remains the same over the entire strain range.

The most interesting feature of the S-variation in figure 7.2.1 is that saturation trapping is achieved by 5% strain. Similar behaviour has been reported by Coleman et al (1979) for a titanium alloy. Experience in most other metals indicates that saturation trapping does not occur until strains in the region of 30%. using equation 2.5.7 for j types of trap, the rate at which saturation is approached will depend on the factor $\tau_f \Sigma_j u_j C_j$. Clearly, early saturation would be encouraged by rather high values of the free lifetime, trapping rates and defect concentrations. Hood et al (1979) evaluated a lifetime of $\sim$ 150 ps in annealed titanium. Much higher lifetimes in the region of 300-400 ps have been reported for alkali metals (Manninen et al, 1975). However, Metals such as Cu, Al and Ni (for which saturation occurs at strains later than 5%) give free positron lifetimes in the range 120-170 ps and, hence, comparable with the value reported by Hood et al for titanium. It is difficult, therefore, to ascribe the lifetime as the cause of early saturation.

Hood et al (1979) suggested that the reason why thermal vacancies are not sensed by heating up Ti to its melting point is because their
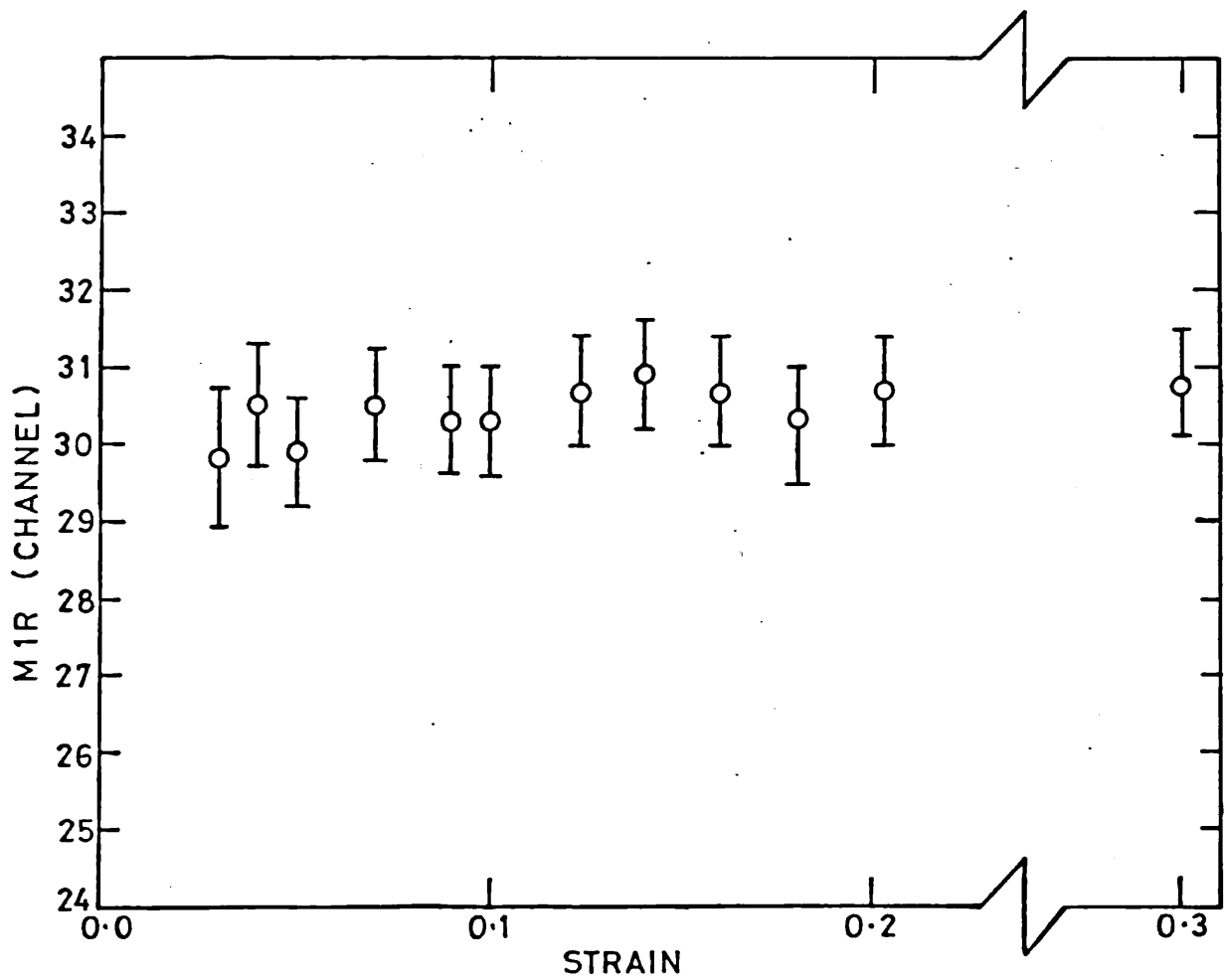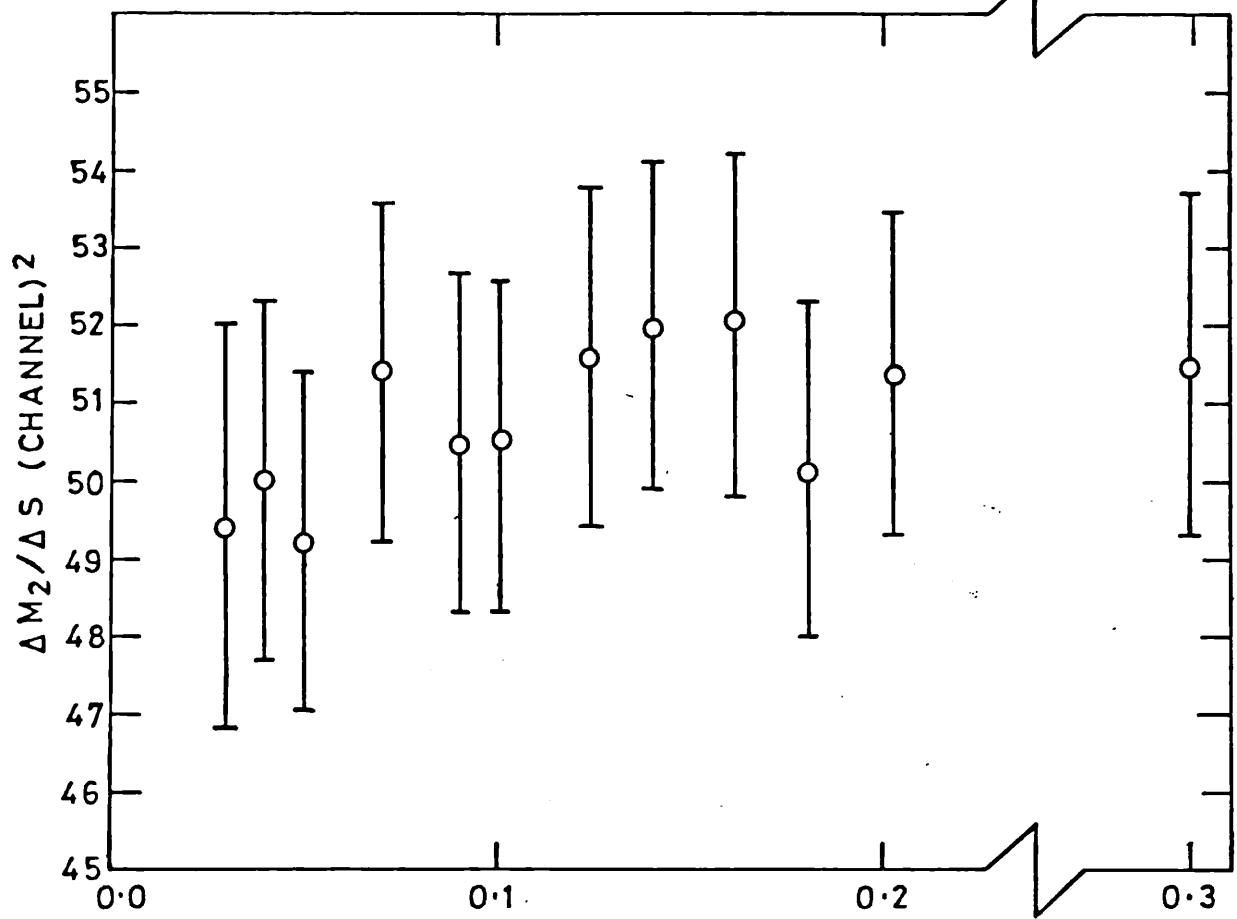
Figure 7.3.2.(a)   Variation of $\Delta M_2/\Delta S$ and M1R for Titanium as a Function of Deformation Strain
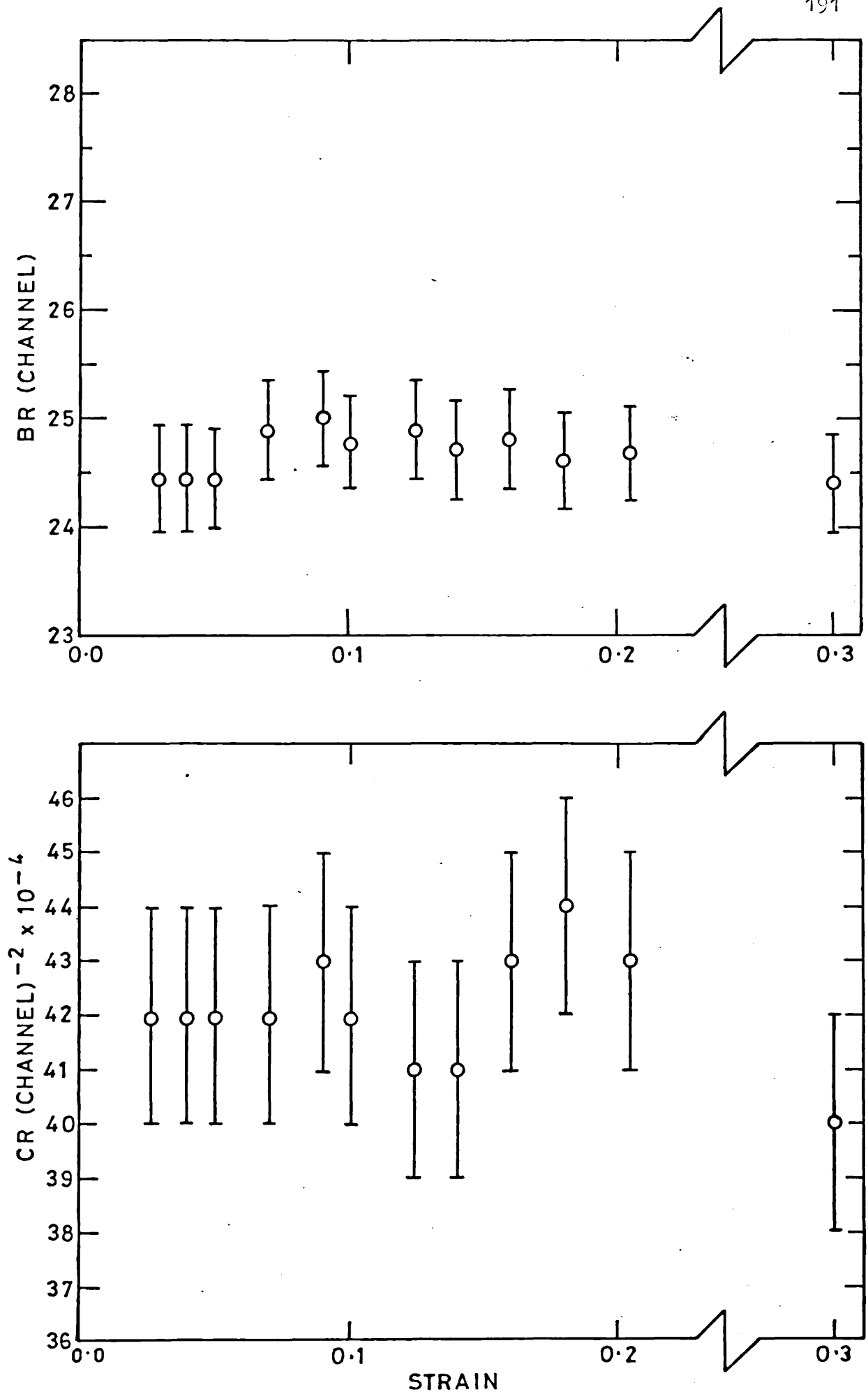
Figure 7.3.2.(b)   Variation of BR and CR for Titanium as a Function of
                    Deformation Strain

concentration is lower than that at which positrons become sensitive to them (i.e. 10^{-6}), and concluded that the monovacancy formation energy was $\geqslant 1.50$ eV. High values of vacancy formation energy (and hence dislocation formation energies) would not encourage the formation of high defect populations/unit strain. Thus, the final option left is high trapping rates - e.g. these may be higher as a result of higher free positron diffusion coefficients in titanium. The possibility of defect traps present in the reference sample which might cause early saturation is discussed in 7.3.3. A trapping model fit to the data has not been attempted in view of the lack of data points in the pre-saturation region.

7.3.3 Positron and Electron Momentum Distributions in Deformed Titanium

The results of model-dependent 'parabola/Gaussin' fits to observed annihilation lineshapes for deformed titanium are shown in table 7.3.1. The fit for undeformed, annealed Ti is illustrated in figure 7.3.3 and it is seen that the Gaussian component accounts for $\sim 80\%$ of the total line intensity.

Table 7.3.1   Results of Model-Dependent Fitting for Deformed Ti

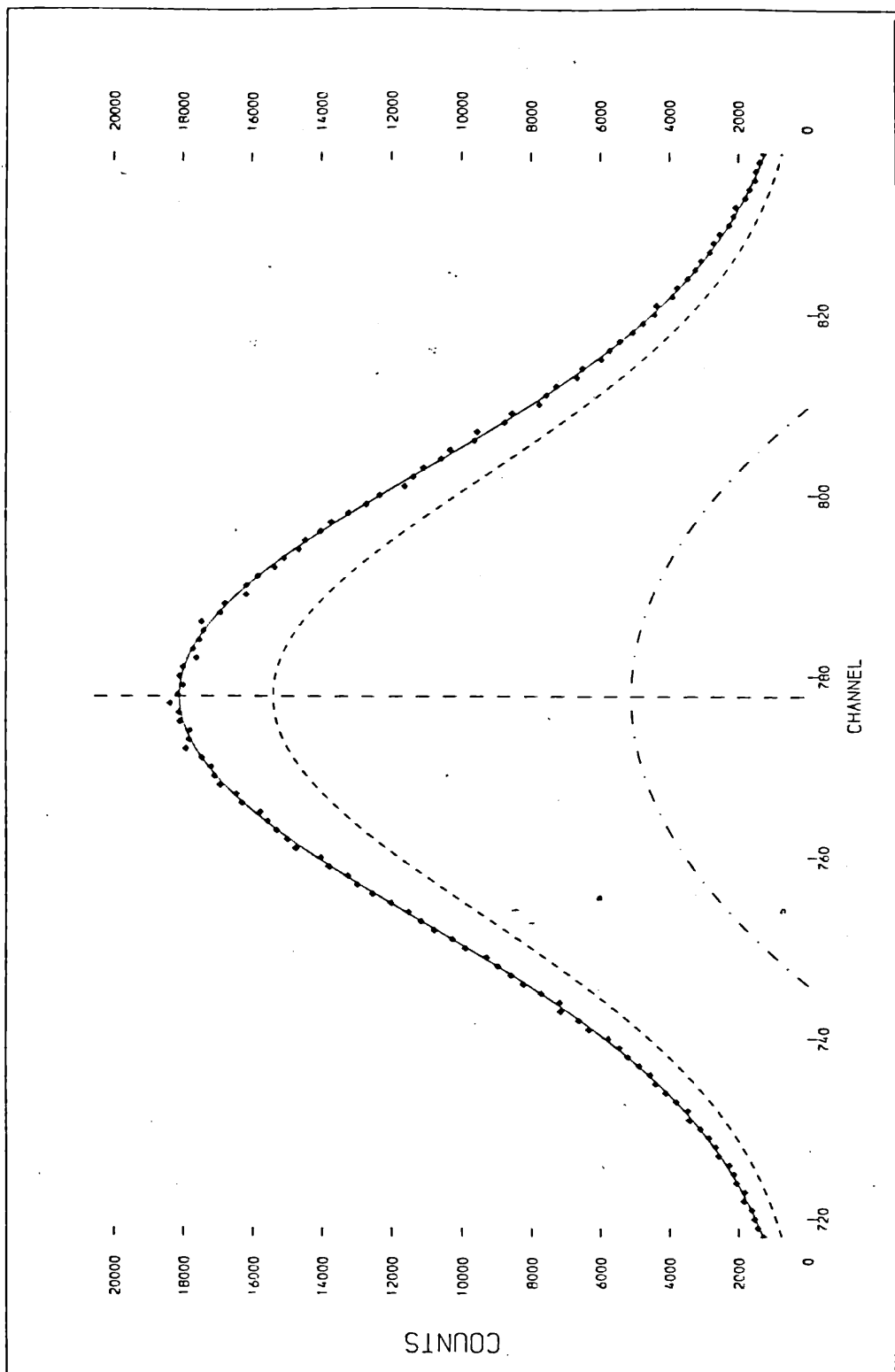| % Strain	Gaussian Width (channel)	Parabola Width (channel)	% Parabola	x^2/ν
0.0	34.64	33.40	20.1	1.420
2.9	31.96	29.96	17.7	1.549
3.97	32.20	29.69	20.6	1.236
5.13	31.96	29.61	20.3	1.256
7.05	31.68	29.64	19.4	1.419
9.06	32.03	30.20	21.8	1.365
10.09	31.85	29.52	19.9	1.311
12.34	31.70	29.94	20.0	1.436
14.07	31.53	29.51	19.7	1.214
16.10	31.58	29.26	18.1	2.172
18.01	31.78	29.17	19.6	2.087
20.26	31.92	29.49	20.4	2.090
30.02	31.90	29.34	19.9	1.816

Figure 7.3.3   Model-Dependent Fitting for the Annealed State of Titanium
--- Gaussian, -·-· Parabola, —— Fit to Data

Inspection of table 7.3.1 does not provide good evidence of a gradual worsening of the fit in the range 0-30%. Also, there is no clear evidence of an increase in parabola % as a function of strain, although both the parabola and Gaussian widths significantly decrease from their annealed values when deformation is introduced. To assess the nature of the positron momenta in both the annealed and deformed states electron momentum distributions have been smeared with the usual positron Gaussian function.

Figures 7.3.4 and 7.3.5 show the variation of χ^2/ν as a function of σ for deformed Ti at 16% and 30% strain respectively. Both strains provide saturation trapping conditions (figure 7.2.1) and the optimum σ found for 30% strain attains a value of 13 channels. In the case of 16% strain, lack of 'fit-data' available for $\sigma = 13$ makes it impossible to determine whether a minimum is reached by this value. However, the trend of the data points would suggest a minimum at $\sigma = 14$.

There is one worrying features of the convoluting analysis. For both 16% and 30% strain, the optimum fit results in a dramatic increase in the value of the Gaussian width compared to its annealed value. This would suggest the improbable ability for positrons to penetrate further into the atomic core whilst undergoing localisation. This inconsistency may be indicating an inability for the simple 'parabola/ Gaussian' electron representation to approximate well the Ti electronic structure. The calculated positron distribution widths σ are seen to be higher than for the case of Cu and Al. In principle this may be due to higher trapping potentials associated with vacancies/dislocations in the case of Ti. Alternatively, the σ values may be indicating the presence of vacancy clusters (section 7.4.2). In view of possible inadequacies in the 'parabola/Gaussian' fit a discussion of such possibilities is not pursued.

Figure 7.3.6 shows a rather unexpected variation of χ^2/ν for the annealed sample. The minimum at $\sigma = 10$ suggests a substantial degree of trapping at defects. At high temperatures Ti has a high affinity for oxygen and nitrogen. Our samples were annealed in a commercial vacuum furnace and it is thought that the vacuum was not of sufficient
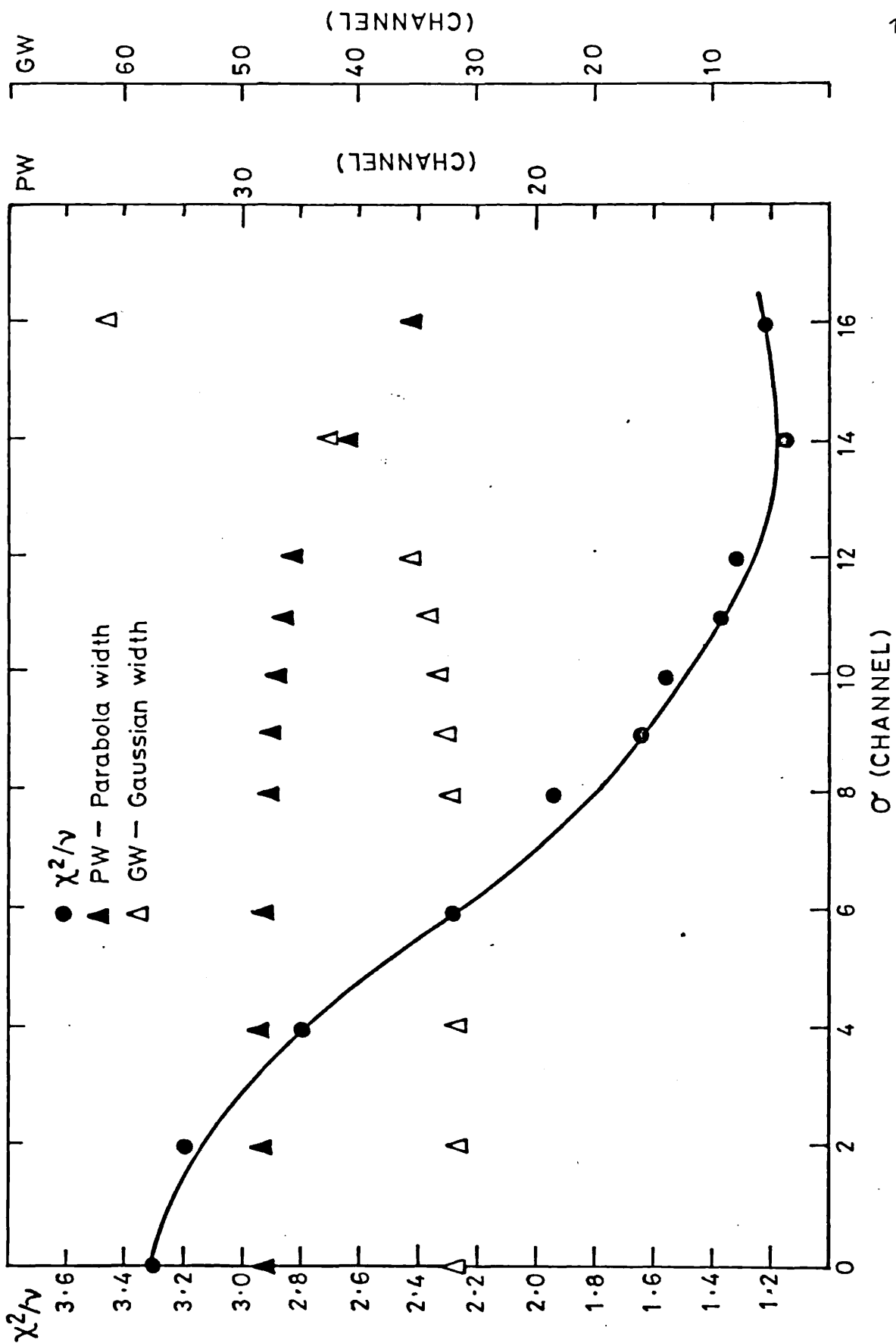
Figure 7.3.4   Variation of χ^2/ν as a Function of σ for Titanium Subjected to 16% Deformation Strain
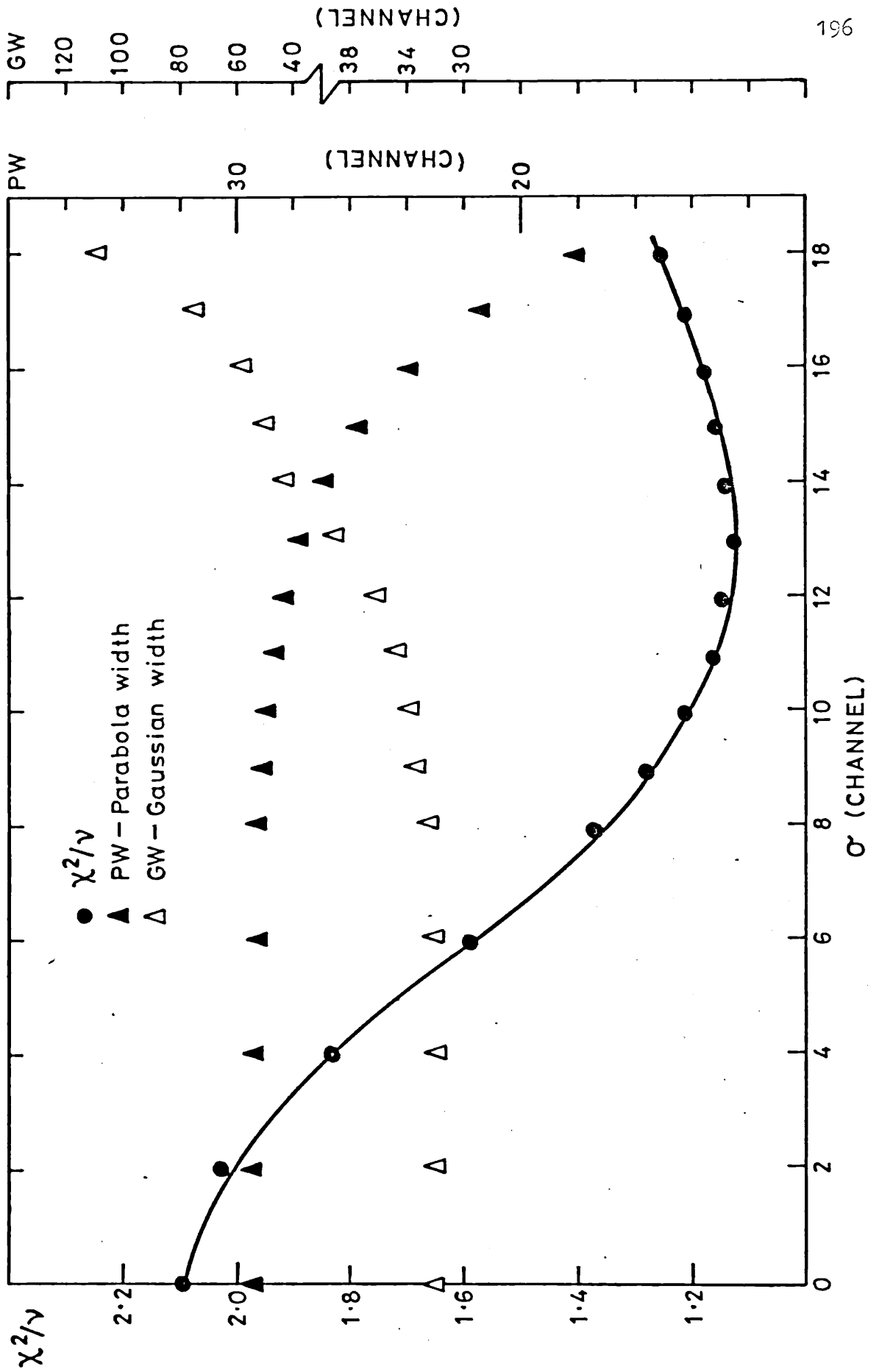
Figure 7.3.5   Variation of χ^2/ν as a Function of σ for Titanium Subjected to 30% Deformation Strain
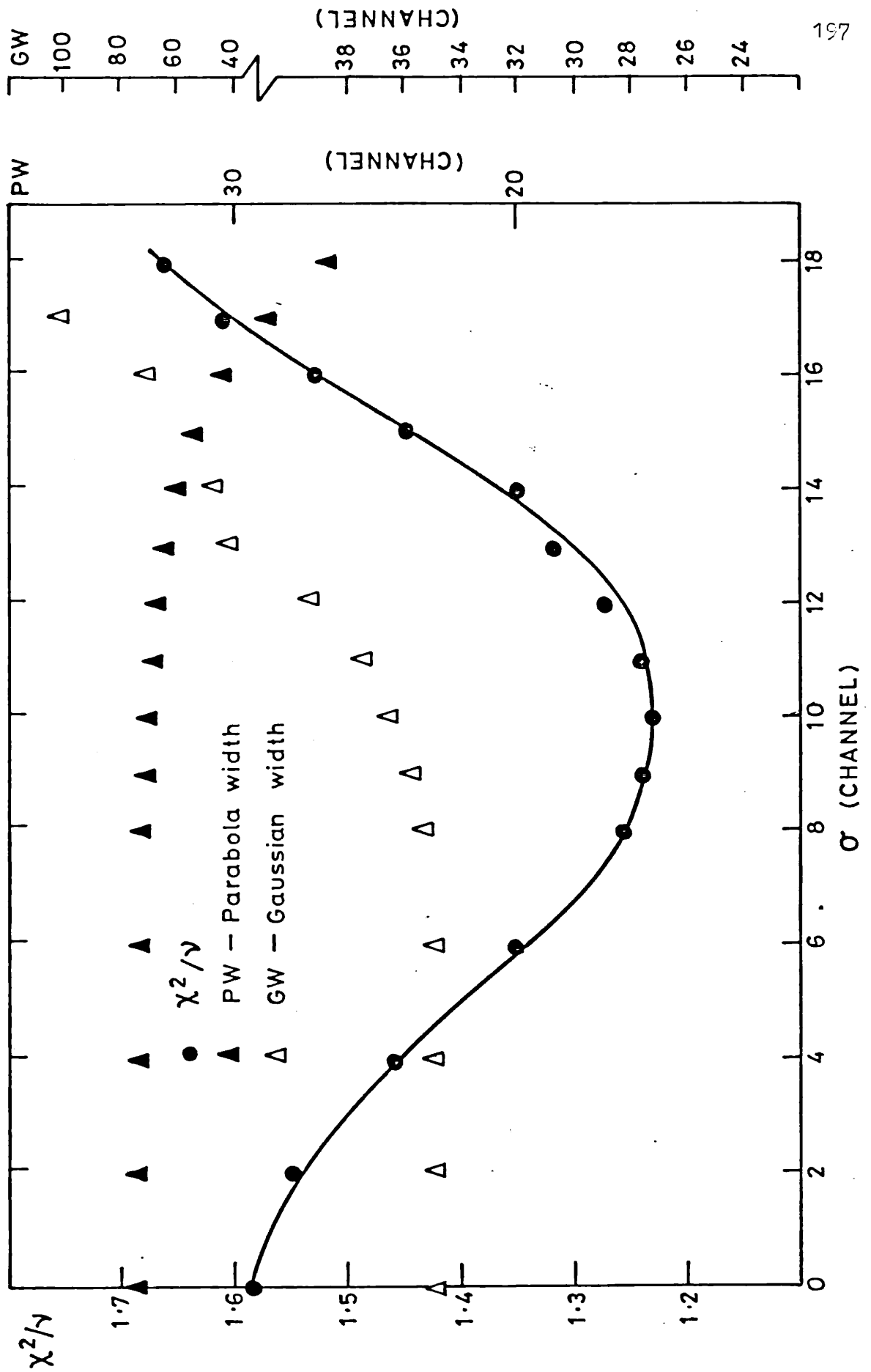
Figure 7.3.6   Variation of χ^2/ν as a Function of σ for Undeformed, Annealed Titanium

quality to prevent absorption of large amounts of these gases. The presence of defects associated with these impurities would certainly explain the large value of σ.

Depending on the type of defects associated with the impurities, their presence might change the deformation strain at which saturation conditions occur. The data of Coleman et al (1979) on Ti alloy found an identical strain at which saturation occurs. Their samples were very carefully annealed in ultra-high vacuum conditions to minimise the oxygen and nitrogen content to levels thought to be incapable of influencing positron behaviour (Hughes, 1981). It was not ruled out, however, that the annealed sample contained significant numbers of traps in the form of phase boundaries and finely dispersed precipitates. These, too, might be responsible for early saturation.

7.4 DEFECTS IN MECHANICALLY DEFORMED IRON

Conflicting reports in the literature exist as to the nature of the defect sites responsible for trapping positrons in mechanically deformed iron. For instance, Hautojarvi et al (1976) measured the Doppler lineshape S parameter as a function of isochronal annealing temperature and found that most of the recovery occurred in the region 400-600°C (recrystallisation region for deformed iron). They concluded that dislocations were responsible for the trapping and attributed an earlier recovery range at $\sim$ 300°C to polygonisation. However, Snead et al (1971) followed the change in the normalised peak height of angular correlation curves and found that most of the defect recovery occurred at $\sim$250°C and attributed it to vacancy migration. McKenzie (1972) studied changes in Doppler lineshape S values and concluded that vacancies were mainly responsible for trapping.

To date, defect-specific analysis has not been performed on deformed iron although Gauster and Wampler monitored the value of the R-parameter during isochronal annealing of a deformed, commercial stainless steel (316 SS). They found that positrons were insensitive to dislocations and believed the major trapping centres to be vacancies.

The following sections seek to establish the nature of the trapping centres through defect-specific and 'model-dependent' analyses.

7.4.1 Isochronal Annealing of Mechanically Deformed Iron

Figure 7.2.5 shows the variation in S as a function of annealing temperature and figures 7.4.1(a)-(b) show the corresponding variations in RID defect-specific parameters. It is seen that the S-value remains constant until $\sim 80°C$ at which temperature a small but significant rise occurs, reaching its maximum value at $\sim 110°C$. Schulte et al (1978) followed the lineshape parameter S as a function of temperature for pure, annealed iron and found $\sim 0.2\%$ change in its value in the temperature range 20-110°C. Our variation in figure 7.2.5 changes by $\sim 0.5\%$ in the same temperature range suggesting that the rise is not due to a temperature effect but, perhaps, to a degree of vacancy clustering (if, indeed, vacancies or even small clusters are present in the deformed state). In the range 110-250°C the S-value remains constant, thus indicating an absence of defect recovery and, finally, beyond 250°C the S-value systematically decreases in order to return to the annealed state.

There is substantial evidence to suggest that recrystallisation in iron does not take place until temperatures of 400°C and above (Ohr et al 1964, Eyre and Bartlett 1965, Gauster and Wampler 1979). Hence the decrease in S at $\sim 250°C$ would indicate that either point defect recovery or polygonisation is taking place.

The S curve in figure 7.2.5 remains constant in the range 110-250°C and, accordingly, a vacancy clustering mechanism in this range may be ruled out (S expected to increase for larger agglomerates). Also, polygonisation is ruled out since the RID parameters do not remain constant. Hence, the most likely explanation of the change in 'shape' is that vacancies and/or vacancy clusters present in the as-deformed state anneal out by 300°C leaving dislocations the only defects available for positron trapping. Thus, the idea that dislocations are the only traps for positrons in the as-deformed state is rejected.
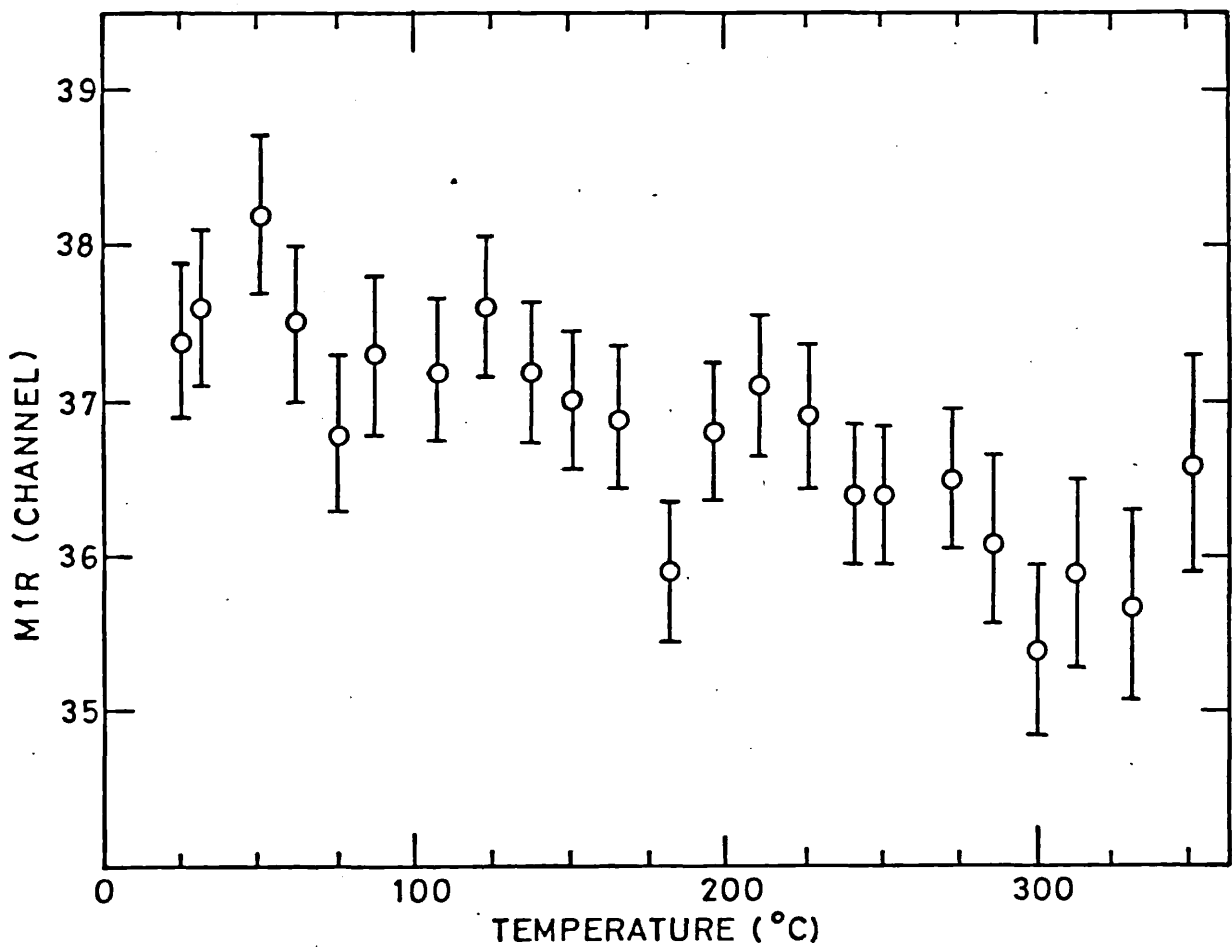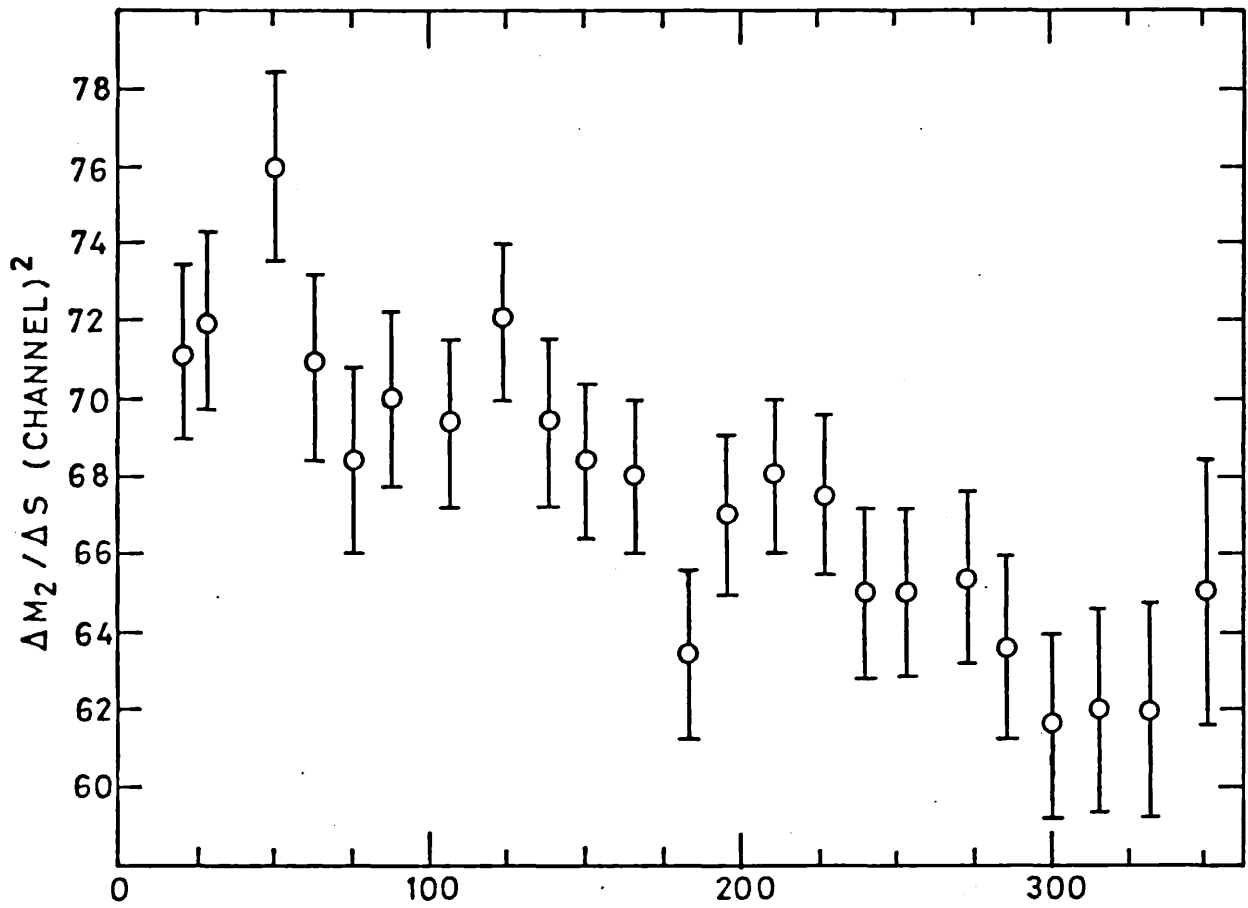
Figure 7.4.1.(a)   Variation of $\Delta M_2/\Delta S$ and M1R as a Function of Annealing
Temperature for Iron Initially Subjected to 10% Deformation
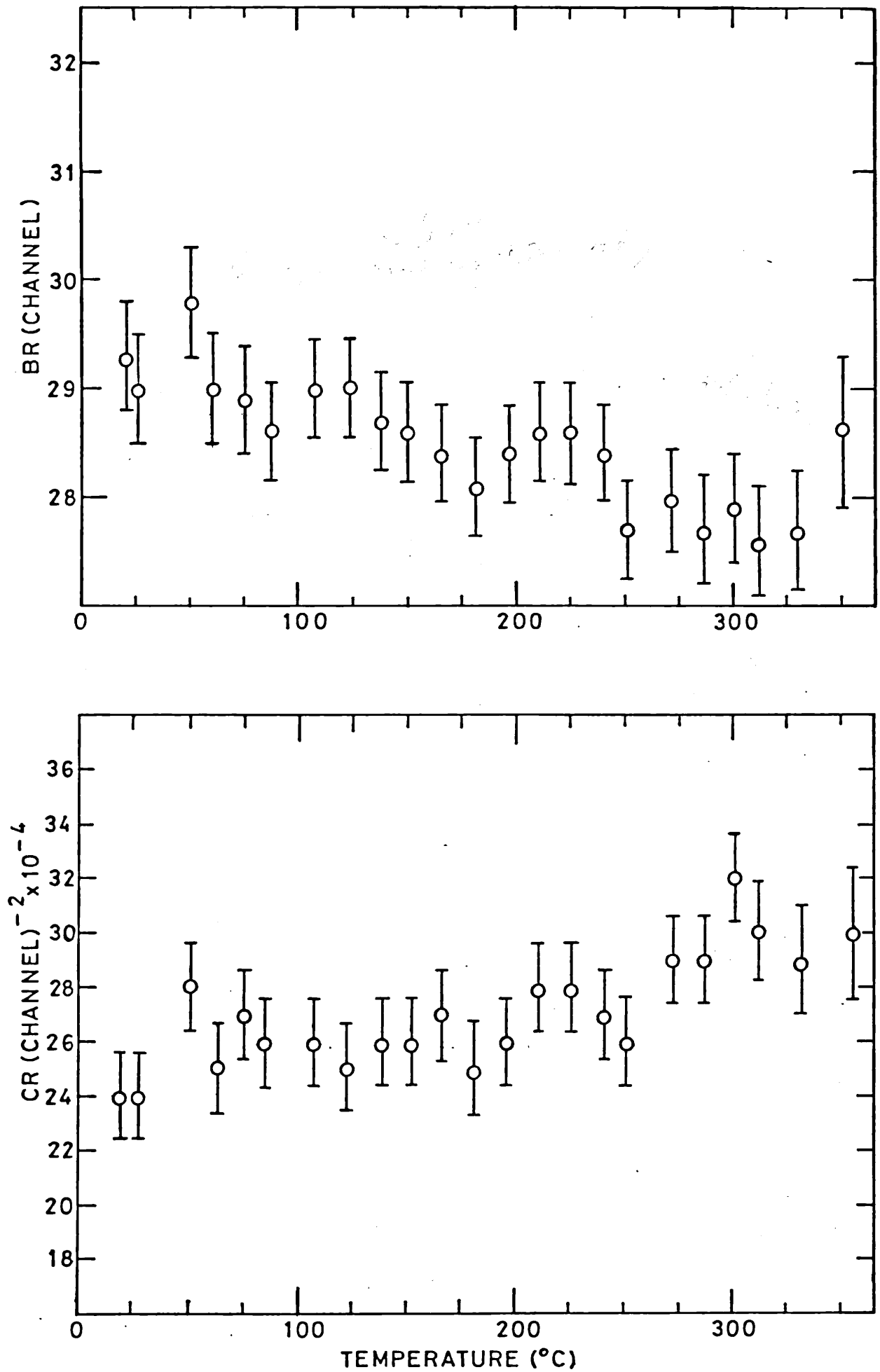Strain

Figure 7.4.1.(b)   Variation of BR and CR as a Function of Annealing
                    Temperature for Iron Initially Subjected to 10% Deformation
                    Strain

The possibility that vacancy clusters might be present in the mechanically deformed state is suggested for two reasons. Firstly, experience in Cu and Al (chapters 5 and 6) shows that RID parameters for vacancies and dislocations are similar. Also, positron-defect trapping potentials appear similar as indicated by the computed zero-point energies. If such similarities are also true of iron then the defect change described above might not have been observed by the RID parameters had vacancies (and dislocations) been the only defects present in the as-deformed state. Secondly, the zero-point energy found for positrons trapped in deformed iron is higher than that for copper and aluminium. This might be indicating the presence of vacancy clusters (section 7.4.2).

7.4.2 Positron and Electron Momentum Distributions in Deformed Fe

The results of model-dependent 'parabola/Gaussian' fits to observed annihilation lineshapes for deformed iron are shown in table 7.4.1. The fit for undeformed, annealed iron is illustrated in figure 7.4.2 and it is seen that the Gaussian component acounts for $\sim$ 83% of the total line intensity.

Table 7.4.1   Results of Model-Dependent fitting for Deformed Fe

| % Strain	Gaussian Width (channel)	Parabola Width (channel)	% Parabola	χ^2/ν
0.0	42.85	32.39	16.95	0.979
0.93	42.69	32.18	17.52	1.173
1.99	42.25	31.54	17.08	1.166
2.99	42.03	30.98	17.25	1.267
3.87	42.30	31.96	17.99	1.546
4.99	42.19	32.69	20.15	1.257
5.91	41.55	32.04	18.03	1.283
6.97	41.36	31.87	18.54	1.301
8.24	41.39	32.00	18.96	1.614
10.11	41.50	32.14	20.28	1.377
11.72	40.87	31.87	19.21	1.330
15.84	30.94	31.84	19.84	1.493
19.91	40.35	32.03	19.26	1.760
24.94	40.29	31.95	19.43	2.284
29.88	40.18	31.86	19.85	2.262
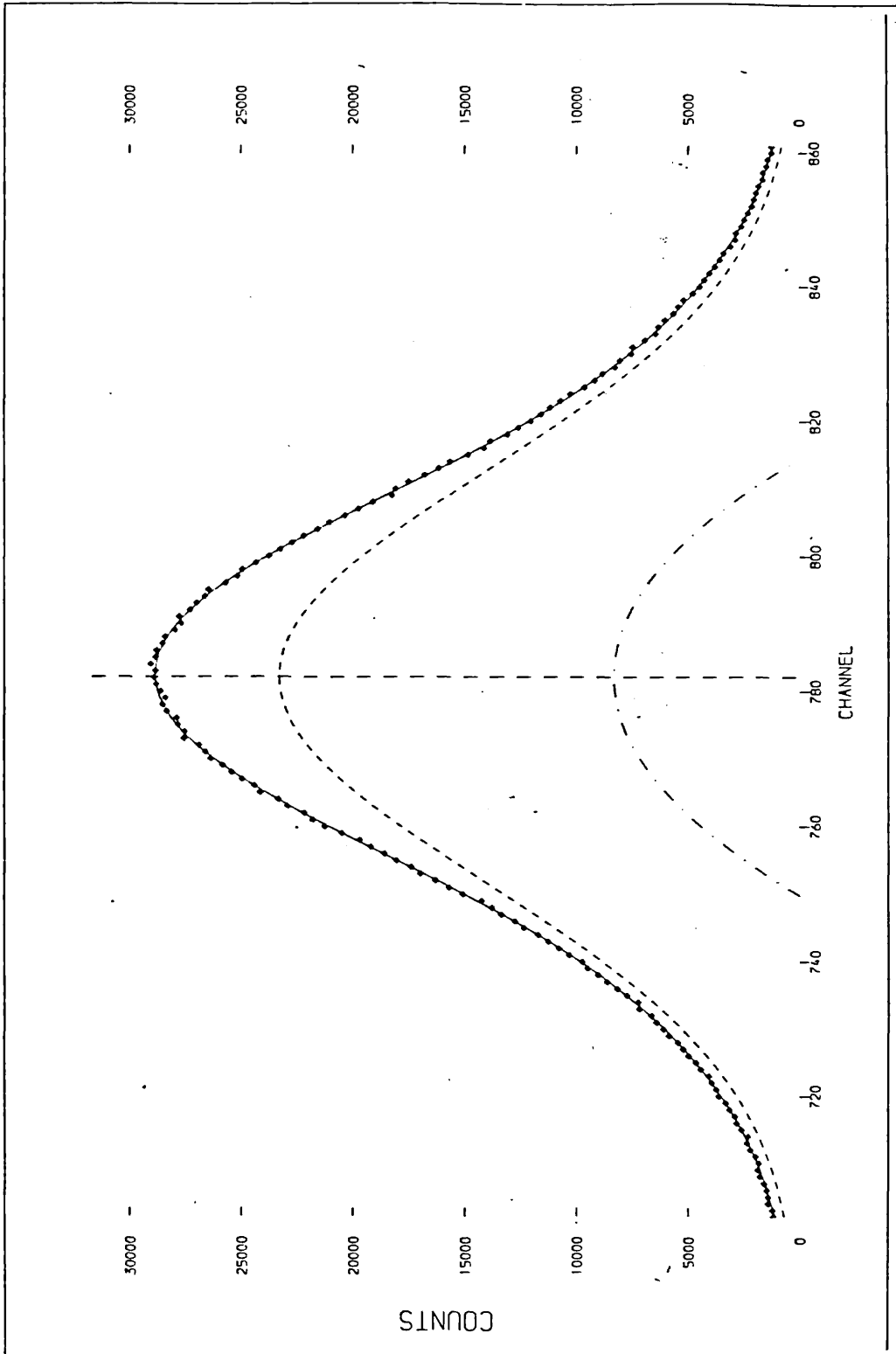
Figure 7.4.2 Model-Dependent Fitting for the Annealed State of Iron
--- Gaussian, -·-· Parabola, —— Fit to Data

As expected, table 7.4.1 shows that both the parabola and Gaussian widths narrow as a function of deformation strain and concomitant with this is an increase in the value of the parabola percentage. There is a gradual worsening of χ^2/ν, and this is taken to be indicative of a positron momentum component not accounted for in the fittings.

Figures 7.4.3 and 7.4.4. illustrate the variation of χ^2/ν as a function of the width σ for the cases of 25% and 30% strain respectively. In both cases an optimum fit is found for $\sigma = 12$ from which is derived a positron zero-point energy of 8.45 eV. This is higher than that obtained in deformed Cu and Al. In view of the similarity of the zero-point energy found for 'vacancy-like' trapping in both Cu and Al - where one might expect to see changes in trapping potential due to the differing valencies - one would expect (within the crude bounds of our analysis) to find a similar energy for 'vacancy-like' trapping in iron. Whilst it may, indeed, be the case that the higher energy found for positrons in deformed Fe is associated with 'vacancy-like' trapping, it is felt that this higher energy may be indicating the presence of stronger point-defect traps - i.e. clusters. This would tie in with the RID curve observations discussed in section 7.4.1.

Figure 7.4.5 shows the variation of χ^2/ν with σ for an annealed, undeformed sample. As has been found in the case of annealed Al and Cu, a shallow minimum is found in the $\bar{\chi}^2/\nu - \sigma$ profile indicating some degree of positron localisation. For the reasons discussed in section 6.3.1.3.2 this may be attributed to point-like trapping at dislocations.

7.4.3 Work-Hardening in Mechanically Deformed Fe

Figures 7.4.6(a)-(b) show the variation in RID defect-specific parameters as a function of deformation strain corresponding to the ΔS variation in figure 7.2.2. Within the limits of statistical error all RID parameters remain constant over this range. However, two distinct levels in the RID parameter values occur for the strain ranges 0-5% and 5-30% - the difference is particularly notable in BR and $\Delta M_2/\Delta S$. This observation is discussed in more detail towards the end of this

Figure 7.4.3   Variation of χ^2/ν as a Function of σ for Iron Subjected to 25% Deformation Strain
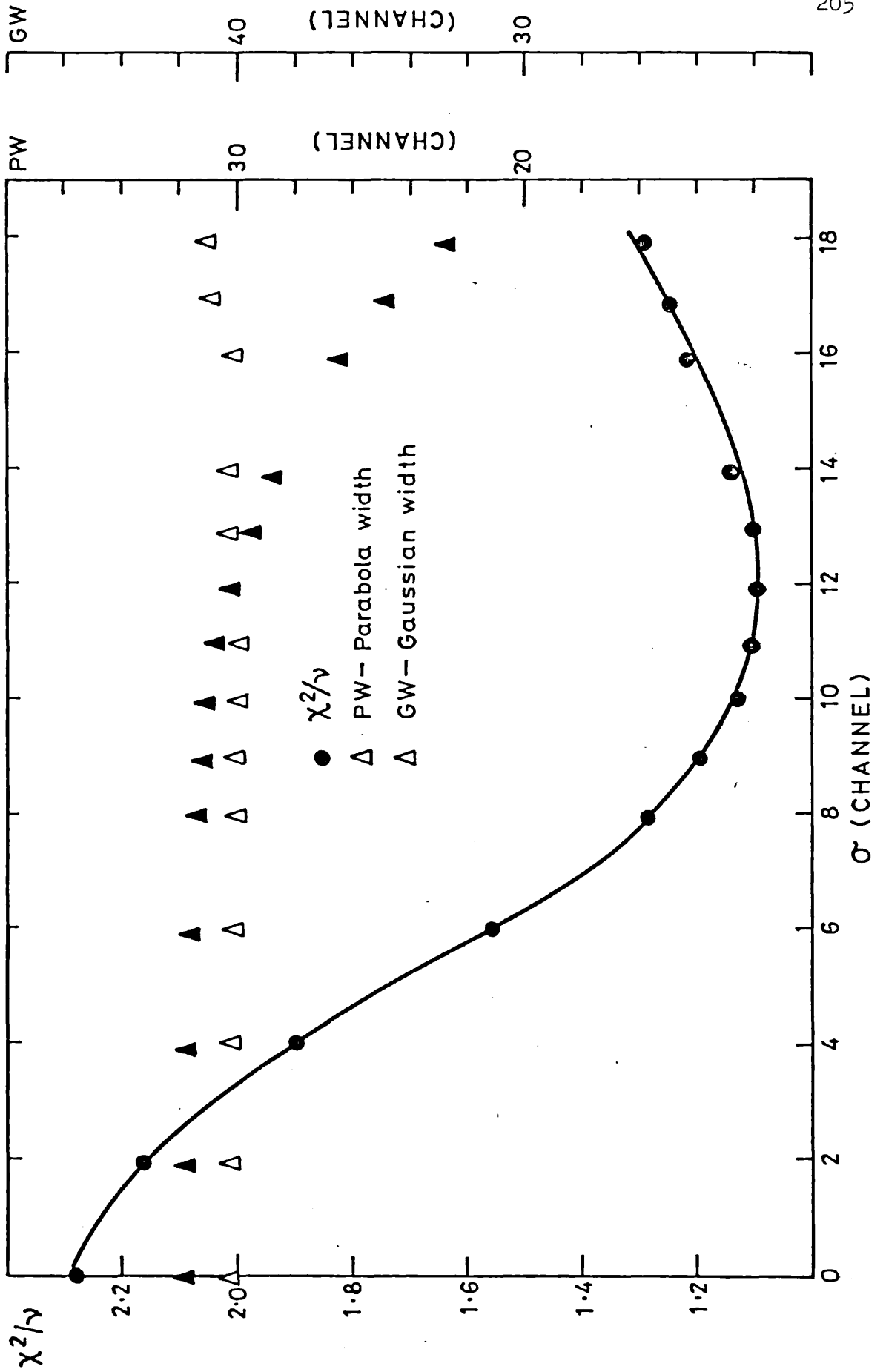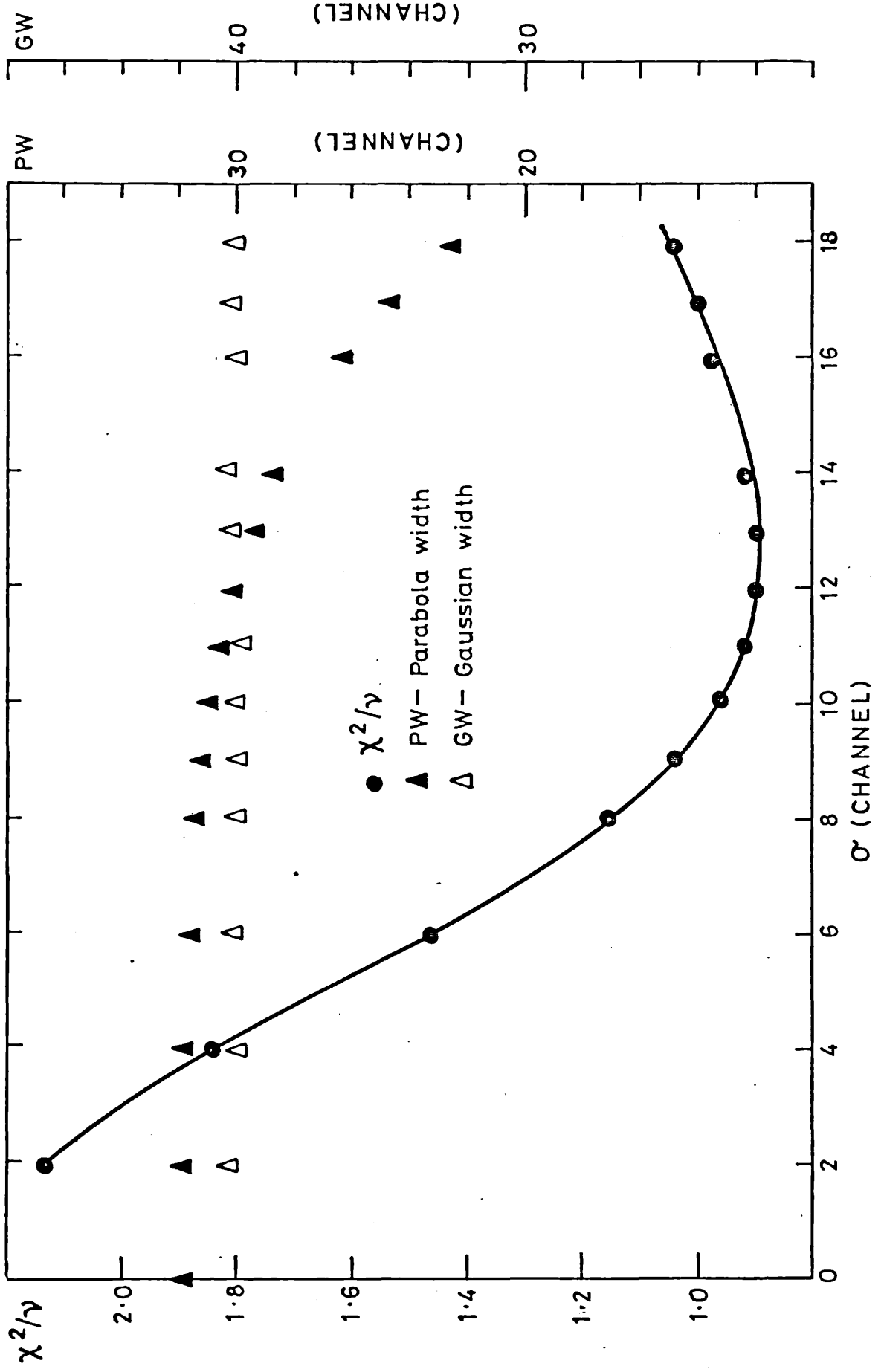
Figure 7.4.4   Variation of χ^2/ν as a Function of σ for Iron Subjected to 30% Deformation Strain
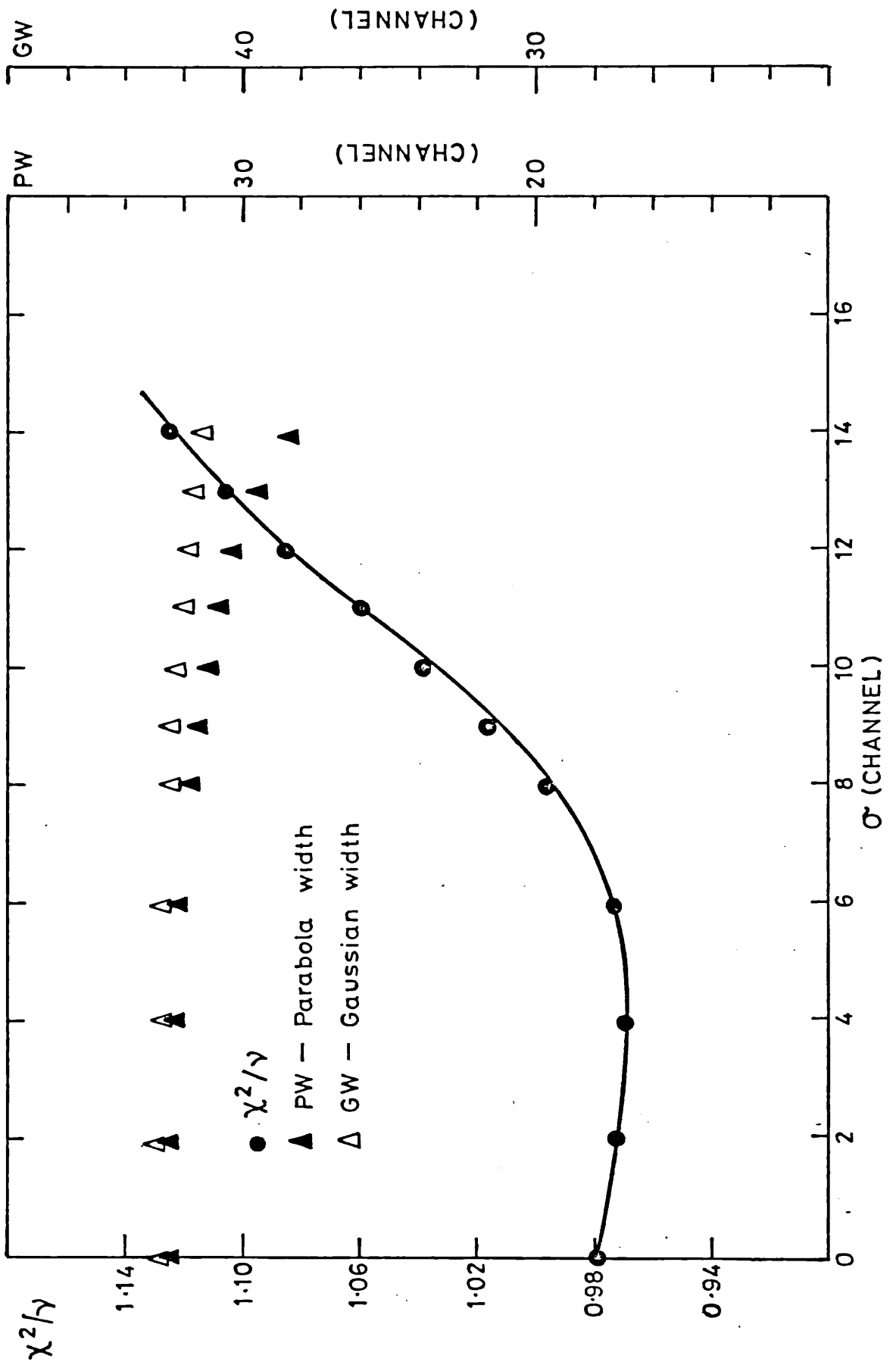
Figure 7.4.5   Variation of χ^2/ν as a Function of σ for Undeformed, Annealed Iron

section. In the meantime, since the differences cannot be resolved as significant, it is assumed that the 'shape' across the entire strain range is constant.

The constancy of 'shape' implies that the defect-types present in the deformed lattice are varying their concentrations by the same proportions. From this it may be concluded that the concentration for each defect-type has the same functional dependence on the strain as the dislocation population. Hence, for a system of i defect types, the concentration, C_i, for each type may be defined by

$$C_i = k_i \, f(e) \qquad\qquad 7.4.1$$

where k_i is a constant and e is the strain. How, from equation 4.2.1

$$S = S_f p_f + \sum_i S_i \, p_i \qquad\qquad 7.4.2$$

where p_f and p_i are the fraction of positrons annihilating in the perfect lattice and ith defect respectively. If, under saturation conditions, α_i is the fraction of positrons annihilating at the ith defect then

$$\sum_i \alpha_i = 1 \qquad\qquad 7.4.3$$

However, since each defect-type varies in concentration by the same proportions, the total trapped fraction, $\sum_i p_i$, under non-saturation conditions may be defined by

$$\sum_i p_i = n \sum_i \alpha_i = n \qquad\qquad 7.4.4$$

where $n < 1$ and, by definition through equation 7.4.4 represents the total trapped fraction. Substituting equations 7.4.4 and 7.4.3 in equation 7.4.2 one obtains

$$S - S_f = n \left\{ \sum_i S_i \, \alpha_i - S_f \right\} = \sum_i p_i \left\{ S_t - S_f \right\}$$
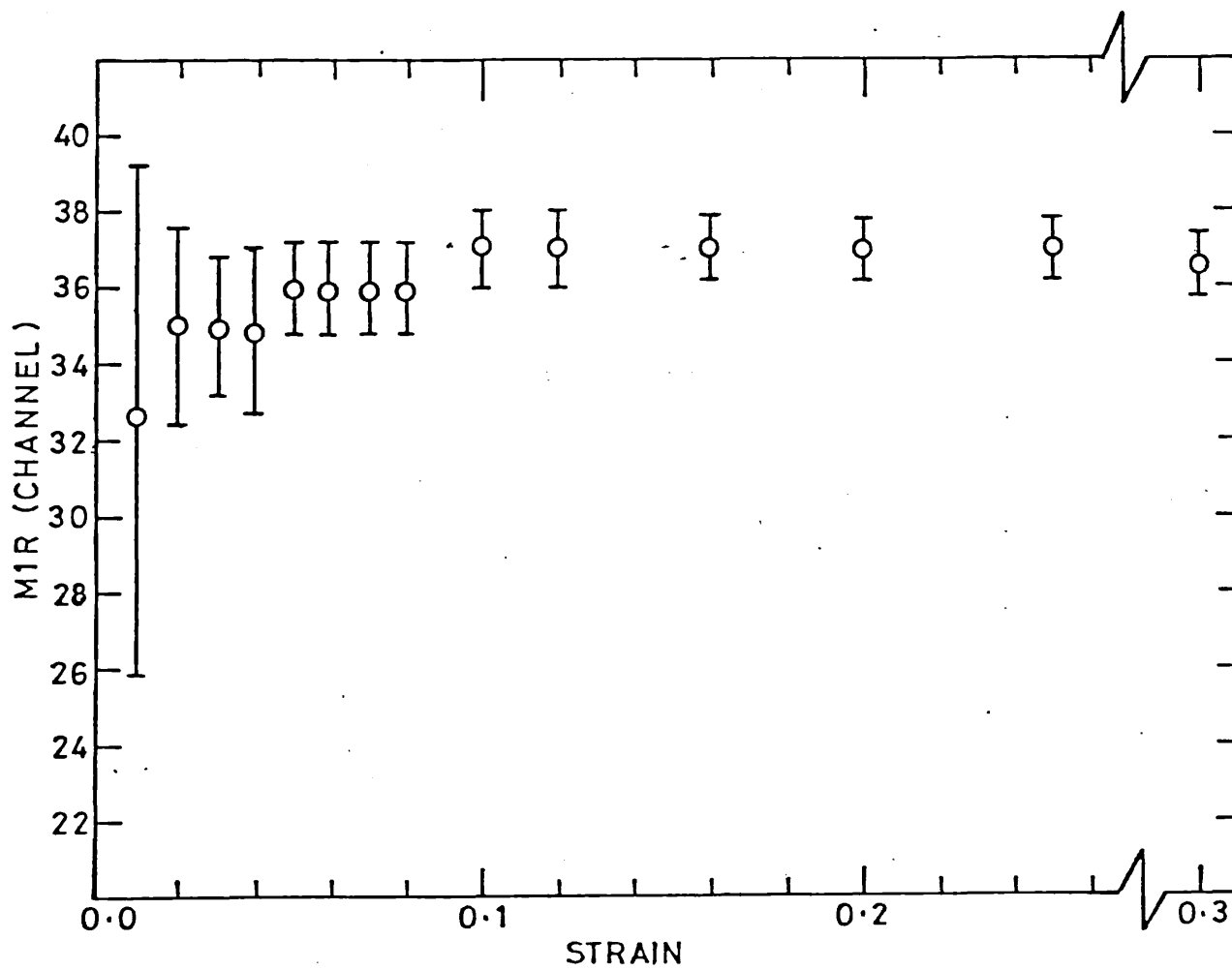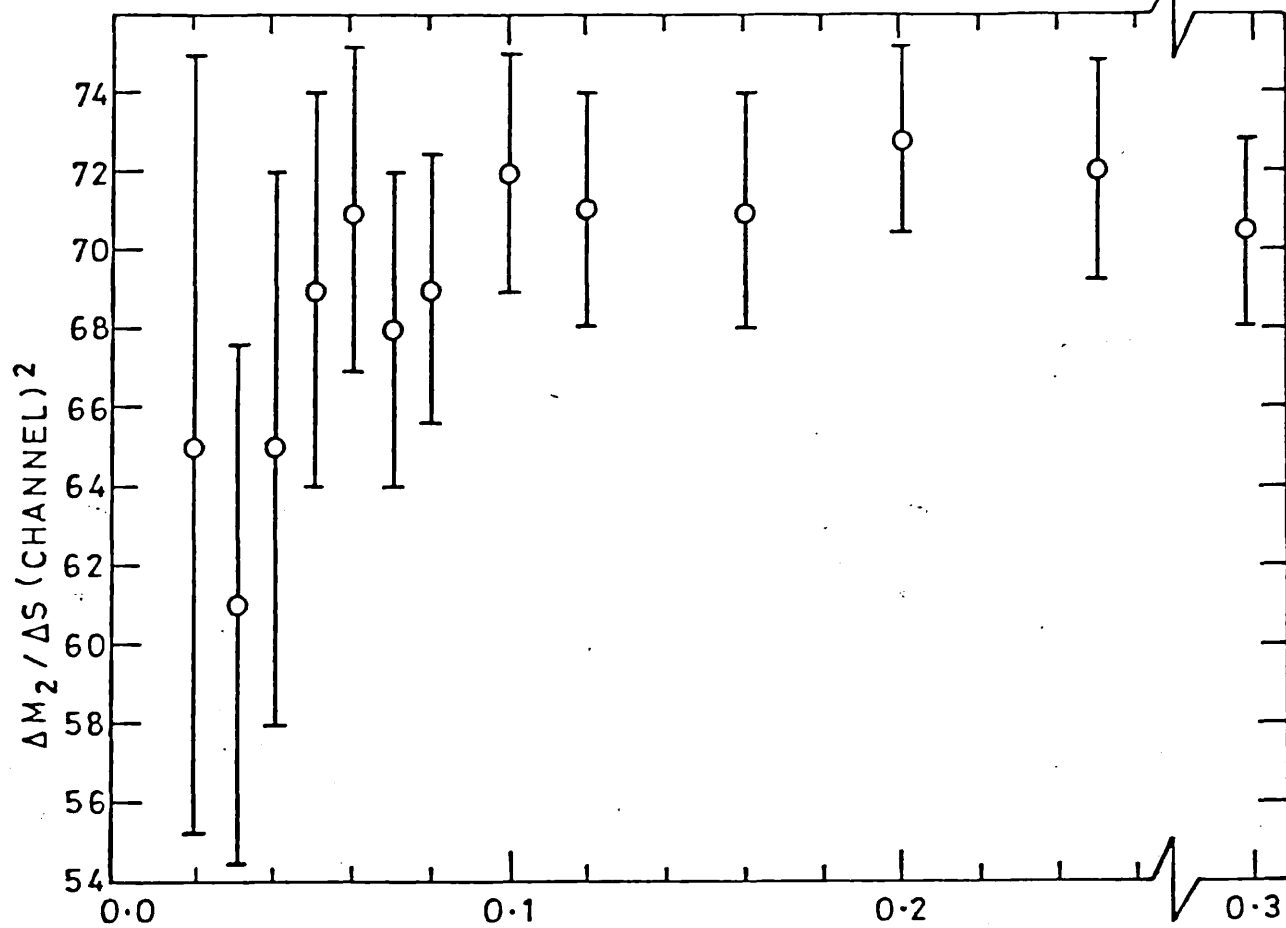
Figure 7.4.6.(a)   Variation of $\Delta M_2/\Delta S$ and M1R for Iron as a Function of Deformation Strain
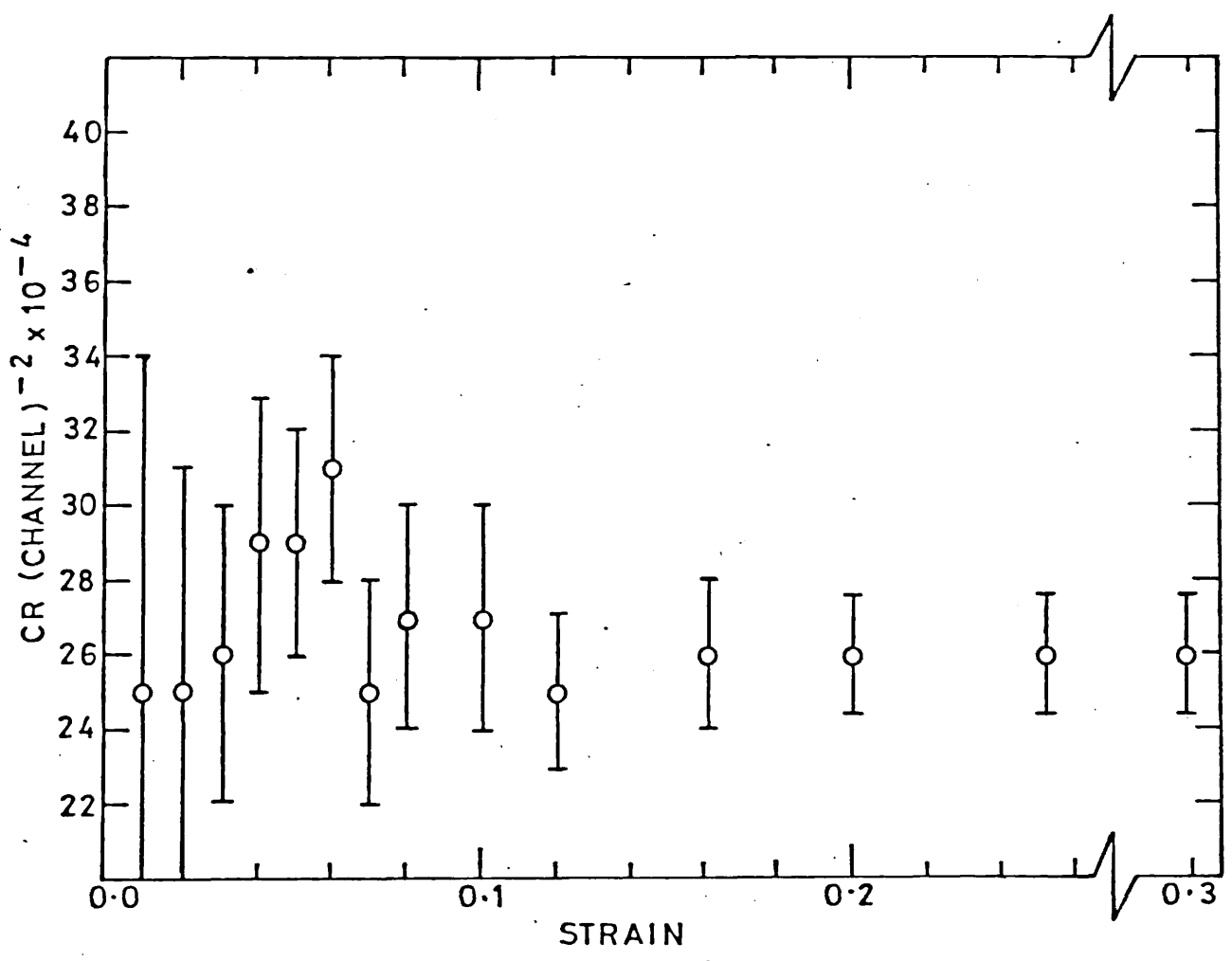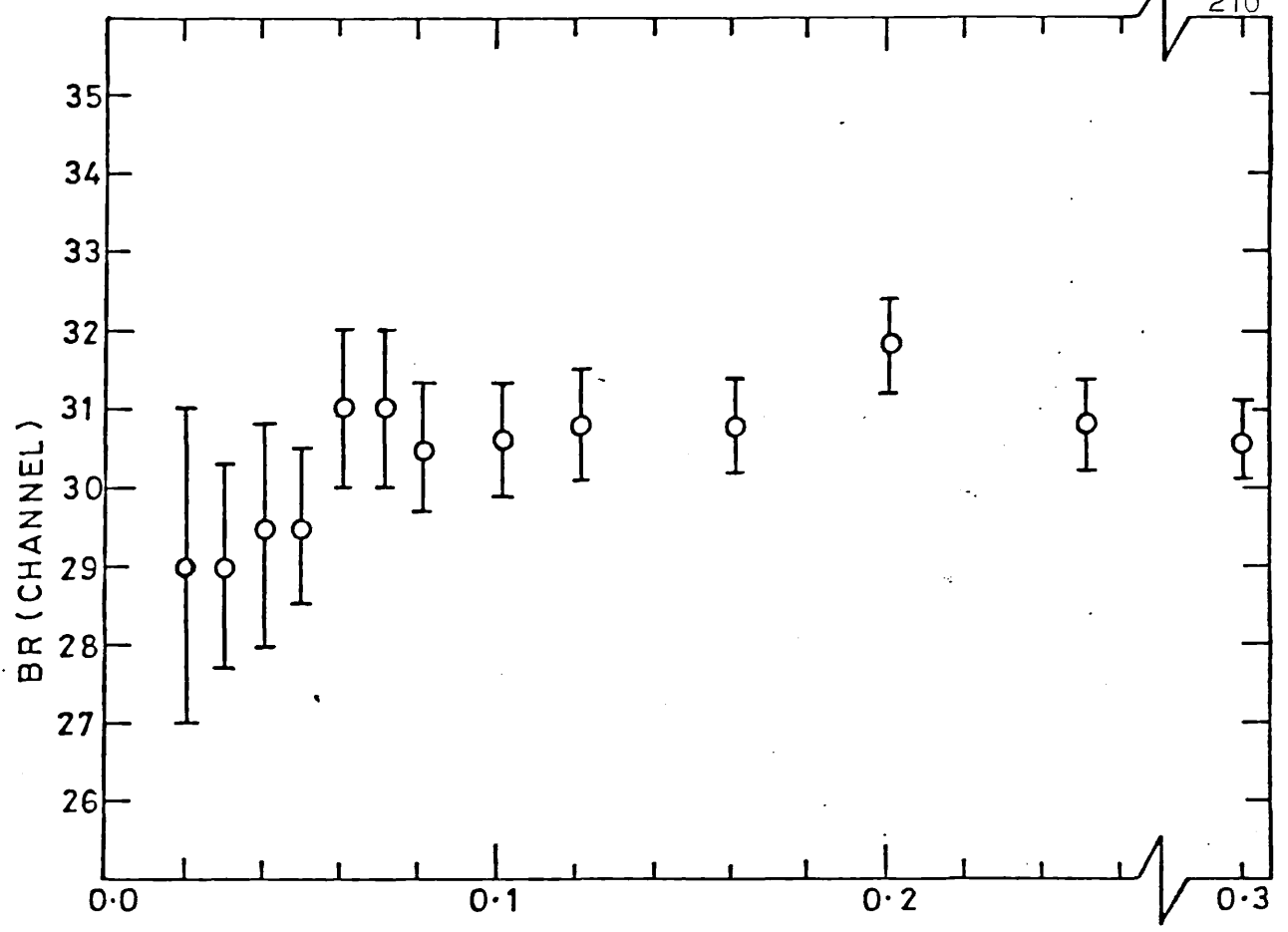
Figure 7.4.6.(b)   Variation of BR and CR for Iron as a Function of Deformation
                    Strain

where $\sum\limits_i S_i \, \alpha_i$ is the observed saturation value S_t. Using equation 2.5.7

$$\frac{S - S_f}{S_t - S_f} = \frac{\Delta S}{\Delta S_{sat}} = \sum_i p_i = \frac{\sum\limits_i \mu_i C_i}{\lambda_f + \sum\limits_i \mu_i C_i} \qquad 7.4.5$$

Writing $f(e) = e^n$ where the value of n defines the work-hardening relationship (section 5.3.4) substitution of 7.4.1 into 7.4.5 yields

$$\frac{e^n}{\Delta S} = \frac{\lambda_f}{\left\{\sum\limits_i \mu_i k_i\right\} \Delta S_{sat}} + \frac{e^n}{\Delta S_{sat}} \qquad 7.4.6$$

To test for the appropriate power-law equation 7.4.6 may be re-written

$$\log\left\{\frac{1}{\Delta S} - \frac{1}{\Delta S_{sat}}\right\} = \log\left\{\frac{\lambda_f}{\sum\limits_i \mu_i k_i \, \Delta S_{sat}}\right\} - n \log e \qquad 7.4.7$$

In order to test for the most likely power of the strain, e, equation 7.4.7 was least-square fitted to the experimental data points in figure 7.2.2 by guessing a value for ΔS_{sat}. The fits yielded

n = 1.25 for ΔS_{sat} = 0.026
n = 1.13 for ΔS_{sat} = 0.028
n = 1.06 for ΔS_{sat} = 0.030

thus favouring a parabolic-hardening relationship. Accordingly, equation 7.4.6 was fitted to the experimental data with n = 1, and the fit is illustrated in figure 7.2.2. The fit yielded the solution

$$\frac{\lambda_f}{\sum\limits_i \mu_i k_i \, \Delta S_{sat}} = 3.274, \quad \Delta S_{sat} = 0.03161$$

and fits well to the observed data. Thus, within our approximation of
'shape' constancy throughout the entire range, the point defect
concentration is a linear function of the applied strain as is, also,
the dislocation density.

Finally, consider the change in the values of RID parameters at
$\sim$5% strain referred to earlier in this section. Whilst it cannot be
proved that change in 'shape' occurs around this strain, there are
definite indications of a change that might be due to a change in the
ratio of proportionality between each defect-type. It is interesting
to note that Cuddy (1968) has shown that except for an initial high
rate of increase for deformations up to 5%, the resistivity attributed
to point defects in iron increases linearly with deformation - in other
words, more point defects are generated per dislocation up to 5% than
thereafter.

In order to test for a change in defect concentration regime at 5%
strain, the data was again fitted by equation 7.4.6 (n = 1) for two
separate strain ranges - i.e. 0-5% and 5-30%. Equation 7.4.6 is valid
if it is assumed that for each strain range the defect concentration
ratios remain the same. The fits yielded

Strain Range	$\dfrac{\lambda_f}{(\sum_i \mu_i k_i)\, \Delta S_{sat}}$	ΔS_{sat}
0-5%	3.5693	0.042
5-30%	3.1286	0.0309

The resulting curve traced almost exactly that illustrated in figure
7.2.2. However, the higher value predicted for ΔS_{sat} in the 0-5%
strain range would indicate a higher fraction of positrons annihilating
in traps stronger than dislocations (which for iron may be vacancies or
clusters). The implication of this analysis would support the findings
of Cuddy et al (1968) - i.e. that more point defects are generated in
the 0-5% strain range than for higher strains.

7.5 DEFECTS IN MECHANICALLY DEFORMED NICKEL

7.5.1 Positron and Electron Momentum Distributions in Deformed Ni

The results of model-dependent 'parabola/Gaussian' fits to observed annihilation lineshapes for deformed Ni are shown in table 7.5.1. The fit for undeformed, annealed Ni is illustrated in figure 7.5.1 and it is seen that the Gaussian component accounts for $\sim$ 79% of the total line intensity.

Table 7.5.1 Results of Model-Dependent Fitting for Deformed Ni

% Strain	Gaussian Width (channel)	Parabola Width (channel)	% Parabola	χ^2/ν
0.0	46.98	30.98	21.3	1.108
2.03	46.02	31.26	24.1	1.277
3.91	44.96	31.11	25.6	1.462
6.00	44.67	31.32	27.7	1.285
8.10	43.94	30.73	28.0	1.581
9.99	43.20	30.17	27.5	1.414
11.98	43.41	30.31	28.1	1.627
14.00	43.64	30.80	29.5	1.860
16.01	42.58	30.18	27.8	1.609
19.85	42.51	29.78	27.8	1.653
24.02	43.11	30.39	30.2	2.231
27.81	41.94	29.42	27.7	2.256
35.14	42.40	29.94	29.5	2.127
39.98	42.78	30.40	30.5	1.444

The width of the Gaussian component decreases as a function of strain. The same is true of the parabola width, although this is not quite so easily seen. As expected, the parabola percentage increases
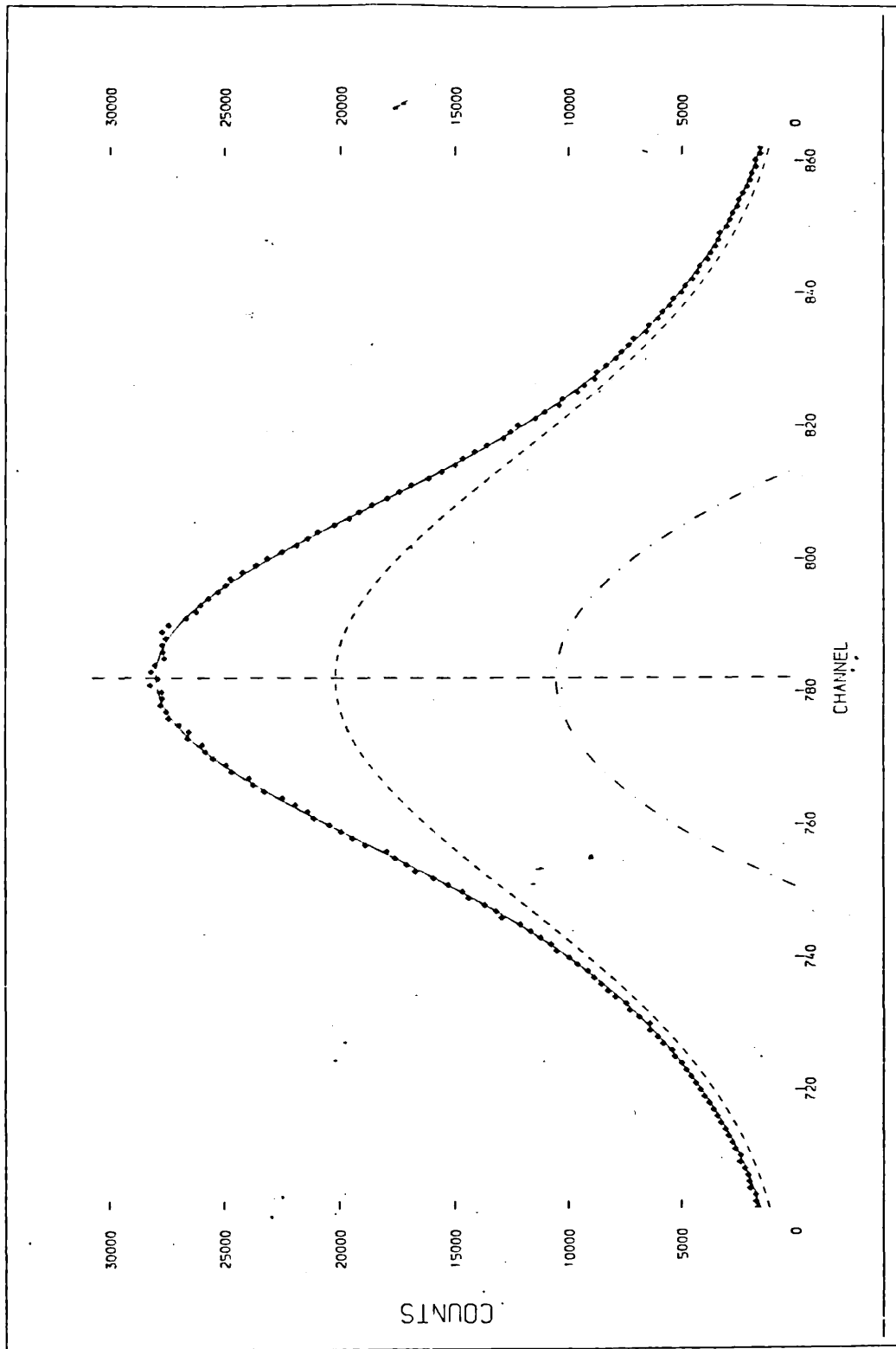
Figure 7.5.1   Model-Dependent Fitting for the Annealed State of Nickel
----Gaussian, -·-· Parabola, ——— Fit to Data

with strain thus reflecting the increase in the ΔS parameter shown in figure 7.2.3. The general worsening of χ^2/ν with increasing strain is taken to be indicative of a positron momentum component not accounted for in the fitting.

Figure 7.2.3 indicates that saturation trapping is achieved by 30-40% strain. Hence, zero-point motion analysis was performed for the cases of 35% and 40% strain. Figures 7.5.2 and 7.5.3 show the variation in χ^2/ν with σ. For each case, an optimum σ of 12 channels is found corresponding to a zero-point energy of 8.45 eV - similar to that found for deformed Fe.

7.5.1.1 Point Defects in Deformed Ni

There is much evidence in the literature suggesting the presence of point defects in the deformed state of Ni at room temperature. For the most part, they are generally believed to be mono-vacancies (e.g. Dlubek et al 1976, Gauster and Wampler 1979). However, the possibility that divacancies might be present in the as-deformed state has been suggested by Dlubek et al (1977a) after isothermal and isochronal annealing experiments on deformed Ni samples. They found that the activation energy for the first defect recovery stage above room temperature was lower than that expected for vacancies. Accordingly, they explained the recovery mechanism as that of migration of divacancies since they have lower migration energies.

Experience in Cu and Al has shown that the calculated zero-point energy for 'vacancy-like' trapping in both metals is identical. However, a higher energy is found for trapping in deformed Ni (8.45 eV) and for the reasons discussed in section 7.4.2 it is suggested that this is indicative of the presence of divacancies or clusters.

7.5.1.2 Positron Behaviour in Annealed Ni

Figure 7.5.4 shows the χ^2/ν - σ variation for an undeformed, annealed sample. As in the cases of Cu, Al and Fe a shallow minimum is found. Again, this is taken to be indicative of point-trapping at dislocations in the annealed state (section 6.3.1.3.2).
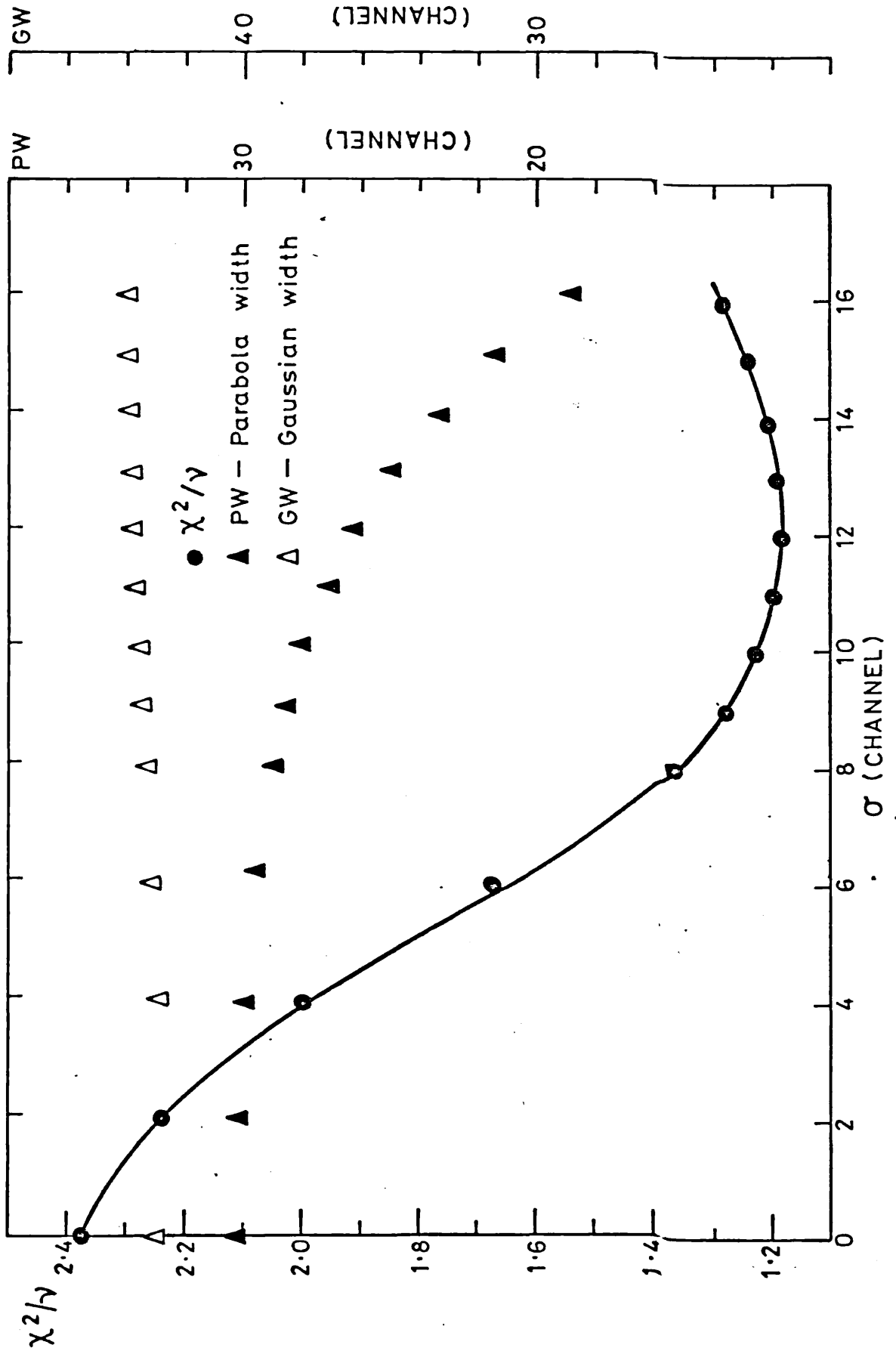
Figure 7.5.2   Variation of χ^2/ν as a Function of σ for Nickel Subjected to 35% Deformation Strain
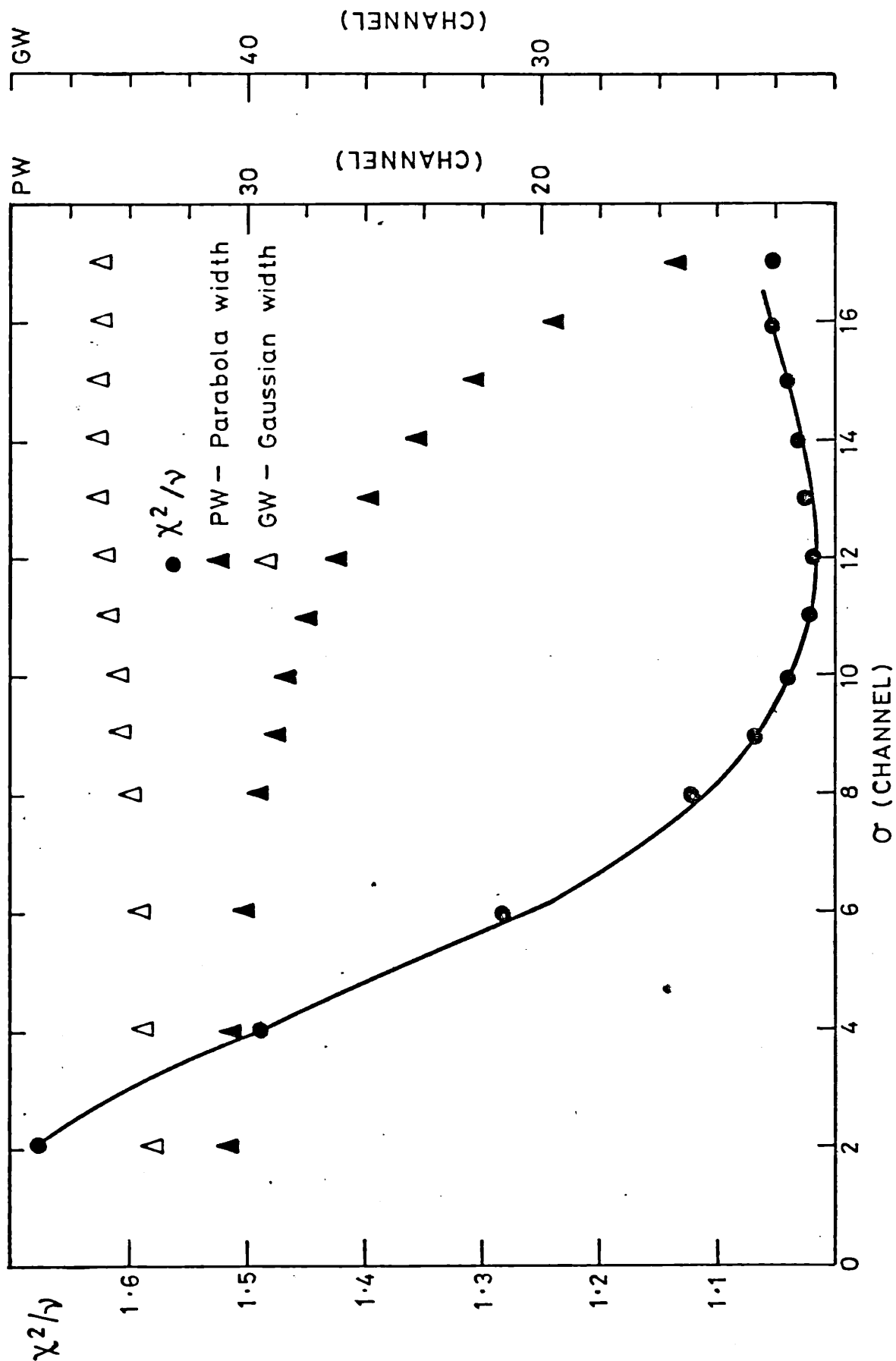
Figure 7.5.3   Variation of χ^2/ν as a Function of σ for Nickel Subjected to 40% Deformation Strain
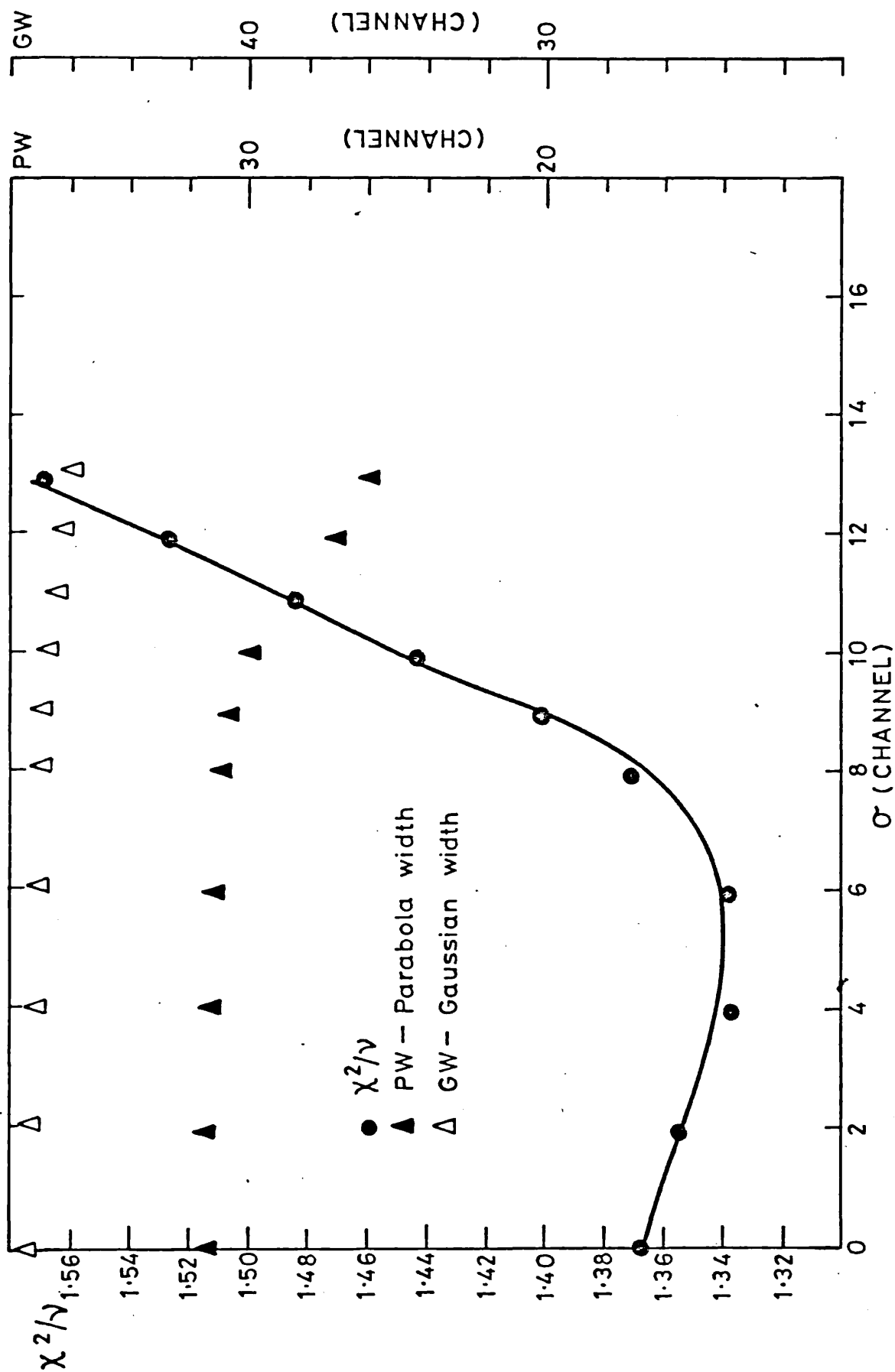
Figure 7.5.4   Variation of χ^2/ν as a Function of σ for Undeformed, Annealed Nickel

7.5.2 Work-Hardening in Mechanically Deformed Ni

Figures 7.5.5(a)-(b) show the variation in RID parameters as a function of strain corresponding to the ΔS variation of figure 7.2.3. The changes indicated in the value of the BR parameter at 14% and 20% strain are considered to be spurious in view of the overall constancy of its value across the entire strain range. $\Delta M_2/\Delta S$ and M1R provide no evidence of 'shape' change.

The constancy of 'shape' across the entire strain range shows that the point defect concentration varies in a similar manner to the dislocation density. Hence, the data in figure 7.2.3 have been fitted to equation 7.4.7 in order to assess the nature of the work-hardening relationship. In the usual manner, a guess was made at the likely value of ΔS_{sat} in order to determine the value of the integer n. The fits yielded

n	ΔS_{sat}
1.33	0.047
1.21	0.048
1.12	0.049
1.05	0.050

thus favouring a parabolic-hardening (n = 1) relationship. Accordingly, equation 7.4.6 was fitted to the data with n = 1, and the fit is illustrated in figure 7.2.3. The fit yielded the solution

$$\frac{\lambda_f}{(\sum_i \mu_i k_i)\, \Delta S_{sat}} = 0.90077, \quad \Delta S_{sat} = 0.05053$$

and provides a good fit to the data.

It is concluded that the point defect concentration in deformed Ni is a linear function of the applied strain as is the dislocation density.
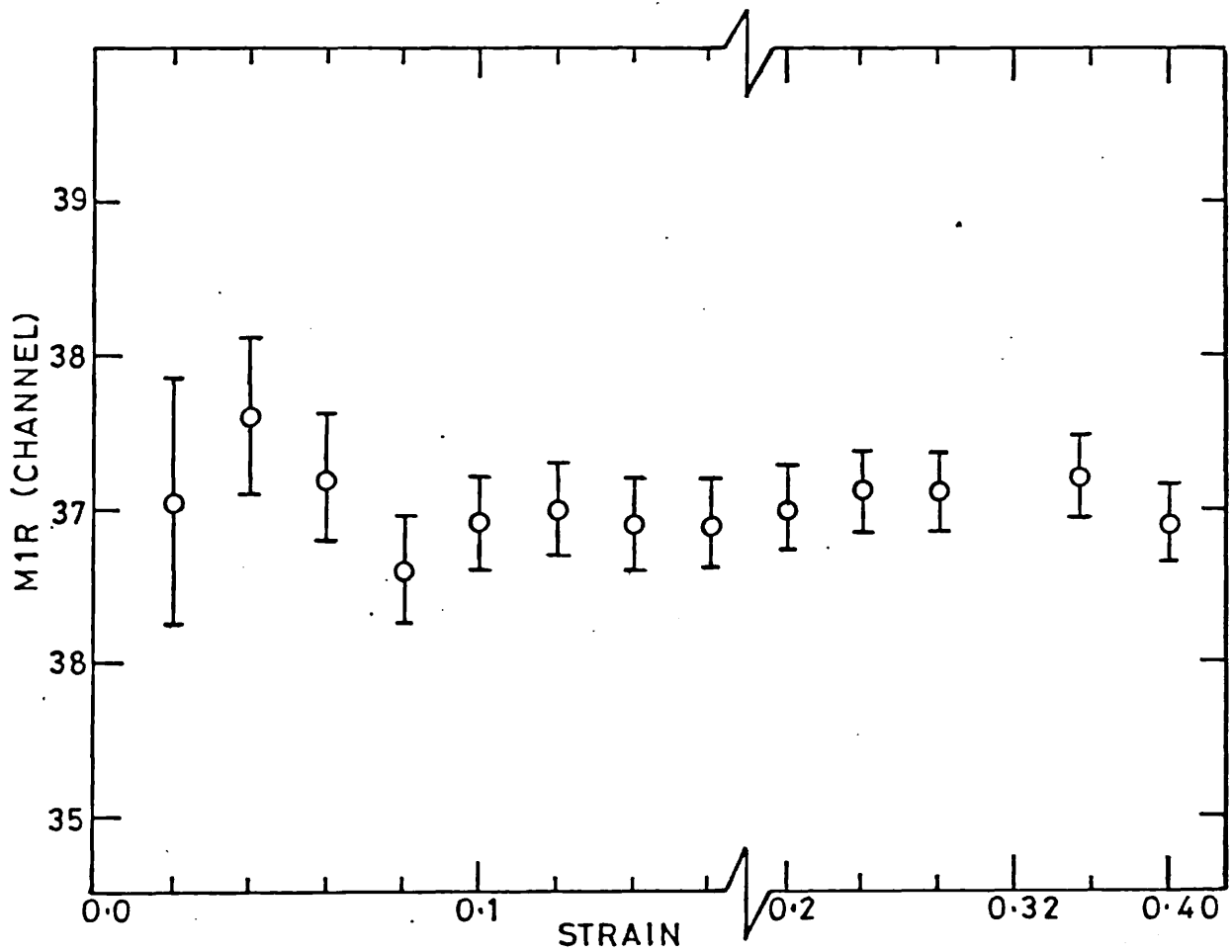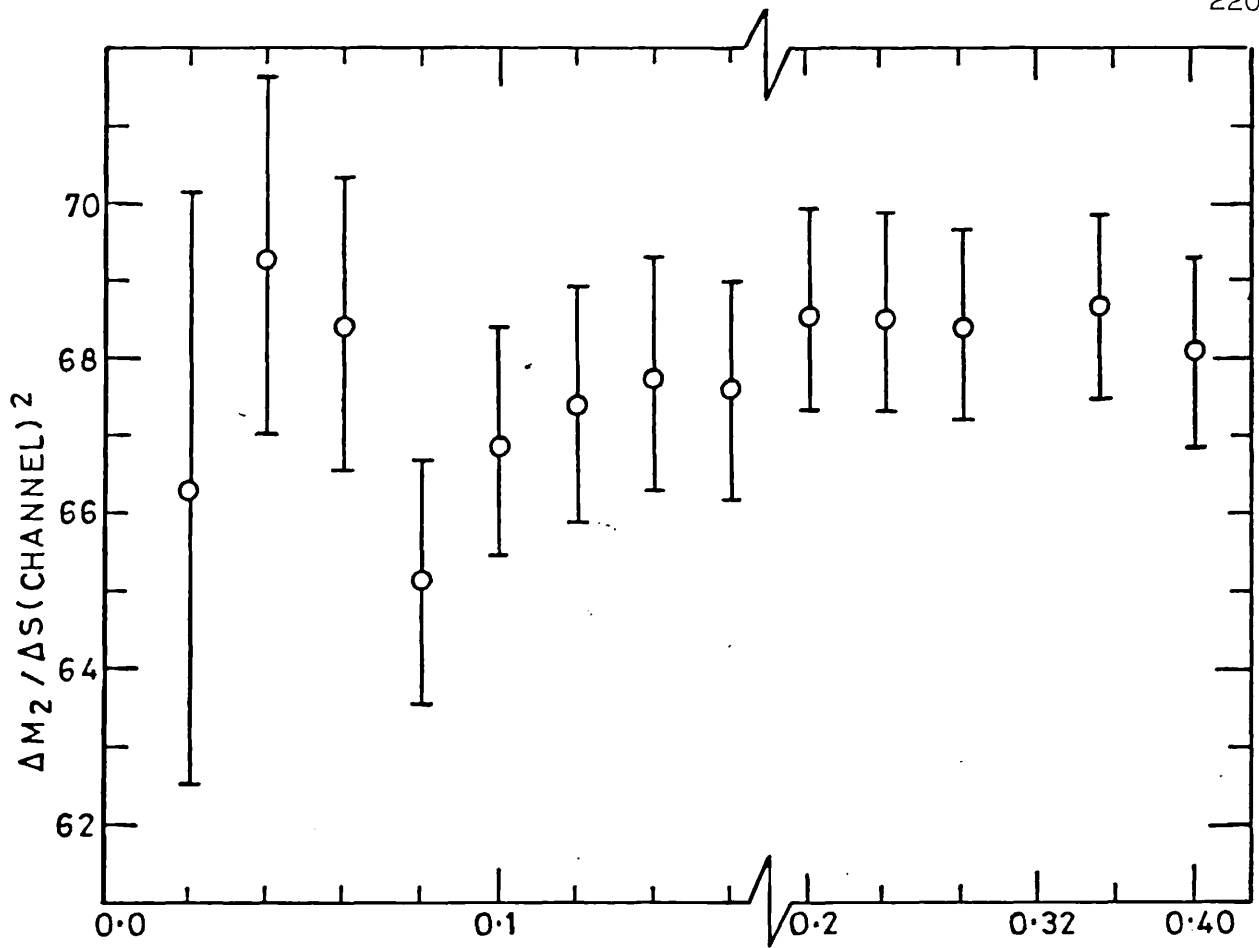
Figure 7.5.5.(a)   Variation of $\Delta M_2/\Delta S$ and M1R for Nickel as a Function of Deformation Strain
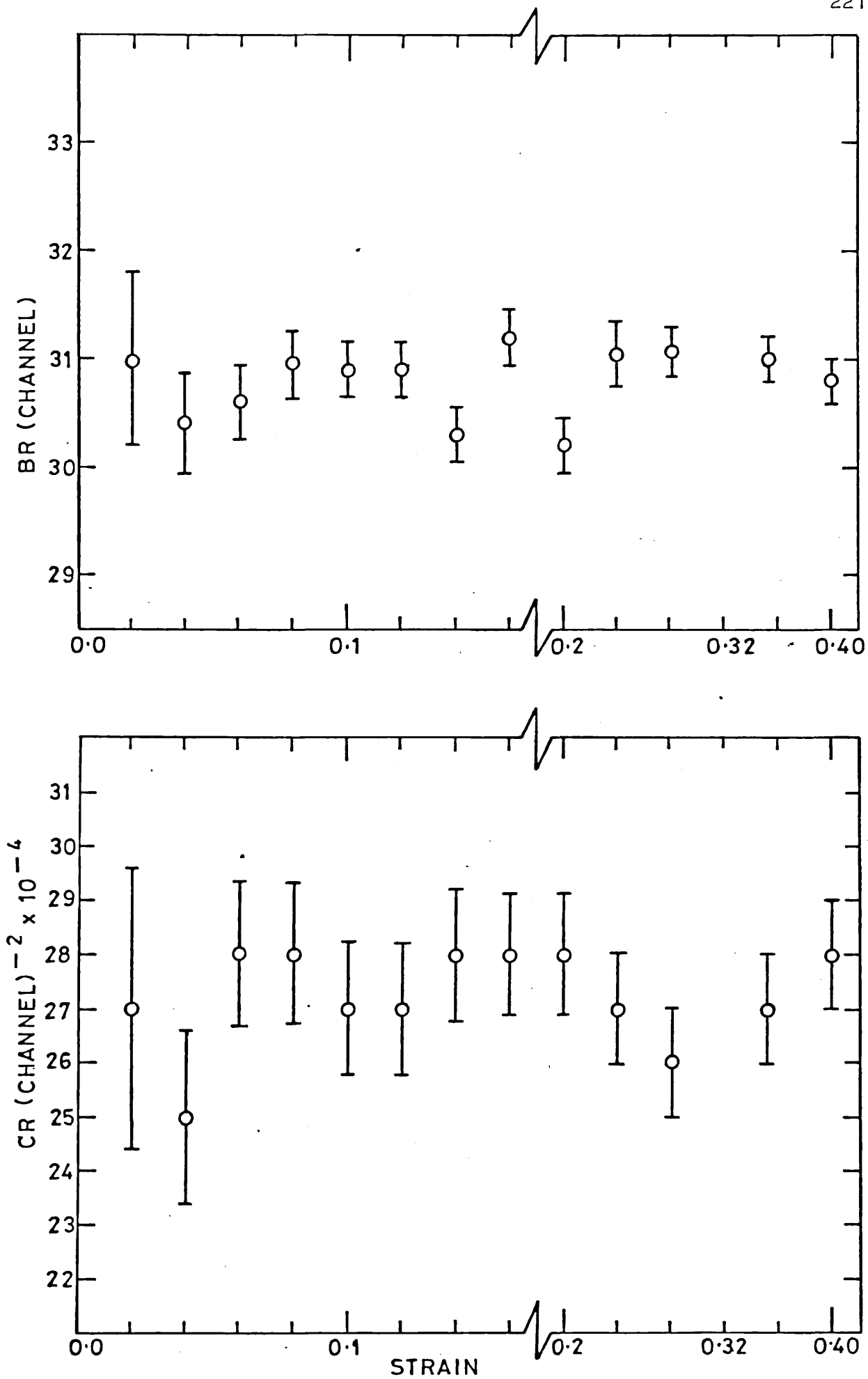
Figure 7.5.5.(b)   Variation of BR and CR for Nickel as a Function of
                    Deformation Strain

7.6 CONCLUSIONS

Analysis has been performed on Ti, Fe and Ni in order to assess the nature of defects in the as-deformed state.

In the case of Ti an isochronal anneal provides evidence of the presence of vacancies. RID curve analysis shows that during deformation the vacancy population varies in the same proportion as the dislocation density.

Evidence found for point defect recovery during an isochronal anneal of deformed Fe through the use of 'shape' parameters has established their presence in the as-deformed state at room temperature. Model dependent analysis provides a zero-point energy of 8.45 eV for positrons trapped at defects in the as-deformed state. A similar value is found for positrons trapped in mechanically deformed Ni. It is suggested that the higher values of the zero-point energy found for Fe and Ni (compared to that derived for Cu and Al) indicate the presence of clusters in the deformed states of Ni and Fe.

· Parabolic work-hardening relationships have been found for both cold-rolled Ni and Fe, and RID curve analysis shown that point defect and dislocation populations have the same functional dependence on the applied strain.

Model-dependent analysis provides evidence for positron localisation in the annealed states of Ni and Fe. This is thought to be due to point-trapping at dislocations.

CHAPTER EIGHT : DEFECTS IN NEUTRON-
IRRADIATED MOLYBDENUM AND TZM

8.1 INTRODUCTION

It is now well established that voids can be formed when molybdenum is neutron-irradiated at suitably elevated temperatures (e.g. Mogensen et al 1972, Cotterill et al 1972, Brimhall et al 1973, Eyre and Evans 1973, Pard and Garr 1975, Mackenzie and Sen 1976). Voids have also been formed as a consequence of post-irradiation annealing of molybdenum samples electron-irradiated at 50°C (Evans and Eldrup 1975).

An original aim of the study presented in this chapter was to characterise voids and vacancies through the use of model-independent and -dependent analyses (chapter 4). Vacancies can be produced in molybdenum by electron-irradiation at room temperature. Unfortunately, an electron-irradiated sample of molybdenum specifically used for the purpose of measuring the positron response at vacancies did not provide any appreciable change in Doppler characteristics compared to a reference, annealed sample - i.e. suggesting an absence of a significant vacancy population. Accordingly, it was not possible to compare the positron characteristics of voids and vacancies. Also, an attempt to characterise voids through the positron zero-point energy derived from model-dependent analysis was unsuccessful due to difficulties - i.e. a low intensity parabola of $\sim$ 5% (see section 6.3.1.3.2) - in fitting a 'parabola/Gaussian' electron momentum distribution regime to the annihilation lineshape of molybdenum. Hence, our analysis is restricted to the use of RID defect-specific parameters.

This study illustrates how RID parameters have monitored changes in the nature of defects found in samples of molybdenum and its alloy TZM (0.5% Ti, 0.1% Zr) irradiated at varying neutron doses and temperatures. Changes in shape parameters correlate well with the changes in defect structure observed by electron-microsocpy. In some circumstances individual defect-types can be characterised. An attempt

is also made to assess the possible role of impurities in the phenomenon of void shrinkage induced by increased neutron dosage (section 8.3.3).

8.2 EXPERIMENTATION AND RESULTS

Samples of zone-refined molybdenum and its alloy TZM irradiated to various neutron doses (E > 0.1 MeV) and at varying temperatures in the Dounreay fast reactor were kindly supplied by Dr. J.H. Evans (AERE, Metallurgy Division). Irradiation details are found in table 8.2.1. Prior to the irradiatios, the samples were annealed in high vacuum at temperatures in excess of 2000°C. The samples irradiated at 8 x 10^{22} n/cm^2 were discs of 3 mm diameter and 0.5 mm thickness. All other samples were derived from the ends of tensile test specimens with the same thickness and roughly the same surface area. After · irradiation, all samples were electropolished before positron measurements were commenced.

The positron source consisted of Na^{22}Cl deposited on a thin aluminium foil. The deposit was subsequently covered with a thin kapton foil attached to a thin strip of sellotape underneath the aluminium foil, thus rendering the Na^{22}Cl deposit intact. The source was then placed between two identically irradiated samples in order to achieve the conventional source/sample sandwich configuratioᵖ. Measurements were taken with the source/sample sandwich positioned at the throat of the detector, gamma collimator by means of an aluminium holder assembly. Counting for each run was performed over a period of 2 hrs. giving rise to $\sim$2 x 10^6 counts for each recorded annihilation lineshape.

Measurements were performed in two separate batches - all measurements on samples irradiated at 8 x 10^{22} n/cm^2 (batch 1) · were performed two months before measurements on samples irradiated to 1.5 and 3.5 x 10^{22} n/cm^2 (batch 2). Although experimentation for both batches was performed under identical geometrical conditions and · at the same detector count-rate, the difference in values of the S-parameters obtained from a common reference molybdenum sample measured in both batches was found to be 0.005 (small but outside

Table 8.2.1 Details of Neutron-Irradiated Molybdenum and TZM

| Material	Irradiation Dose (ncm^{-2})	Irradiation Temperature (°C)	Mean Void Radius (Å)	Void Density (cm^{-3})	Swelling (%)	Dislocation Characteristics
Molybdenum	8×10^{22}	450	23.8	3.5×10^{16}	0.2	Small loops ($\bar{r}_{16} \cong 25$ Å) Density 6×10^{16} cm^{-3}
"	=	550	27.0	1.05×10^{17}	0.87	Coarse dislocation network
"	=	650	29.0	7.7×10^{16}	0.79	Coarse dislocation network
TZM	=	450	Voids not found		<0.01	Small loops, density 1.3×10^{17} cm^{-3}
"	=	550	33.5	6.7×10^{16}	1.06	High density of small loops
"	=	650	25.0	1.14×10^{17}	0.75	Coarse dislocation network
Molybdenum (sample A)	1.5×10^{22}	600	20.0	Not measured	–	Coarse dislocation network
TZM "	=	450	14.5	1.7×10^{17}	0.24	Small loops, density 8×10^{16} cm^{-3}
"	=	650	19.5	Not measured	–	Coarse dislocation network
Molybdenum	3.5×10^{22}	450	22.0	1.3×10^{17}	0.57	Coarse dislocation network
"	=	600	23.0	8.0×10^{16}	0.42	Coarse dislocation network
TZM	=	600	24.0	1.15×10^{17}	0.65	Coarse dislocation network

(Electron microscopy performed by J.H. Evans)
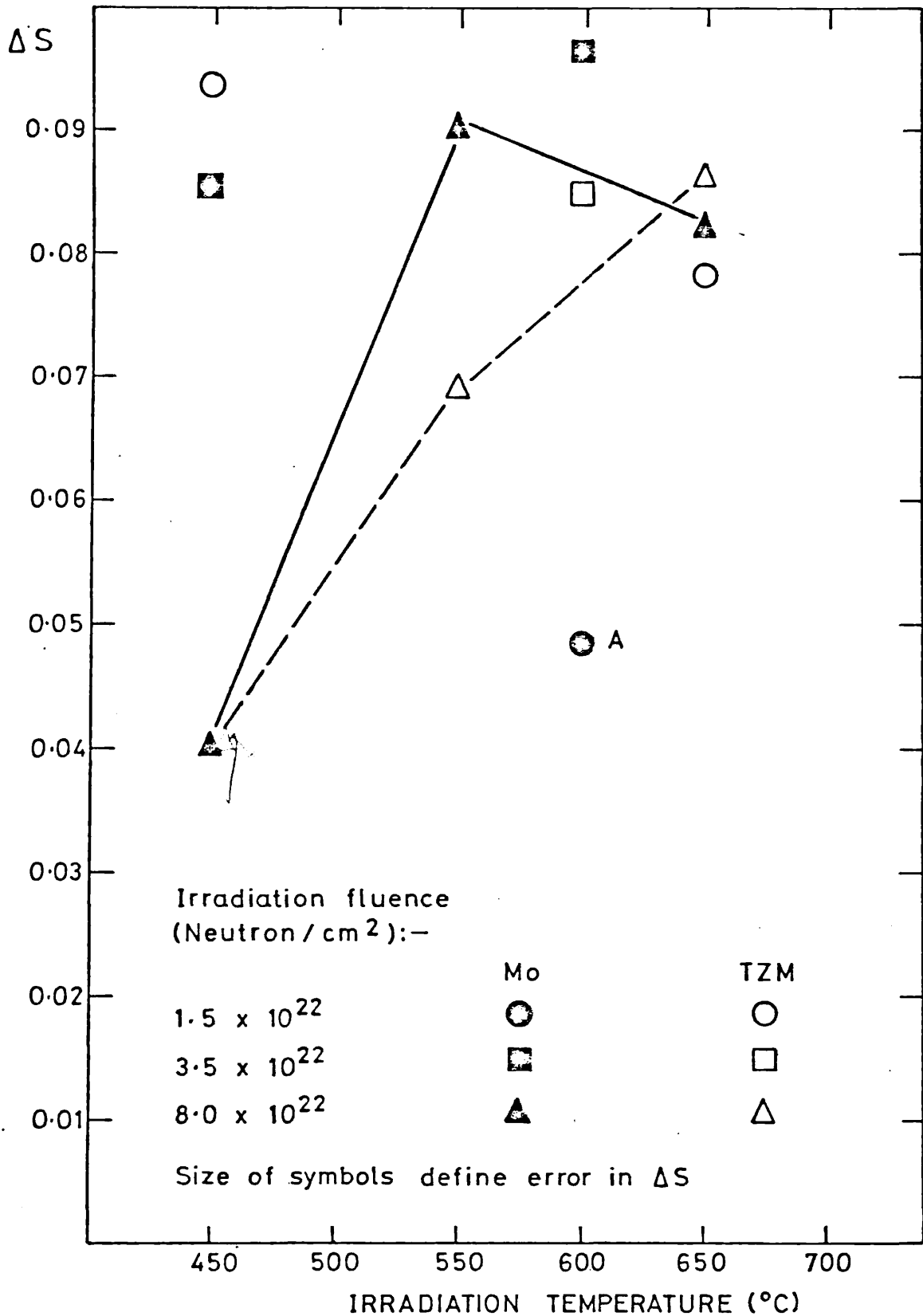
Figure 8.3.1.(a)   Variation of ΔS as a Function of Irradiation Temperature
for Various Neutron Fluences

statistical precision). This is thought to be due to long-term electronic drift. However, RID parameters between both batches may be directly compared because the effect of drift on the 'shape' of the annihilation lines will be eliminated when difference curves are computed.

Figure 8.3.1(a) shows the variation of ΔS as a function of irradiation temperature and dose, and table 8.2.1 summarises the results of electron microscopy as performed by J.H. Evans (AERE - Metallurgy).

8.3 DATA ANLYSIS AND DISCUSSION

8.3.1 Void Formation Mechanisms in Molybdenum

An explanation of why, under certain circumstances, voids can be formed in materials as a consequence of neutron or electron irradiation has been discussed in section 1.5.2.2. Whether or not voids are formed in the lattice will depend on the temperature at which irradiation takes place (e.g. Cheng et al 1976). To help understand why this should be so, and also to serve as an introduction to this study, it would be useful to discuss briefly the formation and development of voids during post-irradiation annealing of molybdenum neutron-irradiated at normal, experimental reactor temperatures ($\sim 60°C$).

A molybdenum sample irradiated with neutrons at normal, reactor (experimental) temperatures will possess an extremely complicated defect structure. As a result of displacement processes (Brinkmann 1953) an assortment of monovacancies, divacancies, vacancy loops and small clusters of vacancies will be present in the lattice. There will also be a large or equivalent number of interstitials trapped at impurities. Free interstitials will not be present as they are capable of migrating below room temperature (Downey and Eyre 1965, Afman 1972). Petersen et al (1974) have given the following interpretation of annealing mechanisms based on the results of positron lifetimes measurements on molybdenum. Essentially, as the lattice is heated up divacancies will first become mobile and will migrate to small vacancy clusters, thus increasing the cluster dimensions. At a later stage (T $> 150°C$) the monovacancies are activated, migrating to vacancy

clusters and loops. At still higher temperatures ($\sim 580°C$) vacancy loops break up and the emitted vacancies travel to the vacancy cluster sinks. The vacancy clusters develop into larger defect pores - i.e. voids. Finally, at temperatures around 750°C the phenomenon of void shrinkage sets in (section 8.3.3).

Roughly similar processes can be expected to occur as a function of temperature for samples irradiated at various temperatures. Although it must be emphasised that neutron-irradiation performed at 60°C, and subsequent annealing to T°C (T > 60°C), will not in general produce entirely the same defect environment as an irradiation carried out at T°C. For example, mobile vacancies produced by irradiation at 300°C may enhance considerably the probability of interstitial-vacancy recombination relative to that for irradiation at 60°C (monovacancies immobile) and thus reduce the numbers of vacancies and interstitials available for feeding vacancy clusters (or loops) respectively. The probability of single interstitial-impurity trapping may even be eliminated if the impurity levels are sufficiently low. However, post-irradiation annealing experiments on samples irradiated at 60°C can be used as a rough guide in assessing the temperature ranges at which certain defect types are likely to either appear or disappear for irradiations taking place at various elevated temperatures.

Table 8.2.1 shows that voids have been formed for most irradiations performed at 450°C. In some cases, a high proportion of loops also exist. A serious discussion of the results for the sample labelled A is not attempted - voids are present but measurements of their density were never performed.

8.3.2 Monitoring Changes in Defect Structure with RID Curve Parameters

This section describes how RID defect-specific parameters have been successful in monitoring changes in defect structure (and have correlated with the findings of electron microscopy) for a series of molybdenum and TZM samples neutron-irradiated at various temperatures. Before discussion commences it is pointed out that the shape and colours of the symbols used in figures 8.3.1(b)-(d) have the same

meanings as those defined in figure 8.3.1(a).

Variation of RID parameters as a function of irradiation temperature for molybdenum subjected to a dose of 8×10^{22} n/cm^2 is shown in figure 8.3.1(b). It is found that all RID parameters undergo significant changes in their values between the temperatures of 450°C and 550°C, thus indicating a change in the defect-types present in the lattice. The results of electron microscopy in table 8.2.1 reveal that molybdenum has a high density of voids and loops at 450°C for an irradiation dosage of 8×10^{22} n/cm^2. However, at 550°C and 650°C the loops are no longer present. It is apparent that the RID parameters have sensed the disappearance of the loops. The electron micrographs (courtesy J.H. Evans) for each irradiation temperature are illustrated in figure 8.3.2 and it is seen that the loop configuration has disappeared at 550°C.

The behaviour of shape parameters with irradiation temperature for TZM, however, is seen to be a little different. RID parameters reveal significant changes at each irradiation temperature, their values at 650°C idential to those found for the case of pure molybdenum. It appears that there exists some evidence ($\Delta M_2/\Delta S$ and BR) of a difference in defect structure between molybdenum and TZM at 450°C, although MIR does not offer such convincing evidence as $\Delta M_2/\Delta S$ and BR. At 550°C all RID parameters show definite, resolvable differences, between molybdenum and TZM, and it is also noted that the RID parameter values for TZM at 550°C are similar to the values for pure molybdenum at 450°C.

Again, reference to table 8.2.1 allows a correlation between RID parameter behaviour and the results of electron microscopy to be found. The table shows that, unlike molybdenum, TZM at 450°C offers no evidence for voids (either because they do not exist or because they exist in low enough concentrations to prevent their detection). This would explain the suggested difference in RID parameters found between molybdenum and TZM at 450°C - the values for TZM may be considered to represent loops only, whereas the values for molybdenum may be considered representative of both loops and voids. Table 8.2.1 reveals the existence of both loops and voids in TZM at 550°C, and this would

Figure 8.3.1.(b)   Variation of RID Curve Parameters as a Function of
                     Irradiation Temperature for Molybdenum and TZM Subjected
                     to a Neutron Fluence of 8.0 x 10^{22} n/cm^2

Figure 8.3.1.(c)   Variation of RID Curve Parameters as a Function of
Irradiation Temeprature for Molybdenum Subjected to
Neutron Fluences of 1.5 and 3.5 x 10^{22} n/cm^2
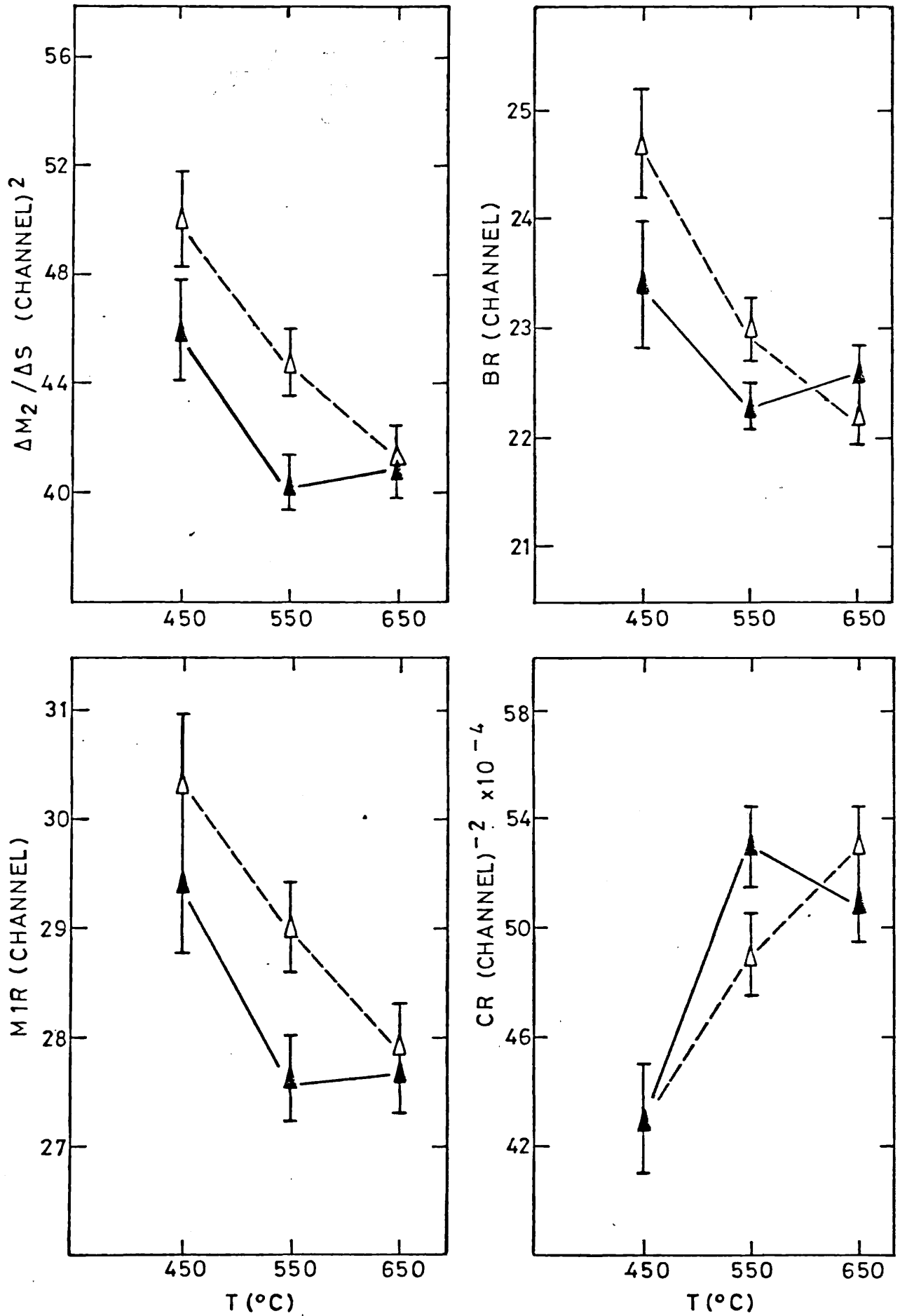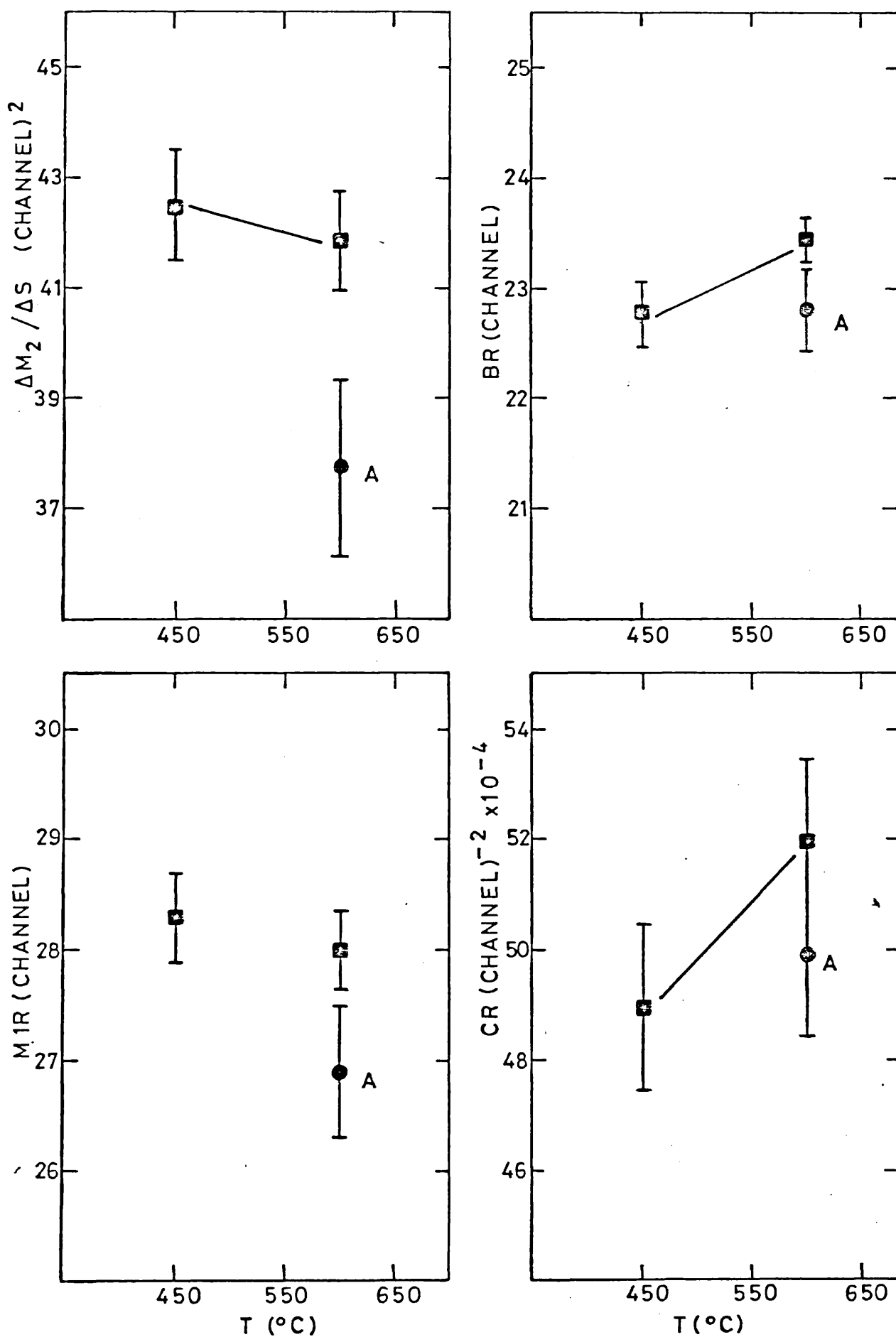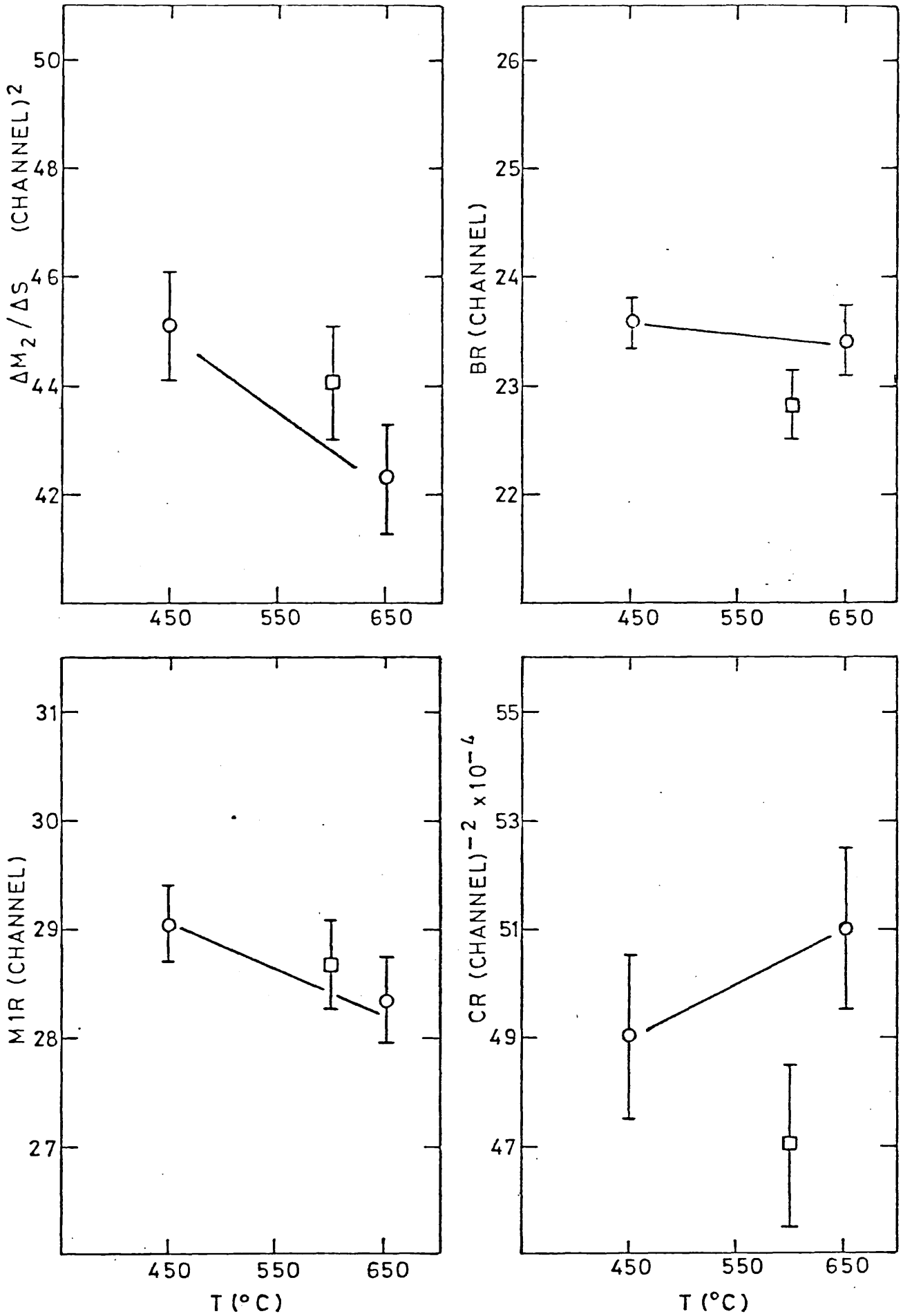
Figure 8.3.1.(d)   Variation of RID Curve Parameters as a Function of
                    Irradiation Temperature for TZM Subjected to Neutron
                    Fluences of 1.5 and 3.5 x 10^{22} n/cm^2

a)
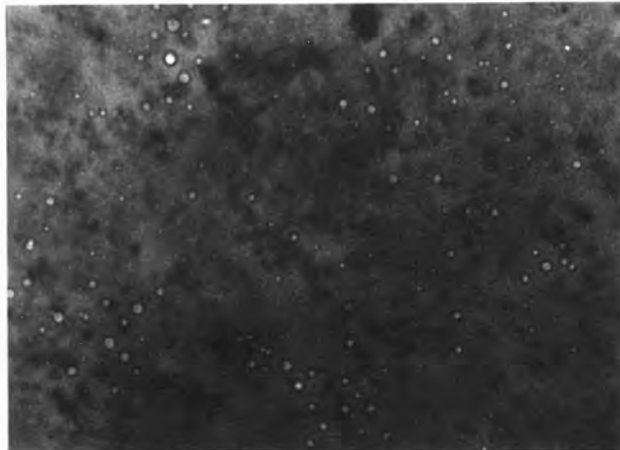
b)

c)
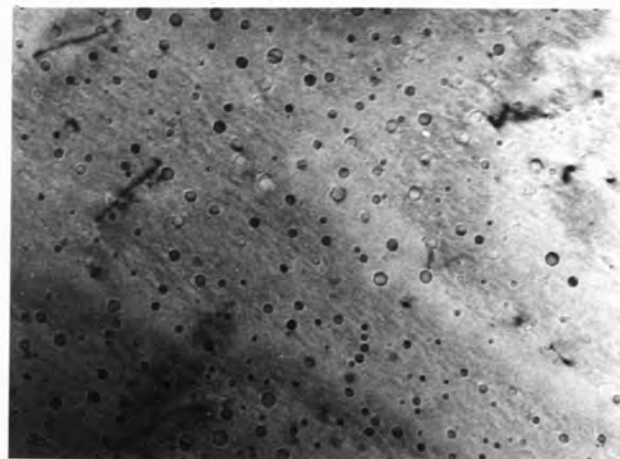
Figure 8.3.2   Electron Micrographs for Molybdenum Irradiated to
A Neutron Fluence of 8.0×10^{22} n/cm^2 at
a) 450°C   b) 550°C   c) 650°C

explain why (i) the RID parameters for TZM have significantly changed from their values at 450°C and (ii) their values are similar to the values found for molybdenum at 450°C (where a mixture of voids and loops exist). Finally, the loop configuration is found to disappear at 650°C thus rendering voids the only traps for positrons. This is signified by the further significant change in RID parameters occurring between 550°C and 650°C.

Similar correlations between RID parameters and electron microscopy measurements can be found for the cases of molybdenum (figure 8.3.1(a)) and TZM (figure 8.3.1(d)) neutron-irradiated to doses of 1.5 and 3.5 x 10^{22} n/cm^2. However, for reasons of repetitiveness, they are not discussed here.

8.3.2.1 Characterisation of Irradiation-Induced Defects

From table 8.2.1 it is apparent that for both molybdenum and TZM irradiated to a fluence of 8 x 10^{22} n/cm^2 at 650°C the measured RID parameters are characteristic of voids. Similarly, TZM irradiated to a fluence of 8 x 10^{22} n/cm^2 at 450°C provides shape parameters characteristic of loops. The ability for positrons to provide such a distinction between two important defect-types encountered in irradiated material could make the positron technique (and shape parameter analysis) extremely valuable in future non-destructive testing of irradiated reactor components.

8.3.3 Void Shrinkage

The percentage volume of material dislodged as a consequence of void formation during irradiation may be quantified by the expression 4/3 $(\pi \bar{R}^3 \rho)$ where $\bar{R}$ is the mean void radius and ρ the void density. This expression is also referred to as the void swelling since the dislodged material is interstitial in nature and the strain fields required for their accommodation in the lattice forces the irradiated sample to macroscopically expand (or swell). Clearly, void swelling advances with both increased void density and mean void radius.

The phenomenon of void shrinkage may be considered to be the opposite of void swelling - i.e. the percentage volume of void space diminishes. Void shrinkage has been observed by electron microscopy after annealing of neutron-irradiated molybdenum at 60°c (e.g. Petersen et al 1975) and also *during* neutron-irradiation performed at suitably elevated temperatures (e.g. Evans 1980).

Temperature-induced void-shrinkage behaviour is relatively well understood (e.g. Evans 1975). Essentially, voids of radius below a critical value at a given temperature become unstable and either shrink in size or disappear (classical Ostwald ripening process). Consequently the void density decreases and the vacancies released from the smaller voids migrate to and coalesce with the larger, stable voids, thus increasing the mean void radius. The rate at which shrinkage and growth occurs depends on the irradiation temperature. Hence, in the temperature range at which voids may be formed, a higher irradiation temperature produces a lower void density with larger mean void radius.

you don't get growth.

Reference to table 8.2.1 illustrates temperature-induced shrinkage for molybdenum at 8 x 10^{22} n/cm^2. It is seen that the irradiation at 650°C provides a lower void density (and a higher mean void radius) than for the case of 550°C. Indeed, the void swelling of 0.87% at 550°C is reduced to 0.79% at 650°C. This behaviour may be seen visually in the electron micrographs of figures 8.3.2(b)-(c).

8.3.3.1 Void Shrinkage as a Function of Irradiation Fluence

So far our discussion has centred on temperature-induced void shrinkage. Up till now it has been expected that swelling induced by neutron-irradiation at suitable temperatures will increase as a function of the irradiation dose - i.e. further supplies of vacancies produced by increased displacement events will nucleate new voids and/or feed the existing ones. However, recent evidence has shown that this is not the case for molybdenum and its alloy TZM. Evans (1979 and 1980) irradiated molybdenum and TZM at 450°C at three different fluences - 1.5, 3.5 and 8.0 x 10^{22} n/cm^2. These irradiations were also performed at 550°C and 650°C. In fact, our positron

annihilation measurements have been performed on some of the above-mentioned molybdenum and TZM samples.

Evans (1979 and 1980) observed a void concentration of 2.8 x 10^{17} cm^{-3} with a mean void radius of 24 Å following electron microscopy on molybdenum samples irradiated at 1.5 x 10^{22} n/cm^2 at 450°C. Inspection of table 8.2.1 reveals that irradiations at 450°C performed on molybdenum at successively higher doses than 1.5 x 10^{22} n/cm^2 have progressively decreased the void concentration with a simultaneous increase in the mean void radius. Clearly, such results manifest the process of void shrinkage. Void shrinkage has been seen to occur more dramatically in TZM as a function of irradiation dose at 450°C - reference to table 8.2.1 shows that voids present at a dose of 1.5 x 10^{22} n/cm^2 have disappeared after a dose of 8.0 x 10^{22} n/cm^2. Evans (1979, 1980) has also found evidence of void shrinkage induced by increased neutron doses at 550°C for both molybdenum and TZM. Evidence of void shrinkage behaviour for irradiations performed at 650°C, however, has not been found.

8.3.3.2 Testing for an Impurity Role in Void Shrinkage Mechanisms

Evans (1979, 1980) has proposed that transmutation-induced impurities migrating to the void surfaces may be responsible for inhibiting the jump of vacancies into voids, thus allowing a net flux of interstitials to the void surface, and so encouraging shrinkage. In the case of TZM the alloying elements may also be migrating to the void surfaces thus producing the more dramatic effect observed. In fact, Marwick (1978) has derived expressions to show that for concentrated alloys solute atom segregation at void surfaces can result in the void rejecting vacancies. The reason why the shrinkage phenomenon has not been found over the considered range of doses at 650°C might then be explained by the thermal emission of impurities from void surfaces at this higher temperature, thus making it more difficult for a given neutron dose to coat the surface with the necessary concentration to induce shrinkage.

Before RID parameters are discussed it is pointed out that the void sizes observed in this study have radii such that positron

behaviour is expected to be independent of the void dimensions (e.g. Hautojarvi et al 1977). This is illustrated in figure 8.3.3 where irradiations performed on molybdenum samples by Bentley (1975) have produced void radii in the range 10-45 Å. The lifetime, τ_2, associated with positrons trapped at voids in these samples (as measured by Thrane et al 1977) is seen to be independent of void size. Also, from measurements taken on the Harwell Doppler-broadening system (AERE, 1978) the shape parameter $\Delta M_2/\Delta S$ has been evaluated and plotted as a function of void radius. The value of $\Delta M_2/\Delta S$ at 330°C varies significantly from its values in the range 400-900°C. This is explained by a significant presence of loops in this sample as observed by Bentley (1975) - otherwise Doppler measurements indicate independence of positron behaviour with void size.

In order to test for the emergence of an impurity presence at the void surface with increasing irradiation dose at 450°C, the most obvious approach is to characterise the positron behaviour at voids for each of the doses 1.5, 3.5 and 8.0 x 10^{22} n/cm^2 in molybdenum and TZM. Changes in positron characteristics may then be attributed to the arrival of impurities at the void surface. Unfortunately, such a comparison cannot be performed with our results since varying doses give rise to varying assortments of defect-types (table 8.2.1) - remember that the shape parameters characterise all the defect-types present in the lattice. In fact, the only pertinent comparison that can be made in this study is that between samples 1 and 2 defined in table 8.3.1. Both samples are pure molybdenum and contain void defects only.

Table 8.3.1   Testing for an impurity role in void shrinkage

Sample No.	Sample Details	$\Delta M_2/\Delta S_2$ (Channel)	M1R (Channel)	BR (Channel)
1	Molybdenum, 3.5 x 10^{22} n/cm^2, 450°C	43.09+1.3	28.60+0.4	20.68+0.4
2	Molybdenum, 8.0 x 10^{22} n/cm^2, 650°C	40.76+1.3	27.69+0.4	20.56+0.4
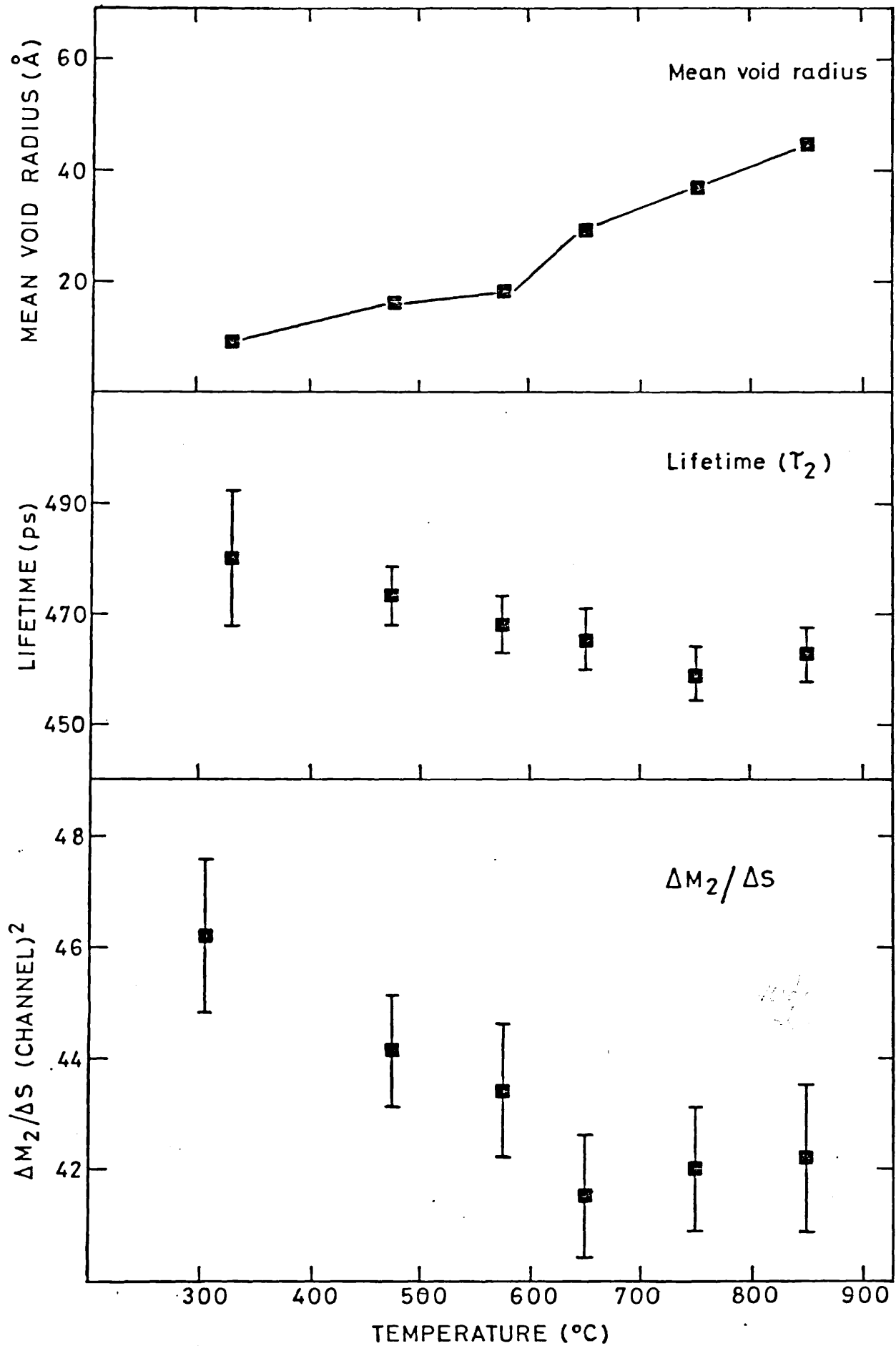
Figure 8.3.3   Dependence on Void Size of the Positron Lifetime (after Thrane et al, 1977) and Shape Parameter, $\Delta M_2/\Delta S$, for the Neutron-Irradiated Samples of Bentley (1975)

From section 8.3.3.1 it is known that void shrinkage mechanisms are operating in sample 1 and so impurities may be at the void surface. Voids in sample 2 are not thought to suffer from void shrinkage and should, therefore, provide voids of 'clean' surface. The comparison between samples 1 and 2 is illustrated in table 8.3.1. The errors quoted include the 25% uncertainty associated with the Monte Carlo evaluation of standard deviations in 'shape' parameters. Both $\Delta M_2/\Delta S$ and M1R provide evidence of a change in defect environment. M1R offers a change just outside standard error and although the variation in $\Delta M_2/\Delta S$ does not match statistical precision it is of comparable magnitude. However, no evidence is found for change in BR. It seems that molybdenum is an example of a metal for which the usefulness of BR is lost because of the large Gaussian component a typical lineshape possesses (section 8.1) - changes in width are probably not as easy to detect as for the case of sharper lineshapes. Accordingly, this section would suggest an impurity presence at voids undergoing the process of shrinkage. It is desirable that further comprehensive study be performed to clarify the situation since shrinkage behaviour has important implications in the field of reactor materials technology.

8.3.4 Conclusions

RID defect-specific parameters have been used to study the defect environment in samples of molybdenum and TZM irradiated at various temperatures and fluences. Changes in shape parameter have indicated changes in defect structure, and correlate well with the results of electron microscopy. It has been possible to characterise dislocation loops and voids. The use of shape parameters has provided some evidence of an impurity role in the process of void shrinkage.

C H A P T E R   9 :   C O N C L U D I N G   R E M A R K S

9.1 SUMMARY AND APPRAISAL OF EXPERIMENTAL AND ANALYTICAL PROGRAMME

This thesis has attempted to assess the nature of defects in the mechanically deformed states of Cu, Al, Fe, Ni and Ti. Evidence of a point defect presence in the cases of Cu and Al has not been found, and positrons appear to undergo 'point-like' trapping at dislocations with a zero-point energy identical to that found for positron trapping at thermally generated vacancies. However, a point defect presence is indicated in the deformed states of Ti, Ni and Fe, and for the latter two cases is tentatively attributed to vacancy clusters. Trapping model fits to data derived from cold-rolled samples have revealed the nature of the stress-strain, work-hardening relationships.

Characterisation of voids and dislocation loops in neutron-irradiated Mo and TZM has been achieved through 'defect-specific' analysis. There is evidence to suggest that void shrinkage behaviour induced by increased irradiation-dose is due to impurities at the void surface.

9.1.1 Model-Independent Analysis

Some shortcomings of RID Curve analysis are now briefly discussed:-

(i) 'Shape' analysis performed on Cu and Al has indicated that the nature of the annihilation radiation emerging from the mechanically deformed state is 'vacancy-like', yet has been incapable of resolving the true nature of the defect-traps (thought to be dislocations following model-dependent analysis). The inability to distinguish between vacancies and dislocations is disappointing and invalidates 'shape' analysis (in its present form) from playing an important role in some kinds of isochronal annealing experiments - i.e. those for which vacancies and dislocations may be the only defect-types present in the test sample. Similarly, the

usefulness of RID parameters in future non-destructive-testing (NDT) applications may be severely limited in view of the inability to distinguish between the vacancy and the dislocation. However, future success in 'characterisation' might be possible if suitable deconvolution techniques are applied.

(ii) Fractional errors associated with RID parameters are large compared with those associated with the S-parameter. Hence, small changes in the nature of defect-types (sometimes indicated by variations in S) may not be sensed by the RID parameters unless the experimenter is prepared to collect many more events than $\sim 10^6$ normally collected in Doppler studies, thereby reducing the 'noise' on difference curves.

(iii) Parameters such as $\Delta M_2/\Delta S$ and MlR are dependent on noise-dominated channels and this can dramatically affect their sensitivity.

However, the following advantages may be ascribed to RID Curve analysis:-

(i) Computation is relatively unsophisticated (important for NDT applications.

(ii) RID parameters have been successful in distinguishing between two important defect-types - i.e. voids and dislocation loops. On this basis 'shape' analysis should be extremely useful in distinguishing between vacancies/dislocations and vacancy clusters, thus rending it useful in certain kinds of defect study and NDT applications.

(iii) Since the analysis is model-independent the dangers of prejudicing the extraction of real, physical changes from run to run due to improper modelling do not exist.

9.1.2 Model-Dependent Analysis

The main disadvantages associated with model-dependent, curve fitting analysis are:-

(i)   Sophisticated computing.

(ii) Difficulties in attaining good fits when one of the fitted functions (i.e. parabola or Gaussian) is dominated in intensity by the other - this limits the number of metals to which our curve fitting technique can be successfully applied.

(iii) The possible risk of disguising real, physical changes from run to run as a consequence of 'force-fitting' an improper (approximate) model.

However, model-dependent analysis has provided estimates of positron zero-point energies and electron Fermi energies at defect sites. In the particular cases of Cu and Al such analysis has indicated that dislocations are the trapping centres for positrons annihilating in the mechanically deformed state.

9.2 TOWARDS THE FUTURE

At the present time, the use of positron annihilation in the study of solid-state crystal defects encompasses a vast spectrum of activity. For instance, recent developments aimed at producing high yields of 'slow-positrons' (e.g. K. Lynn at Brookhaven National Laboratory, USA and R. Howell at Lawrence Livermore Laboratories, USA) are making possible the study of surfaces. Inevitably, such activity ensures that ideas, technologies, experimental and analytical programmes are ever-waiting to be pursued at some future date. Essentially, the work described in this thesis has revolved around the main theme of 'characterisation' of individual defect-types and, accordingly, suggestions for future activity pertinent to this theme are briefly discussed.

Firstly, continued activity in the field of developing deconvolution techniques for annihilation lineshapes would be highly desirable in the absence of immediate advances in the improvement of semiconductor detector resolutions. Such developments would help highlight the intrinsic physical differences that exist between positron and electron characteristics at vacancies and dislocations, and would also provide more useful feedback to the theoretician.

Secondly, the need to characterise vacancies in high melting point metals makes the 'remote-source' method more attractive (section 3.4.4) and, as such, should be more fully explored.

Finally, the 'easily-computed' RID parameters have been capable of distinguishing between dislocation loops and voids (important in nuclear reactor technology). With more refinement of 'shape' parameters (e.g. through development and application of powerful yet unsophisticated deconvolution techniques) distinction between vacancies and dislocations might be achieved. Thus, in NDT applications where assessment of the 'nature of damage' is as important as measurement of the general 'level of defectiveness', RID parameters would be extremely valuable. In view of the potential value of the positron technique in the field of NDT applications, more activity should be encouraged with a view to its development as a standard NDT tool for use 'in-the-field'.

APPENDIX 1 : TO SHOW THAT THE SHAPE OF DIFFERENCE CURVES REMAIN CONSTANT WHEN POSITRONS ARE TRAPPED AT A SELECTION OF DEFECT-TYPES AND ONLY ONE OF THEM VARIES IN CONCENTRATION

Let there be n types of defect in the lattice, all of which trap positrons. The trapping model (section 2.5.2.2) states that the fraction of positrons, P_j, trapping in the jth defect-type is given by

$$P_j = \frac{\mu_j C_j}{\lambda_f + \sum_{j=1}^{n} \mu_j C_j} = \frac{\mu_j C_j}{\lambda_f + \mu_J C_J + \sum_{j=1}^{n, j \neq J} \mu_j C_j} \qquad (1)$$

where $\lambda_f + \mu_J C_J + \sum_{j=1}^{n, j \neq J} \mu_j C_j = \gamma$ (say)

and the symbols have their usual meanings. Now let the concentration of the Jth defect vary to C_J' such that $C_J' = \beta C_J$. The new trapping fractions $(j \neq J)$ will be given by

$$P_j' = \frac{\mu_j C_j}{\lambda_f + \beta \mu_J C_J + \sum_{j=1}^{n, j \neq J} \mu_j C_j} \qquad (2)$$

where $\lambda_f + \beta \mu_J C_J + \sum_{j=1}^{n, j \neq J} \mu_j C_j = \gamma'$ (say)

and dividing equation (1) by equation (2) one obtains

$$P_j' = (\frac{\gamma}{\gamma'}) P_j \quad (j \neq J) \qquad (3)$$

i.e. the trapped fractions for all defect-types $(j \neq J)$ vary by the same factor when only the Jth defect-type varies in concentration.

Consider the observed e^+-e^- momentum distribution F_1 (p) given by

$$F_1 (p) = \alpha_J f_J (p) + \sum_{j=0}^{n, j \# J} \alpha_j f_j (p) \qquad (4)$$

where f_j (p) is the e^+-e^- momentum distribution derived from annihilations at defect-type j with amplitude α_j (j = 0 denotes annihilations in the free state). Since the shape of f_j (p) is unique for the jth defect-type, the amplitude α_j is proportional to the fraction of positrons annihilating in the jth mode. Hence, if the concentration of the Jth defect-type varies to give new amplitudes α_j' such that $\alpha_J' = m\alpha_J$ and (by virtue of equation 3) $\alpha_j' = \beta \alpha_j$ (j≠J) one obtains the distribution F_2 (p) given by

$$F_2 (p) = m \alpha_J f_J (p) + \beta \sum_{j=0}^{n, j \neq J} \alpha_j f_j (p) \qquad (5)$$

Subtraction of equation (5) from equation (4) yields the difference curve D(p) such that

$$D(p) = (\alpha_J - m\alpha_J) f_J(p) + (1 - \beta) \left\{ \sum_{j=0}^{n, j \neq J} \alpha_j f_j(p) \right\} \qquad (6)$$

However, since for the normalised observed distributions

$$\alpha_J + \sum_{j=0}^{n, j \neq J} \alpha_j = 1 \qquad (7)$$

and

$$m\alpha_J + \beta \sum_{j=0}^{n, j \neq J} \alpha_j = 1 \qquad (8)$$

one obtains

$$\beta = \frac{1 - m\alpha_J}{1 - \alpha_J} \qquad (9)$$

Substitution of equation (9) into equation (6) and subsequent manipulation yields the expression

$$D(p) = \alpha_J (m - 1) \left\{ (\frac{1}{1 - \alpha_J}) f(p) - f_J(p) \right\} \tag{10}$$

where

$$f(p) = \sum_{j=0}^{n, j \neq J} \alpha_j f_j(p)$$

Hence, the effect of only varying the Jth defect concentration simply changes the amplitude of the difference profile and not its shape.

APPENDIX 2 : EVALUATION OF THE ZERO-POINT ENERGY ASSOCIATED WITH POSITRONS TRAPPED AT DEFECTS

At a defect, the trapped positron is assumed to behave like a harmonic oscillator in its ground state. The ground state wavefunction is given by

$$\psi_0(x) = \left(\frac{\alpha}{\sqrt{\pi}}\right)^{\frac{1}{2}} e^{-\alpha^2 x^2/2} \tag{1}$$

where

$$\alpha = \left(\frac{m\omega}{\hbar}\right)^{\frac{1}{2}} \tag{2}$$

The zero-point energy (in one cartesian direction) is given by

$$E_0 = \hbar\omega/2 \tag{3}$$

Since the ground state wavefunction is Gaussian in nature, the associated momentum distribution is also Gaussian. The positron distribution to be smeared into the Doppler electron distribution may, therefore, be described by the normal distribution

$$f(\Delta E) = \frac{1}{(2\pi)^{\frac{1}{2}}\sigma} e^{-(\Delta E)^2/2\sigma^2}$$

whose standard deviation is given by σ (defined by the user in the computational generation of the distribution) and the positron Doppler energy shift, ΔE, is related to the positron momentum through the expression $p = 2(\Delta E/C)$. Hence,

$$<p^2> = \frac{4}{c^2} <\Delta E^2> \tag{5}$$

$<p^2>$ may be evaluated from the ground-state wavefunction through the integral

$$\int_{-\infty}^{+\infty} \psi_0^* (x) \; \hat{p}^2 \; \psi_0(x) \; dx$$

where $\psi_0^* (x)$ is the complex conjugate of $\psi_0(x)$ and $\hat{p}^2$ is the square of the momentum operator $-ih \frac{\partial}{\partial x}$. Hence,

$$<p^2> = -\int_{-\infty}^{+\infty} (\frac{\alpha}{\sqrt{\pi}})^{\frac{1}{2}} \; e^{-\alpha^2 x^2/2} \; \hbar^2 \; \frac{\partial^2}{\partial x^2} \; (\frac{\alpha}{\sqrt{\pi}})^{\frac{1}{2}} \; e^{-\alpha^2 x^2/2} \; dx = \tfrac{1}{2} \hbar\omega \, m \qquad (6)$$

Using equations (3), (5) and (6) it is found that

$$E_0 = \frac{4}{m \, c^2} \; <\Delta E^2> \qquad\qquad (7)$$

and since $<\Delta E^2> = \sigma^2$, the one-dimensional oscillator zero-point energy may be written as $4\sigma^2/m \, c^2$. However, for the three dimensional harmonic oscillator $E_0 = 3/2 \; (\hbar\omega)$ and, hence, the total zero-point energy of the positron may be described by

$$E_0 = 3 \left(\frac{4 \; \sigma^2}{m \, c^2} \right) \qquad\qquad (8)$$

A P P E N D I X 3 : MONTE CARLO SIMULATION OF ANNIHILATION LINESHAPES

Program FASMONTE has been written to generate a series of random spectra from a single experimental lineshape. Errors in RID curve parameters can, therefore, be estimated (section 4.2.4). The main features of the program are listed below.

PROGRAM FASMONTE

```
C     TWO SPECTRA (REF. AND DEF.) ARE READ IN FROM STORAGE MAGNETIC
C     TAPE. BOTH THESE SPECTRA ARE FITTED BY A CUBIC SPLINE AND
C     NORMALISED TO A PEAK HEIGHT DEFINED BY THE USER. THE SMOOTHED
C     SPECTRA ARE THEN FED TO THE RANDOM NO. GENERATOR (HARWELL
C     SUBROUTINE FA03A) AND A SERIES OF RANDOM SPECTRA GENERATED.
C     THE ORIGINAL SPECTRA, AS WELL AS THE RANDOM SPECTRA, ARE THEN
C     WRITTEN ONTO MAGNETIC TAPE.
      DIMENSION XPOS(1024),NSPC(1024),RNSPC(1024),CONSPC(1024),
     1NCOMP(1028),NHEAD(4),XWT(1024),XERR(1024),XN(512),FN(512),
     1GN(512),DN(512),THETA(1024),W(11782),FERROR(1024),XSPC(1024),
     1ICNSPC(20000),IRNSPC(20000)
      EQUIVALENCE (NCOMP(1),NHEAD(1)),(NCOMP(4),NSPC(1))
      NPK = 790
      COUNT = 0.0
      MM = 0
      ICOUNT = 0
      II = 0
      INSER = 1
C     INSPEC: RECORD SERIAL NO. TO BE READ IN (REF. SPEC.)
C     NDSPEC: RECORD SERIAL NO. TO BE READ IN (DEF. SPEC.)
C     NRMHT: PEAK HEIGHT OF SPECTRUM TO RANDOM GENERATOR
C     NSER: RUN SERIAL NO. ON NEW STORAGE TAPE
C:    NWT: DEFINES MODE OF ANALYSIS. IF NWT = 0 THEN FIT FOR
C     SPECIFIED LINESHAPE IS FED STRAIHGT TO RANDOM GENERATOR. IF NWT > 0
C     FITTED DEFORMED SPECTRUM IS WEIGHTED SO AS TO SIMULATE ANOTHER
C     DEGREE OF DEFORMATION.
```

```
      READ(5,1) KNOTS,INSPEC,NDSPEC,NRMHT,NSER,IDATE,NWT
     1FORMAT(7I10)
              .            .
           .        .
                 .          .
      READ(60,END=1002) NCOMP
 1002 IF(NHEAD(3).LT.INSPEC) GO TO 1000
      IF(NHEAD(3).EQ.INSPEC) GO TO 10
      IF(NHEAD(3).LT.NDSPEC) GO TO 1000
   10 MM = MM + 1
      DO 20 J = 1,1024
      XPOS(J) = J
      RNSPC(J) = FLOAT(NSPC(J))
      XWT(J) = SQRT(1.0/RNSPC(J))
   20 CONTINUE
C     NOW FIT REQUIRED SPECTRUM TO CUBIC SPLINE  (PERFORMED BY
C     HARWELL SUBROUTINE VC03A)
      KNOTS = 512
      CALL VC03A(1024,KNOTS,XPOS,RNSPC,XWT,XERR,XN,FN,GN,DN,
     1THETA,1,W)
      N = KNOTS
      RNSPC(1) = TG01B(-1,N,XN,FN,GN,XPOS(1))
      DO 30 J = 2,1024
   30 RNSPC(J) = TG01B(10,N,XN,FN,GN,XPOS(J))
      IF(MM.EQ.1) GO TO 21
      GO TO 26
   21 DO 12 J = 1,1024
   12 CONSPC(J) = RNSPC(J)
      GO TO 22
   26 DO 988 J = 1,1024
      RNSPC(J) = ((FLOAT(NWT)*CONSPC(J))+RNSPC(J))/(FLOAT(NWT)+1.0)
  988 CONTINUE
      IF(NWT.NE.0) GO TO 40
   22 DO 35 K = 1,1024
      IF(RNSPC(K).LE.0.0) RNSPC(K) = 1.0
   35 FERROR(K) = (RNSPC(K) - FLOAT(NSPC(K)))/RNSPC(K)
      IF(MM.EQ.1) GO TO 36
      GO TO 40
C     THE NEXT SECTION PRINTS OUT DETAILS OF REFERENCE AND DEFORMED
C     SPECTRA ON LINE-PRINT AND WRITES TWO FITTED SPECTRA ONTO
C     MAGNETIC TAPE
```

```
          .                 .
          .                 .
C       THE FOLLOWING SECTION ALLOWS THE CORRECT SPECTRUM TO BE FED
C       TO THE RANDOM GENERATOR
 1001 J1 = NPK - 40
      J2 = NPK + 40
      XA = 0.0
      XB = 0.0
      DO 70 J = J1,J2
      IF(CONSPC(J).GT.XA) XA = CONSPC(J)
   70 IF(RNSPC(J).GT.XB) XB = RNSPC(J)
      XFAC1 = FLOAT(NRMHT)/XA
      XFAX2 = FLOAT(NRMHT)/XB
      DO 100 K = 1,30
      COUNT = COUNT + 1.0
      XX = COUNT/2.0
      IX = XX
      REM = XX - FLOAT(IX)
      IF(REM.GT.0.0) GO TO 25
      DO 24 J = 1,1024
   24 XSPC(J) = RNSPC(J)*XFAC2
      XFAC = XFAC1
   28 DO 80 J = 1,1024
      STD = SQRT(XSPC(J))                    -
      CALL FA03A(STD,YN)
      XSPC(J) = (XSPC(J) + YN)/XFAC
   80 NSPC(J) = XSPC(J)
C       NEWLY GENERATED SPECTRA ARE NOW WRITTEN ONTO MAGNETIC
C       TAPE
          .                 .
          .   .             .


      STOP
      END
```

A P P E N D I X 4 : COMPUTATIONAL DESCRIPTION OF ANNIHILATION LINESHAPE FITTING

The library program NIHILIB (consisting of a series of subroutines) has been written to perform all aspects of control line and annihilation line analysis. The main elements of this program that relate specifically to annihilation lineshape fitting are illustrated below.

```
      SUBROUTINE NRMLIZE
C
C     THIS ROUTINE NORMALISES THE EXPERIMENTAL RESOLUTION FUNCTION
C     AND, IF REQUIRED, SMEARS THEM WITH A POSITRON GAUSSIAN
C     DISTRIBUTION
C
      COMMON/COMPS/POSTCOMP
C     POSTCOMP IS THE STD. DEV. OF NORMALISED POSITRON
C     DISTRIBUTION (DEFINED BY USER)
            .          .

            .          .

      DIMENSION RESADJ(1023)
      DATA RESADJ  /1023*0.0/
      DATA ROOT2PI /2.506628/
      READ (7) COUNTS

            .          .

            .          .

C     SUBTRACT BACKGROUND
      CALL BKGRND(LRSB1, LRSB2, LRSB3, LRSB4, 0.0)
      WRITE(6,9100)
 9100 FORMAT("RESOLUTION PEAK")
      WRITE(6,9500) (CORCNTS(I),I=LRSB2,LRSB3)
C     CONVOLUTE RESOLUTION FUNCTION WITH GAUSSIAN TO EMULATE
C     TRAPPED POSITRON CONTRIBUTION.  LOOP IF NO POSITRON TRAPPING
      IF(POSCOMP.EQ.0.0) GO TO 1000
      DO 800 I = LRSB2,LRSB3
      RESADJ(I) = CORCNTS(I)/(ROOT2PI*POSCOMP)
  800 CONTINUE
      NCONVS = POSCOMP*3
      DO 900 NXCONV = 1, NCONVS
      COEFF = EXP(-(NXCONV*NXCONV)/(2.0*POSCOMP*POSCOMP))/
     1(ROOT2PI*POSCOMP)
```

```
      DO 850 I = LRSB2, LRSB3
      IF((I + NXCONV).LE.1023) RESADJ(I + NXCONV) =
     1RESADJ(I + NXCONV) + CORCNTS(I)*COEFF
      IF((I - NXCONV).GT.0) RESADJ(I - NXCONV) =
     2RESADJ(I- NXCONV) + CORCNTS(I)*COEFF
  850 CONTINUE
  900 CONTINUE

          .          .

          .          .

      RETURN
      END


      SUBROUTINE ANIFIT(IANNO,CENTRE,HEIGHT)
C     ROUTINE CONTROLS CURVE FITTING OF ANNIHILATION LINE BASED
C     ON GAUSSIAN AND PARABOLIC COMPONENTS

          .          .

          .          .

      EXTERNAL MONITOR
      EXTERNAL NXITER
C     SET DESIRED ACCURACY
      DATA EPS /0.01/
C     SET STEP LENGTH FOR NEXT ESTIMATE
      DATA DSTEP /1.0E-5/
C     SET MAX ERROR OF INITIAL GUESS
      DATA DMAX /1.0/
C     SET MAX. NO. CALLS
      DATA MAXITER /500/
C     SET FREQUENCY OF CALLS TO MONITOR ROUTINE
      DATA IPRINT /10/
C     PRESET NO. OF PARAMETERS
      DATA NPARAMS /5/

          .          .

          .          .

C     CALC. SCALING FACTORS FOR PARAMS BASED ON THEIR EXPECTED SIZES
  100 FACTORS(1) = CENTRE
      FACTORS(2) = HEIGHT*GUESS(1,1)
      FACTORS(3) = GUESS(2,1)
      FACTORS(4) = HEIGHT*GUESS(1,2)
      FACTORS(5) = GUESS(2,2)
```

```
C       RESET INITIAL GUESSES
        DO 200 I = 1, NPARAMS
        FITPRMS(I) = 1.0
   200 CONTINUE
C       PERFORM FITTING
        IFAIL = 1
        CALL EO4FBF(NPNTS,NPARAMS,FITPRMS,CLCPNTS,SUMSQR,EPS,DSTEP,
       1DMAX,WORKSPA,2*NPARAMS*NPNTS+2*NPARAMS*NPARAMS+2*NPNTS+
       25*NPARAMS,NXITER,MONITOR,IPRINT,MAXITER,IFAIL)
C       THE FITTED SPECTRUM IS RETURNED AND CHI-SQUARE/DEG. FREEDOM
C       CALCULATED

            .           .

            .           .

        RETURN
        END


        SUBROUTINE NXITER(NPNTS,NFITPRM,FITPRMS,CLCPNTS)
C       ROUTINE CALCULATES NEXT SET OF PREDICTED POINTS BASED ON
C       LATEST FIT PARAMETERS SUPPLIED IN FITPRMS

            .           .

            .           .

C       SCALE FITTED PARAMETER GUESS TO CORRECT MAGNITUDE
        FITTED(I) = FITPRMS(I)*FACTORS(I)
C       CALCULATE UNCONVOLUTED COUNTS
        NXCLC = 0
        DO 300 NXCHAN = LANB2,LANB3
        NXCLC = NXCLC + 1
C       CALCULATE GUASSIAN COMPONENT
        TSQR = (FITTED(1)-NXCHAN**2)
        GWIDTH = TSQR/(FITTED(3)**2)
        GAUSS = 0.0
        IF(GWIDTH.LT.200.0) GAUSS = FITTED(2)*EXP(-GWIDTH)
C       CALCULATE PARABOLIC COMPONENT
        PWIDTH = TSQR/(FITTED(5)**2)
        PARAB = 0.0
        IF(PWIDTH.LT.1.0) PARAB = FITTED(4)*(1.0 - PWIDTH)
        UNCONV(NXCLC) = GAUSS + PARAB
        CLCPNTS(NXCLC) = 0.0
```

```fortran
  300 CONTINUE
C     FIND CHOSEN RESOLUTION FUNCTION
      IRESNO = NOUSE(IANNO)
C     FIND CENTRE OF NORM. RES. FUNCTION
      NRMAX = RSFTCNL(IRESNO)
C     PERFORM CONVOLUTION
      CALL CONVLUT (RSNRMLS(1,IRESNO), NRMAX, NXCLC, CLCPNTS)
            .                 .
            .                 .
      RETURN
      END
```

ACKNOWLEDGEMENTS

References

Afman, H.B., Phys. Stat. Sol., 13 (1972), 623.

Akhiezer, A.I. and Berestetskii, V.B., Quantum Electrodynamics, (New York, Interscience Publishers, 1965).

Alam, A., Fellows, P., McGervey, J.D. and West, R.N., Rad. Eff. Lett., 50, (1979), 27.

Anderson, C.D., Science, 76 (1932), 238.

Arias-Limonta, J. and Varlashkin, P., Phys. Rev. B, 1, no. 1 (1970), 142.

Atomic Energy Office, 'Accident at Windscale No. 1 Pile on 10th october 1957', Prime Ministerial Address to House of Commons (HMSO, London, 1957).

Baraff, G.A. and Schluter, M., Phys. Rev. B, 19, no. 10 (1979), 4965.

Barshay, S., Leber, R. and Lambrecht, R., Appl. Phys., 5, (1974), 67.

Bentley, J., Ph.D. Thesis, University of Birmingham (1975).

Bergersen, B. and McMullen, T., Sol. State. Comm., 24 (1977), 421.

Berko, S. and Plaskett, J., Phys. Rev., 112, no. 6 (1958), 1877.

Berko, S. and Mader, J., Appl. Phys. 5 (1975), 287.

Bhattacharyya, F. and Singwi, K., Phys. Rev. Lett., 29 (1972), 22.

Blackett, P. and Occhialini, G., Proc. Roy. Soc., 139 (1933), 699.

Blewitt, T., Coltmann, R. and Redman, J., Defects in Crystalline Solids, (The Physical Society, London, 1955), 369.

Brandt, W. in 'Positron Annihilation' (Academic Press, New York, 1967), 155.

Brimhall, J., Simonen, E. and Kissinger, H., J. nucl. Mat., 48 (1973), 339.

Brinkmann, J., J. Appl. Phys., 25 (1953), 961.

Broom, T.. Adv. Phys., 3 (1954), 26.

Burton, L. and Huang, W., Am. Jn. Phys., 46, no. 11 (1978).

Cahn, Physical Metallurgy (North Holland Pub. Com., 1965).

Cawthorne, C. and Fulton, E., Nature, 216 (1966), 575.

Chaglar, I., Ph.D. Thesis, Univ. of London (1978).

Cheng, L., Sen, P., MacKenzie, I. and Kissinger, H., Sol. State Comm., 20 (1976), 953.

Coleman, C., Smith, F. and Hughes, A.E., AERE Harwell Report, R-9148 (1978).

Coleman, C., Appl. Phys., 19 (1979), 87.

Coleman, C., Hughes, A.E. and Smith, F., NDT Int. (1979), 267.

Coleman, C., Smith, F. and Hughes, A.E., AERE Harwell Report, R8551 (1976).

Connors, D. and West, R., Phys. Lett., A30 (1969), 24.

Corbett, J., Smith, R. and Walker, , Phys. Rev., 114 (1959), 1452.

Cotterill, R., MacKenzie, I., Smedskjaer, L., Trumpy, G. and Traff, J., Nature, 239 (1972), 99.

Cotterill, R., Peterson, K., Trumpy, G., and Traff, J., J. Phys. F, 2 (1972) 459.

Cottrell, A., Dislocations and Plastic Flow in Crystals (Oxford Univ. Press, 1953).

Cottrell, A., Dislocations and Mechanical properties of Crystals, John Wiley and Sons, New York, 1957) 361.

Cuddy, L., Acta. Met., 16 (1968), 23.

Dannefaer, S. and Kerr, D., Nucl. Inst. and Meth., 131 (1975), 119.

Davé, N. and LeBlanc, R., Appl. Phys., 15 (1978), 197.

Dekhtyar, I.Ya., Levina, D. and Mikhalenkov, V., Sov. Phys. Dokl., 9 (1964), 492.

Dekhtyar, I.Ya., Physics Reports 9C, no. 5 (1974).

Dirac, P.A.M., Proc. Roy. Soc., A117 (1928), 610.

Dirac, P.A.M., Proc. Roy. Soc., A CXXVI (1930a), 360.

Dirac, P.A.M., Proc. Camb. Phil. Soc., 26 (1930b), 361.

Dlubek, G., Brummer, O. and Hensel, E., Phys. Stat. Sol. (a), 34 (1976), 737.

Dlubek, G., Brummer, O., Kristall and Technik, 12, no. 5 (1977), 487.

Dlubek, G., Brummer, O. and Sickert, P., Phys. Stat. Sol. (a), 39 (1977a), 401.

Dlubek, G., Brummer, O., Hautojarvi, P. and Yli-Kauppica, J., Report TKK-F-A416 (1980).

Donaghy, J. and Stewart, A., Phys. Rev., <u>164</u>, no. 2 (1967), 391.

Downey, M. and Eyre, B., Phil. Mag., <u>11</u> (1965), 53.

Doyama, M. and Cotterill, R., Proc. 5th Int. Conf. on Pos. Ann., Japan (1979), 89.

Duncan, R., RCA Review, <u>33</u> (1972), 248.

Dupasquier, A., Gallone, A. and Regazzoni, C., Sol. State Comm., <u>35</u>, (1980), 415.

Eldrup, M., Evans, J., Morgensen, O. and Singh, B., Rad. Eff., (1981), in press.

El Khangi, F., Ph.D. Thesis, Univ. of London (1980).

Evans, J., AERE Harwell Report R7966 (1975).

Evans, J. and Eldrup, M., Nature, <u>254</u> (1975), 685.

Evans, J., Nature, <u>278</u> (1979), 728.

Evans, J., Jn. of Nucl. Mat., <u>88</u> (1980), 31.

Eyre, B. and Bartlett, A., Phil. Mag., <u>12</u> (1965), 261.

Eyre, B. and Evans, J., 'Effects of Radiation on Substructure and Mechanical Properties of Metals and Alloys', ASTM-STP529 (1973), 184.

Fluss, M. and Smedskjaer, L., Appl. Phys., <u>18</u> (1979), 305.

Frank, F. and Read, T., Phys. Rev., <u>79</u> (1950), 722. .

Frank, W. and Seeger, A., Appl. Phys., <u>3</u> (1974), 61.

Frois, C., Acta. Met., <u>14</u> (1966), 1325.

Gauster, W., Jn. of Nucl. Mat., <u>62</u> (1976), 118.

Gauster, W., Wampler, W., Jones, W. and Van den Avyle, Proc. 5th Int. Conf. on Pos. Ann., Japan (1979), 125.

Gilman, J., Jn. Appl. Phys., <u>33</u> (1962), 2703.

Goldanski, V., 'Positron Annihilation', Atom. Energy Rev. 6 (Int. At. Energy Agency, Vienna, 1968).

Grosskreutz, J. and Millett, W., Phys. Lett., <u>28A</u>, no. 9 (1969), 621.

Gustafson, D., MacKintosh, A. and Saffarano, D., Phys. Rev., <u>130</u>, no. 4 (1963), 1455.

Hanson, N., The Concept of the Positron (Univ. Press, Camb., 1963).

Harrison, W., Pseudopotentials in the Theory of Metals (Benjamine, New York, 1966).

Hautojarvi, P., Tamminen, A. and Jauho, P., Phys. Rev. Lett., 24, no. 9 (1970), 459.

Hautojarvi, P., Sol. State Comm., 11 (1972), 1049.

Hautojarvi, P. and Vehanen, A., Appl. Phys., 11 (1976), 191.

Hautojarvi, P., Heino, J., Manninen, M. and Nieminen, R., Proc. 4th Int. Conf. on Pos. Ann., Helsinger, Denmark (1976).

Hautojarvi, P., Heino, J., Manninen, M. and Niemenen, R., Phil. Mag., 35 (1977), 973.

Herlach, D. and Maier, K., Appl. Phys., 11 (1976), 197.

Herlach, D., Stoll, H., Trost, W., Metz., H., Jackmann, T., Maier, K., Schaefer, H. and Seeger, A., J. Appl. Phys., 12 (1977), 59.

Hinode, K., Tanigawa, S., Doyama, M., Jn. Phys. Soc. Jap., 42, no. 5, (1977), 1591.

Hodges, C., Phys. Rev. Lett., 25, no. 5 (1970), 284.

Hodges, C. and Scott, M., Sol. State Comm., 12 (1973), 1153.

Hodges, C., J. Phys. F, 4 (1974), L230.

Hood, G., Schultz, R. and Carpenter, G., Phys. Rev. B, 14, no. 4 (1976), 1503.

Hood, G., Eldrup, M. and Petersen, K., Proc. 5th Int. Conf. on Pos. Ann., Japan (1979).

Hughes, A.E. and Pooley, D., Real Solids and Radiation (Wykeham Publications, 1975).

Hughes, A.E., Private Communication.

Jackmann, T., Lichtenberger, P. and Schulte, C., Appl. Phys. 5, (1974a), 259.

Jackmann, T., Schulte, C., Campbell, J., Lichtenberger, P., MacKenzie, I., Wormald, M., J. Phys. F, 4 (1974b), L1.

Johnson, M., Panchanadeeswaran, S., Saterlie, S. and Byrne, J., Phys. Stat. Sol. (a), 42 (1977), K175.

Johnson, M., Saterlie, S. and Byrne, J., Mett. Trans., 9A (1978), 841.

Jorch, H. and Campbell, J., Nucl. Inst. and Meth., (1977), 551.

Kirkegaard, P. and Eldrup, M., Comp. Phys. Comm., 3 (1972), 240.

Kittel, C., Introduction to Solid State Physics (John Wiley and Sons, 5th ed., 1976.

Kohn, W. and Sham, L., Phys. Rev., 140 (1965), 471.

Kopetskii, C., Kulesko, G., Kokhanchik, L. and Zharikov, O., Phys. Stat. Sol. (a), 22 (1974), 185.

Kuhlmann-Wilsdorf, D., Trans. Met. Soc. AIME, 224 (1962), 1047.

Kusmiss, J. and Steart, A., Adv. Phys., 16 (1967), 471.

Lee-Whiting, G., Phys. Rev., 97 (1955), 1557.

Levinstein, H. and Robinson, W., 'The Relations Between Structure and the Mechanical Properties of Metals', Symposium at the National Physical Laboratory, HMSO (1963).

Manninen, M., Nieminen, R., Hautojarvi, P. and Arponen, J., Phys. Rev. B, 12 (1975), 4012.

Mantl, S. and Trifthauser, W., Phys. Rev. Lett., 34, no. 25 (1975), 1554.

Mantl, S. and Trifthauser, W., Phys. Rev. B, 17, no. 4 (1978), 1645.

Mantl, S., Kesternich, W. and Trifthauser, W., Jn. of Nucl. Mat., 69 and 70 (1978), 593.

Martin, J. and Paetsch, R., J. Phys. F, 2 (1972), 997.

Masima, M. and Sachs, G., Z. Physik, 50 (1928a), 161.

Masima, M. and Sachs, G., Z. Physik, 51 (1928b), 321.

Meechan, C. and Sosin, A., Phys. Rev., 113 (1959), 422.

Mijnarends, P., Phys. Rev., 178, no. 2 (1969), 622.

Mogensen, O., Petersen, K., Cotterill, R., Hudson, B., Nature, 239 (1972), 98.

Myllyla, R., karras, M. and Miettinen, T., Appl. Phys., 13 (1977), 387.

MacKenzie, I., Khoo, T., McDonald, A. and McKee, B., Phys. Rev. Lett., 19 (1967), 946.

MacKenzie, I., Eady, J., Gingerich, R., Phys. Lett., 33A, no. 5 (1970), 279.

MacKenzie, I., Phys. Stat. Sol. (a), 12 (1972), K87.

MacKenzie, I. and Sen, P., Phys. Rev. lett., 37, no. 19 (1976), 1296.

McGervey, J. and Trifthauser, W., Phys. Lett., 44A (1973), 53.

McKee, B., Jost, A. and MacKenzie, I., Can. Jnl. Phys., 50 (1972), 415.

McKee, B., Saimoto, S., Stewart, A. and Stott, M., Can. Jn. Phys., 52 (1974), 759.

McLarnon, J. and Williams, D., Jn. Phys. Soc. Jap., 43, no. 4 (1977), 1244.

Nanao, S., Kuribayashi, K., Taniguwa, S. and Doyama, M., J. phys. F, 7, no. 8 (1977), 1403.

Nielsen, B. and Petersen, K., proc. 4th Int. Conf. on Pos. Ann., helsinger, Denmark (1976).

Nieminen, R. and Laakkonen, J., Appl. Phys., 20 (1979), 181.

Niemenen, R., Laakkonen, J., Hautojarvi, P., and Veharen, A., Phys. Revi. B, 19, no. 3 (1979), 1397.

Ohr, S. and Beshers, D., Phil. Mag., 10 (1964), 219.

Ore, A. and Powell, J., Phys. Rev., 75 (1949), 1696.

Pard, A. and Garr, K., 'Radiation Damage and Tritium Technology for Fusion Reactors", US-ERDA Conf. 750989, 1 (1975), 312.

Petersen, K., Thrane, N. and Cotterill, R., Phil. Mag., 29 (1974), 9.

Petersen, K., Evans, J. and Cotterill, R., Phil. Mag., 32 (1975), 427.

Petersen, K., Thrane, N. and Trumpy, G., Appl. Phys., 10 (1976), 85.

Petersen, k., 'Crystal Defects Studied by Positrons', Lab. of Appl. Phys. II, Technical Univ. of Denmark, Report LTF II : 1 (1978), 87.

Pry, R. and Henning, R., Acta. Met., 2 (1954), 318.

Rice-Evans, P., Hlaing, T. and Rees, D., J. Phys. F, 6, no. 6 (1976), 1079.

Rice-Evans, P. and Hlaing, T., J. Phys. F, 7, no. 5 (1977), 821.

Rice-Evans, P., Chaglar, I. and El Khangi, F., Phys. Rev. Lett., 40, no. 11 (1978), 716.

Rice-Evans, P., Chaglar, I. and El Khangi, F., Proc. 5th Int. Conf. on pos. Ann., Japan (1979), 235.

Saimoto, S., McKee, B. and Steart, A., Phys. Stat. Sol. (a), 21 (1974), 623.

Schilling, W., Vacancies and Interstitials in Metals (Amsterdam, North Holland, 1970).

Schulte, C., Goland, A., Kusmiss, J., Haung, H. and Meade, R., Phys. Rev. B, 3, no. 2 (1971), 275.

Schultz, P., Ollerhead, R., Lichtenberger, P., Nickel, B., MacDonald, J. and MacKenzie, I., Can. Jn. Phys., 59, no. 3 (1981), 325.

Seeger, A., Dislocations and Mechanical Properties of Crystals, (John Wiley and Sons, New York, 1957), 243.

Seeger, A., Diehl, J., mader, S. and Rebstock, H., Phil. Mag., 2 (1957), 323.

Seeger, A., Proc. 2nd Int. Conf. on the Peaceful Uses of Atomic Energy, Geneva, 6 (1958), 260.

Seeger, A., Kronmuller, H., Mader, S. and Trauble, H., Phil. Mag., 6 (1961), 639.

Segre, E., Experimental Nuclear Physics (Wiley, New York, 1953).

Seighbahn, K., Alpha, Beta and Gamma-ray Spectroscopy (North Holland, Amsterdam, 1965), 21.

Semat, H. and Albright, J., introduction to Atomic and Nuclear Physics (Chapman and Hall, 5th ed., London, 1971).

Shizuma, K., Nucl. Inst. and Meth., 150 (1978), 447.

Simmons, R. and Ballufi, R., Phys. Rev., 117 (1960), 52.

Singhal, S. and Callaway, J., Phys. Rev. B., 19, no. 10 (1979), 5049.

Smedskjaer, L., manninen, M. and Fluss, M., J. Phys. F, 10 (1980a), 2237.

Smedskjaer, 1., legnini, D. and Siegel, R., J. Phys. F, 10 (1980b) L1.

Snead, C., Goland, A., Kusmiss, J., Haung, H. and Meade, R., Phys. Rev. B, 3, no. 2 (1971), 275.

Stewart, A., Can Jn. Phys., 35 (1957), 168.

Takamura, J. and Greenfield, I., Jn. Appl. Phys., 33 (1962), 247.

Taylor, G., Proc. Roy. Soc., A145 (1934), 362.

Thompson, M., Defects and Radiation Damage in Metals (Cambridge Univ. press, 1969).

Thrane, N., Petersen, K. and Evans, J., Appl. Phys., 12 (1977), 187.

Trifthauser, W. and McGervey, J., Appl. Phys., 6 (1975), 177.

Walker, R., Radiation Damage in Solids (Academic Press, London, 1962), 594.

Wallace, P., Sol. State Phys., 10 (1960), 1.

Wampler, W. and Gauster, W., J. phys. F, 8, no. 1 (1978), L1.

Wampler, W. and Gauster, W., phys. letts., 68A, no. 3, 4 (1978), 363.

Weisberg, H. and Berko, S., Phys. Rev., 154 (1967), 249.

West, R., Borland, R., Cooper, J. and Cusack, N., Proc. Phys. Soc., 92 (1967), 195.

West, R., Positron Studies of Condensed Matter (Taylor and Francis Ltd., 1974).

Wilenfeld, J. and Joh, J., IRT Corporation REPORT INTEL-RT 6084-002 (1976).

Young, F., Jn. Appl. Phys., 33 (1962), 963.